Phosphatases and microRNAs: Investigations in the Context of DNA Damage

Phosphatases and microRNAs:

Investigations in the Context of DNA Damage

A dissertation presented

by

Sanket Shyamkant Acharya

to

The Division of Medical Sciences

in partial fulfillment of the requirements

for the degree of

Doctor of Philosophy

in the subject of

Immunology

Harvard University

Cambridge, Massachusetts

November 2015

Dissertation Advisor: Dr. Dipanjan Chowdhury Sanket Shyamkant Acharya

Phosphatases and microRNAs:

Investigations in the Context of DNA Damage

Abstract

Integrity of the cellular genome is constantly threatened by various sources of DNA damage that cause a variety of lesions including double strand breaks. Cells respond to such insults by upregulating the DNA damage response, a carefully orchestrated set of molecular events that leads to transcriptional changes, cell cycle arrest and/or apoptosis. In this dissertation we provide evidence supporting a role for phosphatases and microRNAs (miRNAs) in the cellular response to DNA damage.

53BP1 (tumor suppressor p53 binding protein 1) is a critical mediator of DNA repair signaling and its activity is regulated by several post-translational modifications. Here we show that 53BP1 is phosphorylated during mitosis on two residues, T1609 and S1618, located in the ubiquitination-dependent recruitment motif. These residues are dephosphorylated in late mitosis/early G1 by the PP4C/R3β phosphatase complex, which is required for 53BP1 accumulation at DNA breaks. We discovered that R3β preferentially interacts with 53BP1 in stalled mitosis and determined that this interaction is dependent on the phosphorylation of R3β residue S840 by the cyclin-dependent kinase family member CDK5. We also found that 53BP1 is deliberately excluded from

chromatin during mitosis to prevent genomic instability. Ectopic reactivation of 53BP1 in mitosis causes increased micronuclei and lagging chromosome formation, which can be partially reversed by inhibiting the non-homologous end-joining pathway.

In a more clinical scenario, accidental radiation exposure can cause DNA damage that manifests itself in complex malignancies including bone marrow failure and cancer. In order to accurately predict radiation exposure for better management of radiation accidents, we identified serum microRNA (miRNA) signatures capable of indicating the long-term impact of total body irradiation in animals. Using different doses of radiation we systematically studied the impact of TBI on the hematopoietic system and then identified three miRNA signatures that effectively distinguished between animals exposed to control, sublethal, and lethal radiation. Furthermore, we used radioprotective and radiomitigating agents to show that serum miRNAs can predict not only the dose of radiation but also its impact on animal health. Finally, to investigate the relevance of these miRNAs in humans, we validated our findings in a humanized mouse model.

TABLE OF CONTENTS

Dedicated to my guru,

Ustad Allarakha

And to my parents,

Mr. Shyamkant and Mrs. Padma Acharya

ACKNOWLEDGEMENTS

I want to thank my advisor, Dr. Dipanjan Chowdhury for giving me the opportunity to work in his laboratory. His outstanding mentorship and dedication to excellence has made this dissertation a great learning experience. I also want to thank my DAC committee, Drs. Shiv Pillai, Judy Lieberman, Alan D'Andrea, and Shannon Turley for their invaluable scientific insights. Many thanks go to the outstanding postdoctoral fellows and technicians in the Chowdhury lab who not only work on challenging projects but also strive to generate an exciting research environment.

I want to thank mentors and well-wishers throughout my education without whom I would not be remotely close to completing this doctorate. I am grateful to Dr. Rushdia Yusuf, who taught me much more than laboratory techniques and often helped me navigate turbulent waters. I also want to thank my undergraduate mentor, Dr. Merle Bruno, my undergraduate research advisor Dr. Ellen Rothenberg, and my English teacher in high-school, late Mrs. Sheela Joshi.

Apart from experiments, my greatest source of happiness lays in my music. I pay homage to my gurus Ustad Allarakha and Pandit Nana Oak, who were senior *tabla* maestros and a guiding light for countless musicians around the world. I also wish to thank my Indian classical music teachers Aviraj Tayade, Promod Bhadkamkar and Subhash Dasakkar. Ustad Zakir Hussain, my elder guru-brother, has perhaps been my greatest inspiration in life. I consider myself extremely fortunate to have been his student and shared the stage with him in

concert. His creativity, intelligence, and novelty never fail to amaze me and drive me to go that extra mile.

I am extremely thankful to my Boston friends Rajiv, Shashi, Satya, and Kavita who have brightened evenings with memorable dinners and weekends with game nights and enjoyable conversations. My high-school and undergraduate friends Zankar, Prashant, and Satish deserve a special mention for their selflessness and camaraderie till present.

Words cannot express how indebted I am to my dear parents, Mr. Shyamkant and Mrs. Padma Acharya for instilling in me a passion for science and music and for enriching my life with diverse educational experiences. I want to thank my younger sister, Sonali, whose innocence and simplicity3 continues to inspire me to reach for the stars. Many thanks also go to my in-laws Mr. Somkant and Dr. Alaka Padhye and Richa, who never failed to appreciate every little achievement.

I cannot forget the unwavering support of my lovely wife, Dr. Snehal Padhye. Thank you Snehal for your understanding, your simplicity, and your wisdom, which has made this journey so much more worthwhile. Finally, I want to thank my daughter Meera, who has only been with us for little over a year, yet has completely transformed our lives in so many ways. Thank you Meera for your genuine affection and for adding another reason to thrive and excel.

LIST OF TABLES AND FIGURES

Tables

Figures

Chapter 1: Introduction

Chapter 2: Dephosphorylation enables the recruitment of 53BP1 to double-strand DNA breaks.

Chapter 3: CDK5 regulates 53BP1 recruitment to double strand breaks by phosphorylating R3β S840.

Chapter 4: Serum microRNAs are early indicators of survival after radiation-induced hematopoietic injury.

Chapter 5: Discussion

CHAPTER 1

Introduction

The cellular genome is constantly exposed to exogenous and endogenous sources of DNA damage that cause a variety of toxic lesions. If left unrepaired, these lesions get incorporated in the genome during subsequent cell division cycles in the form of mutations or chromosomal rearrangements. Cells respond to DNA damage by upregulating the DNA damage response (DDR), a highly orchestrated series of events that lead to transcriptional changes, cell cycle arrest, repair of damaged DNA, and/or apoptosis (Chapman et al., 2012b; Goldstein and Kastan, 2015; Lee and Chowdhury, 2011; Lord and Ashworth, 2012). A number of DNA repair pathways have evolved to counteract the various types of lesions that occur (Fig. 1.1). These include mismatch repair, base excision repair, nucleotide excision repair, intra-strand crosslink repair and single strand break repair pathways (Ciccia and Elledge, 2010; Iyama and Wilson, 2013; Moldovan and D'Andrea, 2009). Double strand breaks (DSBs) are a particularly lethal form of DNA damage because their persistence can lead to genomic instability and cancer. DSBs are repaired by two major pathways, homologous recombination (HR) and non-homologous end joining (NHEJ) (Lieber et al., 2010; San Filippo et al., 2008; West, 2003). The evolution of several repair pathways with diverse yet specific functions in counteracting various types of damage underscores the importance of DNA repair in the survival of an organism. In this dissertation, we mainly focus on the molecular mechanisms involved in the repair of DSBs.

DNA Damage Sensors Activate DDR

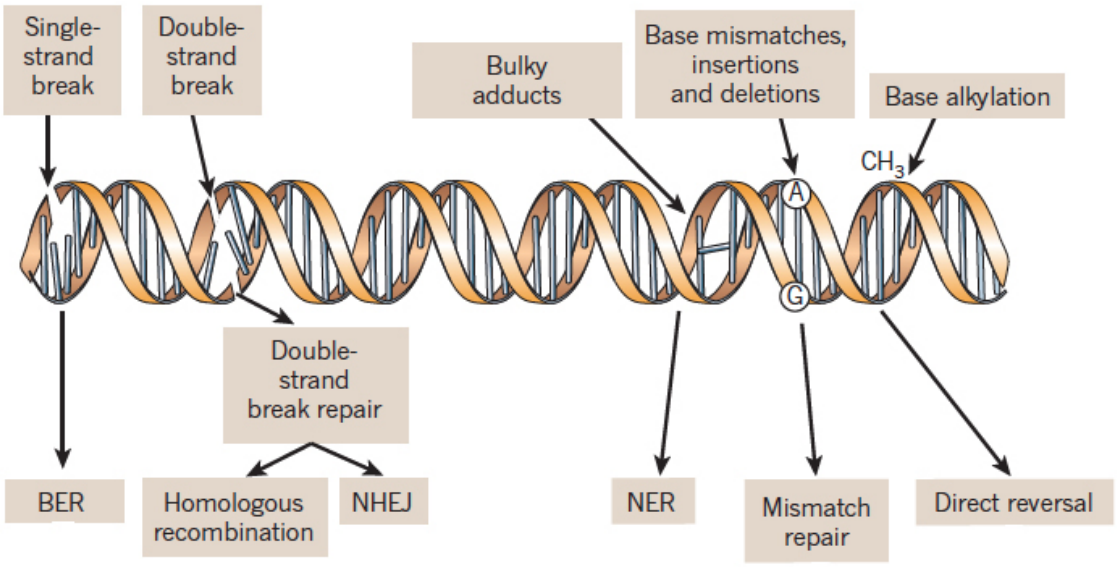

Figure 1.1: DNA repair pathways have evolved to counteract DNA damage caused by endogenous and exogenous sources. The specific pathway employed for repair depends on a type of lesion as well as the stage of the cell cycle (Lord and Ashworth, 2012).

The DDR is highly conserved from yeast to humans and many of the important players in the damage response have been identified. These players can be classified into damage sensors, mediators, transducers and effectors (FitzGerald et al., 2009). One of the earliest events involved in sensing of DNA damage is the activation of the phosphoinositide 3-kinase-like kinases (PIKKs). Three major PIKKs characterized, ATM (ataxia-telangiectasia, mutated), ATR (ATM and Rad3 related), and DNA-PK (DNA-dependent protein kinase), are activated by different types of DNA damage (Cimprich and Cortez, 2008; Shiloh and Ziv, 2013; Smith and Jackson, 1999). ATM and DNA-PK are activated by DNA damaging agents that cause DSBs such as IR or X-rays, while ATR is activated by RPA (replication protein A)-coated ssDNA or DSBs resulting from replication stress. Other sensor proteins such as PARP1 (poly-ADP ribose polymerase 1) and PARP2 may also be activated by SSBs and DSBs (Ciccia and Elledge, 2010).

While DNA-PK has a specific role in regulating proteins involved in end joining pathways, ATM/ATR regulate a plethora of substrates that further orchestrate the downstream response to DNA damage (Bennetzen et al., 2010; Bensimon et al., 2010; Matsuoka et al., 2007). These include the mediator proteins MDC1 (mediator of DNA damage checkpoint protein 1), 53BP1, and BRCA1 (breast cancer 1, early onset), which upon phosphorylation by ATM/ATR localize to damage sites. Apart from the E3 ubiquitin ligase activity of BRCA1, mediator proteins have no apparent enzymatic activity, but may be thought of as recruitment platforms for other DDR proteins involved in repair (FitzGerald et al.,

2009). The damage signal amplified by sensors and mediators is then transmitted to transducers, namely CHK1 (checkpoint kinase 1) (Liu et al., 2000; Zhao and Piwnica-Worms, 2001) and CHK2 (checkpoint kinase 2) (Ahn et al., 2000; Buscemi et al., 2006) (Matsuoka et al., 2000).

In addition to activating factors after DNA damage that constitute the DDR, cells also employ various mechanisms to slow down cell cycle progression. These mechanisms, collectively known as the checkpoint response, provide extra time to allow cells to repair their DNA before cell division thereby inhibiting the transmission of mutations to daughter cells (Li and Zou, 2005) (Lukas et al., 2004). There are three major checkpoints that can be activated in response to DNA damage: the G1/S checkpoint (primarily mediated by p53 halting progression from G1 to S phase), the intra-S checkpoint (activated by stalled replication forks leading to inhibition of DNA replication), and the G2/M checkpoint (activated by negative regulation of CDK1 and suppresses entry into mitosis). By employing checkpoints at different stages during the cell cycle, the cell ensures that the genetic information passed on to daughter cells is accurate.

Double Strand Break Repair Pathways

As mentioned earlier, DSBs can be lethal if left unrepaired. Therefore, it is not surprising that cells have evolved two major pathways to repair double strand breaks, namely HR and NHEJ, although alternative NHEJ (alt-NHEJ) and single-strand annealing (SSA) pathways may be used to repair DSBs in specific scenarios (Hartlerode and Scully, 2009; Lieber, 2010; San Filippo et al., 2008).

The choice of pathway employed to repair DNA is largely dependent on the cell cycle and whether the DNA ends need to be resected (Fig. 1.2).

NHEJ is an error-prone repair pathway and is initiated by the recruitment of the Ku70-Ku80 heterodimer and the DNA-PK catalytic subunit (DNA-PKcs) to the break site (Lieber et al., 2010). DNA-PKcs mediates several phosphorylation reactions that protect the DNA ends from getting resected (Meek et al., 2008). Successful NHEJ requires that the DSB ends be protected from resection by factors such as CTIP (C-terminal binding protein-interacting protein), and EXO1 (exonuclease 1). Recent data suggests that resection is prevented during NHEJ by ATM-dependent phosphorylation of the histone variant H2AX (known as γ-H2AX) (Helmink et al., 2011) and 53BP1 recruitment to damage sites (Bunting et al., 2010; Chapman et al., 2012a). Following binding to DSBs, DNA-PKcs is involved in autophosphorylating itself, which leads to destabilization of its interaction with DNA. This allows end-processing enzymes such as ARTEMIS, and ligases XRCC4 (X-ray repair complementing defective repair in Chinese hamster cells 4), LIG4 (ligase 4), and XLF (XRCC4-like factor 1) to join DNA ends and complete repair (Ciccia and Elledge, 2010; Lieber, 2010).

HR or homology directed repair (HDR) is an error-proof pathway that relies on the availability of a repair template and therefore is more likely to occur during the S and G2 phases of the cell cycle (Heyer et al., 2010; San Filippo et al., 2008). DSBs are recognized by the sensor proteins MRE11-Rad50-Nbs1 (MRN complex) leading to ATM/ATR activation. These proteins orchestrate the

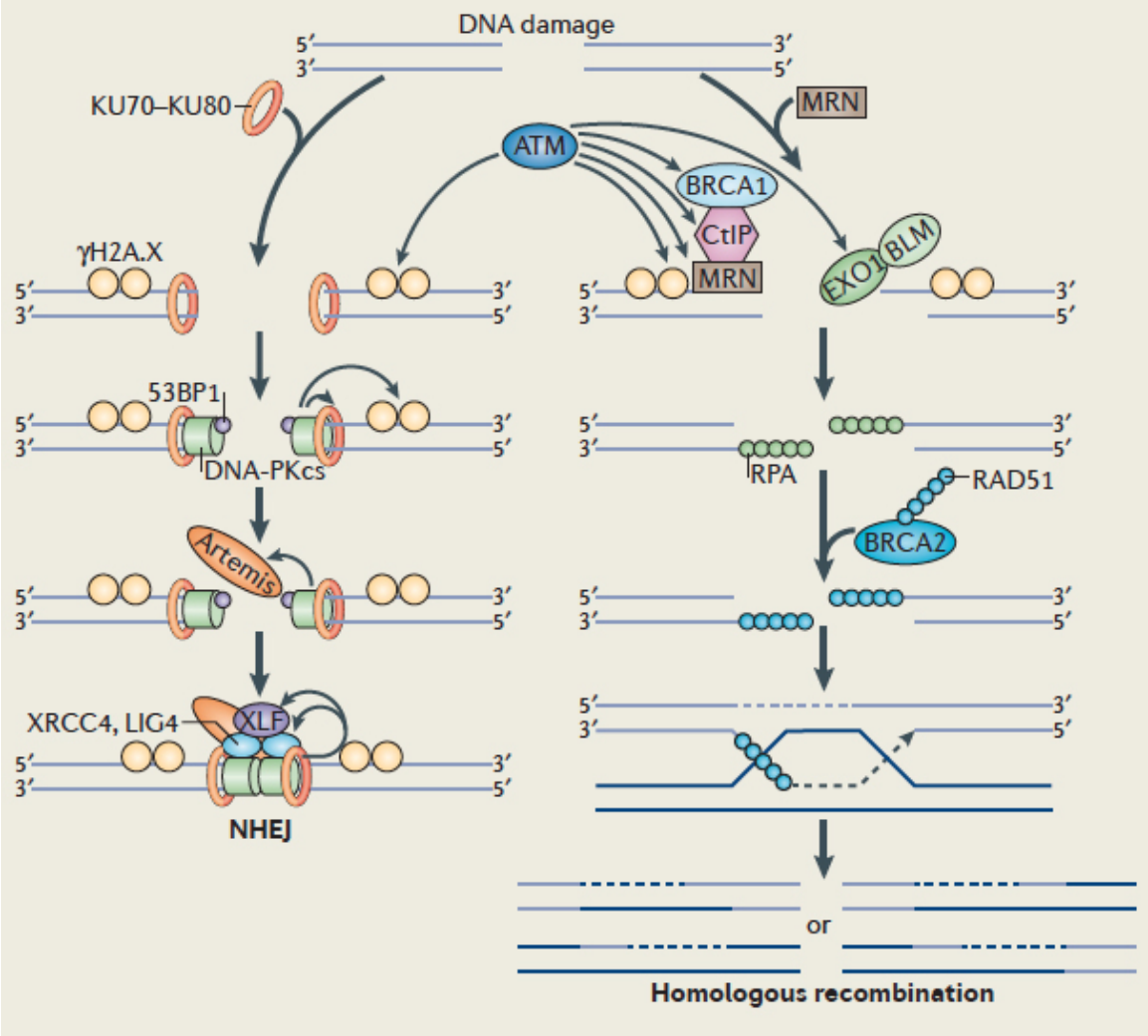

Figure 1.2: Mammalian cells respond to lethal double strand breaks using two major pathways: non-homologous end joining and homologous recombination. Schematic gives an overview of the major molecular players in each pathway (Chowdhury et al., 2013).

subsequent steps of DSB identification and repair by phosphorylating a plethora of DNA repair substrates such as CTIP (You and Bailis, 2010), BRCA1 (Huen et al., 2010), EXO1 and BLM (blooms syndrome RecQ helicase-like) (Bolderson et al., 2010). Single stranded DNA generated as a result of resection is coated with RPA and then replaced with RAD51 in the presence of BRCA2. RAD51 nucleofilaments are involved in invasion of sister chromatid arms in search of homology to form D-loops. The D-loop is then resolved by anti-recombinases and resolvases such as RTEL1 (regulator of telomere length protein 1), MUS81 (ultraviolet-sensitive 81), GEN1 (Gen homologue 1), and EME1 (essential meiotic endonuclease 1) (West et al., 2015).

53BP1

53BP1 has emerged as an important player in DNA damage signaling following DSBs. It was first identified in 1994 using yeast two-hybrid assays as a binding partner of the tumor suppressor p53 and was postulated to be involved in suppressing cellular transformation (Iwabuchi et al., 1994). 53BP1 is a large protein of 1972 amino acids and its domain structure has been well characterized. Among its many structural elements include an ATM-dependent S/T-Q motif (serine or threonine residues followed by a glutamine) at the N-terminus, an oligomeraization domain, a GAR (glycine-arginine rich) domain, a tandem Tudor domain that binds to H4K20me2 (dimethylated lysine 20 of histone 4), a UDR (ubiquitylation- dependent recruitment) motif that interacts with H2AK15ub (ubiquitylated H2A at lysine 15), and a BRCT (BRCA-1 C-terminal)

domain (Fradet-Turcotte et al., 2013; Huyen et al., 2004; Panier and Boulton, 2014; Zgheib et al., 2009) (Figure 1.3). The yeast counterparts of 53BP1, Rad9 in *Saccharomyces cerevisiae* and Crb2 (Rhp9) in *Schizosaccharomyces pombe*, lack sequence homology with mammalian 53BP1, yet both mammalian and yeast 53BP1 are capable of activating checkpoint kinases following DNA damage by stimulation of ATM activity (Harrison and Haber, 2006). This occurs through interaction of the 53BP1 BRCT domain with the RAD50 component of the MRN complex, one of the first sensors of DNA damage (Lee et al., 2010b).

In addition to being involved in stimulating ATM activity, mammalian 53BP1 plays a much broader role in coordinating the DSB response. It has a pivotal role in the joining of DSBs during the process of class switch recombination (CSR) (Manis et al., 2004; Ward et al., 2004). The process of CSR takes place in the germinal centers of lymph nodes wherein antigen-stimulated B cells replace the constant regions of their surface IgM molecules with the constant region of a different antibody isotype. While the generation of these breaks depends on the activity of AID (activation-induced cytidine deaminase) (Muramatsu et al., 2000; Revy et al., 2000), the repair of these breaks is mediated by NHEJ and particularly sensitive to the presence of 53BP1. For example, in the absence of 53BP1, there is ~90% decrease in the efficiency of CSR.

Furthermore, 53BP1 also plays a pivotal role in the regulation of NHEJ versus HR pathway choice and has also been implicated in the joining of deprotected telomeres (Dimitrova et al., 2008). When components of the

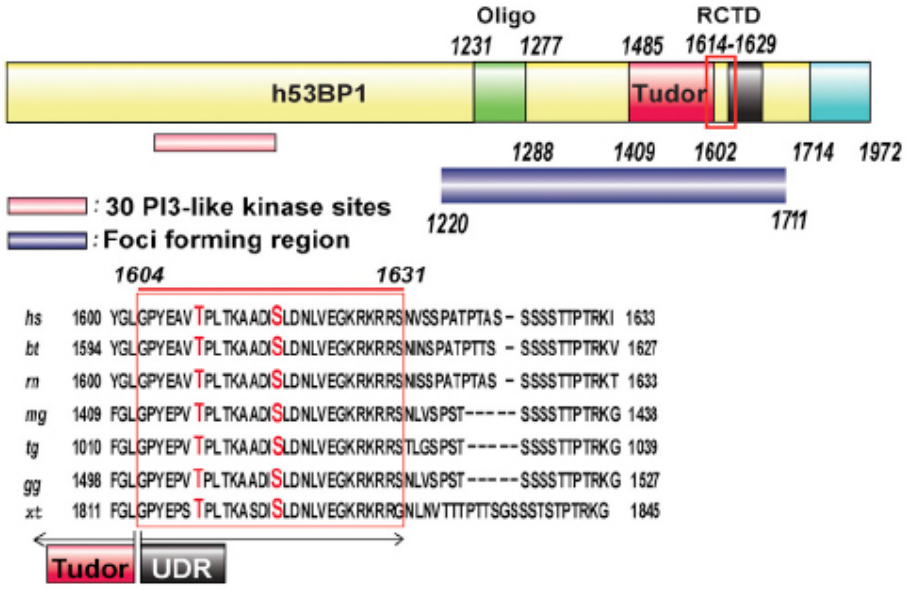

Figure 1.3: 53BP1 domain architecture. This 1972 amino-acid protein contains N terminal PI3-like kinase sites, an oligomerization domain, a tandem Tudor domain, a UDR domain, and a BRCT domain. The minimal region required for 53BP1 focus formation on chromatin is indicated. Figure also shows evolutionary conservation of residues in the Tudor-UDR region of 53BP1 necessary for its recruitment to chromatin following DNA damage (Lee et al., 2014).

protective shelterin complex around telomeres are removed, the deprotected telomeres are exposed as broken DSB ends. This activates the ATM/ATR kinases, which in turn recruit 53BP1 to repair the DSBs by NHEJ. This process typically results in the formation of detrimental chromosome fusions (Zimmermann and de Lange, 2014).

53BP1 and Pathway Choice

53BP1 along with BRCA1 has been shown to be one of the key drivers of DSB repair pathway choice. As mentioned earlier, the cell repairs DSBs using two major pathways, HR and NHEJ. Employing the appropriate pathway in a given cell cycle stage is critical to the fidelity of DNA repair and has a direct impact on genomic stability. In a normal cellular context, the choice of which pathway to employ is tightly controlled by allowing the majority of NHEJ to occur in the G1 phase while restricting HR-based repair to S and G2 phases of the cell cycle when a sister chromatid template becomes available (Chapman et al., 2012b; Symington and Gautier, 2011). However, how the choice between NHEJ and HR is regulated at a molecular level was a mystery for a long time. Recent landmark studies discussed below have begun to paint a clearer picture of pathway choice from a molecular standpoint.

While BRCA1 has long been acknowledged as a core factor in the HR machinery, 53BP1's pro-NHEJ role has only recently been recognized (Bouwman et al., 2010; Bunting et al., 2010; Iwabuchi et al., 2006; Nakamura et al., 2006b). In these studies, the observation that loss of 53BP1 in a Brca1-null

background rescues HR and allows cells to become resistant to PARP inhibitors, first implicated 53BP1 in pathway choice. Further evidence came from the discovery of two factors, namely RIF1 (RAP-1 interacting factor) and PTIP (Pax-transactivation domain- interacting protein) that through distinct phospho-protein interactions, mediated 53BP1's function in inhibiting DNA resection (Callen et al., 2013; Chapman et al., 2013; Di Virgilio et al., 2013; Escribano-Diaz et al., 2013).

Following DNA damage, RIF1 interacts with 53BP1 by binding to its N-terminal ATM-dependent S/T-Q sites. Mutating 28 of these S/T-Q residues in 53BP1 to alanine generated the $53BP1^{28A}$ mutant that abolished interaction between 53BP1 and RIF1 in addition to abrogating recruitment of RIF1 to chromatin (Di Virgilio et al., 2013). Furthermore, when it was observed that depletion of the *Rif1* gene specifically in B cells resulted in a CSR defect similar to the ablation of 53BP1, it became clear that RIF1 acts as a functional effector of 53BP1. Another effector of 53BP1 recently discovered is PTIP. This protein has a known function in regulating transcription initiation by binding with H3K4me3 methyltransferases MLL3 (mixed lineage leukemia 3) and MLL4. However, a separate pool of PTIP also plays a role in DDR and has been linked to both HR and NHEJ (Callen et al., 2013; Munoz et al., 2007). In the same experimental vein as RIF1, replacing endogenous 53BP1 with the $53BP1^{28A}$ mutant compromised PTIP recruitment to DSB foci. Moreover, mutating the first 8 S/T-Q sites in 53BP1 to generate $53BP1^{8A}$ inhibited PTIP localization to DSB sites but not RIF1, suggesting that 53BP1 interacts with RIF1 and PTIP through distinct phosphor-protein interactions. These findings suggest that 53BP1 tips the

balance towards NHEJ in the G1 phase by specifically recruiting effector proteins such as RIF1 that suppress resection and inhibit HR (Fig. 1.4).

It has been proposed that the genomic instability in Brca1-deficient cells results from failure to inhibit 53BP1 from suppressing resection in S phase (Bouwman et al., 2010; Bunting et al., 2010). Consistent with this model, presence of BRCA1 in S phase may then allow exclusion of pro-NHEJ factors such as 53BP1 and RIF1 from DSBs thereby favoring end resection. Indeed recent data using super-resolution microscopy have showed that while 53BP1 can localize to DSB foci in G1, S, and G2 phases it is excluded from the core S phase foci in a BRCA1-dependent manner (Chapman et al., 2012a). Such cell cycle phase dependent temporal control of 53BP1 localization appears to allow the cell to choose HR over NHEJ.

The observation that the BRCA1 S1655A mutant failed to inhibit RIF1 recruitment to DSB foci in S/G2 provided an important clue towards identifying an effector of BRCA1 (Escribano-Diaz et al., 2013; Feng et al., 2013). This mutant compromises the BRCT-dependent interaction of BRCA1 with its binding partners, FANCJ (Fanconi anemia group J protein), CTIP, and ABRA1. However, only depletion of CTIP reproduced the S1655A phenotype suggesting that CTIP is the BRCA1 effector protein that limits RIF1 localization to S phase foci thereby promoting end resection.

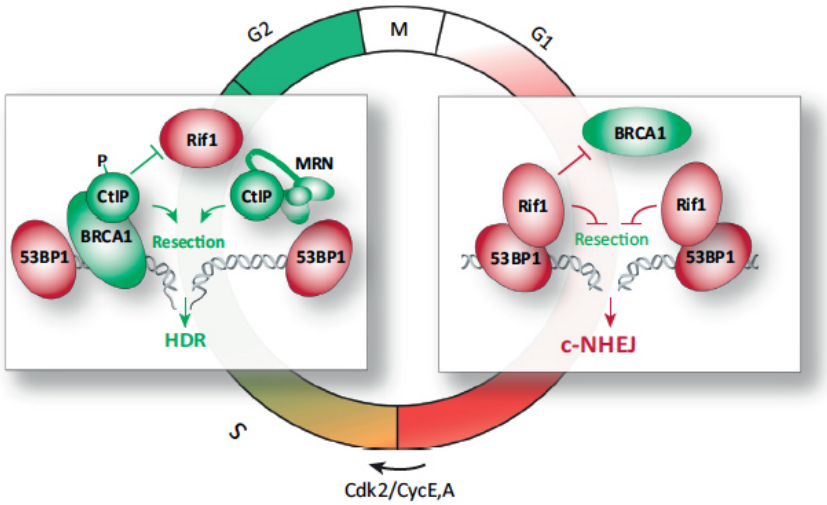

Figure 1.4: Regulation of DNA repair pathway choice by antagonism between mediator-effector pairs 53BP1-RIF1 and BRCA1-CTIP. In G1, the 53BP1-RIF1 complex inhibits BRCA1-mediated resection, thus promoting NHEJ. In S/G2, CDK-phosphorylation of CTIP causes it to interact with BRCA1. BRCA1-bound CTIP prevents chromatin binding of 53BP1-RIF1 thereby promoting HR (Zimmermann and de Lange, 2014).

Recruitment of 53BP1 to Sites of DNA Damage

The kinetics of accumulation of 53BP1 (and many other repair proteins) at DSBs after DNA damage can be visualized by microscopy. Damage response factors form distinct sub-nuclear foci that may be defined as collections of proteins actively involved in the repair process. The existence of these foci can be followed over the course of the cell cycle allowing one to study DNA damage in both time and space. The molecular cascade leading to 53BP1 localization to damage foci is complex and involves the following major events: 1) sensing of the damage by the MRN complex, 2) ATM-phosphorylation of the H2A variant H2AX at Ser139 forming γ-H2AX, 3) Recruitment and phosphorylation of MDC1, and finally 4) Recruitment of RNF8 and RNF168 that modify damaged chromatin.

In addition to the sequential recruitment of upstream DDR factors, distinct epigenetic chromatin modifications are required for 53BP1 localization to DNA damage foci and these findings are recently coming to light (Fig. 1.5). An early insight regarding the mechanism of 53BP1 focus formation came from experiments showing that 53BP1 binding to chromatin required an intact Tudor domain capable of recognizing H4K20me2 (Botuyan et al., 2006). Point mutations in this domain caused a drastic impairment in focal recruitment of 53BP1. Moreover, X-ray crystal structure and nuclear magnetic resonance analysis showed the existence of a five residue 53BP1 binding cage, also conserved in yeast Crb2, that specifically accommodated a di-methyl lysine but excluded a tri-methyl lysine, thus explaining the affinity of 53BP1 to H4K20me or H4K20me2 but not H4K20me3 (Botuyan et al., 2006).

It is intriguing however that H4K20me2 is widely present on chromatin even in the absence of DNA damage. One report suggests that over 80% of nucleosomes in asynchronous cells contain H4K20me2 (Pesavento et al., 2008). Even more intriguing is the observation that a significant fraction of the cellular 53BP1 pool is constitutively associated with methylated H4K20 in the absence of DNA damage (Bekker-Jensen et al., 2005; Santos et al., 2010). How then is recruitment and retention of 53BP1 to chromatin regulated in the presence of DNA damage? The answer to this question came from a recent study, which elegantly showed that successful 53BP1 localization to damaged chromatin requires RNF168-dependent ubiquitylation of histone H2A (H2AK15ub) in addition to H4K20me2 (Fradet-Turcotte et al., 2013).

While the Tudor domains of 53BP1 mediate interaction with H4K20me2, association with H2AK15ub is dependent on the newly characterized UDR motif located adjacent to the Tudor domain (Fig. 1.3). Fradet-Turcotte and colleagues performed binding assays with RNF168-modified nucleosome core particles and Tudor-UDR fragments and found strong evidence for a direct interaction between the UDR motif and H2AK15ub. Interestingly, point mutations in the UDR motif compromised interaction of 53BP1 with H2AK15ub but did not affect binding with H4K20me2, suggesting that 53BP1 binds to H4K20me2 independent of the H2AK15ub. Furthermore, it was shown that the UDR motif is also necessary for 53BP1 function as point mutations in this domain significantly decreased the accumulation of RIF1 at damage sites and abrogated CSR from IgM to IgG1.

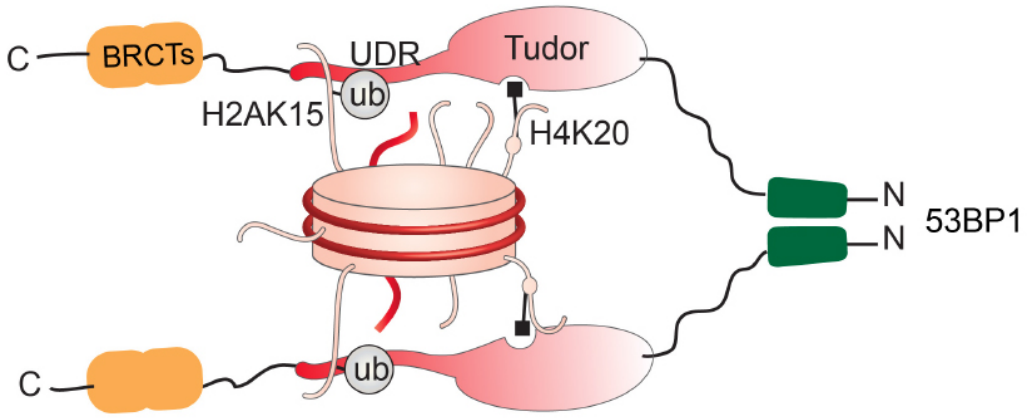

Figure 1.5: Model depicting two major chromatin modifications required for 53BP1 localization to chromatin- H4K20me2 and H2AK15ub (Fradet-Turcotte et al., 2013).

Phosphatases

One of the best-studied DNA-damage induced post-translational protein modifications is phosphorylation. Kinase-dependent phosphorylation events during DNA damage have been well documented and until recently were thought to be the sole drivers of the DDR response. However, recent work highlights the importance of dephosphorylation (in addition to phosphorylation) in the initiation and maintenance of a robust DDR (Bennetzen et al., 2010; Bensimon et al., 2010). A third of the captured phosphopeptides in the above studies were dephosphorylated after DNA damage and a fraction of these proteins showed dephosphorylation very early during the DDR response. These global proteomics studies suggest that phosphatases actively participate in the cellular response to DNA damage and are critical for the fidelity of the process (Lee and Chowdhury, 2011) (Zheng et al., 2015).

Serine/Threonine (Ser/Thr) phosphatases can be classified based on sequence, structure, and biochemical properties such as dependence on metal ions. So far only a few phosphatases have been implicated in DDR and involve members of the phosphoprotein phosphatase (PPP) family (PP1, PP2A-like, and PP4) and the Mg^{2+}/Mn^{2+}-dependent phosphatase (PPM) family member, WIP1 (wild-type p53 induced phosphatase 1, also known as PPM1D). Specific examples of the involvement of Ser/Thr phosphatases in DDR are found in many current studies. Recently, it was shown that PP2A-mediated dephosphorylation of the histone H2A variant (H2AX) is important for removal of phosphorylated H2AX from chromatin. An inability to remove γ-H2AX results in an impaired DSB

response and hypersensitivity to DNA damage (Chowdhury et al., 2005). In addition, PP2A also regulates the activity of the major kinases involved in sensing DNA damage, namely ATM (Goodarzi et al., 2004), ATR (Li et al., 2007), and DNA-PK (Douglas et al., 2001).

PP4 Phosphatase

The PP2A phosphatase is relatively well studied (Van Hoof and Goris, 2003). However, less is known about other members of the PP2A-like phosphatase family, which comprise PP4 and PP6. PP4 is ubiquitously expressed in mammals and is responsible for a number of essential cellular functions ranging from organelle assembly and apoptosis signaling to recovery from the DNA damage checkpoint (Cohen et al., 2005; Gingras et al., 2005; Hastie et al., 2006). PP4C, the catalytic subunit of PP4 phosphatase, shares 65% homology to the PP2AC catalytic subunit and it functions in complex with five known regulatory subunits, PP4 R1, R2, R3α, and R3β, R4 (Fig. 1.6) (Chen et al., 2008a; Mourtada-Maarabouni and Williams, 2008, 2009; Zhang et al., 2005). Many current reports strongly suggest involvement of PP4 in regulating DDR proteins. Removal of γ-H2AX generated during DNA replication has been shown to require the activity of PP4 (Chowdhury et al., 2008; Nakada et al., 2008). This role is distinct from the role of PP2A in dephosphorylating γ-H2AX during repair of exogenous DNA damage. Furthermore, PP4-mediated dephosphorylation of RPA2 is essential for the efficiency of homologous recombination and the regulation of the G2/M checkpoint (Lee et al., 2010a). PP4

is also necessary for dephosphorylation of the transcriptional repressor KAP-1 thereby facilitating cell-cycle progress after repair of DNA damage (Lee et al., 2012).

Rewiring of DDR in Mitosis

As has been discussed earlier, following DNA damage the DDR machinery activates cell cycle checkpoints to halt the cell cycle and resolve DNA breaks before proceeding through the rest of the phases. This response ensures that the integrity of the genome is protected and deleterious mutations are not passed on to daughter cells. Recent advancements in our understanding of DNA repair suggest that while the cell cycle signaling network is a target of the DDR machinery, it can also act as a regulator of DDR by enforcing molecular constraints on which repair pathway can be used during a given phase or whether DNA can be repaired at all (Heijink et al., 2013).

Back in 1953, Zirkle and Bloom made the striking observation that cells traversing through mitosis were oblivious to microbeam-radiation and continued to complete mitosis without repairing broken chromosomes (Zirkle and Bloom, 1953). It was subsequently noted that while cells passed uninterrupted through mitosis even in the presence of damaged chromosomes, the chromosomes stained positive for γ-H2AX. This observation suggested that DNA damage was still detected in mitotic cells, but the subsequent activation of downstream signaling components was inhibited. We now know that this occurs primarily due

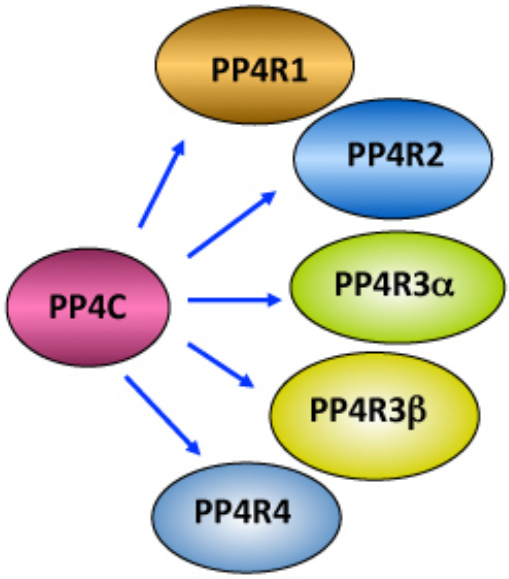

Figure 1.6: Subunits of PP4 Phosphatase. The PP4C catalytic subunit can pair with either of the substrate-specific regulatory subunits leading to possible dephosphorylation of a large number of substrates (Gingras et al., 2005).

to the activation of mitotic kinases such as CDK1 and PLK1 that dampen the DDR response in mitosis.

In mitotic cells the MRN complex is capable of sensing damage, ATM can be activated, and H2AX is phosphorylated (Kato et al., 2009; Nakamura et al., 2006a). Recruitment of MDC1, which is based on H2AX phosphorylation and ATM activation, is also observed in mitosis (Giunta et al., 2010). However, activation of the downstream factors RNF8 and RNF168 cannot occur until cells reach anaphase. Since 53BP1 recruitment requires the ubiquitylation of histone H2A surrounding DNA breaks, the absence of RNF8/RNF168 ultimately inhibits DNA 53BP1 from localizing to DNA breaks (Giunta et al., 2010; Giunta and Jackson, 2011).

CHK1 and CHK2 are also suppressed in mitosis by the action of PLK1, which mediates degradation of the CHK1 cofactor Claspin during mitosis and interferes with ATM-dependent activation of CHK2 (Mailand et al., 2006; Peschiaroli et al., 2006; van Vugt et al., 2010). In addition, CHK2 activation is dependent on 53BP1 (Wang et al., 2002), which also does not localize to mitotic chromosomes (Giunta et al., 2010; Nelson et al., 2009). In this way while DNA breaks are marked during mitotic progression, the breaks are not actively repaired demonstrated by the dampening of downstream effector responses.

Potential Role of Phosphatases in the Regulation of DDR in Mitosis

It is conceivable that like kinases, protein phosphatases play a role in regulating cell cycle-specific activation or repression of DDR factors. Previously

discussed examples suggest that Ser/Thr phosphatases either reset DDR factors to their inactive state after completion of DNA repair or remove inhibitory phosphorylation from DDR factors to allow their participation in the DDR response. In this dissertation, we present a striking example of phosphatase-mediated activation of the key DDR factor 53BP1. In late G2/mitosis, mitotic kinases phosphorylate two conserved residues located in the UDR motif of 53BP1, T1609 and S1618. These modifications block 53BP1 from localizing to DSBs. However, at the end of mitosis/ in early G1, 53BP1 is actively dephosphorylated at T1609 and S1618 by a PP4/R3β complex, which primes 53BP1 to repair damaged DNA in G1. Furthermore, our data supports the claim that reactivation of 53BP1 to DSBs in mitosis is deleterious and leads to mitotic defects that can be reversed by blocking NHEJ.

We further investigate the cell cycle specific activation of PP4/R3β complex in dephosphorylating 53BP1 and identify a key residue S840 in the regulatory subunit R3β. Increasing evidence suggests that this residue may be phosphorylated by the action of the cyclin-dependent kinase family member CDK5 in mitosis, thereby activating the 53BP1-specific activity of PP4. Ectopic expression of phosphomimic S840D in the absence of CDK5 partly rescued 53BP1 recruitment to DSB foci in G1 suggesting a potential role for CDK5 in regulating 53BP1 activity.

Acute Radiation Syndrome

In addition to upregulating the DDR, ionizing radiation-induced DNA damage can also cause a number of systemic effects when assessed at the organismal level. These system-level changes in physiology are defined as the acute radiation syndrome (ARS), which consists of hematopoietic, cerebrovascular, and gastrointestinal components (Dainiak et al., 2003; Waselenko et al., 2004). The hematopoietic system is the most vulnerable to the damaging effects of total body irradiation (TBI) and can be affected by exposure of at least 1 Gy at a relatively high dose-rate. Low to moderate radiation exposure causes a rapid decrease in blood cell counts primarily characterized by lymphopenia and loss of hematopoietic progenitors (Greenberger and Epperly, 2009). After a moderate TBI dose of 2-6 Gy, mitotically active hematopoietic progenitors may be able to support hematopoietic recovery. However, this occurs at the cost of decreased self-renewal. At doses higher than 6 Gy, non-recoverable bone marrow damage can result from myelosuppression, loss of marrow repopulating ability and senescence or complete loss of hematopoietic stem cells (HSC) (Mauch et al., 1995; Simonnet et al., 2009; Wang et al., 2006). At this stage, survival is questionable without cytokine therapies or bone marrow transplants (Dainiak et al., 2003; Waselenko et al., 2004). In a radiation disaster scenario caused by industrial accidents, terrorist attacks, or use of nuclear weapons, identifying the dose of radiation sustained by each exposed individual presents a significant challenge to medical responders. This has led to the development of a number of biodosimetry techniques to screen and triage patients exposed to different doses of radiation.

Current Biodosimetry Methods

Biodosimetry is the measurement of biological response as a surrogate to assess the dose of radiation. A number of hematological, cytogenetic, and DNA damage-based biodosimetry techniques exist for dose estimation (Sullivan et al., 2013). However, most still have notable limitations and only a few have been standardized for use in patient triage. For example, the lymphocyte depletion kinetics (LDK) assay can be used to estimate the dose of radiation by taking three to four lymphocyte counts to generate an LDK curve (Parker and Parker, 2007) (Goans et al., 1997). The kinetics of depletion has been shown to correlate directly with the absorbed dose. One of the strengths of this assay is the ability to perform this analysis outside a specialized laboratory. However, since a number of measurements are needed to get a dose estimate, this technique may be impractical to use in a mass casualty scenario.

Another technique known as the chromosome dicentrics assay (DCA) is currently considered the “gold standard” for estimation of radiation dose and has been used to assess exposure in a number of exposed and suspected individuals (Lloyd et al., 2000; Pinto et al., 2010; Prasanna et al., 2010). The assay involves taking a blood sample and incubating cells in the presence of a mitogen to generate metaphase spreads that can be scored for the presence of dicentric chromosomes. Dicentrics are formed by the fusion of two centromere-containing chromosome fragments, which occur at very low levels in unexposed cells making this assay highly sensitive. However, the DCA has a relatively low

dose range of upto 5 Gy, tedious scoring methods, and requires a long processing time.

One DNA damage-based assay is based on the scoring of γ-H2AX subnuclear foci after radiation exposure. However, the peak of γ-H2AX foci occurs between 30 min- 2 h after exposure and declines rapidly after 24 h (Andrievski and Wilkins, 2009; Riecke et al., 2010). Therefore, although this assay is sensitive, it may allow accurate dose determination during a small time window. Other DNA damage-based assays such as the cytokinesis block micronucleus assay (CBMN) rely on the scoring of micronuclei formed by chromosome mis-segregation during mitosis (Vral et al., 2011). Efforts are underway to automate sample processing, which will allow application at a population level (Willems et al., 2010).

MicroRNA Biomarkers

An analysis of existing biodosimetry techniques thus suggests that they do not accurately predict the severity of radiation injury to various organs and systems thereby complicating effective radiation countermeasures (Sullivan et al., 2013). Therefore, there exists a need for the development of radiation-specific biomarkers that can predict acute and delayed damage at the organismal level, to facilitate precise and timely medical intervention. MicroRNA (miRNAs) are short, non-coding nucleic acids that were discovered in the early 1990s and have since been implicated in multiple physiological and pathological states from organogenesis and development to immune disease and cancer (Mendell and

Olson, 2012; Ryan et al., 2010). These molecules repress gene expression by binding to the 3' untranslated regions of mRNA molecules thereby triggering either translational repression or target mRNA degradation.

In addition to their intracellular role in gene regulation, miRNAs have also been detected in a cell-free form in multiple body fluids including serum and plasma. The physiological role of these circulating miRNAs is yet to be investigated but many groups have reported disease and stress-dependent changes in their patterns of expression (Chen et al., 2008b; Chim et al., 2008; Lawrie et al., 2008; Mitchell et al., 2008; Park et al., 2011). Most of these studies were done with the goal of providing an early diagnostic tool for cancer detection. However, several studies (including one from our group) have correlated changes in their levels in response to ionizing radiation (Acharya et al., 2015; Cui et al., 2011; Templin et al., 2011). The inherent stability of miRNAs under harsh conditions and reproducible levels in individuals of the same species make circulating miRNAs attractive candidates for use as biomarkers (Mitchell et al., 2008; Schwarzenbach et al., 2014)

In this dissertation, in addition to studying the molecular interplay between DNA damage factors, we also examined a potential role for serum miRNAs as biomarkers for total body radiation-induced hematopoietic injury. We studied the effect of ionizing radiation on the bone marrow using two animal models and then correlated the extent of injury with changes in the expression of specific miRNAs. We were thus able to identify miRNA signatures that distinguished between low, sublethal, and high doses of radiation. Importantly, these miRNA changes could

predict the extent of hematopoietic injury within the first 24 hours after radiation exposure whereas symptoms of radiation sickness can typically take weeks or even months to appear. Furthermore, we were also able to correlate changes in the expression of specific miRNAs to animal survival, suggesting that miRNAs may be used to predict the impact of radiation on animal health in addition to the dose.

REFERENCES

Acharya, S.S., Fendler, W., Watson, J., Hamilton, A., Pan, Y., Gaudiano, E., Moskwa, P., Bhanja, P., Saha, S., Guha, C*., et al.* (2015). Serum microRNAs are early indicators of survival after radiation-induced hematopoietic injury. Science translational medicine *7*, 287ra269.

Ahn, J.Y., Schwarz, J.K., Piwnica-Worms, H., and Canman, C.E. (2000). Threonine 68 phosphorylation by ataxia telangiectasia mutated is required for efficient activation of Chk2 in response to ionizing radiation. Cancer Res *60*, 5934-5936.

Andrievski, A., and Wilkins, R.C. (2009). The response of gamma-H2AX in human lymphocytes and lymphocytes subsets measured in whole blood cultures. Int J Radiat Biol *85*, 369-376.

Bekker-Jensen, S., Lukas, C., Melander, F., Bartek, J., and Lukas, J. (2005). Dynamic assembly and sustained retention of 53BP1 at the sites of DNA damage are controlled by Mdc1/NFBD1. The Journal of cell biology *170*, 201-211.

Bennetzen, M.V., Larsen, D.H., Bunkenborg, J., Bartek, J., Lukas, J., and Andersen, J.S. (2010). Site-specific phosphorylation dynamics of the nuclear proteome during the DNA damage response. Mol Cell Proteomics *9*, 1314-1323.

Bensimon, A., Schmidt, A., Ziv, Y., Elkon, R., Wang, S.Y., Chen, D.J., Aebersold, R., and Shiloh, Y. (2010). ATM-dependent and -independent dynamics of the nuclear phosphoproteome after DNA damage. Sci Signal *3*, rs3.

Bolderson, E., Tomimatsu, N., Richard, D.J., Boucher, D., Kumar, R., Pandita, T.K., Burma, S., and Khanna, K.K. (2010). Phosphorylation of Exo1 modulates homologous recombination repair of DNA double-strand breaks. Nucleic Acids Res *38*, 1821-1831.

Botuyan, M.V., Lee, J., Ward, I.M., Kim, J.E., Thompson, J.R., Chen, J., and Mer, G. (2006). Structural basis for the methylation state-specific recognition of histone H4-K20 by 53BP1 and Crb2 in DNA repair. Cell *127*, 1361-1373.

Bouwman, P., Aly, A., Escandell, J.M., Pieterse, M., Bartkova, J., van der Gulden, H., Hiddingh, S., Thanasoula, M., Kulkarni, A., Yang, Q*., et al.* (2010). 53BP1 loss rescues BRCA1 deficiency and is associated with triple-negative and BRCA-mutated breast cancers. Nat Struct Mol Biol *17*, 688-695.

Bunting, S.F., Callen, E., Wong, N., Chen, H.T., Polato, F., Gunn, A., Bothmer, A., Feldhahn, N., Fernandez-Capetillo, O., Cao, L*., et al.* (2010). 53BP1 inhibits homologous recombination in Brca1-deficient cells by blocking resection of DNA breaks. Cell *141*, 243-254.

Buscemi, G., Carlessi, L., Zannini, L., Lisanti, S., Fontanella, E., Canevari, S., and Delia, D. (2006). DNA damage-induced cell cycle regulation and function of novel Chk2 phosphoresidues. Molecular and cellular biology *26*, 7832-7845.

Callen, E., Di Virgilio, M., Kruhlak, M.J., Nieto-Soler, M., Wong, N., Chen, H.T., Faryabi, R.B., Polato, F., Santos, M., Starnes, L.M*., et al.* (2013). 53BP1 mediates productive and mutagenic DNA repair through distinct phosphoprotein interactions. Cell *153*, 1266-1280.

Chapman, J.R., Barral, P., Vannier, J.B., Borel, V., Steger, M., Tomas-Loba, A., Sartori, A.A., Adams, I.R., Batista, F.D., and Boulton, S.J. (2013). RIF1 is essential for 53BP1-dependent nonhomologous end joining and suppression of DNA double-strand break resection. Mol Cell *49*, 858-871.

Chapman, J.R., Sossick, A.J., Boulton, S.J., and Jackson, S.P. (2012a). BRCA1-associated exclusion of 53BP1 from DNA damage sites underlies temporal control of DNA repair. Journal of cell science *125*, 3529-3534.

Chapman, J.R., Taylor, M.R., and Boulton, S.J. (2012b). Playing the end game: DNA double-strand break repair pathway choice. Mol Cell *47*, 497-510.

Chen, G.I., Tisayakorn, S., Jorgensen, C., D'Ambrosio, L.M., Goudreault, M., and Gingras, A.C. (2008a). PP4R4/KIAA1622 forms a novel stable cytosolic complex with phosphoprotein phosphatase 4. J Biol Chem *283*, 29273-29284.

Chen, X., Ba, Y., Ma, L., Cai, X., Yin, Y., Wang, K., Guo, J., Zhang, Y., Chen, J., Guo, X*., et al.* (2008b). Characterization of microRNAs in serum: a novel class of biomarkers for diagnosis of cancer and other diseases. Cell Res *18*, 997-1006.

Chim, S.S., Shing, T.K., Hung, E.C., Leung, T.Y., Lau, T.K., Chiu, R.W., and Lo, Y.M. (2008). Detection and characterization of placental microRNAs in maternal plasma. Clin Chem *54*, 482-490.

Chowdhury, D., Choi, Y.E., and Brault, M.E. (2013). Charity begins at home: non-coding RNA functions in DNA repair. Nat Rev Mol Cell Biol *14*, 181-189.

Chowdhury, D., Keogh, M.C., Ishii, H., Peterson, C.L., Buratowski, S., and Lieberman, J. (2005). gamma-H2AX dephosphorylation by protein phosphatase 2A facilitates DNA double-strand break repair. Mol Cell *20*, 801-809.

Chowdhury, D., Xu, X., Zhong, X., Ahmed, F., Zhong, J., Liao, J., Dykxhoorn, D.M., Weinstock, D.M., Pfeifer, G.P., and Lieberman, J. (2008). A PP4-phosphatase complex dephosphorylates gamma-H2AX generated during DNA replication. Mol Cell *31*, 33-46.

Ciccia, A., and Elledge, S.J. (2010). The DNA damage response: making it safe to play with knives. Mol Cell *40*, 179-204.

Cimprich, K.A., and Cortez, D. (2008). ATR: an essential regulator of genome integrity. Nat Rev Mol Cell Biol *9*, 616-627.

Cohen, P.T., Philp, A., and Vazquez-Martin, C. (2005). Protein phosphatase 4--from obscurity to vital functions. FEBS letters *579*, 3278-3286.

Cui, W., Ma, J., Wang, Y., and Biswal, S. (2011). Plasma miRNA as biomarkers for assessment of total-body radiation exposure dosimetry. PLoS One *6*, e22988.

Dainiak, N., Waselenko, J.K., Armitage, J.O., MacVittie, T.J., and Farese, A.M. (2003). The hematologist and radiation casualties. Hematology / the Education Program of the American Society of Hematology. American Society of Hematology. Education Program, 473-496.

Di Virgilio, M., Callen, E., Yamane, A., Zhang, W., Jankovic, M., Gitlin, A.D., Feldhahn, N., Resch, W., Oliveira, T.Y., Chait, B.T.*, et al.* (2013). Rif1 prevents resection of DNA breaks and promotes immunoglobulin class switching. Science *339*, 711-715.

Dimitrova, N., Chen, Y.C., Spector, D.L., and de Lange, T. (2008). 53BP1 promotes non-homologous end joining of telomeres by increasing chromatin mobility. Nature *456*, 524-528.

Douglas, P., Moorhead, G.B., Ye, R., and Lees-Miller, S.P. (2001). Protein phosphatases regulate DNA-dependent protein kinase activity. J Biol Chem *276*, 18992-18998.

Escribano-Diaz, C., Orthwein, A., Fradet-Turcotte, A., Xing, M., Young, J.T., Tkac, J., Cook, M.A., Rosebrock, A.P., Munro, M., Canny, M.D.*, et al.* (2013). A cell cycle-dependent regulatory circuit composed of 53BP1-RIF1 and BRCA1-CtIP controls DNA repair pathway choice. Mol Cell *49*, 872-883.

Feng, L., Fong, K.W., Wang, J., Wang, W., and Chen, J. (2013). RIF1 counteracts BRCA1-mediated end resection during DNA repair. J Biol Chem *288*, 11135-11143.

FitzGerald, J.E., Grenon, M., and Lowndes, N.F. (2009). 53BP1: function and mechanisms of focal recruitment. Biochem Soc Trans *37*, 897-904.

Fradet-Turcotte, A., Canny, M.D., Escribano-Diaz, C., Orthwein, A., Leung, C.C., Huang, H., Landry, M.C., Kitevski-LeBlanc, J., Noordermeer, S.M., Sicheri, F.*, et al.* (2013). 53BP1 is a reader of the DNA-damage-induced H2A Lys 15 ubiquitin mark. Nature *499*, 50-54.

Gingras, A.C., Caballero, M., Zarske, M., Sanchez, A., Hazbun, T.R., Fields, S., Sonenberg, N., Hafen, E., Raught, B., and Aebersold, R. (2005). A novel, evolutionarily conserved protein phosphatase complex involved in cisplatin sensitivity. Mol Cell Proteomics *4*, 1725-1740.

Giunta, S., Belotserkovskaya, R., and Jackson, S.P. (2010). DNA damage signaling in response to double-strand breaks during mitosis. The Journal of cell biology *190*, 197-207.

Giunta, S., and Jackson, S.P. (2011). Give me a break, but not in mitosis: the mitotic DNA damage response marks DNA double-strand breaks with early signaling events. Cell cycle *10*, 1215-1221.

Goans, R.E., Holloway, E.C., Berger, M.E., and Ricks, R.C. (1997). Early dose assessment following severe radiation accidents. Health physics *72*, 513-518.

Goldstein, M., and Kastan, M.B. (2015). The DNA damage response: implications for tumor responses to radiation and chemotherapy. Annu Rev Med *66*, 129-143.

Goodarzi, A.A., Jonnalagadda, J.C., Douglas, P., Young, D., Ye, R., Moorhead, G.B., Lees-Miller, S.P., and Khanna, K.K. (2004). Autophosphorylation of ataxia-telangiectasia mutated is regulated by protein phosphatase 2A. EMBO J *23*, 4451-4461.

Greenberger, J.S., and Epperly, M. (2009). Bone marrow-derived stem cells and radiation response. Semin Radiat Oncol *19*, 133-139.

Harrison, J.C., and Haber, J.E. (2006). Surviving the breakup: the DNA damage checkpoint. Annual review of genetics *40*, 209-235.

Hartlerode, A.J., and Scully, R. (2009). Mechanisms of double-strand break repair in somatic mammalian cells. The Biochemical journal *423*, 157-168.

Hastie, C.J., Vazquez-Martin, C., Philp, A., Stark, M.J., and Cohen, P.T. (2006). The Saccharomyces cerevisiae orthologue of the human protein phosphatase 4 core regulatory subunit R2 confers resistance to the anticancer drug cisplatin. The FEBS journal *273*, 3322-3334.

Heijink, A.M., Krajewska, M., and van Vugt, M.A. (2013). The DNA damage response during mitosis. Mutation research *750*, 45-55.

Helmink, B.A., Tubbs, A.T., Dorsett, Y., Bednarski, J.J., Walker, L.M., Feng, Z., Sharma, G.G., McKinnon, P.J., Zhang, J., Bassing, C.H.*, et al.* (2011). H2AX prevents CtIP-mediated DNA end resection and aberrant repair in G1-phase lymphocytes. Nature *469*, 245-249.

Heyer, W.D., Ehmsen, K.T., and Liu, J. (2010). Regulation of homologous recombination in eukaryotes. Annual review of genetics *44*, 113-139.

Huen, M.S., Sy, S.M., and Chen, J. (2010). BRCA1 and its toolbox for the maintenance of genome integrity. Nat Rev Mol Cell Biol *11*, 138-148.

Huyen, Y., Zgheib, O., Ditullio, R.A., Jr., Gorgoulis, V.G., Zacharatos, P., Petty, T.J., Sheston, E.A., Mellert, H.S., Stavridi, E.S., and Halazonetis, T.D. (2004). Methylated lysine 79 of histone H3 targets 53BP1 to DNA double-strand breaks. Nature *432*, 406-411.

Iwabuchi, K., Bartel, P.L., Li, B., Marraccino, R., and Fields, S. (1994). Two cellular proteins that bind to wild-type but not mutant p53. Proc Natl Acad Sci U S A *91*, 6098-6102.

Iwabuchi, K., Hashimoto, M., Matsui, T., Kurihara, T., Shimizu, H., Adachi, N., Ishiai, M., Yamamoto, K., Tauchi, H., Takata, M.*, et al.* (2006). 53BP1 contributes to survival of cells irradiated with X-ray during G1 without Ku70 or Artemis. Genes to cells : devoted to molecular & cellular mechanisms *11*, 935-948.

Iyama, T., and Wilson, D.M., 3rd (2013). DNA repair mechanisms in dividing and non-dividing cells. DNA repair *12*, 620-636.

Kato, T.A., Okayasu, R., and Bedford, J.S. (2009). Signatures of DNA double strand breaks produced in irradiated G1 and G2 cells persist into mitosis. Journal of cellular physiology *219*, 760-765.

Lawrie, C.H., Gal, S., Dunlop, H.M., Pushkaran, B., Liggins, A.P., Pulford, K., Banham, A.H., Pezzella, F., Boultwood, J., Wainscoat, J.S.*, et al.* (2008). Detection of elevated levels of tumour-associated microRNAs in serum of patients with diffuse large B-cell lymphoma. Br J Haematol *141*, 672-675.

Lee, D.H., Acharya, S.S., Kwon, M., Drane, P., Guan, Y., Adelmant, G., Kalev, P., Shah, J., Pellman, D., Marto, J.A.*, et al.* (2014). Dephosphorylation enables the recruitment of 53BP1 to double-strand DNA breaks. Molecular cell *54*, 512-525.

Lee, D.H., and Chowdhury, D. (2011). What goes on must come off: phosphatases gate-crash the DNA damage response. Trends in biochemical sciences *36*, 569-577.

Lee, D.H., Goodarzi, A.A., Adelmant, G.O., Pan, Y., Jeggo, P.A., Marto, J.A., and Chowdhury, D. (2012). Phosphoproteomic analysis reveals that PP4 dephosphorylates KAP-1 impacting the DNA damage response. EMBO J *31*, 2403-2415.

Lee, D.H., Pan, Y., Kanner, S., Sung, P., Borowiec, J.A., and Chowdhury, D. (2010a). A PP4 phosphatase complex dephosphorylates RPA2 to facilitate DNA repair via homologous recombination. Nat Struct Mol Biol *17*, 365-372.

Lee, J.H., Goodarzi, A.A., Jeggo, P.A., and Paull, T.T. (2010b). 53BP1 promotes ATM activity through direct interactions with the MRN complex. The EMBO journal *29*, 574-585.

Li, G., Elder, R.T., Qin, K., Park, H.U., Liang, D., and Zhao, R.Y. (2007). Phosphatase type 2A-dependent and -independent pathways for ATR phosphorylation of Chk1. J Biol Chem *282*, 7287-7298.

Li, L., and Zou, L. (2005). Sensing, signaling, and responding to DNA damage: organization of the checkpoint pathways in mammalian cells. Journal of cellular biochemistry *94*, 298-306.

Lieber, M.R. (2010). The mechanism of double-strand DNA break repair by the nonhomologous DNA end-joining pathway. Annu Rev Biochem *79*, 181-211.

Lieber, M.R., Gu, J., Lu, H., Shimazaki, N., and Tsai, A.G. (2010). Nonhomologous DNA end joining (NHEJ) and chromosomal translocations in humans. Sub-cellular biochemistry *50*, 279-296.

Liu, Q., Guntuku, S., Cui, X.S., Matsuoka, S., Cortez, D., Tamai, K., Luo, G., Carattini-Rivera, S., DeMayo, F., Bradley, A.*, et al.* (2000). Chk1 is an essential kinase that is regulated by Atr and required for the G(2)/M DNA damage checkpoint. Genes & development *14*, 1448-1459.

Lloyd, D.C., Edwards, A.A., Moquet, J.E., and Guerrero-Carbajal, Y.C. (2000). The role of cytogenetics in early triage of radiation casualties. Applied radiation and isotopes : including data, instrumentation and methods for use in agriculture, industry and medicine *52*, 1107-1112.

Lord, C.J., and Ashworth, A. (2012). The DNA damage response and cancer therapy. Nature *481*, 287-294.

Lukas, J., Lukas, C., and Bartek, J. (2004). Mammalian cell cycle checkpoints: signalling pathways and their organization in space and time. DNA repair *3*, 997-1007.

Mailand, N., Bekker-Jensen, S., Bartek, J., and Lukas, J. (2006). Destruction of Claspin by SCFbetaTrCP restrains Chk1 activation and facilitates recovery from genotoxic stress. Mol Cell *23*, 307-318.

Manis, J.P., Morales, J.C., Xia, Z., Kutok, J.L., Alt, F.W., and Carpenter, P.B. (2004). 53BP1 links DNA damage-response pathways to immunoglobulin heavy chain class-switch recombination. Nature immunology *5*, 481-487.

Matsuoka, S., Ballif, B.A., Smogorzewska, A., McDonald, E.R., 3rd, Hurov, K.E., Luo, J., Bakalarski, C.E., Zhao, Z., Solimini, N., Lerenthal, Y.*, et al.* (2007). ATM and ATR substrate analysis reveals extensive protein networks responsive to DNA damage. Science *316*, 1160-1166.

Matsuoka, S., Rotman, G., Ogawa, A., Shiloh, Y., Tamai, K., and Elledge, S.J. (2000). Ataxia telangiectasia-mutated phosphorylates Chk2 in vivo and in vitro. Proc Natl Acad Sci U S A *97*, 10389-10394.

Mauch, P., Constine, L., Greenberger, J., Knospe, W., Sullivan, J., Liesveld, J.L., and Deeg, H.J. (1995). Hematopoietic stem cell compartment: acute and late effects of radiation therapy and chemotherapy. Int J Radiat Oncol Biol Phys *31*, 1319-1339.

Meek, K., Dang, V., and Lees-Miller, S.P. (2008). DNA-PK: the means to justify the ends? Advances in immunology *99*, 33-58.

Mendell, J.T., and Olson, E.N. (2012). MicroRNAs in stress signaling and human disease. Cell *148*, 1172-1187.

Mitchell, P.S., Parkin, R.K., Kroh, E.M., Fritz, B.R., Wyman, S.K., Pogosova-Agadjanyan, E.L., Peterson, A., Noteboom, J., O'Briant, K.C., Allen, A.*, et al.* (2008). Circulating microRNAs as stable blood-based markers for cancer detection. Proc Natl Acad Sci U S A *105*, 10513-10518.

Moldovan, G.L., and D'Andrea, A.D. (2009). How the fanconi anemia pathway guards the genome. Annual review of genetics *43*, 223-249.

Mourtada-Maarabouni, M., and Williams, G.T. (2008). Protein phosphatase 4 regulates apoptosis, proliferation and mutation rate of human cells. Biochimica et biophysica acta *1783*, 1490-1502.

Mourtada-Maarabouni, M., and Williams, G.T. (2009). Protein phosphatase 4 regulates apoptosis in leukemic and primary human T-cells. Leukemia research *33*, 1539-1551.

Munoz, I.M., Jowsey, P.A., Toth, R., and Rouse, J. (2007). Phospho-epitope binding by the BRCT domains of hPTIP controls multiple aspects of the cellular response to DNA damage. Nucleic Acids Res *35*, 5312-5322.

Muramatsu, M., Kinoshita, K., Fagarasan, S., Yamada, S., Shinkai, Y., and Honjo, T. (2000). Class switch recombination and hypermutation require activation-induced cytidine deaminase (AID), a potential RNA editing enzyme. Cell *102*, 553-563.

Nakada, S., Chen, G.I., Gingras, A.C., and Durocher, D. (2008). PP4 is a gamma H2AX phosphatase required for recovery from the DNA damage checkpoint. EMBO reports *9*, 1019-1026.

Nakamura, A., Sedelnikova, O.A., Redon, C., Pilch, D.R., Sinogeeva, N.I., Shroff, R., Lichten, M., and Bonner, W.M. (2006a). Techniques for gamma-H2AX detection. Methods in enzymology *409*, 236-250.

Nakamura, K., Sakai, W., Kawamoto, T., Bree, R.T., Lowndes, N.F., Takeda, S., and Taniguchi, Y. (2006b). Genetic dissection of vertebrate 53BP1: a major role in non-homologous end joining of DNA double strand breaks. DNA repair *5*, 741-749.

Nelson, G., Buhmann, M., and von Zglinicki, T. (2009). DNA damage foci in mitosis are devoid of 53BP1. Cell cycle *8*, 3379-3383.

Panier, S., and Boulton, S.J. (2014). Double-strand break repair: 53BP1 comes into focus. Nat Rev Mol Cell Biol *15*, 7-18.

Park, J.Y., Helm, J., Coppola, D., Kim, D., Malafa, M., and Kim, S.J. (2011). MicroRNAs in pancreatic ductal adenocarcinoma. World J Gastroenterol *17*, 817-827.

Parker, D.D., and Parker, J.C. (2007). Estimating radiation dose from time to emesis and lymphocyte depletion. Health physics *93*, 701-704.

Pesavento, J.J., Yang, H., Kelleher, N.L., and Mizzen, C.A. (2008). Certain and progressive methylation of histone H4 at lysine 20 during the cell cycle. Molecular and cellular biology *28*, 468-486.

Peschiaroli, A., Dorrello, N.V., Guardavaccaro, D., Venere, M., Halazonetis, T., Sherman, N.E., and Pagano, M. (2006). SCFbetaTrCP-mediated degradation of Claspin regulates recovery from the DNA replication checkpoint response. Mol Cell *23*, 319-329.

Pinto, M.M., Santos, N.F., and Amaral, A. (2010). Current status of biodosimetry based on standard cytogenetic methods. Radiation and environmental biophysics *49*, 567-581.

Prasanna, P.G., Moroni, M., and Pellmar, T.C. (2010). Triage dose assessment for partial-body exposure: dicentric analysis. Health physics *98*, 244-251.

Revy, P., Muto, T., Levy, Y., Geissmann, F., Plebani, A., Sanal, O., Catalan, N., Forveille, M., Dufourcq-Labelouse, R., Gennery, A.*, et al.* (2000). Activation-induced cytidine deaminase (AID) deficiency causes the autosomal recessive form of the Hyper-IgM syndrome (HIGM2). Cell *102*, 565-575.

Riecke, A., Ruf, C.G., and Meineke, V. (2010). Assessment of radiation damage-the need for a multiparametric and integrative approach with the help of both clinical and biological dosimetry. Health physics *98*, 160-167.

Ryan, B.M., Robles, A.I., and Harris, C.C. (2010). Genetic variation in microRNA networks: the implications for cancer research. Nat Rev Cancer *10*, 389-402.

San Filippo, J., Sung, P., and Klein, H. (2008). Mechanism of eukaryotic homologous recombination. Annu Rev Biochem *77*, 229-257.

Santos, M.A., Huen, M.S., Jankovic, M., Chen, H.T., Lopez-Contreras, A.J., Klein, I.A., Wong, N., Barbancho, J.L., Fernandez-Capetillo, O., Nussenzweig, M.C.*, et al.* (2010). Class switching and meiotic defects in mice lacking the E3 ubiquitin ligase RNF8. The Journal of experimental medicine *207*, 973-981.

Schwarzenbach, H., Nishida, N., Calin, G.A., and Pantel, K. (2014). Clinical relevance of circulating cell-free microRNAs in cancer. Nat Rev Clin Oncol *11*, 145-156.

Shiloh, Y., and Ziv, Y. (2013). The ATM protein kinase: regulating the cellular response to genotoxic stress, and more. Nat Rev Mol Cell Biol *14*, 197-210.

Simonnet, A.J., Nehme, J., Vaigot, P., Barroca, V., Leboulch, P., and Tronik-Le Roux, D. (2009). Phenotypic and functional changes induced in hematopoietic stem/progenitor cells after gamma-ray radiation exposure. Stem Cells *27*, 1400-1409.

Smith, G.C., and Jackson, S.P. (1999). The DNA-dependent protein kinase. Genes & development *13*, 916-934.

Sullivan, J.M., Prasanna, P.G., Grace, M.B., Wathen, L.K., Wallace, R.L., Koerner, J.F., and Coleman, C.N. (2013). Assessment of biodosimetry methods for a mass-casualty radiological incident: medical response and management considerations. Health physics *105*, 540-554.

Symington, L.S., and Gautier, J. (2011). Double-strand break end resection and repair pathway choice. Annual review of genetics *45*, 247-271.

Templin, T., Amundson, S.A., Brenner, D.J., and Smilenov, L.B. (2011). Whole mouse blood microRNA as biomarkers for exposure to gamma-rays and (56)Fe ion. Int J Radiat Biol *87*, 653-662.

Van Hoof, C., and Goris, J. (2003). Phosphatases in apoptosis: to be or not to be, PP2A is in the heart of the question. Biochimica et biophysica acta *1640*, 97-104.

van Vugt, M.A., Gardino, A.K., Linding, R., Ostheimer, G.J., Reinhardt, H.C., Ong, S.E., Tan, C.S., Miao, H., Keezer, S.M., Li, J.*, et al.* (2010). A mitotic phosphorylation feedback network connects Cdk1, Plk1, 53BP1, and Chk2 to inactivate the G(2)/M DNA damage checkpoint. PLoS biology *8*, e1000287.

Vral, A., Fenech, M., and Thierens, H. (2011). The micronucleus assay as a biological dosimeter of in vivo ionising radiation exposure. Mutagenesis *26*, 11-17.

Wang, B., Matsuoka, S., Carpenter, P.B., and Elledge, S.J. (2002). 53BP1, a mediator of the DNA damage checkpoint. Science *298*, 1435-1438.

Wang, Y., Schulte, B.A., LaRue, A.C., Ogawa, M., and Zhou, D. (2006). Total body irradiation selectively induces murine hematopoietic stem cell senescence. Blood *107*, 358-366.

Ward, I.M., Reina-San-Martin, B., Olaru, A., Minn, K., Tamada, K., Lau, J.S., Cascalho, M., Chen, L., Nussenzweig, A., Livak, F.*, et al.* (2004). 53BP1 is required for class switch recombination. The Journal of cell biology *165*, 459-464.

Waselenko, J.K., MacVittie, T.J., Blakely, W.F., Pesik, N., Wiley, A.L., Dickerson, W.E., Tsu, H., Confer, D.L., Coleman, C.N., Seed, T.*, et al.* (2004). Medical management of the acute radiation syndrome: recommendations of the Strategic National Stockpile Radiation Working Group. Ann Intern Med *140*, 1037-1051.

West, S.C. (2003). Molecular views of recombination proteins and their control. Nat Rev Mol Cell Biol *4*, 435-445.

West, S.C., Blanco, M.G., Chan, Y.W., Matos, J., Sarbajna, S., and Wyatt, H.D. (2015). Resolution of Recombination Intermediates: Mechanisms and Regulation. Cold Spring Harbor symposia on quantitative biology.

Willems, P., August, L., Slabbert, J., Romm, H., Oestreicher, U., Thierens, H., and Vral, A. (2010). Automated micronucleus (MN) scoring for population triage in case of large scale radiation events. Int J Radiat Biol *86*, 2-11.

You, Z., and Bailis, J.M. (2010). DNA damage and decisions: CtIP coordinates DNA repair and cell cycle checkpoints. Trends in cell biology *20*, 402-409.

Zgheib, O., Pataky, K., Brugger, J., and Halazonetis, T.D. (2009). An oligomerized 53BP1 tudor domain suffices for recognition of DNA double-strand breaks. Molecular and cellular biology *29*, 1050-1058.

Zhang, X., Ozawa, Y., Lee, H., Wen, Y.D., Tan, T.H., Wadzinski, B.E., and Seto, E. (2005). Histone deacetylase 3 (HDAC3) activity is regulated by interaction with protein serine/threonine phosphatase 4. Genes & development *19*, 827-839.

Zhao, H., and Piwnica-Worms, H. (2001). ATR-mediated checkpoint pathways regulate phosphorylation and activation of human Chk1. Molecular and cellular biology *21*, 4129-4139.

Zheng, X.F., Kalev, P., and Chowdhury, D. (2015). Emerging role of protein phosphatases changes the landscape of phospho-signaling in DNA damage response. DNA repair *32*, 58-65.

Zimmermann, M., and de Lange, T. (2014). 53BP1: pro choice in DNA repair. Trends in cell biology *24*, 108-117.

Zirkle, R.E., and Bloom, W. (1953). Irradiation of parts of individual cells. Science *117*, 487-493.

CHAPTER 2

Dephosphorylation enables the recruitment of 53BP1 to double-strand DNA breaks

Dong-Hyun Lee, Sanket S. Acharya*, Mijung Kwon*, Pascal Drane, Yinghua Guan, Guillaume Adelmant, Peter Kalev, Jagesh Shah, David Pellman, Jarrod A. Marto and Dipanjan Chowdhury

* Equal Contribution

Collaborations:

Jarod Marto Laboratory, Dana-Farber Cancer Institute

Jagesh Shah Laboratory, Harvard Medical School

David Pellman Laboratory, Dana-Farber Cancer Institute

ABSTRACT

Excluding 53BP1 from chromatin is required to attenuate the DNA damage response during mitosis, yet the functional relevance and regulation of this exclusion is unclear. Here we show that 53BP1 is phosphorylated during mitosis on two residues, T1609 and S1618, located in its well-conserved ubiquitination-dependent recruitment (UDR) motif. Ectopic recruitment of 53BP1-T1609A/S1618A to mitotic DNA lesions was associated with significant mitotic defects that could be reversed by inhibiting non-homologous end joining. We also reveal that protein phosphatase complex, PP4C/R3β dephosphorylates T1609 and S1618 to allow the recruitment of 53BP1 to chromatin in G1 phase. Our results identify key sites of 53BP1 phosphorylation during mitosis, identify the counteracting phosphatase complex that restores the potential for DDR during interphase, and establish the physiological importance of this regulation.

INTRODUCTION

53BP1 (p53 binding protein 1) is a multi-domain protein with a complex and unique role in the repair of double-strand DNA breaks (DSBs). Recruitment of 53BP1 to DSB sites is essential for its function in the DNA damage response (DDR), and the minimal region (residues 1220 to 1711) required for its recruitment includes the oligomerization domain, a tandem Tudor domain and a carboxy terminal extension termed the ubiquitination dependent recruitment (UDR) motif (Fradet-Turcotte et al., 2013; Huyen et al., 2004; Iwabuchi et al., 2003; Zgheib et al., 2009). At the chromatin end, dimethylated lysine 20 of histone H4 (Botuyan et al., 2006; Pei et al., 2011), and ubiquitinated lysine 15 of histone H2A (Fradet-Turcotte et al., 2013) are necessary for the recruitment of 53BP1 to chromatin. Recent studies suggest that 53BP1 plays a critical role in choice of DSB repair pathway by promoting non-homologous end joining (NHEJ) mediated repair of a DSB and specifically countering the function of the homologous-recombination (HR) repair protein BRCA1 at a DSB (Bouwman et al., 2010; Bunting et al., 2010; Chapman et al., 2012). This is evident as loss of 53BP1 in a BRCA1-deficient cell restores HR-mediated DSB repair.

Function of 53BP1 in DDR is regulated in the course of the cell cycle (Giunta and Jackson, 2011). 53BP1 is hyperphosphorylated during mitosis and this correlates with its exclusion from chromatin and DNA lesions (Giunta et al., 2010; Nelson et al., 2009; van Vugt et al., 2010). The phosphorylation of 53BP1 dissipates as cells move into the G1-phase and participation of 53BP1 in DSB

repair is completely restored. We hypothesized that dephosphorylation of 53BP1 is necessary for its role in DSB repair in G1 cells.

We and others have shown that protein phosphatase, PP4C, a PP2A-like phosphatase, regulates the activity of critical DNA repair factors, H2AX, RPA2 and KAP-1 (Chowdhury et al., 2008; Lee et al., 2012; Lee et al., 2010a; Liu et al., 2012; Nakada et al., 2008). To systematically identify proteins dephosphorylated by, PP4C, we recently conducted a quantitative phosphoproteomic screen based on the rationale that sites hyperphosphorylated in the absence of PP4C are putative substrates (Lee et al., 2012). We identified two phosphoresidues of 53BP1, threonine 1609 (T1609) and serine 1618 (S1618) that were hyperphosphorylated in the absence of PP4C. Here we demonstrate that the residues T1609 and S1618 are phosphorylated during mitosis to prevent the recruitment of 53BP1 to DNA lesions. These residues get dephosphorylated by a PP4C/R3β complex as cells transit to the G1 phase, and this dephosphorylation event is necessary for the participation of 53BP1 in the DDR. Furthermore, allowing the recruitment of 53BP1 to DNA breaks in mitosis via mutations of T1609 and S1618 leads to defective chromosome segregation.

MATERIALS AND METHODS

Cell Culture, antibodies, and reagents

U2OS, HeLa, and RPE1-Fucci, 53BP1$^{-/-}$ MEFs cells were grown in DMEM supplemented with 10% (v/v) FBS. 53BP1$^{-/-}$ MEFs were gifts from Penelope A. Jeggo (University of Sussex). U2OS cells stably expressing GFP-RNF168, kindly gifted by Daniel Durocher (University of Toronto) was grown in McCoy 5A supplemented with 10% (v/v) FBS. BRCA1-mutant ovarian line, UWB1.289 was obtained from ATCC and grown in RPMI-1640 supplemented with 50% MEGM (Mammary Epithelial Growth Medium) from Clonetics/Lonza and 3% (v/v) FBS. Antibodies used were against PP4 R1 (Bethyl), R2 (Bethyl), R3α (Bethyl), R3β (Bethyl), PP4C (Bethyl), Phospho-histone H3 (Cell Signaling), 53BP1 (Cell Signaling), pS1618-53BP1 (Cell Signaling), γ-H2AX (Cell Signaling), γ-H2AX (Mouse, Millipore), FLAG (Sigma) and Tubulin (Sigma). Rabbit polyclonal anti-pT1609/S1618-53BP1 antibody was produced by Antagene (Sunnyvale, CA) with a peptide, Cys -NRLREQYGLGPYEAV(p)TPLTKAADI(p)SLDN. SB203580 and SB202190 (p38 MAPK inhibitors), MK-2206 (AKT inhibitor), BI2536 (PLK1 inhibitor) and NU7441 (DNA-PK inhibitor) were obtained from Selleckchem. Nocodazole, thymidine and aphidicolin were obtained from Sigma-Aldrich.

siRNAs and plasmid transfection

siRNA duplexes (Invitrogen) were transfected using RNAiMAX (Invitrogen). The PP4 siRNAs were described previously (Lee et al., 2010a).

The following 53BP1 siRNA was used: 5´-AGGAGACGGUAAUAGUGGG-3’.

The siRNA-resistant 53BP1 expression vector has been previously described (Noon et al., 2010) and obtained from Penelope A. Jeggo in University of Sussex. 53BP1 cDNA was subcloned into pOZ-N-FH or pLVX-AcGFP1-C1 vector. We constructed phospho-mutants of 53BP1 (T1609A/S1618A, T1609E/S1618D) by QuickChange II XL site-directed mutagenesis kit (Stratagene) according to the manufacturer's instructions. To replace endogenous 53BP1 with WT or phospho-mutants, HeLa and UWB1.289 cells were reverse transfected with 53BP1 siRNA by RNAiMAX and after 30 h, transfected with siRNA-resistant 53BP1 plasmids using Lipofectamine 2000 (Invitrogen).

In vitro dephosphorylation assay

The *in vitro* dephosphorylation assay was performed as described (Lee et al., 2012; Lee et al., 2010a). PP4C WT and D82A mutant proteins were purified using the Bac-to-Bac Baculovirus Expression System (Invitrogen) according to the manufacturer's manual. For the dephosphorylation assay, phosphorylated FH-53BP1 was prepared by immunoprecipitation of 53BP1 from nocodazole-arrested mitotic cells with anti-FLAG antibody conjugated agarose. Phosphatase reactions with phosphorylated FH-53BP1 were performed in 20 mM Tris-HCl, pH 7.4, 50 mM NaCl, 0.2 mM EDTA, 0.2% β-mercaptoethanol for 30 min at 30°C. Reactions were resolved on 12% (v/v) SDS-PAGE and relative phosphatase activity was determined by loss of phospho-FH-53BP1 immunoreactivity as determined by p1618 and p(1609-1618) antibody staining.

Co-immunoprecipitation and immunoblotting

These techniques were performed as previously described in (Lee et al., 2012; Lee et al., 2010a). Briefly, cell lysates from U2OS cells, expressing 53BP1 WT or phosphomutants, were incubated with anti–Flag agarose (Sigma) at 4 °C for 16 h and immunoprecipitated proteins were resolved by SDS-PAGE and analyzed by immunoblot. Immunoblots were visualized using the Odyssey Infrared Imaging System. After primary antibody incubation, blots were incubated with goat anti–mouse IR Dye 800CW or goat anti–rabbit IR Dye 680 (LI-COR) and scanned using the LI-COR scanner. Images were visualized and quantified by Odyssey V3.0 software (http://biosupport.licor.com). Chromatin fractionation was performed as described previously (Lee et al, 2010). Quantification of fractions for equal loading was done using NanoDrop 1000 (Thermo Scientific).

Immunofluorescence

Immunofluorescence was performed as previously described (Lee et al., 2010a). Briefly, U2OS, RPE1-Fucci, 53BP1$^{-/-}$ MEF cells were plated on glass slides, fixed, permeablized and incubated with primary and secondary antibodies prior to being mounted using DapiFuoromount-G (SouthernBiotech). Secondary Alexa Fluor IgG antibodies used were: 488 goat anti-rabbit, 488 goat anti-mouse, 594 goat anti-rabbit, 594 goat anti-mouse, 647 donkey anti-goat, goat anti-rabbit 568, and goat anti-human 660 (Invitrogen). A stack of images for each sample was collected with 100X objective (1.35 N.A.) using Olympus FV1000 confocal microscope and presented as maximum intensity projection.

Live-cell imaging

MPL-induced DNA Damage and Fluorescence Image acquisition. A Mai Tai@ Ultrafast Ti:Sapphire Laser (Spectra-Physics, Santa Clara, CA, USA, 100 fs pulse, 80 MHz repetition rate) was aligned into a Nikon Ti microscope (Nikon, Melville, NY, USA) via a custom-built open beam optical path. The laser was expanded to overfill the back aperture of a 60X1.4 numerical aperture objective (Nikon). A 675 nm low pass dichroic mirror (Chroma Technology Corp., Bellows Falls, VT, USA) was mounted in the microscope to reflect the laser into the objective. An average power level of 25 mW at 780 nm was used for all DNA damage experiments. The power was measured in the optical path outside of the microscope and is approximately three times higher than the power at the sample. Focus formation was monitored by accumulation of a GFP-tagged full--length 53BP1 wild type or AA and ED mutant via epifluorescence excitation. Cells were incubated in a HEPES Leibovitz-15 based live cell media to permit a pH buffered environment for imaging on the CCD camera (The PhotometricsCoolSNAPHQ Monochrome camera). Each set of data collection began with the capture of four fluorescence images prior to DNA damage followed by exposure to the laser for five seconds. A time-lapse movie was collected for 10 min after DNA damage induction with a frame interval of 10 seconds for the first 5 minutes and 30 seconds for the second 5 minutes. Data movies were analyzed in MATLAB@ (The MathWorks, Natick, MA, USA) with a custom algorithm to follow focus movement, quantify intensity and generate a plot of fluorescence accumulation over time.

Clonogenic assay

HeLa ($0.3X10^6$ cells/well) cells were reverse transfected with 30 nM of scrambled control siRNA or 53BP1 siRNA, followed by transfection with FH-53BP1 WT or phospho-mutants. After 2 days, 1000 cells were seeded in 6-well plates in quadruplicate and incubated overnight. Cell were irradiated at indicated doses on the following day and allowed to form colonies for 2 weeks before being stained by 0.1% crystal violet solution. Surviving colonies of greater than 1mm diameter were counted.

Colorimetric assay

BRCA1-mutant ovarian line, UWB1.289 ($0.3X10^6$ cells/well) were transfected with 30 nM of scrambled control siRNA or 53BP1 siRNA, followed by transfection with 2μg of FH-53BP1 WT or phospho-mutants. After 2 days, 2000 cells were seeded in 96-well plates in six replicates and incubated overnight. PARP inhibitor [ABT888, (purchased from ChemieTek)] was added to the growth media at indicated concentrations. Cells were allowed to form colonies for 5 days before being quantified by CellTiter-Glo® Luminescent Cell Viability Assay (Promega).

Mitotic 53BP1 imaging

U2OS cells expressing RFP-H2B were transfected with wildtype or mutant GFP-53BP1 constructs. For aphidicolin experiments, transfected cells were treated with 0.2μM aphidicolin for 12 hrs and released to regular medium prior to

imaging. For irradiation experiments, transfected cells were arrested in mitosis with 100 ng/ml of nocodazole (Noc) for 6 hrs and released to regular medium prior to imaging. Live-cell imaging was performed using a TE2000-E2 inverted Nikon microscope equipped with the Nikon Perfect Focus system enclosed within a temperature- and CO2-controlled environment. In parallel, Noc-arrested irradiated cells were fixed and stained for γ-H2AX (1:300). For consistency, only cells with comparable and moderate level 53BP1 were subjected for the quantitation by gauging fluorescent intensity of 53BP1. Time from anaphase onset to the first appearance of discrete 53BP1 foci was quantified.

RESULTS

53BP1 is a novel substrate of PP4C/R3β

A recent phosphoproteomic screen performed in the lab to identify substrates of PP4 phosphatase showed hyperphosphorylation of two essential 53BP1 residues T1609 and S1618 in the absence of PP4. Interestingly, these two residues are located in the UDR motif, which is essential for 53BP1 recruitment to DSB sites (Fradet-Turcotte et al., 2013). These residues have also been shown to be phosphorylated during mitosis (Dephoure et al., 2008), (Grosstessner-Hain et al., 2011). We independently verified the phosphorylation of these residues by using isotopically-encoded synthetic phosphopeptide analogs for pT1609 and pS1618 (Fig. 2.1). These experiments were done in collaboration with Jarod Marto's laboratory, Dana-Farber Cancer Institute. The MS/MS spectra of tryptic peptide derived from immunoprecipitated endogenous 53BP1 (Fig. 2.1 upper spectra) and of isotope-encoded synthetic analog (Fig. 2.1 lower spectra) illustrate the alignment of the major b-type (blue) and y-type (red) fragment ions containing the original peptide N- and C- termini, respectively, for both phosphorylated peptides. Peptide sequences above each spectra are annotated to show phosphorylated residues (green), isotope-encoded amino-acid (boxed) and sequence-specific fragments detected in each MS/MS spectrum (with blue and red underlines). Hyperphosphorylation of 53BP1 during mitosis is detected by a mobility shift during gel electrophoresis (Giunta et al., 2010; van Vugt et al., 2010) therefore we silenced the subunits of PP4 and evaluated the mobility of 53BP1 during the transition from mitosis to G1 (Gingras et al., 2005).

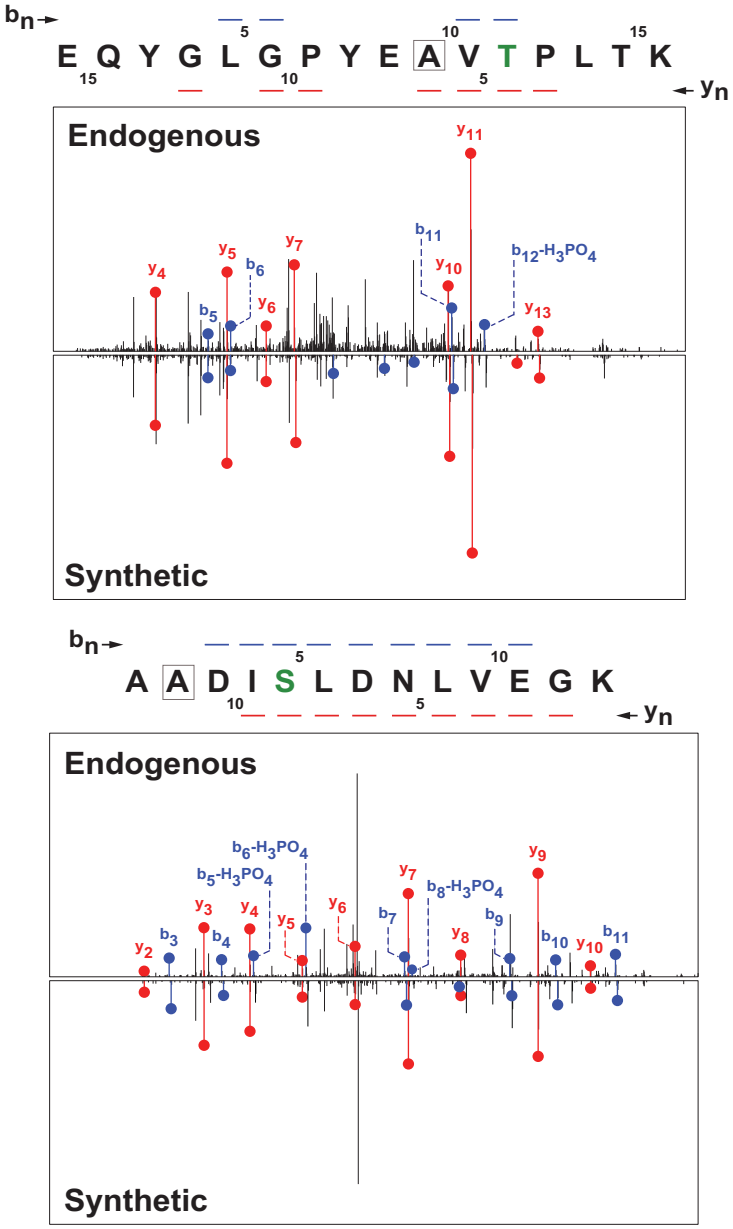

Figure 2.1: MS/MS spectra to verify 53BP1 phosphorylation.
Isotope-encoded synthetic phosphopeptide analogs to verify sequence assignment and localization of the phosphorylated residues for pT1609 *(top panel)* and pS1618 *(bottom panel)*. (Data generated in collaboration with Jarod Marto's laboratory at Dana-Farber Cancer Institute.)

There is one catalytic subunit (PP4C) are several regulatory subunits of PP4, namely R1, R2, R3α, R3β, and R4. We transfected HeLa cells with siRNAs against the major regulatory and catalytic subunit of PP4 and synchronized cells in mitosis using nocodazole (a microtubule polymerization inhibitor). We then assessed 53BP1 mobility during the mitosis to G1 transition by harvesting cells at different time points after G1 release. Only silencing PP4C and R3β, led to a shift in 53BP1 mobility in G1 cells (Fig. 2.2A) while silencing other PP4 regulatory subunits (R2, R1 and R3α) did not impact the mobility of 53BP1. Immunoblot presented in Fig. 2.2B shows the knockdown efficiency of siRNAs used against PP4 catalytic and regulatory subunits. Since we found that depletion of PP4C and R3β affected 53BP1 mobility, we asked if these subunits interacted with 53BP1. We stably transduced U2OS cells with Flag- HA (FH) tagged 53BP1 and synchronized cells in mitosis for 8h using nocodazole. Consistent with previous results, only PP4C and R3β interact with 53BP1 and this association was significantly enhanced in cells synchronized in mitosis (Fig. 2.2C).

Next we generated a phospho-specific antibody to confirm that the residues T1609 and S1618 are indeed phosphorylated in mitosis and that their phosphorylation status is influenced by a PP4C/R3β complex. Using HeLa cells expressing FH-53BP1 wild-type (WT) or mutants T1609A or T1609A, we confirmed that the phospho-antibody recognized the combination of phosphorylated T1609 and phosphorylated S1618. When either of these residues were mutated, the antibody signal was significantly reduced. (Fig. 2.3A).

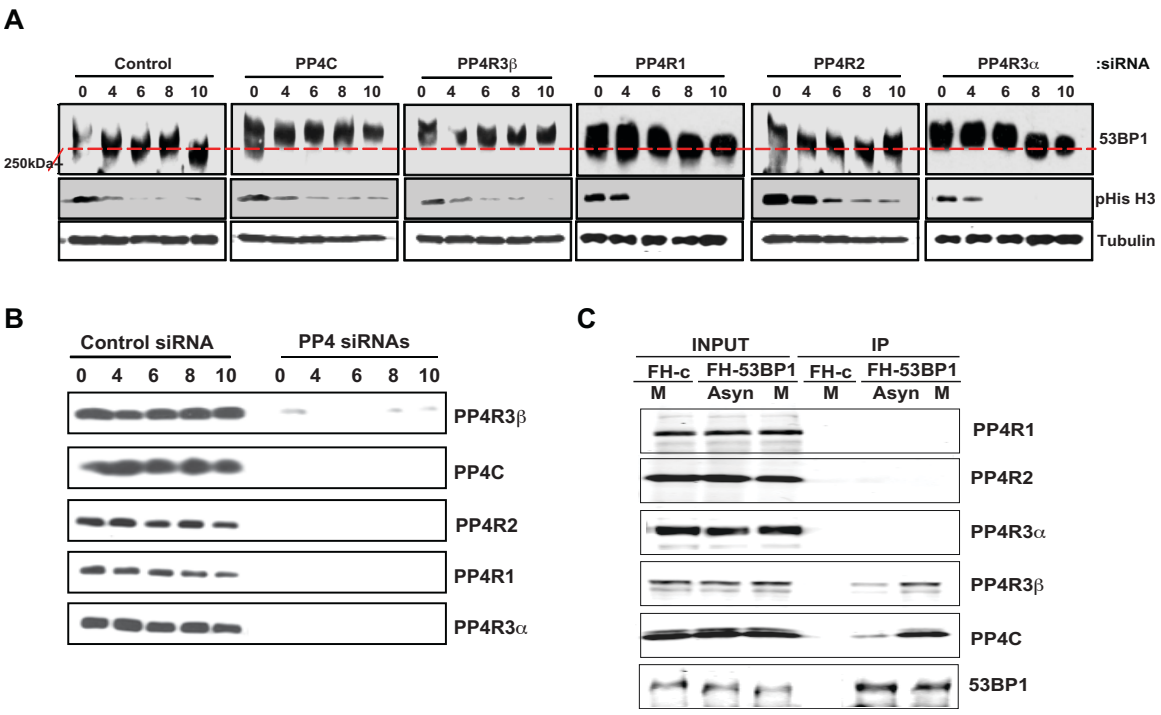

Figure 2.2: Impact of PP4C and R3β silencing on 53BP1 phosphorylation. **(A)** HeLa cells were transfected with siRNAs against PP4C or the indicated PP4 regulatory subunits and synchronized in mitosis with 100 ng/ml nocodazole for 8h. Cells were released from mitosis and harvested at the indicated time points in G1 phase. 53BP1 mobility shift was assessed by gel electrophoresis. Mitotic exit was monitored using phospho-histone H3 (pHistoneH3) antibody. Tubulin was used as a loading control. The 250 kDa marker is shown as a reference. **(B)** Cells harvested to assess 53BP1 mobility shift were also analyzed in parallel by immunoblot for knockdown of PP4C and the indicated PP4 regulatory subunits. **(C)** Interaction of 53BP1 with PP4C and R3β. U2OS cells, stably expressing FH-Empty vector (FH-c) or FH-53BP1 were harvested after 8h synchronization in mitosis (M) using nocodazole or left in an asynchronous state (Asyn). Whole cell extracts were immunoprecipitated with anti-FLAG agarose beads and analyzed by immunoblotting using indicated antibodies.

After validating the phospho-antibody, we used it in combination with a commercially available phospho-S1618 antibody to study the dynamics of T1609 and S1618 phosphorylation in mitosis and G1. In control siRNA treated cells, T1609 and S1618 were phosphorylated in mitosis. However, their phosphorylation dissipated as cells entered into G1. But when PP4C or R3β was silenced in these cells, a detectable increase in phospho-T1609 and phospho-S1618 signal was observed in the G1 phase (Fig. 2.3C). To ascertain that cells transfected with PP4C or R3β and released into G1 were not stuck in mitosis, we performed propidium iodide (PI) staining (Fig. 2.3B), which showed that PP4C or R3β silenced cells entered G1 phase as expected.

To further validate these results we monitored the kinetics of dephosphorylation as cells transit from mitosis to G1 and observed that depletion of PP4C or R3β blocked the dephosphorylation of T1609 and S1618 at various time-points in G1 (Fig. 2.4A). While phosphorylation of T1609/S1618 gradually decreased by 3h in control cells, the phospho signal remained strong in cells depleted of PP4C or R3β upto 7h after mitotic release.

A recent phosphoproteomic study (Grosstessner-Hain et al., 2011) reported that S1618 is phosphorylated by PLK1. We were able to confirm these results using the pS1618 specific phospho-antibody and the PLK-1 inhibitor, BI2536 (Fig. 2.5A). HeLa cells were treated with nocodazole for 6h and BI-2536 was added at 0.5, 3, and 6h during the 6h nocodazole incubation. Decrease in the phosphorylation signal of S1618 correlated with the amount of BI2536 exposure suggesting that inhibition of PLK1 blocked S1618 phosphorylation. Similarly,

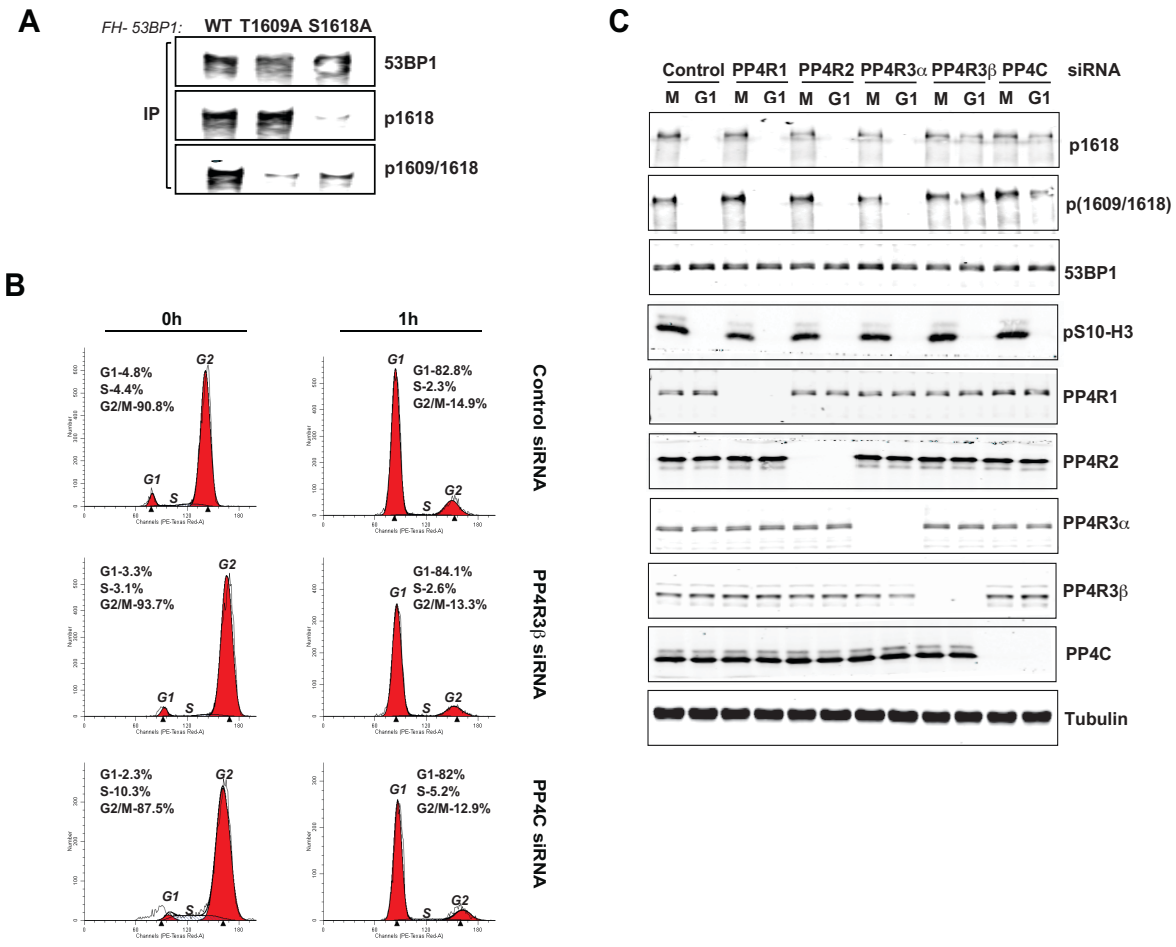

Figure 2.3: Analysis of 53BP1 phosphorylation using phospho-53BP1 antibody.

(A) Phospho-53BP1 antibody specificity. The phospho-antibody against pT1609/pS1618-53BP1 is specific for the combination of pT1609/pS1618 and does not recognize individual phospho-residues. HeLa cells expressing FH-53BP1 WT or indicated phospho-mutants were synchronized in mitosis and harvested by mitotic shake-off. Anti-FLAG agarose beads were used to immunopreciptate WT 53BP1 or indicated phospho-mutants. The immunopreciptate was analyzed by immunoblotting using antibodies against 53BP1, 53BP1-p1618, and 53BP1 p(1609/1618). **(B)** FACS plots of propidium iodide (PI) staining of HeLa cells transfected with the indicated siRNAs. At 60h after siRNA transfection, cells were incubated in nocodazole for 8h. Resulting mitotic cells were released into media without drug and harvested at 0 and 1h. Peaks for G1, S, and G2/M phases are indicated in addition to percent cells in each phase. By 1h after release 80-85% of cells exit mitosis and enter G1. **(C)** Impact of PP4C and R3β silencing on 53BP1 phosphorylation as measured by the phospho-53BP1 antibody. HeLa cells were transfected with indicated siRNAs against PP4 subunits for 60h and synchronized in mitosis with 100 ng/ml nocodazole for 8h. Cells were released by mitotic shake-off into media without drug and harvested after 5h (G1 phase). Whole-cell lysates were probed

Figure 2.3 (Continued):
with 53BP1 phospho-1618 (p1618) and 53BP1 phospho-1609/1618 (p1609-1618) antibodies. Total 53BP1 and tubulin were used as loading controls. Phospho-Ser10-histone H3 (pS10-H3) was used to indicate mitotic (M) cells. Cells were probed in parallel with antibodies against PP4R1, PP4R2, R3α, R3β, and PP4C to determine knockdown efficiency and specificity.

while T1609 has also been reported to be phosphorylated during mitosis (Dephoure et al., 2008), the kinase phosphorylating T1609 has not been identified. Based on the prediction algorithm of the Group-based Prediction System (GPS 2.1.2) (Xue et al., 2008), we predicted that several isoforms of the p38 mitogen-activated protein kinase (MAPK) potentially phosphorylate T1609 (Fig. 2.5B). We have previously shown that p38 MAPK is active during mitosis and has been implicated in mitotic checkpoints (Lee et al., 2010b). Similar to the PLK1 inhibitor strategy used to confirm S1618 phosphorylation, we used two different inhibitors of p38 MAPK, SB203580 and SB202190, to demonstrate that phosphorylation of T1609 is likely to be mediated by p38 MAPK (Fig. 2.5C). The phosphorylation of S1618 is not affected by the inhibitors of p38 MAPK as evident from stable pS1618 signal in the presence of these inhibitors. Since the in-house phospho- antibody detected phosphorylation at both T1609 and S1618 and the commercial antibody only detected S1618 phosphorylation, loss of signal with the in-house but not the commercial antibody was indicative of T1609 phosphorylation. However sequence based predictions have limited accuracy, and chemical inhibitors may have 'off-target' effects, therefore we cannot formally rule out that other kinases, such as CDK1 or NEK2, are also involved in the phosphorylation of T1609.

We reasoned that the elevated levels of phospho-T1609 and phospho-S1618 in PP4C/R3β silenced G1 cells could be due to ectopic activation of PLK1 and p38 MAPK. In this scenario continued PLK1 and p38 MAPK activity would be necessary for maintaining the pT1609/pS1618 signal in the G1 phase of PP4-

deficient cells. To evaluate this possibility, we inhibited PLK1 and the p38 MAPK immediately after mitotic exit. In control siRNA treated cells, addition of the inhibitors for PLK1 and p38 MAPK led to a complete loss of pT1609/pS1618 signal within 3 hours of G1 release (Fig. 2.4B). However, depletion of PP4C or R3β, caused persistence of phospho-T1609 and phospho-S1618 in G1 cells even in the presence of inhibitors for PLK1 and the p38 MAPK (Fig. 2.4B) for up to 7 hours. This result suggested that elevated level of phospho-T1609 and phospho-S1618 in PP4C/R3β depleted cells was due to the lack of dephosphorylation, and not ectopic reactivation of kinases that would lead to phosphorylation of these residues.

Finally, we wanted to determine whether phospho-T1609 and phospho-S1618 are directly targeted by PP4C. To this end, we immunopurified endogenous phospho-53BP1 from mitotic cells and performed dephosphorylation assays. We found that PP4C dephosphorylated both phospho-T1609 and phospho-S1618 in a dose-dependent manner (Fig. 2.4C). To confirm that the phosphorylation was indeed due to the catalytic activity of PP4C, we used a catalytically inactive PP4C mutant D82A, which failed to dephosphorylate 53BP1 even at high concentrations. Incubation of mitotic extracts with l-protein phosphatase (PP) served as a positive control. Together these results strongly suggested to us that PP4C directly dephosphorylates phosphoresidues, T1609 and S1618 of 53BP1.

Dephosphorylation of 53BP1 is necessary for recruitment to DSBs

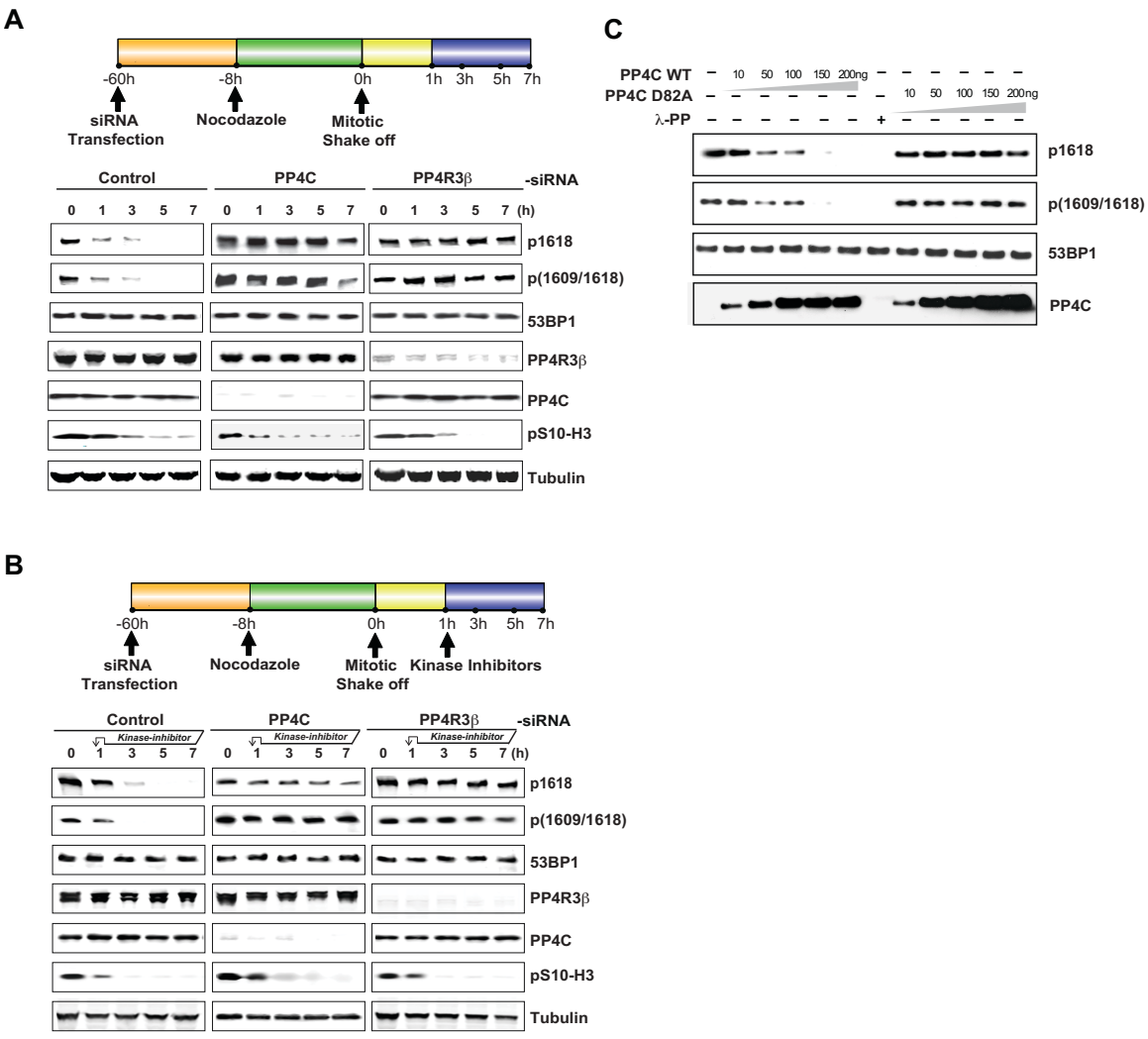

Figure 2.4: Kinetics of 53BP1 phosphorylation in mitosis/ G1.
(A) Kinetics of 53BP1 hyperphosphorylation in PP4C/R3β silenced cells during transition from mitosis to G1 phase. *Upper panel:* Schematic to study kinetics of 53BP1 hyperphosphorylation. *Lower panel:* HeLa cells transfected with control, PP4C or R3β siRNAs, synchronized in mitosis with nocodazole, released by mitotic shake-off, and harvested at indicated time points for western blot analysis. Cell lysates were probed with indicated antibodies.**(B)** Inhibition of kinases PLK-1 and p38-MAPK in PP4C/R3β silenced cells does not affect hyperphosphorylation of 53BP1 at T1609 and S1618. *Upper panel:* Schematic to study PLK-1 and p38-MAPK inhibition in PP4C/R3β silenced cells. *Lower panel:* HeLa cells were transfected with indicated siRNAs and treated with nocodazole. Kinase inhibitors against PLK-1 (BI2536, 20nM) and p38-MAPK (SB202190, 10μM) were added to the cells 1h following release from mitosis. Cells were harvested at various time-points after mitotic release and lysates were probed with indicated antibodies. **(C)** Recombinant PP4C incubated with mitotic extracts shows a dose-dependent decrease in phosphorylation at T1609 and S1618 whereas the catalytically

Figure 2.4 (Continued):
inactive PP4C D82A mutant protein fails to dephosphorylate even at high concentrations. Extract was also incubated with l-protein phosphatase (PP) as a positive control.

A

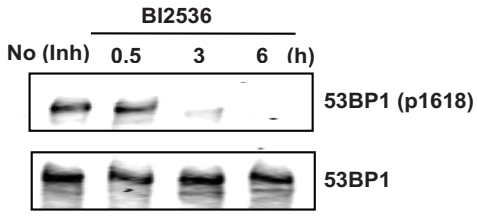

B

GPS: 2.1.2 Prediction of Kinase : Q Y G L G P Y E A V T P L T K A A D I

Predicted sites:

ID	Position	Code	Kinase	Peptide	Score	Cutoff
53BP1 T1609	11	T	CMGC/MAPK/p38/MAPK13	LGPYEAVTPLTKAAD	9.333	8.333
53BP1 T1609	11	T	CMGC/MAPK/p38/MAPK11	LGPYEAVTPLTKAAD	9.333	8.0
53BP1 T1609	11	T	CMGC/MAPK/ERK/MAPK3	LGPYEAVTPLTKAAD	8.299	7.747
53BP1 T1609	14	T	STE/STE7/MAP2K1	YEAVTPLTKAADT**	10	7.0
53BP1 T1609	14	T	Other/NEK/NEK2	YEAVTPLTKAADT**	9.333	6.667
53BP1 T1609	11	T	CMGC/MAPK/p38/MAPK14	LGPYEAVTPLTKAAD	6.14	5.72
53BP1 T1609	11	T	CMGC/CDK/CDK4/CDK6	LGPYEAVTPLTKAAD	6.25	5.25
53BP1 T1609	11	T	CMGC/MAPK/JNK/MAPK9	LGPYEAVTPLTKAAD	5.158	4.947
53BP1 T1609	11	T	CMGC/MAPK/JNK	LGPYEAVTPLTKAAD	5.562	4.688
53BP1 T1609	11	T	CMGC/JSK/JSK3B	LGPYEAVTPLTKAAD	4.816	4.102

C

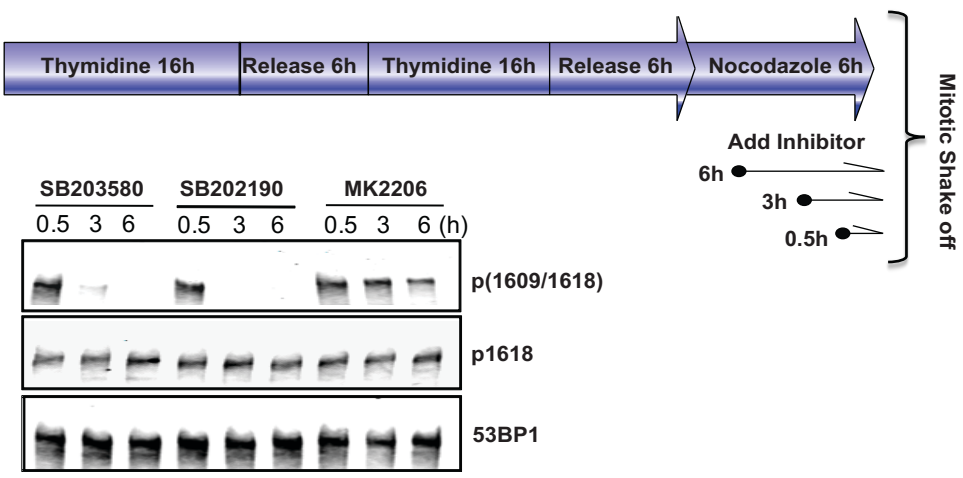

Figure 2.5: 53BP1 S1618 is phosphorylated by PLK-1 and T1609 likely phosphorylated by p38-MAPK.

(A) S1618 of 53BP1 is phosphorylated by PLK-1. HeLa cells were treated with PLK-1 inhibitor (BI-2536, 20nM) at various time points during 6h incubation with nocodazole. Mitotic cells were harvested and lysates were used for immunoblotting with antibodies against p1618-53BP1 and 53BP1. **(B)** T1609 is likely phosphorylated by p38-MAPK. Group-based Prediction System (GPS 2.1.2) was employed to predict kinase(s) that phosphorylate T1609 of 53BP1. **(C)** *Upper panel:* Experimental scheme for inhibiting p38 MAPK in mitotic cells.

Figure 2.5 (Continued):
HeLa cells were synchronized in mitosis by a thymidine block followed by nocodazole treatment for 6 hr. During the 6hr nocodazole treatment to arrest cells in mitosis, SB203580/SB202190 (0.5 μM, p38 kinase inhibitors) or MK-2206 (0.5 μM, Akt inhibitor) were added at three different time points. MK-2206 was used as a negative control. *Lower panel*: Immunoblot of cells treated with the indicated kinase inhibitors during nocodazole arrest. Antibodies against 53BP1 (p1618), 53BP1 p(1609/1618) and 53BP1 were used for immunoblotting.

After DNA damage, 53BP1 and other DDR proteins form distinct sub-nuclear foci that consist of collections of DDR proteins (Panier and Boulton, 2014). By tracking both the formation and dissolution of these foci using microscopy, we can study the kinetics of the repair process as DDR proteins are sequentially recruited to break sites and then removed after successful repair of damaged DNA. Since 53BP1 can be detected at these foci after DNA damage, we hypothesized that PP4C/R3β mediated dephosphorylation of 53BP1 is necessary for its localization to DSB in G1 cells. To test this idea we evaluated the localization of 53BP1 in the G1 phase of synchronized HeLa cells at various time points after ionizing radiation (IR), in the presence and absence of PP4C and R3β. We depleted PP4C and R3β and synchronized cells in mitosis. Cells were released into G1, irradiated at 10 Gy, and then fixed at different time-points in G1. When 53BP1 localization was studied using immunofluorescence (IF), we observed a striking reduction of 53BP1 foci in PP4C and R3β silenced cells (Fig. 2.6A). To further confirm the cell cycle phase specificity of this phenotype we utilized the Fucci system (Sakaue-Sawano et al., 2008) to visualize the G1 phase in RPE-1 cells. Cells engineered with the Fucci system allow dual-color imaging to distinguish cells in the G1 phase from those in S/G2/M phases. Cells in G1 phase emit red florescence owing to the expression of mKO2-hCDT1 and those in S/G2/M emit green florescence owing to mAG-hGem. As anticipated, absence of PP4C and R3β causes a significant reduction in 53BP1 foci in G1 cells (Fig. 2.6B). DSBs were marked by staining for γ–H2AX.

To evaluate the precise impact of dephosphorylating 53BP1, the two residues T1609 and S1618 that are hyperphosphorylated in the absence of PP4C were altered to phosphonull (T1609A and S1618A) and phosphomimetic mutants (T1609E and S1618D). These mutations were introduced individually and in combination (53BP1-AA and 53BP1-ED) in FH- tagged full-length 53BP1. Using the FLAG antibody the recruitment of these mutants to DSB sites was monitored in HeLa cells. None of the individual mutants have a significant impact on localization of 53BP1 to DSB sites (Fig. 2.7). Quantitation of more than 100 cells per condition showed that the percentage of 53BP1 foci positive cells in G1 were comparable for all single mutants. The 53BP1-AA double mutant was also recruited to DNA repair foci at similar levels compared to wild-type. However, we observed almost a complete block in the localization of the 53BP1-ED mutant to DSBs (Fig 2.7).

To assess the recruitment pattern of 53BP1-WT, 53BP1-AA or 53BP1-ED to DSBs, we released cells transfected with FH-tagged proteins from nocodazole block, irradiated them following G1 entry, and followed 53BP1 foci formation at different time points. 53BP1 foci measured by the FLAG antibody were detectable as early as 0.5h after radiation. The kinetics of 53BP1 foci formation was similar for both 53BP1-WT and 53BP1-AA mutant. However, when recruitment of 53BP1-ED was monitored, we saw complete absence of 53BP1 foci even at 10h after radiation (Fig. 2.8A).

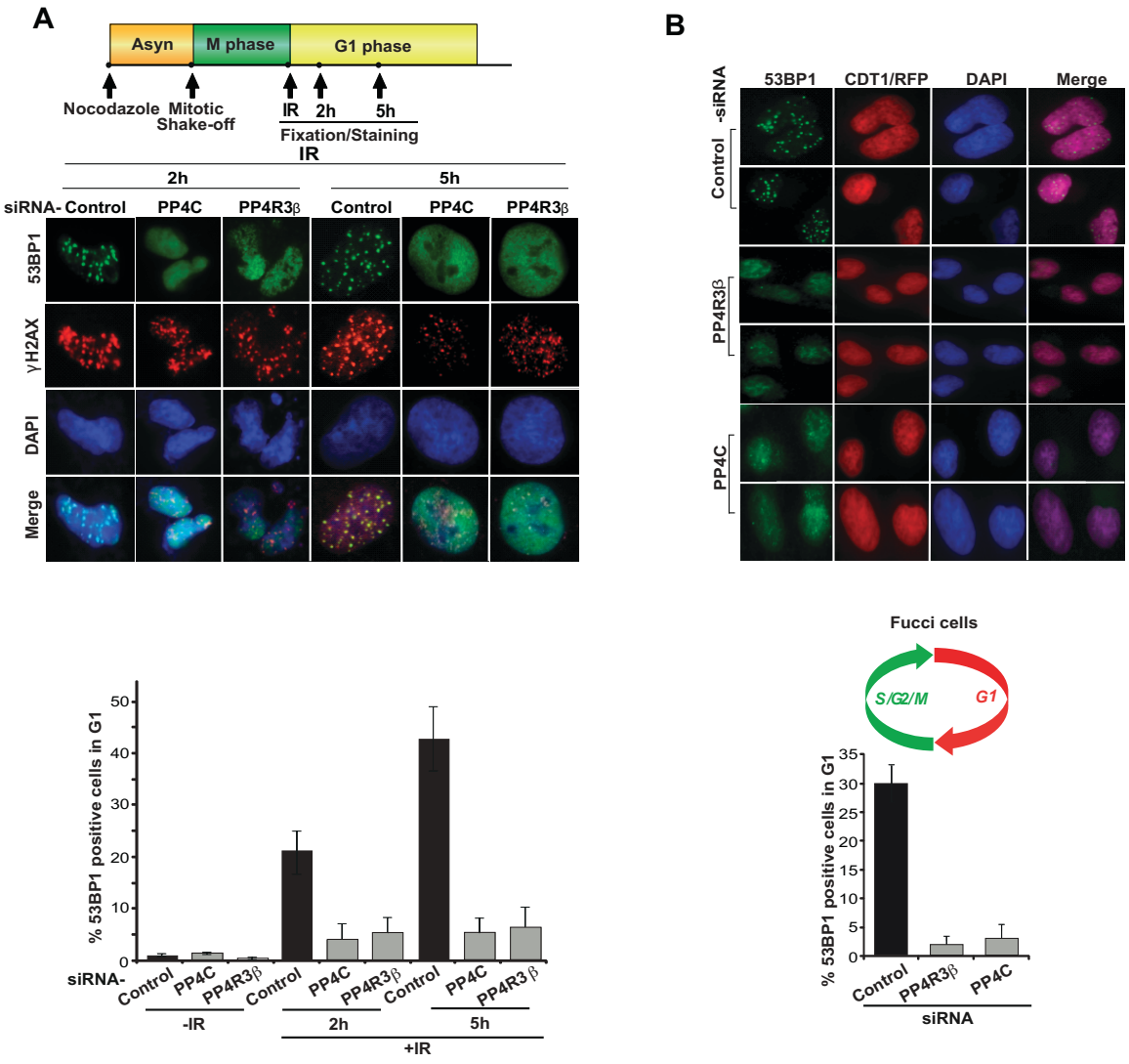

Figure 2.6: PP4C/R3β depletion abrogates 53BP1 foci in G1 cells.
(A, B) Schematic shows protocol for assessing 53BP1 activity in G1 cells irradiated immediately after mitotic shake-off. PP4C or R3β was depleted by siRNA transfection of HeLa cells (A) or Fucci-RPE1 cells (B). Mitotic cells were collected after 8h nocodazole treatment, irradiated immediately after release (10 Gy), fixed and co-stained with antibodies for 53BP1 (A, B) and γ-H2AX (A) at indicated times in G1 phase. CDT1/RFP is an internal Fucci cell marker that illuminates cells in G1 phase. Quantitation shows percent 53BP1 positive cells in G1. Cells displaying ≥ 10 foci were counted as positive. The data are expressed as mean ± S.D; n = 3. More than 100 cells were quantified per condition.

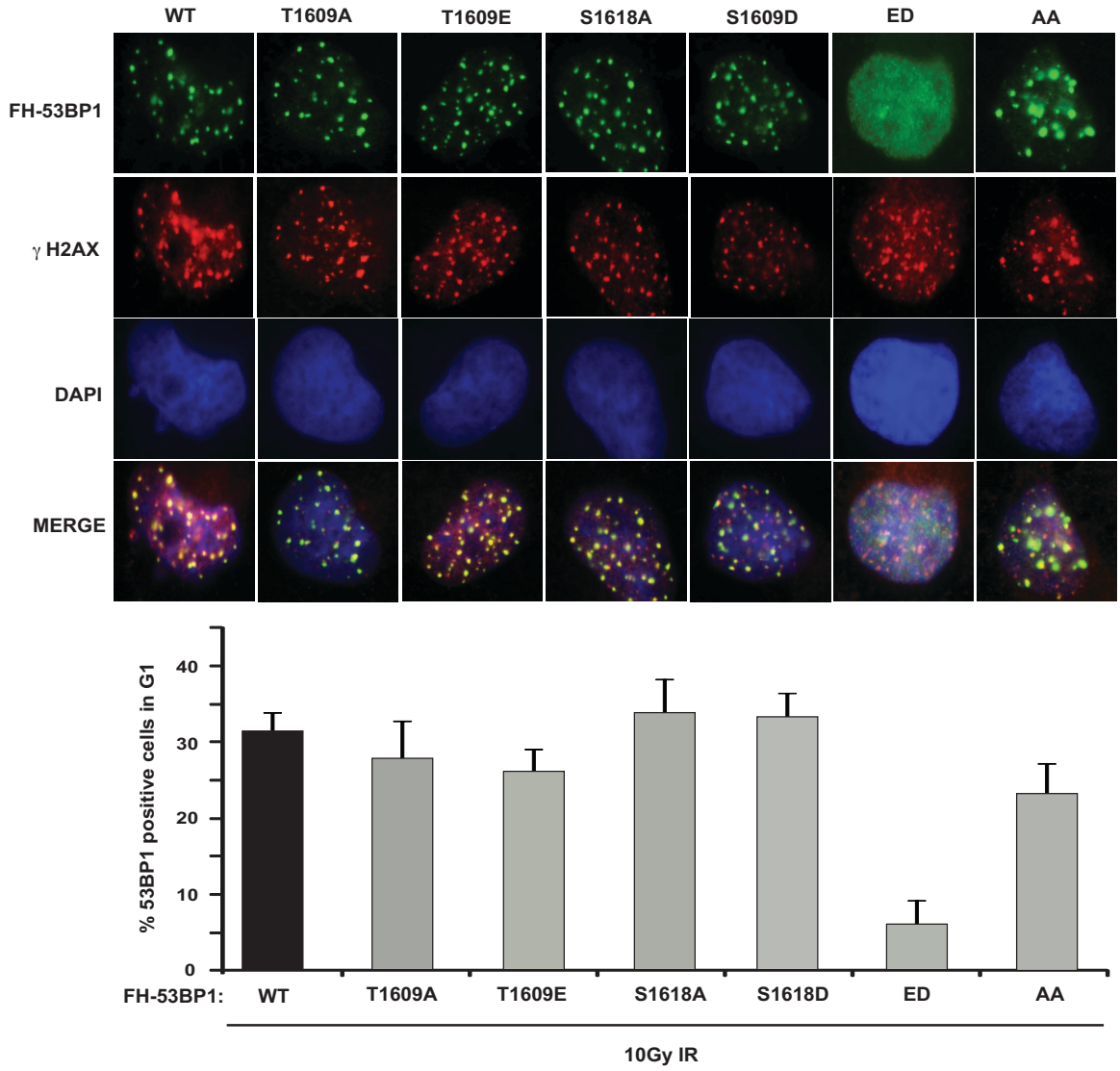

Figure 2.7: Individually mutating T1609 and S1618 has no impact on 53BP1 foci formation.

Upper panel: HeLa cells expressing FH-53BP1 WT or the indicated single or double phospho-mutants were treated with nocodazole, exposed to IR (10 Gy) and processed for immunofluorescence. *Lower panel:* Quantitation of 53BP1 foci positive cells (>100 cells were quantified per condition.) γ-H2AX staining was used to visualize DSBs. Cells with >10 foci were counted as positive.

So far, we have described that the phosphorylation of 53BP1 at T1609 and S1618 correlates with the loss of 53BP1 foci. This can be a result of defective recruitment of 53BP1 to DSB sites or impaired retention of 53BP1 at DSB sites. To address this issue and rigorously quantify the kinetics of 53BP1 recruitment to DSBs we utilized a multi-photon laser (MPL) system that induces DSBs in defined subfemtoliter volumes of the nucleus (Botvinick and Shah, 2007; Hartlerode et al., 2012). These experiments were done in collaboration with Jagesh Shah's lab at Harvard Medical School. To assess the kinetics of recruitment by the MPL-based live cell imaging, we fused GFP to full-length 53BP1 and stably expressed WT and mutant constructs in U2OS cells. As before, cells synchronized in the G1-phase were utilized for these assays. Consistent with previous data, 53BP1 WT and 53BP1-AA were recruited with in a few minutes to laser induced DSBs. However, there was virtually no recruitment of the 53BP1-ED mutant (Fig.2.8B). This result indicates that constitutive phosphorylation of 53BP1 at T1609 and S1618 blocks its recruitment to DNA lesions. These experiments suggested that diminished 53BP1 recruitment to DSBs in case of the 53BP1-ED mutant was due to a fundamental defect in 53BP1 accumulation and not due to impaired retention at damage-induced foci. Since these experiments were conducted in cells expressing endogenous 53BP1 we further confirmed our results by expressing the FH-53BP1 WT, and the 53BP1 phosphomutants (AA and ED) in 53BP1-deficient mouse embryonic fibroblasts (Fig. 2.9A).

It is also likely that the impaired recruitment of 53BP1 to DSBs is due to a defect in the localization of upstream DDR factors. To negate this possibility, we studied the localization of RNF-168, which ubiquitylates histone H2A around DSBs at K15 prior to accumulation of 53BP1 (also refer to Chapter 1). We observed that absence of PP4C and R3β had no impact on the localization of RNF-168, indicating that depletion of phosphatase subunits specifically affected 53BP1 localization (Fig. 2.9B).

We have shown that depletion of PP4C/R3β has an impact on 53BP1 foci formation in G1 cells that was comparable to the phenotype induced by the expression of phosphomimetic 53BP1-ED mutant (Fig. 2.6A and Fig. 2.8A). Taking these findings into consideration, we reasoned that if indeed the impact of R3β on 53BP1 recruitment was due to the dephosphorylation of S1618 and T1609, then the effect of silencing R3β would be reversed by expressing the 53BP1 phosphonull (53BP1-AA) mutant. Consistent with this notion, localization of 53BP1 to DSB sites in R3β-silenced cells was restored by the 53BP1-AA mutant, but not in 53BP1-WT or the 53BP1-ED expressing cells (Fig. 2.10). This result strongly suggested that PP4C/R3β-mediated dephosphorylation of 53BP1 at T1609 and S1618 is necessary for its localization to DSBs in G1 cells.

Functional relevance of dephosphorylating 53BP1 at T1609 and S1618

Distinct nuclear bodies visible in G1 cells represent endogenous DNA damage that occurs during DNA replication and are carried through mitosis

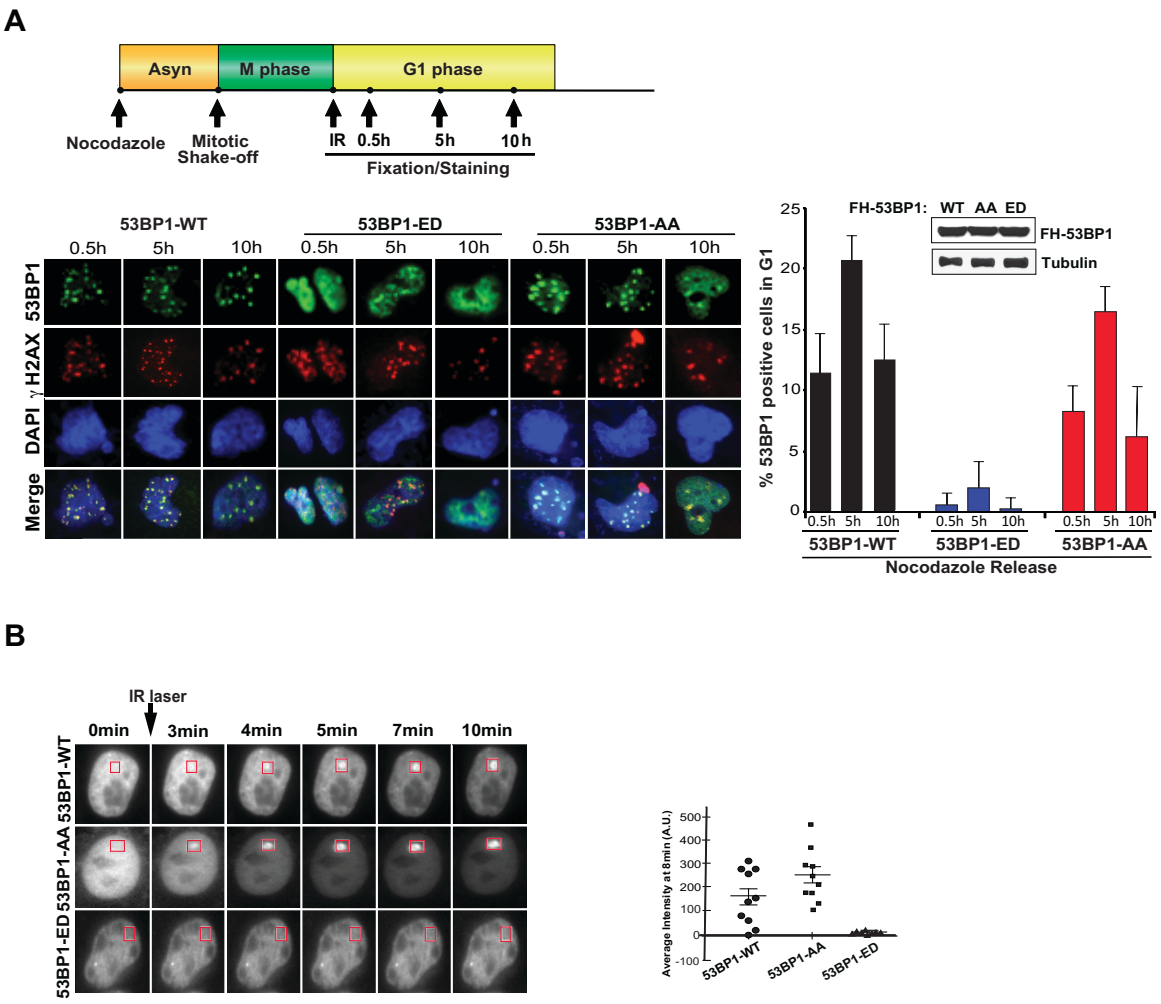

Figure 2.8: Analysis of 53BP1 phospho-mutant recruitment to DNA lesions. **(A)** Phosphomimetic 53BP1 mutant is not recruited to DSBs. *Upper panel:* Schematic to study 53BP1 focal recruitment. *Lower left panel:* HeLa cells stably expressing full-length FH-53BP1 (WT, AA, or ED) were prepared for immunofluorescence after mitotic shake-off and 10Gy IR. 53BP1 foci were visualized using anti-FLAG antibody. γ-H2AX was stained to mark sites of DNA damage. *Lower right panel*: Quantitation shows percent 53BP1 positive cells in G1 for WT and phospho-mutants. Cells displaying ≥ 10 foci were counted as positive. The data is expressed as mean ± S.D; n = 3; > 100 cells quantified per mutant. *Lower right panel inset:* Immunoblot showing equal expression levels of different FH-53BP1 constructs (WT, AA, and ED). Irradiated cells released into G1 were analyzed in parallel for expression using anti-FLAG antibody. Tubulin was used as a loading control.**(B)** Kinetics of 53BP1 recruitment to DNA lesions. To quantify the kinetics of 53BP1 recruitment to DSBs, a multi-photon laser (MPL) system was used. U2OS cells stably expressing full-length GFP-53BP1 (WT, AA, or ED) were treated with nocodazole for 6h and released into G1. *Left panels:* Representative freeze-frame images from live-cell movies for each sample. A total of 10 cells were monitored per condition for 53BP1 recruitment to DSBs.

Figure 2.8 (Continued):
Right panel: Quantitation of 53BP1 recruitment was done by comparison of average signal intensity at 8 min in individual cells represented by a single dot; mean ± S.D; n = 3. (Experiments performed in collaboration with Jagesh Shah's laboratory, Harvard Medical School.)

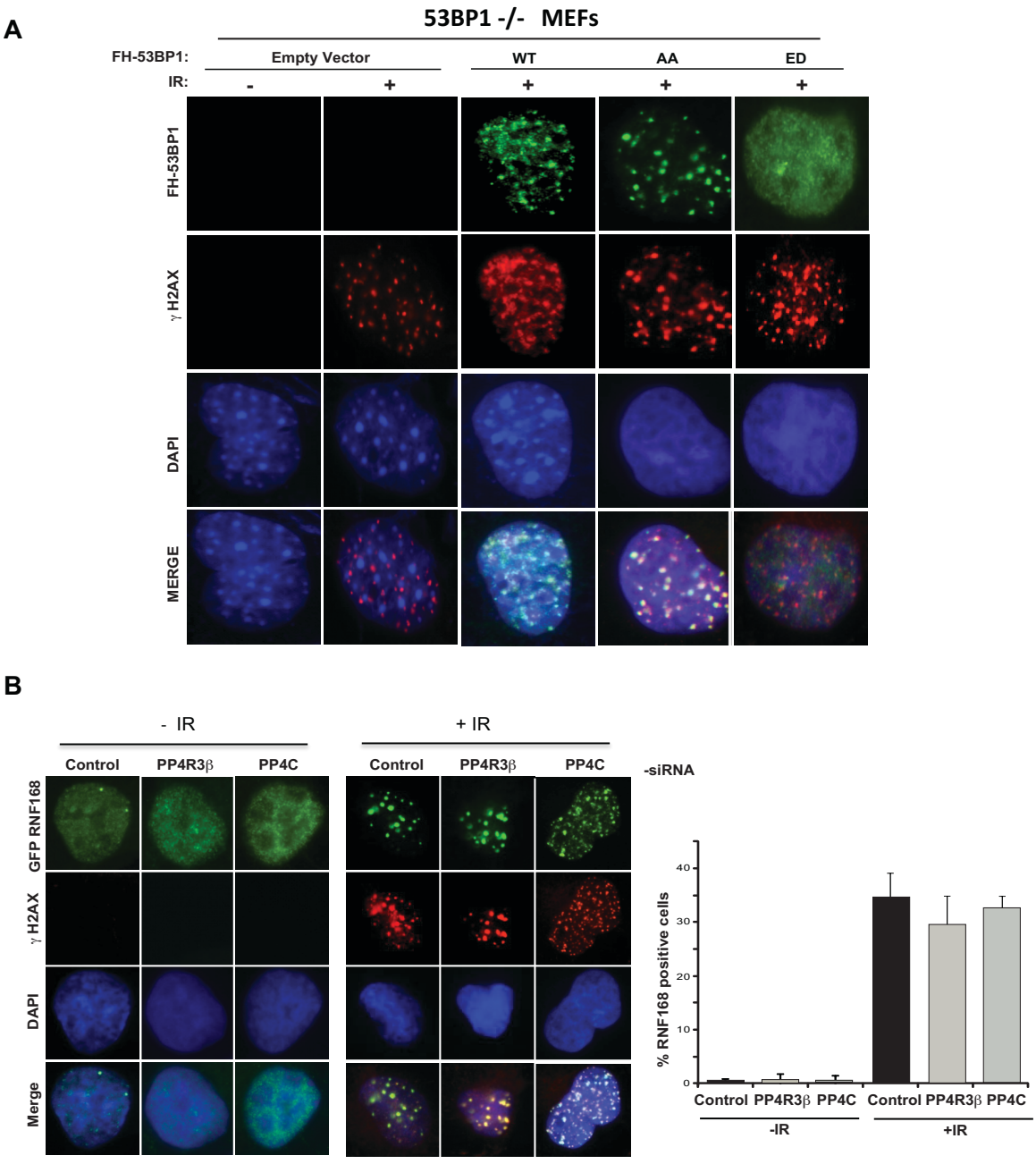

Figure 2.9: 53BP1 foci in 53BP1 -/- MEFs and RNF168 recruitment in the absence of PP4C and R3β.

(A) 53BP1-WT and AA but not 53BP1-ED forms foci in 53BP1$^{-/-}$ MEFs. FH-53BP1 WT and the indicated phospho-mutants were expressed in 53BP1-deficient mouse embryonic fibroblasts (MEFs) and exposed to 10 Gy IR. FH-c (Empty vector) was transfected as a control. Cells were fixed and stained with anti-FLAG antibody. γ-H2AX was used to visualize DSBs. **(B)** RNF168 foci formation is not affected by silencing PP4C and R3β. *Left panel:* U2OS cells expressing GFP-RNF168 were transfected with siRNAs against PP4C or

Figure 2.9 (Continued):
R3β. Cells were synchronized in mitosis, exposed to 10 Gy IR immediately following release, and fixed for immunofluorescence. Representative images are shown. *Right panel:* Quantitation of RNF168 foci positive cells (>100 cells were quantified per condition.) Data are expressed as mean ±S.D. γ-H2AX staining was used to visualize DSBs.

(Harrigan et al., 2011; Lukas et al., 2011). Low doses of aphidicolin increases the frequency of nuclear bodies in cells without triggering the cellular checkpoints.53BP1 is recruited to nuclear bodies in G1 cells and plays a role in the resolution of these DNA lesions (Lukas et al., 2011). We transfected U2OS cells with GFP-tagged wild-type 53BP1 and the 53BP1 phospho-mutants (AA and ED), treated the cells with aphidicolin and stained them with cyclin A to distinguish G2/M cells (Fig. 2.11). Consistent with their exclusion from DNA lesions, 53BP1-ED phosphomimetic mutants are not recruited to nuclear bodies whereas the 53BP1-AA phosphonull mutants are localized at nuclear bodies at levels comparable to wild-type 53BP1. Together these results suggest that recruitment of 53BP1 to endogenous and exogenous DNA lesions is compromised by constitutive phosphorylation of the T1609 and the S1618 residue.

Based on these results we hypothesized that 53BP1 constitutively phosphorylated at T1609 and S1618 is functionally equivalent to the loss of 53BP1. 53BP1-deficient cells have increased radiosensitivity and loss of 53BP1 in BRCA1-deficent tumors induces resistance to PARP inhibitors. Therefore we assessed the radiosensitivity of HeLa cells where endogenous 53BP1 was replaced with the phosphomutants (AA and ED). Cells expressing the 53BP1-ED mutant are significantly more radiosensitive than cells expressing the wild-type 53BP1 and the 53BP1-AA mutant (Fig. 2.12A). Similarly, the BRCA1-mutant ovarian line UWB1.289 was manipulated to replace endogenous 53BP1 with the phosphomutants, (AA and ED) and used to assess sensitivity to clinical grade

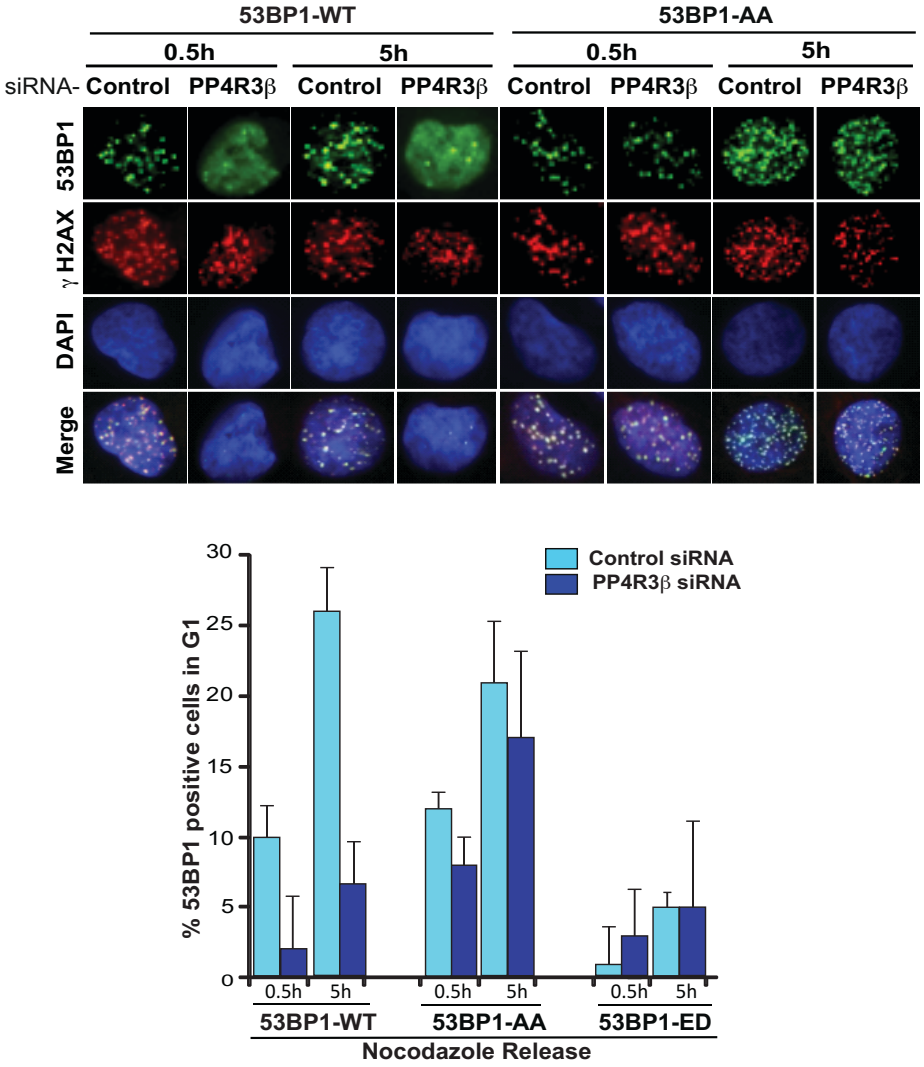

Figure 2.10: The failure of 53BP1 to form foci in R3β silenced cells is rescued by expressing the 53BP1 AA mutant. *Left panel:* HeLa cells expressing FH-53BP1 WT or indicated phosphor-mutants were transfected with control siRNA or siRNA against R3β and prepared for immunofluorescence. Anti-FLAG antibody was used to visualize 53BP1. γ-H2AX was stained to mark sites of DNA damage. *Right panel*: Quantitation shows percent 53BP1 positive cells in G1 for WT and phospho-mutants. Cells displaying ≥ 10 foci were counted as positive. The data is expressed as mean ± S.D; n = 3; > 100 cells quantified per mutant.

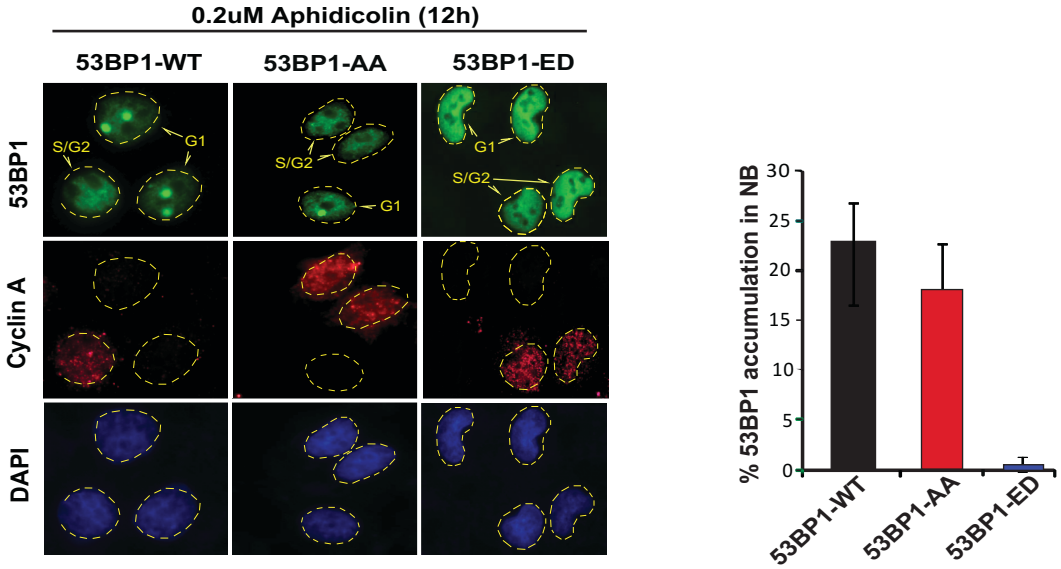

Figure 2.11: Constitutive phosphorylation of 53BP1 at T1609 and S1618 alters 53BP1 recruitment to nuclear bodies. Recruitment of 53BP1 to replication stress induced nuclear bodies in G1. U2OS cells, stably expressing full-length GFP-53BP1 (WT, AA or ED) were exposed to low dose of aphidicolin (0.2 μM) for 12 h and stained with anti-Cyclin A, which illuminates S/G2 cells. Representative images and quantitation of 53BP1 accumulation in nuclear bodies are shown; >100 Cyclin A negative cells were quantified; mean ± S.D; n = 3.

PARP inhibitor, ABT-888. As anticipated the expression of the 53BP1-ED mutant confers resistance to ABT-888 whereas cells expressing the wildtype 53BP1 or the 53BP1-AA mutant remain sensitive to ABT-888 (Fig. 2.12B). Together these results highlight the importance of T1609 and S1618 in regulating 53BP1 activity and suggest that the phosphorylation status of the UDR motif in 53BP1 may have relevance in cancer. Therefore, to identify any mutations and deletions in the UDR motif we scanned The Cancer Genome Atlas (TCGA) 2012 (Cancer Genome Atlas, 2012). Sequencing of 482 invasive breast carcinomas revealed three sporadic missense mutations in 53BP1, and one of the mutations was the conversion of the isoleucine (Ile) residue at 1617 (I1617) to serine (I1617S) (Fig. 2.13A). The I1617S mutation has a significant impact on recruitment of 53BP1 to DSBs (Fig. 2.13B) and cells expressing the I1617S-53BP1 mutant have increased sensitivity to IR (Fig. 2.14A). Furthermore, the BRCA1-mutant ovarian line UWB1.289 expressing the I1617S-53BP1 mutant is relatively resistant to ABT-888 (Fig. 2.14B).

Ectopic recruitment of 53BP1 to chromatin in mitosis causes mitotic defects

Dephosphorylation of T1609 and S1618 in G1 is necessary for the recruitment of 53BP1 to chromatin and specifically to DSBs. A key question is whether the loss of phosphorylation at these two residues is sufficient to allow the recruitment of 53BP1 to DNA lesions in mitosis. 53BP1 and upstream factors

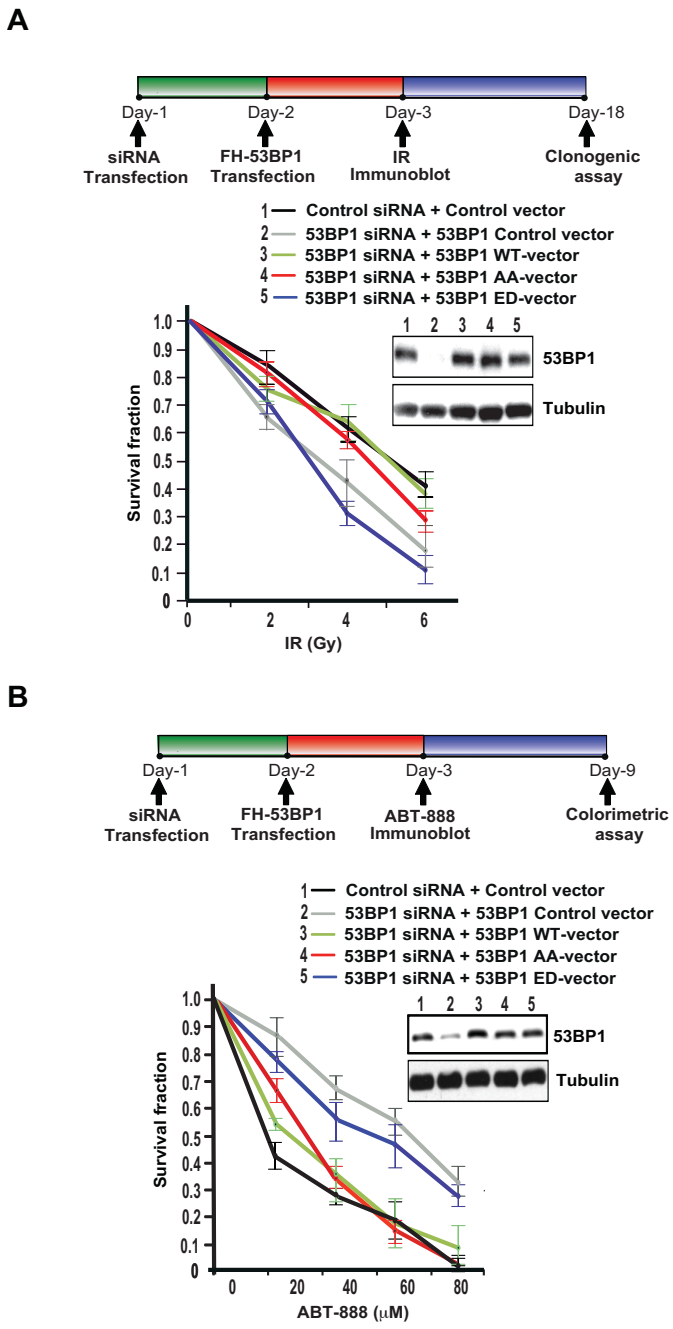

Figure 2.12: Radiosensitivity and PARP inhibitor sensitivity of 53BP1 phospho-mutants.

(A) Radiosensitivity of 53BP1 phosphomutants. Endogenous 53BP1 was silenced in HeLa cells with siRNA and replaced with siRNA-resistant 53BP1 constructs (WT, AA, or ED). At 72 h after siRNA transfection, cells were irradiated at the indicated doses and viability was evaluated by clonogenic survival. Immunoblots performed to confirm siRNA efficiency and expression of siRNA-resistant constructs are shown. Data are expressed as mean ± S.D. n =3.

(B) Phosphomimetic 53BP1 mutant rescues PARP inhibitor sensitivity in BRCA1-deficient cells. Endogenous 53BP1 was replaced with siRNA-resistant 53BP1

Figure 2.12 (Continued):
constructs (WT, AA, or ED) in the BRCA1-deficient ovarian cancer line UWB1.289, and sensitivity to clinical-grade PARP inhibitor ABT888 was assessed by CellTiter-Glo colorimetric viability assay. Immunoblots performed to confirm siRNA efficiency and expression of siRNA-resistant constructs are shown. Data are expressed as mean ± S.D. n =3.

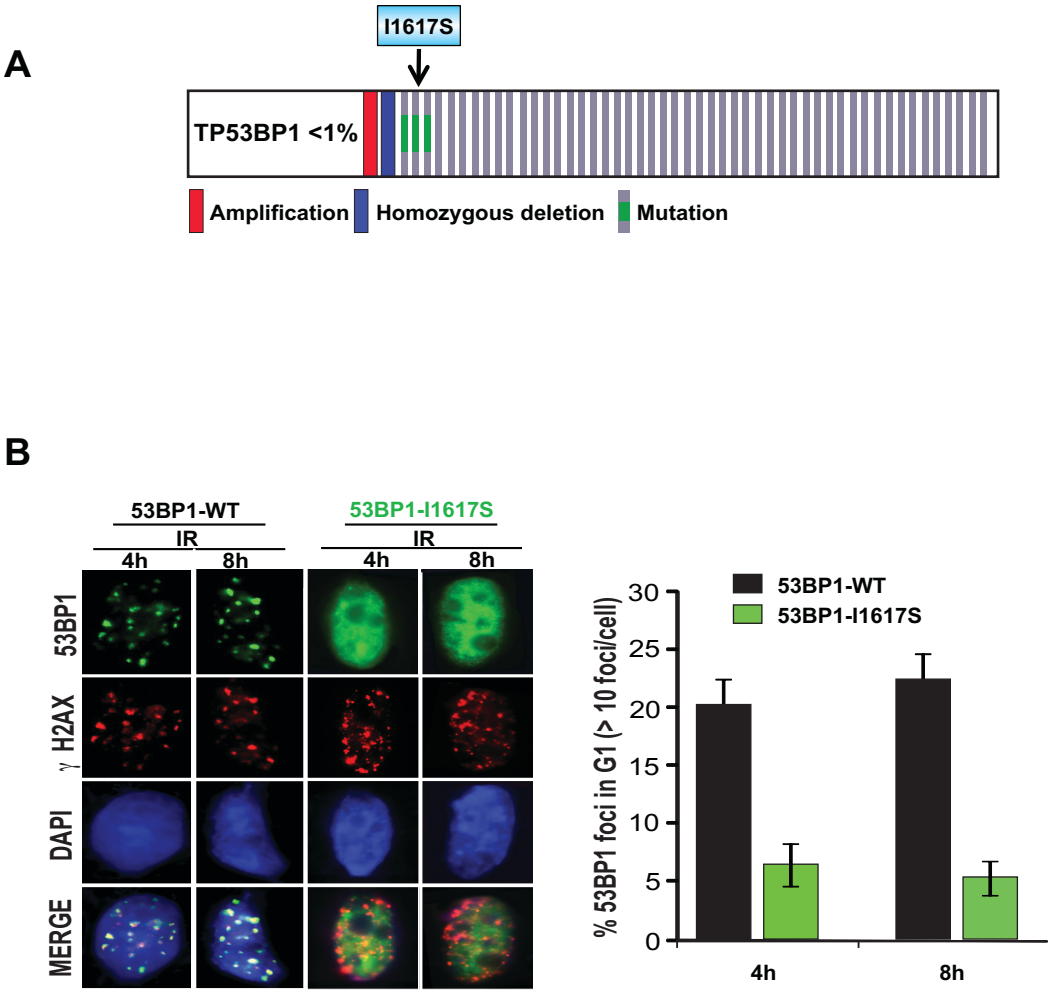

Figure 2.13: Characterization of breast cancer mutation 53BP1 I1617S.
(A) Oncoprint from cBioPortal (http://www.cbioportal.org/public-portal) showing occurrence of the missense mutation I1617S. **(B)** *Left panels:* Impaired recruitment of 53BP1 I1617S mutant to DSB repair foci. FH- WT or 53BP1 I1617S mutant was introduced into HeLa cells and 53BP1 foci were visualized using anti-Flag antibody in G1. Representative images of 53BP1 foci and γ-H2AX staining are shown. *Right panel*: Quantitation of percent 53BP1 foci in G1 phase in cells expressing 53BP1 WT or I1617S.

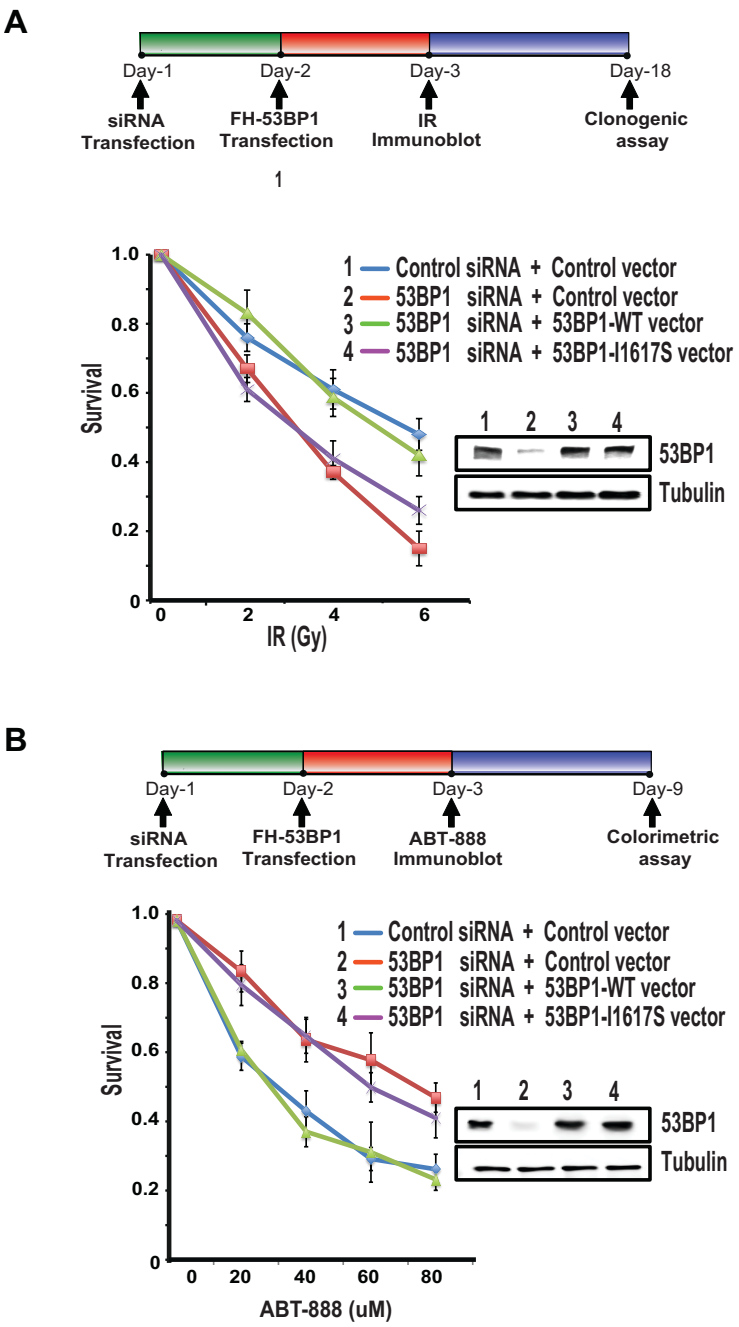

Figure 2.14: Radiosensitivity and PARP inhibitor sensitivity of 53BP1-I1617S.

(A) Radiosensitivity of 53BP1-I1617S. Endogenous 53BP1 was silenced in HeLa cells with siRNA and replaced with siRNA-resistant 53BP1 constructs (WT or I1617S). At 72 h after siRNA transfection, cells were irradiated at the indicated doses and viability was evaluated by clonogenic survival. Immunoblots performed to confirm siRNA efficiency and expression of siRNA-resistant constructs are shown. Data are expressed as mean ± S.D. n =3. **(B)** Replacing endogenous 53BP1 with I1617S causes resistance to PARP inhibition in ovarian

Figure 2.14 (Continued):
cancer line UWB1.289.Endogenous 53BP1 was replaced with siRNA-resistant 53BP1 constructs (WT or I1617S) in the BRCA1-deficient ovarian cancer line UWB1.289, and sensitivity to clinical-grade PARP inhibitor ABT888 was assessed by CellTiter-Glo colorimetric viability assay. Immunoblots performed to confirm siRNA efficiency and expression of siRNA-resistant constructs are shown. Data are expressed as mean ± S.D. n =3.

(RNF8 and RNF168) are excluded from DSBs during early and mid-mitosis. In late-mitosis (anaphase/telophase) RNF8 and RNF168 are recruited to DSBs while 53BP1 continues to be excluded (Giunta et al., 2010; Giunta and Jackson, 2011). A possible interpretation of this result is that RNF168-mediated ubiquitylation of H2A at DNA lesions in late mitosis is not sufficient to recruit 53BP1. We hypothesized that the phosphorylation of 53BP1 at T1609 and S1618 prevents its recruitment to DNA lesions in late mitosis. To test our hypothesis we utilized U2OS cells expressing RFP-H2B (to visualize chromatin) and GFP-tagged 53BP1 WT or 53BP1 phospho-mutants (AA and ED). These experiments were done in collaboration with David Pellman's laboratory at Dana-Farber Cancer Institute. Cells were treated with low doses of aphidicolin to induce replication-induced DNA lesions and time-lapse imaging was conducted to monitor the sub-cellular localization of 53BP1 during mitosis. Consistent with previous studies wildtype 53BP1 is not recruited to chromatin during mitosis, and the 53BP1 foci become visible in G1 cells. As anticipated the 53BP1-ED mutant remains excluded from chromatin both in mitosis and G1 cells. However, the 53BP1-AA mutant formed distinct foci during late mitosis, (transition of anaphase/telophase), (Fig. 2.15A). Quantification of the time required for 53BP1 to form foci after anaphase onset showed that the 53BP1-AA mutant was forming foci significantly faster than wildtype 53BP1 (Fig. 2.15A). Interestingly, in some cells the 53BP1-AA mutant is recruited to chromatin as early as 10-20 minutes after anaphase onset when the chromosomes remain condensed (Fig. 2.15, 20' time point).

To examine the functional consequences of 53BP1 recruitment to DNA lesions in mitosis we synchronized cells in metaphase and exposed them to low dose of IR (0.5 Gy) prior to release. Surprisingly cells expressing 53BP1-AA mutant exposed to IR had a significant increase in mitotic errors manifested as increases in lagging chromosomes and micronuclei (Fig. 2.15B). Micronuclei (MN) formed by whole chromosome mis-segregation contain kinetochores (Fenech, 2010), therefore we evaluated the presence of kinetochores in MN generated by IR in cells expressing 53BP1-AA mutant. In cells expressing the wildtype 53BP1 the proportion of kinetochore-positive and kinetochore-negative MN were comparable. In contrast cells expressing the 53BP1-AA mutant had a striking increase in kinetochore-positive MN (Fig. 2.16). 53BP1 promotes aberrant NHEJ at uncapped telomeres leading to genomic_instability (Dimitrova et al., 2008). Interestingly, blocking NHEJ by incubation with the DNA-PK inhibitor 'rescued' the mitotic defects induced by the 53BP1-AA mutant (Fig. 2.16). These results suggest that phosphorylation of 53BP1 at T1609 and S1618 during mitosis is necessary and sufficient to prevent its recruitment to DNA lesions in late mitosis. Furthermore, inappropriate recruitment of 53BP1 to mitotic DNA lesions impairs chromosome segregation.

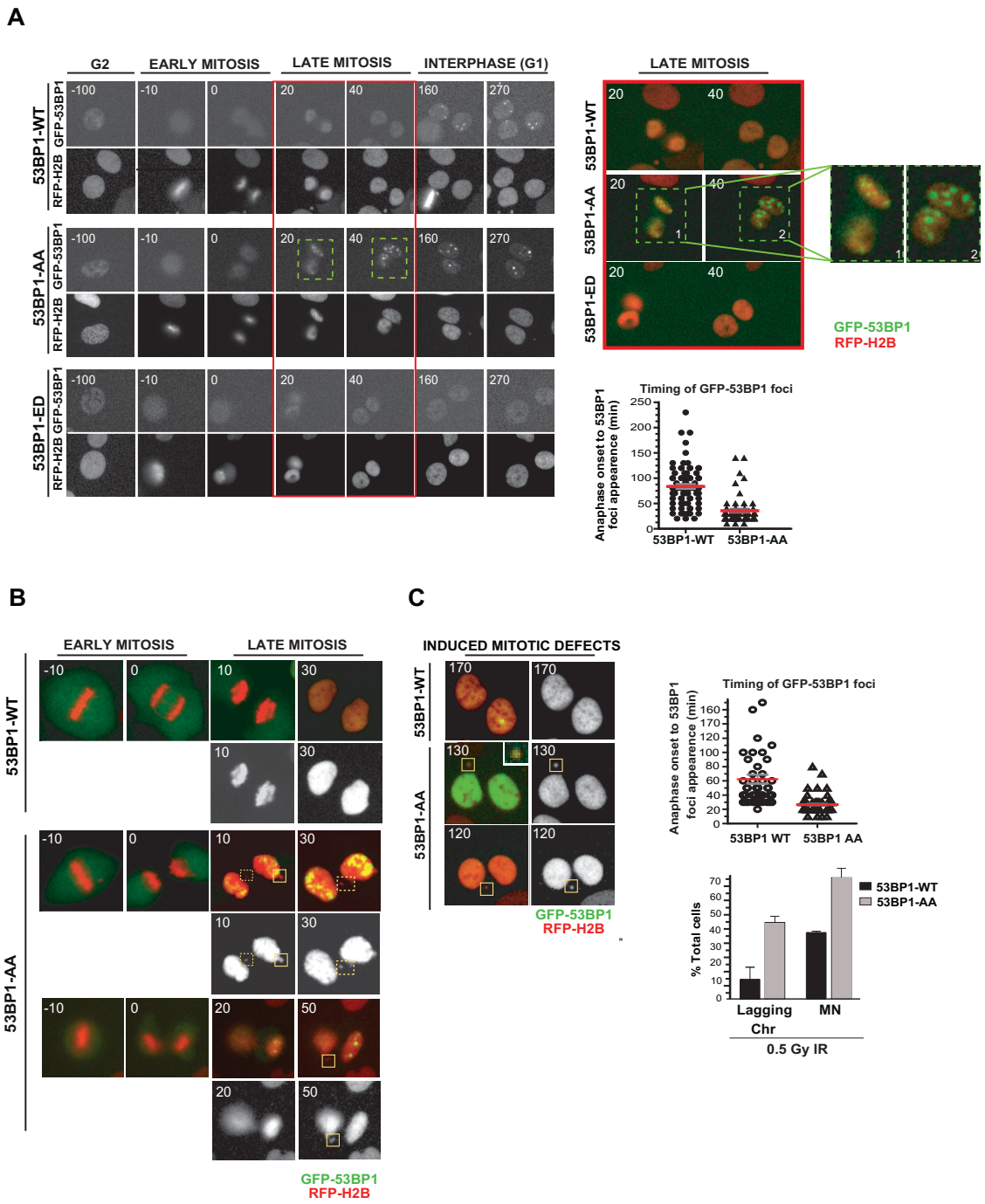

Figure 2.15: Loss of T1609 and S1618 phosphorylation allows 53BP1 to localize to DNA breaks in mitosis and promotes genomic instability.
(A) Premature recruitment of 53BP1-AA mutant to DNA lesions during mitosis. To examine the kinetics of 53BP1 foci formation, U2OS cells expressing RFP-H2B were transfected with different GFP-53BP1 constructs (WT, AA, ED), treated with 0.2μM aphidicolin for 12 h and released prior to live cell imaging.

Figure 2.15 (Continued):
Left panels: Representative time-lapse still images of cells expressing RFP-H2B and GFP tagged 53BP1-WT (top panels) or 53BP1-AA (middle panels) or 53BP1-ED (bottom panels) during G2, mitosis (early and late) and the following G1 phase. Time is shown in minutes (t=0, anaphase onset). *Upper right panels:* late mitotic cells (red box region) with premature 53BP1-AA foci formation are illustrated in overlaid images along with high magnification images (boxes 1 and 2). GFP-53BP1 and RFP-H2B are shown in green and red, respectively. *Bottom right panels:* Corresponding quantitation of the timing of 53BP1 foci formation ($p < 0.0001$, non-parametric t-test). Averages are shown in red bars. **(B)** Premature mitotic 53BP1-AA foci formation is accompanied by increased mitotic defects. U2OS cells expressing RFP-H2B were transfected with different GFP-53BP1 constructs (WT, AA) and exposed to 0.5Gy IR during mitosis prior to live cell imaging. Overlaid images with GFP-53BP1 (green) and RFP-H2B (red, also shown at the bottom with RFP-H2B only). Cells containing premature mitotic 53BP1-AA foci progress through cell cycle with increased mitotic defects, such as lagging chromosomes (dashed boxes) and micronuclei (MN, boxes). **(C)** Corresponding mitotic defects that persist as MN in G1. Note that some MN contain 53BP1-AA (Box, 130 min, GFP in primary nuclei is overexposed to accentuate 53BP1 signal in MN). *Upper right panel:* Corresponding quantification for the timing of 53BP1 foci formation in indicated conditions ($p < 0.0001$, non-parametric t-test). *Lower right panel*: percentage of cells that display lagging chromosomes and MN in indicated conditions. Only newly arising defects in cells exiting mitosis were scored ($p < 0.0001$, non-parametric t-test). Errors bars indicate S.E.M.

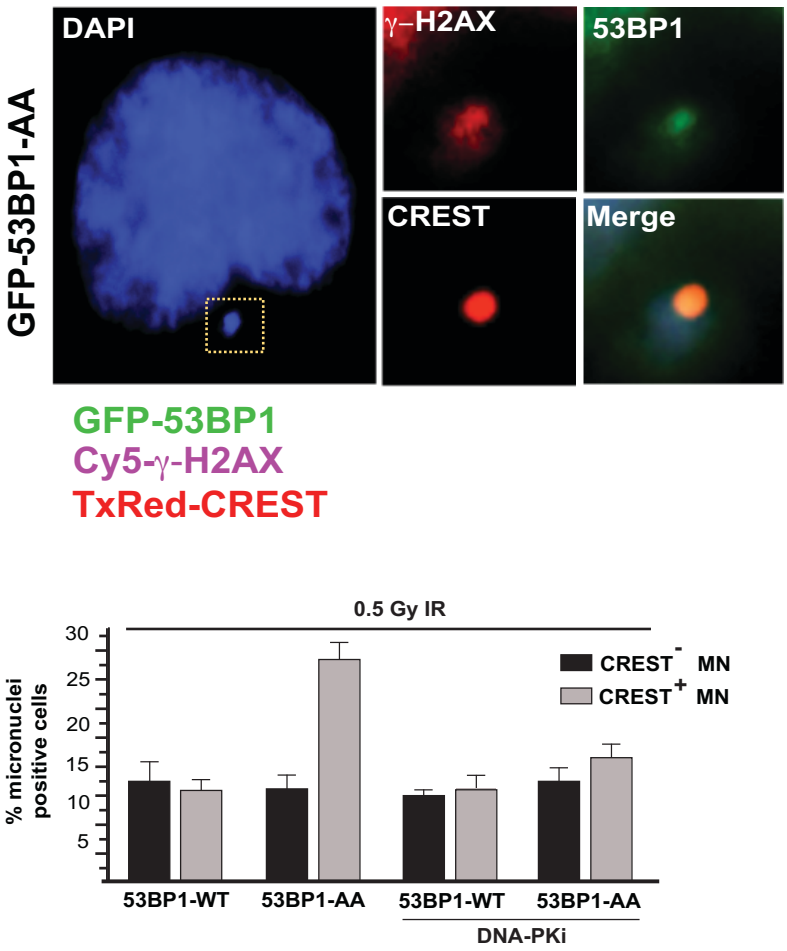

Figure 2.16: Ectopic recruitment of 53BP1-AA causes an increase in CREST$^+$ MN.

U2OS cells expressing different GFP-53BP1 constructs (WT or AA) were treated with nocodazole for 6h. Resulting mitotic cells were irradiated at low-dose (0.5 Gy) and released into normal media. At 6h following release, cells were fixed and co-stained with antibodies for γ-H2AX and CREST (kinetochore marker) to visualize kinetochore-positive (CREST$^+$) MN. Where indicated, transfected cells were pretreated with DNA-PK inhibitor (DNA-PKi) (NU7441, 10μM) 1h prior to irradiation. Quantification of CREST$^-$ and CREST$^+$ MN in cells expressing WT or AA GFP-53BP1 with or without DNA-PKi is shown. The data are expressed as mean ± S.D; n = 3 (> 100 cells were quantified).

DISCUSSION

Phosphorylation of 53BP1 has been comprehensively investigated (Jowsey et al., 2007), and recent studies demonstrate that generating phosphonull mutants of a combination of 28 phosphosites (PI3-like kinase; S/TPQ motifs) in the N-terminus of 53BP1 disrupts interaction with critical factors such as Rif1 (Callen et al., 2013; Chapman et al., 2013; Di Virgilio et al., 2013; Escribano-Diaz et al., 2013; Zimmermann et al., 2013) and abrogates its function in class-switch recombination and DNA repair (Bothmer et al., 2011; Di Virgilio et al., 2013; Ward et al., 2006). However there is no understanding of how dephosphorylation may directly regulate 53BP1 activity.

Large scale phosphoproteomic studies have revealed that a significant number of the DDR factors are constitutively phosphorylated in the course of the cell cycle (Dephoure et al., 2008; Grosstessner-Hain et al., 2011; Hegemann et al., 2011) and over one-third of observed phosphorylation sites are down-regulated within minutes of DNA damage (Bennetzen et al., 2010; Bensimon et al., 2010). How the constitutive phosphorylation and potential dephosphorylation of the DDR proteins impact their function remains unclear. Studies on the role of phosphatases in the DDR, including ones from our group, have been limited to demonstrating their significance in later stages of the DDR, largely in relieving the cell cycle checkpoint and restoring the cell to its 'pre-DNA damage' state (Lee and Chowdhury, 2011; Peng and Maller, 2010). Our results on the PP4C/R3β complex mediated dephosphorylation of 53BP1 counter the existing paradigm regarding the role of phosphatases in DSB repair. Here we provide an example

where a phosphatase by regulating the critical step of 53BP1 recruitment to DSB sites, influences the process of DNA repair, and the choice of DSB repair pathway.

Mitotic cells are distinct from inter-phase cells in their ability to tolerate the presence of DSBs as cells progress through the mitotic phase without triggering a checkpoint response (Heijink et al., 2013). More recent studies have demonstrated that the 'sensors' of the DSBs such as the MRN complex and the Ku complex (Gomez-Godinez et al., 2010; Peterson et al., 2011) are recruited to DSBs in mitosis and γ-H2AX is normally phosphorylated (Giunta et al., 2010; Nelson et al., 2009; van Vugt et al., 2010). A fundamental and important question is why do cells block the 'secondary' steps of the DSB repair process in mitosis, specifically the recruitment of 53BP1 to DNA lesions. Our results with the 53BP1-AA mutant suggest that allowing 53BP1 to localize to DSBs and chromatin in late mitosis counter-intuitively promotes genomic instability, and leads to mitotic defects that are manifested in increased number of kinetochore positive micronuclei and lagging chromosomes. The underlying mechanism for this observation remains unclear but it is feasible that stress induced telomere de-protection in mitosis (Hayashi et al., 2012) coupled with the ability of 53BP1 to promote end-joining of telomeres by increasing chromatin mobility (Dimitrova et al., 2008) may contribute to this striking phenotype. Blocking NHEJ in the 53BP1-AA expressing cells does resolve the mitotic defects giving some credence to this idea. Another important question is whether other DDR factors have a similar regulatory mechanism where dephosphorylation is a pre-requisite for their

participation in the DDR. The evolutionary conservation of the phosphoresidues (T1609 and S1618) and the flanking amino acids give some credence to the idea that similar 'dephosphorylation-dependent chromatin recruitment motifs', maybe present in other DNA repair proteins. Preliminary computational predictions support this notion (unpublished results, SD and DC) but significant experimental work is necessary to confirm the functional relevance of these predictions. Future studies will elucidate the molecular details of how protein phosphatases regulate the activity of 53BP1 and DNA repair proteins in the early steps of the DDR.

REFERENCES

Bennetzen, M.V., Larsen, D.H., Bunkenborg, J., Bartek, J., Lukas, J., and Andersen, J.S. (2010). Site-specific phosphorylation dynamics of the nuclear proteome during the DNA damage response. Mol Cell Proteomics *9*, 1314-1323.

Bensimon, A., Schmidt, A., Ziv, Y., Elkon, R., Wang, S.Y., Chen, D.J., Aebersold, R., and Shiloh, Y. (2010). ATM-dependent and -independent dynamics of the nuclear phosphoproteome after DNA damage. Sci Signal *3*, rs3.

Bothmer, A., Robbiani, D.F., Di Virgilio, M., Bunting, S.F., Klein, I.A., Feldhahn, N., Barlow, J., Chen, H.T., Bosque, D., Callen, E.*, et al.* (2011). Regulation of DNA end joining, resection, and immunoglobulin class switch recombination by 53BP1. Mol Cell *42*, 319-329.

Botuyan, M.V., Lee, J., Ward, I.M., Kim, J.E., Thompson, J.R., Chen, J., and Mer, G. (2006). Structural basis for the methylation state-specific recognition of histone H4-K20 by 53BP1 and Crb2 in DNA repair. Cell *127*, 1361-1373.

Botvinick, E.L., and Shah, J.V. (2007). Laser-based measurements in cell biology. Methods in cell biology *82*, 81-109.

Bouwman, P., Aly, A., Escandell, J.M., Pieterse, M., Bartkova, J., van der Gulden, H., Hiddingh, S., Thanasoula, M., Kulkarni, A., Yang, Q.*, et al.* (2010). 53BP1 loss rescues BRCA1 deficiency and is associated with triple-negative and BRCA-mutated breast cancers. Nat Struct Mol Biol *17*, 688-695.

Bunting, S.F., Callen, E., Wong, N., Chen, H.T., Polato, F., Gunn, A., Bothmer, A., Feldhahn, N., Fernandez-Capetillo, O., Cao, L.*, et al.* (2010). 53BP1 inhibits homologous recombination in Brca1-deficient cells by blocking resection of DNA breaks. Cell *141*, 243-254.

Callen, E., Di Virgilio, M., Kruhlak, M.J., Nieto-Soler, M., Wong, N., Chen, H.T., Faryabi, R.B., Polato, F., Santos, M., Starnes, L.M.*, et al.* (2013). 53BP1 mediates productive and mutagenic DNA repair through distinct phosphoprotein interactions. Cell *153*, 1266-1280.

Cancer Genome Atlas, N. (2012). Comprehensive molecular portraits of human breast tumours. Nature *490*, 61-70.

Chapman, J.R., Barral, P., Vannier, J.B., Borel, V., Steger, M., Tomas-Loba, A., Sartori, A.A., Adams, I.R., Batista, F.D., and Boulton, S.J. (2013). RIF1 is essential for 53BP1-dependent nonhomologous end joining and suppression of DNA double-strand break resection. Mol Cell *49*, 858-871.

Chapman, J.R., Sossick, A.J., Boulton, S.J., and Jackson, S.P. (2012). BRCA1-associated exclusion of 53BP1 from DNA damage sites underlies temporal control of DNA repair. Journal of cell science.

Chowdhury, D., Xu, X., Zhong, X., Ahmed, F., Zhong, J., Liao, J., Dykxhoorn, D.M., Weinstock, D.M., Pfeifer, G.P., and Lieberman, J. (2008). A PP4-phosphatase complex dephosphorylates gamma-H2AX generated during DNA replication. Mol Cell *31*, 33-46.

Dephoure, N., Zhou, C., Villen, J., Beausoleil, S.A., Bakalarski, C.E., Elledge, S.J., and Gygi, S.P. (2008). A quantitative atlas of mitotic phosphorylation. Proc Natl Acad Sci U S A *105*, 10762-10767.

Di Virgilio, M., Callen, E., Yamane, A., Zhang, W., Jankovic, M., Gitlin, A.D., Feldhahn, N., Resch, W., Oliveira, T.Y., Chait, B.T.*, et al.* (2013). Rif1 prevents resection of DNA breaks and promotes immunoglobulin class switching. Science *339*, 711-715.

Dimitrova, N., Chen, Y.C., Spector, D.L., and de Lange, T. (2008). 53BP1 promotes non-homologous end joining of telomeres by increasing chromatin mobility. Nature *456*, 524-528.

Escribano-Diaz, C., Orthwein, A., Fradet-Turcotte, A., Xing, M., Young, J.T., Tkac, J., Cook, M.A., Rosebrock, A.P., Munro, M., Canny, M.D.*, et al.* (2013). A Cell Cycle-Dependent Regulatory Circuit Composed of 53BP1-RIF1 and BRCA1-CtIP Controls DNA Repair Pathway Choice. Mol Cell.

Fenech, M. (2010). The lymphocyte cytokinesis-block micronucleus cytome assay and its application in radiation biodosimetry. Health physics *98*, 234-243.

Fradet-Turcotte, A., Canny, M.D., Escribano-Diaz, C., Orthwein, A., Leung, C.C., Huang, H., Landry, M.C., Kitevski-LeBlanc, J., Noordermeer, S.M., Sicheri, F.*, et al.* (2013). 53BP1 is a reader of the DNA-damage-induced H2A Lys 15 ubiquitin mark. Nature *499*, 50-54.

Gingras, A.C., Caballero, M., Zarske, M., Sanchez, A., Hazbun, T.R., Fields, S., Sonenberg, N., Hafen, E., Raught, B., and Aebersold, R. (2005). A novel, evolutionarily conserved protein phosphatase complex involved in cisplatin sensitivity. Mol Cell Proteomics *4*, 1725-1740.

Giunta, S., Belotserkovskaya, R., and Jackson, S.P. (2010). DNA damage signaling in response to double-strand breaks during mitosis. The Journal of cell biology *190*, 197-207.

Giunta, S., and Jackson, S.P. (2011). Give me a break, but not in mitosis: the mitotic DNA damage response marks DNA double-strand breaks with early signaling events. Cell cycle *10*, 1215-1221.

Gomez-Godinez, V., Wu, T., Sherman, A.J., Lee, C.S., Liaw, L.H., Zhongsheng, Y., Yokomori, K., and Berns, M.W. (2010). Analysis of DNA double-strand break response and chromatin structure in mitosis using laser microirradiation. Nucleic Acids Res *38*, e202.

Grosstessner-Hain, K., Hegemann, B., Novatchkova, M., Rameseder, J., Joughin, B.A., Hudecz, O., Roitinger, E., Pichler, P., Kraut, N., Yaffe, M.B.*, et al.* (2011). Quantitative phospho-proteomics to investigate the polo-like kinase 1-dependent phospho-proteome. Molecular & cellular proteomics : MCP *10*, M111 008540.

Harrigan, J.A., Belotserkovskaya, R., Coates, J., Dimitrova, D.S., Polo, S.E., Bradshaw, C.R., Fraser, P., and Jackson, S.P. (2011). Replication stress induces 53BP1-containing OPT domains in G1 cells. J Cell Biol *193*, 97-108.

Hartlerode, A.J., Guan, Y., Rajendran, A., Ura, K., Schotta, G., Xie, A., Shah, J.V., and Scully, R. (2012). Impact of histone H4 lysine 20 methylation on 53BP1 responses to chromosomal double strand breaks. PloS one *7*, e49211.

Hayashi, M.T., Cesare, A.J., Fitzpatrick, J.A., Lazzerini-Denchi, E., and Karlseder, J. (2012). A telomere-dependent DNA damage checkpoint induced by prolonged mitotic arrest. Nat Struct Mol Biol *19*, 387-394.

Hegemann, B., Hutchins, J.R., Hudecz, O., Novatchkova, M., Rameseder, J., Sykora, M.M., Liu, S., Mazanek, M., Lenart, P., Heriche, J.K.*, et al.* (2011). Systematic phosphorylation analysis of human mitotic protein complexes. Sci Signal *4*, rs12.

Heijink, A.M., Krajewska, M., and van Vugt, M.A. (2013). The DNA damage response during mitosis. Mutation research.

Huyen, Y., Zgheib, O., Ditullio, R.A., Jr., Gorgoulis, V.G., Zacharatos, P., Petty, T.J., Sheston, E.A., Mellert, H.S., Stavridi, E.S., and Halazonetis, T.D. (2004). Methylated lysine 79 of histone H3 targets 53BP1 to DNA double-strand breaks. Nature *432*, 406-411.

Iwabuchi, K., Basu, B.P., Kysela, B., Kurihara, T., Shibata, M., Guan, D., Cao, Y., Hamada, T., Imamura, K., Jeggo, P.A.*, et al.* (2003). Potential role for 53BP1 in DNA end-joining repair through direct interaction with DNA. J Biol Chem *278*, 36487-36495.

Jowsey, P., Morrice, N.A., Hastie, C.J., McLauchlan, H., Toth, R., and Rouse, J. (2007). Characterisation of the sites of DNA damage-induced 53BP1 phosphorylation catalysed by ATM and ATR. DNA Repair (Amst) *6*, 1536-1544.

Lee, D.H., and Chowdhury, D. (2011). What goes on must come off: phosphatases gate-crash the DNA damage response. Trends in biochemical sciences *36*, 569-577.

Lee, D.H., Goodarzi, A.A., Adelmant, G.O., Pan, Y., Jeggo, P.A., Marto, J.A., and Chowdhury, D. (2012). Phosphoproteomic analysis reveals that PP4 dephosphorylates KAP-1 impacting the DNA damage response. Embo J *31*, 2403-2415.

Lee, D.H., Pan, Y., Kanner, S., Sung, P., Borowiec, J.A., and Chowdhury, D. (2010a). A PP4 phosphatase complex dephosphorylates RPA2 to facilitate DNA repair via homologous recombination. Nat Struct Mol Biol *17*, 365-372.

Lee, K., Kenny, A.E., and Rieder, C.L. (2010b). P38 mitogen-activated protein kinase activity is required during mitosis for timely satisfaction of the mitotic checkpoint but not for the fidelity of chromosome segregation. Molecular biology of the cell *21*, 2150-2160.

Liu, J., Xu, L., Zhong, J., Liao, J., Li, J., and Xu, X. (2012). Protein phosphatase PP4 is involved in NHEJ-mediated repair of DNA double-strand breaks. Cell Cycle *11*, 2643-2649.

Lukas, C., Savic, V., Bekker-Jensen, S., Doil, C., Neumann, B., Pedersen, R.S., Grofte, M., Chan, K.L., Hickson, I.D., Bartek, J.*, et al.* (2011). 53BP1 nuclear bodies form around DNA lesions generated by mitotic transmission of chromosomes under replication stress. Nat Cell Biol *13*, 243-253.

Nakada, S., Chen, G.I., Gingras, A.C., and Durocher, D. (2008). PP4 is a gamma H2AX phosphatase required for recovery from the DNA damage checkpoint. EMBO reports *9*, 1019-1026.

Nelson, G., Buhmann, M., and von Zglinicki, T. (2009). DNA damage foci in mitosis are devoid of 53BP1. Cell cycle *8*, 3379-3383.

Noon, A.T., Shibata, A., Rief, N., Lobrich, M., Stewart, G.S., Jeggo, P.A., and Goodarzi, A.A. (2010). 53BP1-dependent robust localized KAP-1 phosphorylation is essential for heterochromatic DNA double-strand break repair. Nat Cell Biol *12*, 177-184.

Panier, S., and Boulton, S.J. (2014). Double-strand break repair: 53BP1 comes into focus. Nat Rev Mol Cell Biol *15*, 7-18.

Pei, H., Zhang, L., Luo, K., Qin, Y., Chesi, M., Fei, F., Bergsagel, P.L., Wang, L., You, Z., and Lou, Z. (2011). MMSET regulates histone H4K20 methylation and 53BP1 accumulation at DNA damage sites. Nature *470*, 124-128.

Peng, A., and Maller, J.L. (2010). Serine/threonine phosphatases in the DNA damage response and cancer. Oncogene *29*, 5977-5988.

Peterson, S.E., Li, Y., Chait, B.T., Gottesman, M.E., Baer, R., and Gautier, J. (2011). Cdk1 uncouples CtIP-dependent resection and Rad51 filament formation during M-phase double-strand break repair. J Cell Biol *194*, 705-720.

Sakaue-Sawano, A., Kurokawa, H., Morimura, T., Hanyu, A., Hama, H., Osawa, H., Kashiwagi, S., Fukami, K., Miyata, T., Miyoshi, H.*, et al.* (2008). Visualizing spatiotemporal dynamics of multicellular cell-cycle progression. Cell *132*, 487-498.

van Vugt, M.A., Gardino, A.K., Linding, R., Ostheimer, G.J., Reinhardt, H.C., Ong, S.E., Tan, C.S., Miao, H., Keezer, S.M., Li, J.*, et al.* (2010). A mitotic phosphorylation feedback network connects Cdk1, Plk1, 53BP1, and Chk2 to inactivate the G(2)/M DNA damage checkpoint. PLoS biology *8*, e1000287.

Ward, I., Kim, J.E., Minn, K., Chini, C.C., Mer, G., and Chen, J. (2006). The tandem BRCT domain of 53BP1 is not required for its repair function. J Biol Chem *281*, 38472-38477.

Xue, Y., Ren, J., Gao, X., Jin, C., Wen, L., and Yao, X. (2008). GPS 2.0, a tool to predict kinase-specific phosphorylation sites in hierarchy. Molecular & cellular proteomics : MCP *7*, 1598-1608.

Zgheib, O., Pataky, K., Brugger, J., and Halazonetis, T.D. (2009). An oligomerized 53BP1 tudor domain suffices for recognition of DNA double-strand breaks. Molecular and cellular biology *29*, 1050-1058.

Zimmermann, M., Lottersberger, F., Buonomo, S.B., Sfeir, A., and de Lange, T. (2013). 53BP1 regulates DSB repair using Rif1 to control 5' end resection. Science *339*, 700-704.

CHAPTER 3

CDK5 regulates 53BP1 recruitment to double strand breaks by phosphorylating R3β S840

Sanket S. Acharya, Xiao-Feng Zheng, Guillaume Adelmant, Jarod Marto, Amar Natarajan, Kavita Shah, Dipanjan Chowdhury

Collaborations:

Amar Natarajan Laboratory, University of Nebraska Medical Center

Kavita Shah Laboratory, Purdue University

ABSTRACT

PP4C/R3β phosphatase complex directly interacts with and regulates the dephosphorylation of 53BP1, a key mediator of DNA damage signaling. Here we characterize the molecular nature of this interaction by identifying a C-terminal region in the regulatory subunit that is sufficient for association with 53BP1. This C-terminal fragment, termed C5, contains multiple serine/threonine residues that are unique to R3β and not found in its closest relative R3α. Using MS/MS analysis we identify that the C5 residue S840 is phosphorylated during mitosis and that this modification is required for both 53BP1- R3β interaction and PP4C/R3β-mediated dephosphorylation of 53BP1 at T1609 and S1618. Furthermore, we discover a role for the cyclin dependent kinase CDK5 in the phosphorylation of R3β S840 and show that absence of CDK5 negatively affects 53BP1 accumulation at DNA breaks. The effect of CDK5 depletion is partially reversed by ectopic expression of an S840 phospho-mimetic mutant, suggesting that the phosphorylation status of S840 governs the 53BP1-related function of R3β. Finally, we identify a cancer-relevant mutation in R3β, S840F that also fails to interact with 53BP1 and thus highlights the physiological relevance of this regulation.

INTRODUCTION

As mentioned before serine/threonine phosphatases such as PP4 have one catalytic subunit and multiple regulatory subunits allowing for various catalytic and regulatory subunit combinations (Chen et al., 2008; Cohen et al., 2005). Changing the regulatory subunit changes the specificity of the phosphatase for a given substrate (Lee and Chowdhury, 2011; Zheng et al., 2015). Multiple studies have implicated PP4 in regulation of the DDR. It has been shown to be involved in the dephosphorylation of γ–H2AX and phosphor-RPA2, thereby mediating efficient repair of DNA and recovery from the G2/M checkpoint (Chowdhury et al., 2008; Lee et al., 2010; Nakada et al., 2008).

However, increasing evidence points to a role for phosphatases in the initiation and maintenance of DDR proteins in addition to facilitating their restoration to a pre-damage state (Bennetzen et al., 2010; Bensimon et al., 2010; Lee and Chowdhury, 2011). Previously, we presented work from our group in support of this idea by demonstrating that the PP4C/ R3β phosphatase complex actively dephosphorylates 53BP1 during the transition from mitosis to G1 thereby allowing it to participate in DSB repair in G1 phase (Lee et al., 2014a). The regulatory subunit specific for 53BP1 is R3β, while the catalytic subunit that mediates the actual dephosphorylation is PP4C (Fig. 2.4C). Interestingly, we have observed that the expression levels of both R3β and PP4C do not change in the course of the cell cycle. However, R3β preferentially interacts with 53BP1 during mitosis with only low levels of interaction seen in interphase cells. Furthermore, although this interaction is detected in stalled mitosis, the dephosphorylation occurs only in late mitosis/early G1. Therefore a key question

that remains unanswered is how is the R3β-53BP1 regulated. These initial findings motivated us to study the R3β-53BP1 interaction in more detail.

CDKs represent a family of serine/threonine kinases that regulate the cell division cycle by associating with cyclins. While most CDKs are involved in facilitating efficient cell cycle progression, several new studies indicate that certain CDK family members are involved in other processes. An important example of this paradigm is CDK5, which has mainly been characterized in development and function of the nervous system (Liebl et al., 2011; Tarricone et al., 2001). Interestingly, CDK5 is not activated by cyclins. Its activation is dependent on the p35 and p39 proteins that are primarily expressed in post-mitotic neurons(Dhavan and Tsai, 2001). Conversion of the p35 to p25 results in a hyperactive CDK5 that is associated with pathogenesis of neurodegenerative disease (Sun et al., 2008; Zheng et al., 2010).

CDK5 has also been implicated in DDR in neuronal cells. Studies suggest a possible role for CDK5 in mediating the neuronal response to oxidative stress and DNA damaging agents such as campothecin and mitomycin C (Lee and Kim, 2007; Strocchi et al., 2003; Tian et al., 2009). Here, we identify CDK5 as a potential modulator of the R3β-53BP1 interaction and present findings supporting the hypothesis that CDK5 mediates a post-translational modification of R3β during mitosis that prepares the phosphatase to interact with 53BP1. We show that in stalled mitosis CDK5 mediates productive R3β-53BP1 interaction by phosphorylating R3β residue S840 and this correlates with the dephosphorylation of 53BP1 at T1609 and S1618 in G1. Furthermore, we examine the effect of depleting CDK5 on 53BP1 accumulation at DSBs and show that CDK5 mediates its effect on 53BP1 via regulation of R3β.

Specific inhibition of CDKs (including CDK5) using small molecule inhibitors has been a challenge (Liebl et al., 2011). We propose the use of a novel chemical genetics approach to specifically modulate CDK5 activity during mitosis. Finally, by studying a cancer-relevant melanoma mutation identified in R3β, we assess the physiological significance of R3β phosphorylation.

MATERIALS AND METHODS

Cell Culture, antibodies, and reagents

U2OS, HeLa, and 293T cells were grown in DMEM supplemented with 10% (v/v) FBS. Antibodies used were against R3β (Bethyl), PP4C (Bethyl), Phospho-histone H3 (Cell Signaling), 53BP1 (BD), 53BP1 (Santa Cruz), γ-H2AX (Mouse, Millipore), Myc (SantaCruz), and Tubulin (Sigma). Rabbit polyclonal anti-pT1609/S1618-53BP1 antibody was produced by Antagene (Sunnyvale, CA) with a peptide, Cys -NRLREQYGLGPYEAV(p)TPLTKAADI(p)SLDN. Nocodazole (microtubule polymerization inhibitor) and RO-3306 (CDK1 inhibitor) were obtained from Sigma-Aldrich. Nocodazole was used at 100 ng/ml and RO-3306 was used at 9 μM final concentration.

siRNAs and plasmid transfection

siRNA duplexes (Invitrogen) were transfected using RNAiMAX (Invitrogen). We used the following siRNAs knockdown expression.

R3β ORF siRNA: 5'-CCAUCUAUAUUGCGUAGUA-3';

R3β 3'UTR siRNA: 5'-CACUUUCUUUGAAUCAUCC-3';

CDK5 siRNA 1: 5'-UUGCGGCUAUGACAGAAUC-3';

CDK5 siRNA 2: 5'-GAUGUCGAUGACCAGUUGA-3'

R3β and phospho-mutants were subcloned into the pcDNA3.1-HisA-6xmyc mammalian expression vector. R3β mutants S840A, S840D, and S840F were generated using QuickChange II XL site-directed mutagenesis kit (Stratagene) according to the manufacturer's instructions. To replace endogenous R3β with

wildtype or phospho-mutants, HeLa and U2OS cells were reverse transfected with R3β 3'UTR siRNA by RNAiMAX and after 30 h, transfected with siRNA-resistant R3β plasmids using Lipofectamine 2000 (Invitrogen).

Co-immunoprecipitation

293T cells expressing R3β or phospho-mutants, were lysed in lysis buffer containing 50 mM Tris-HCl, pH 7.5, 250 mM NaCl, 5 mM EDTA, 1 % (v/v) NP-40 and protease inhibitor cocktail (Roche). Cell lysates were incubated with 53BP1 antibody (Santa Cruz) at 4°C for 2h and then incubated Protein A/G Plus Agarose (Santa Cruz) for 12-16h. The immunoprecipitates were washed three times with lysis buffer. Resulting immunoprecipitated proteins were resolved by SDS-PAGE and analyzed by immunoblot. Quantification of fractions for equal loading was done using NanoDrop 1000 (Thermo Scientific).

Immunoblotting

Immuoblots were visualized using the Odyssey Infrared Imaging System. After primary antibody incubation, blots were incubated with goat anti–mouse IR Dye 800CW or goat anti–rabbit IR Dye 680 (LI-COR) for 1 h and scanned using the Li-COR imaging system. Images were visualized by Odyssey V3.0 software (http://biosupport.licor.com).

Immunofluorescence

U2OS cells were plated on glass slides, harvested at different time points and fixed for 15 min with 4% (v/v) paraformaldehyde. Fixed cells were permeabilized for 15 min with 0.1% (v/v) Triton X-100 in PBS, washed and blocked in blocking solution (2% FBS in PBS) for 2 h at room temperature (RT). Next, cells were incubated with primary antibodies diluted in blocking solution for 2 h at RT. Following primary antibody incubation, cells were washed, incubated with secondary antibody diluted in PBS for 1 h at RT, and washed before being mounted using DapiFuoromount-G (SouthernBiotech). Secondary Alexa Fluor IgG antibodies used were: 488 goat anti-rabbit, 488 goat anti-mouse, 594 goat anti-rabbit, 594 goat anti-mouse (Invitrogen). Stacks of images for each cell were collected with a 100X objective (1.35 N.A.) using Olympus FV1000 confocal microscope and presented as maximum intensity projections.

Synthesis of selective CDK5 inhibitor 20-223

The aminopyrazole analog (CP-668863 or 20-223) was reported at the Society for Medicines Research Symposium as a selective CKD5 inhibitor (Eli Lilly Research Center, Surrey UK, June 2007). The analog was reported to have a Ki = 2.9 nM versus CDK5 and was 5.7-fold selective versus CDK2. We synthesized 20-223 in four steps from commercially available starting materials with an overall yield of 32%. The inhibitor was used at different concentrations to test its efficiency. (Synthesis performed in the laboratory of Amarnath Natarajan, University of Nebraska Medical Center.)

Generation of CRISPR knockout cells

We cloned the following CDK5-targed guide RNA sequences in the Lenti-Guide-Puro vector (addgene #52963):

Guide 1: 5'-TGAAGCCTAGGGCAAAAGAAGGG -3'

Guide 2: 5'-GCAGGACGTCATGAAGCCTAGGG-3'

Guide 3: 5'-CTGTGACCAGGTGAAAGGCGGGG-3'

Lentiviruses expressing the above guide RNAs were generated and used to infect U2OS cells expressing Cas9 (maintained in 10 μg/ml blasticidin). Successfully infected clones were selected using puromycin (2 μg/ml).

Protein expression and purification

His-tagged CDK5 and p25 cloned into the pFastBac vector were expressed using the Bac-to-Bac baculovirus expression system. Cell pellets of each protein were combined and lysed in Tris buffer (pH 8) containing 150mM NaCl and 1% NP-40 and batch purified using 100μL of Ni-NTA beads. The wildtype and phospho-resistant mutant were expressed in BL21 DE3 *E. coli* cells. Cells were grown at 37ºC to an OD_{600} of ~0.5 and expression was induced with 500μM IPTG followed by overnight growth at room temperature. Frozen pellets were lysed in Tris buffer (pH 8.0) containing 500mM NaCl, 10% glycerol, and 1% NP-40 via french press and batch purified using 100μL Ni-NTA beads. Protein levels were normalized using coomassie staining prior to the kinase assay.

In vitro kinase assay

Following purification, CDK5/p25 was washed twice with Tris buffer (pH 8.0) containing 10mM Imidazole and twice with 1X kinase Buffer (Tris pH 8.0, 5mM $MgCl_2$). Excess buffer was removed (leaving ~150µL bead slurry) and cold ATP and imidazole were added to a final concentrations of ~2mM and 25mM respectively. The beads were then incubated for 2 hours at RT with shaking. Following incubation the bead suspension was diluted with 50mM tris buffer (pH 8.0) so that the final concentration of imidazole was <5mM and incubated at 4ºC on an end-over-end rotator for 1 hour. The beads were then washed with 1x kinase buffer to remove excess ATP and imidazole. It is critical to use the kinase immediately as to not lose activity. The cdk5/p25-loaded beads were added to substrate cocktail containing kinase buffer and the reaction was initiated with the addition of $AT^{32}P$. Phosphorylation reactions were carried out for 15 min at RT with shaking and terminated using 4X SDS buffer. Samples were boiled at 95ºC for 4 min and separated using a 15% SDS-page gel followed by overnight transfer to PVDF membrane. Protein bands were visualized using ponceau staining.

RESULTS

Our previous work has shown that 53BP1 interacts with the PP4 phosphatase complex via the R3β regulatory subunit and that this interaction is significantly enhanced in stalled mitosis (Lee et al., 2014a). We observed that PP4C/R3β complex dephosphorylates 53BP1 in late mitosis/early G1 restoring its function in DDR. However, since PP4C/R3β is expressed and active throughout mitosis how the dephosphorylation of 53BP1 by this phosphatase complex is restricted to the late mitosis/early G1 phase remains unclear. We hypothesized that the key to this question is the regulated association of R3β with 53BP1. In order to identify the regulation of R3β-53BP1 interaction, we first asked whether a specific region of the R3β protein is required for its interaction with 53BP1. To this end, we performed deletion-based mutagenesis of the 849 amino-acid residues in R3β and identified residues 721-849 at the C-terminus of R3β (termed C5 fragment) that is sufficient for its interaction with 53BP1 (Fig. 3.1A and B).

Interestingly, R3α interacts weakly with 53BP1 (Fig. 3.1B) and R3β and R3α share 67% homology differing significantly only at their respective C-termini (Fig. 3.2). Thus, differences in the C-terminal sequences of R3α and R3β likely account for the difference in their specificity for 53BP1. We hypothesized that a post-translational modification at the C-terminus of R3β mediates its interaction with 53BP1. Analysis of annotated post-translational modifications of the human SMEK2 (R3β) protein using Phosphosite Plus 2014 (Hornbeck et al., 2015) revealed a number of phosphorylated residues (Fig. 3.3).

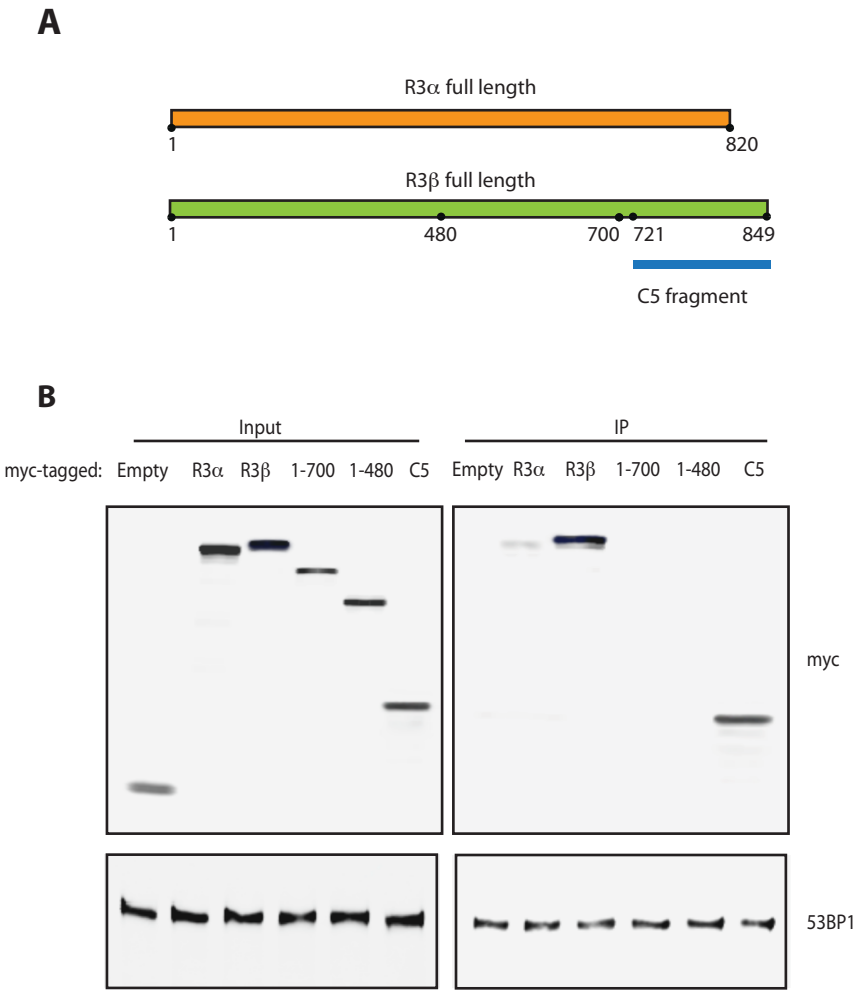

Figure 3.1: The C5 fragment of R3β is sufficient for interaction with 53BP1. **(A)** Schematic showing the two closely related regulatory subunits of PP4- R3α and R3β. Also shown is the C5 fragment spanning R3β residues 721-849. **(B)** Myc-tagged empty vector (Empty), R3α, and various deletion mutants of R3β (1-700, 1-480, C5) were introduced in 293T cells. After nocodazole (100 ng/ml) treatment for 8h, cells were harvested and lysates were subjected to endogenous 53BP1 immunoprecipiration.

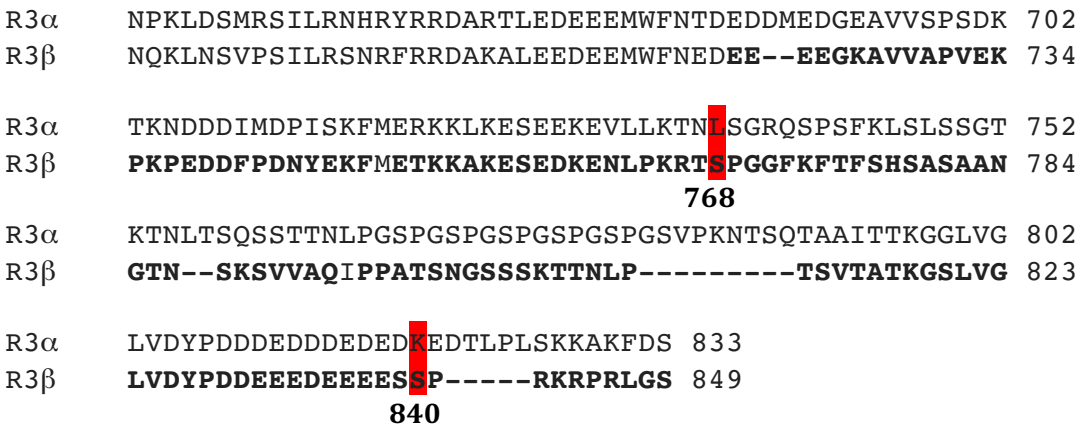

Figure 3.2: Multiple Sequence Alignment of the C-terminus of R3α and R3β. Sequence in bold represents the C5 fragment. Residues highlighted in red show the location of two serine residues in R3β that are absent in R3α.

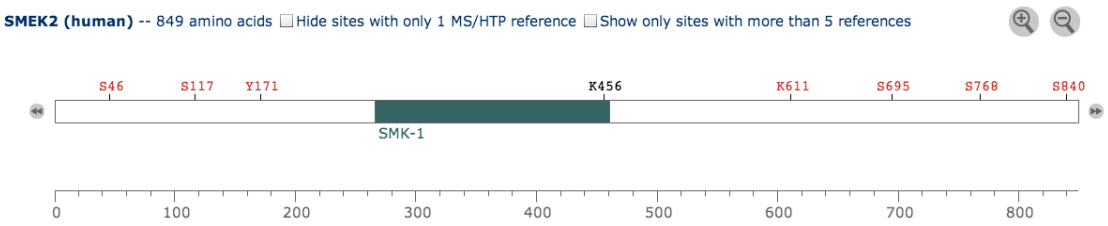

Figure 3.3: Analysis of SMEK2 post-translational modification using PhosphoSitePlus 2014.
Post-translational modifications documented in various studies have been annotated.

We examined whether any of the phosphorylated residues detected were specific to R3β by comparing C-terminal R3α and R3β sequences. This comparison revealed the existence of two unique serine residues in R3β - S768 and S840 (Fig. 3.2). S840 is phosphorylated in mitosis (Beausoleil et al., 2006; Grosstessner-Hain et al., 2011) and we also independently verified phosphorylation of S840 using MS/MS analysis of the C5 peptide (Fig. 3.4A).

In our MS/MS analysis we found that S840 was the only R3β residue phosphorylated when cells are arrested in mitosis. We therefore asked whether the phosphorylation status of S840 impacts the interaction of R3β with 53BP1. We transfected myc-tagged R3β WT or phospho-null S840A in 293T cells, arrested cells in mitosis using the microtubule polymerization inhibitor nocodazole, and immunoprecipirated endogenous 53BP1 to visualize R3β-53BP1 interaction. We found that in stalled mitosis, mutating S840 to alanine significantly decreased the interaction of 53BP1 with R3β (Fig. 3.4B). Furthermore, substituting S840 with the phospho-mimetic S840D was sufficient to restore this interaction to wild-type levels. These data suggested that the interaction of 53BP1 with R3β is dependent on the phosphorylation of R3β S840.

Depletion of either PP4C or R3β blocks the dephosphorylation of 53BP1 in G1 cells exhibited by an increase in phospho-T1609 and phospho-S1618 signal (Chapter 2, Fig. 2.4A). In order to investigate whether the phosphorylation of R3β at S840 in turn impacts phosphorylation status of 53BP1 at T1609 and S1618, we depleted endogenous R3β in HeLa cells and ectopically expressed myc-tagged, si-resistant R3β WT, S840A or S840D mutants. Cells synchronized in mitosis were released into

G1 and the kinetics of phosphorylation of 53BP1 T1609 and S1618 was evaluated using the p (1609/1618) antibody. Consistent with our previous results, cells treated with control siRNA exhibited reduction in 53BP1 phosphorylation by 3h post G1 release and absence of R3β blocked dephosphorylation even at later time points (Fig. 3.5). Also as expected, replacing endogenous R3β with the si-resistant wildtype version reversed this block in dephosphorylation. Moreover, we found that while cells expressing R3β S840D mutant were also able to normally dephosphorylate 53BP1, those expressing S840A blocked dephosphorylation similar to R3β depletion. Taken together, these data indicates that mutating the R3β S840 residue to S840A compromised the function of R3β in dephosphorylating 53BP1 at T1609 and S1618.

R3β interacts strongly with 53BP1 in stalled mitosis, however 53BP1 dephosphorylation happens only in late mitosis (Lee et al., 2014a). Therefore, investigating the molecular details of dephosphorylation will require understanding of the precise timing of this interaction. One limitation of using nocodazole for synchronization is that it arrests cells in mitosis at the pro-metaphase stage (Benada et al., 2015), which precludes studying molecular interactions in late G2 or early mitosis. To circumvent this issue, we used another chemical agent, RO-3306, which is a selective CDK1 inhibitor that blocks cells at the G2/M boundary (Vassilev et al., 2006). We exposed U2OS cells expressing myc-tagged wildtype R3β to RO-3306 for 12-16h. The resulting late G2 synchronized cells were released from RO-3306 block and monitored at time points in mitosis/G1. Cells collected at each time point were subjected to endogenous 53BP1 pull-down to study the extent of 53BP1-R3β interaction (Fig. 3.6A). Untreated asynchronous cells served as a control. We found

A

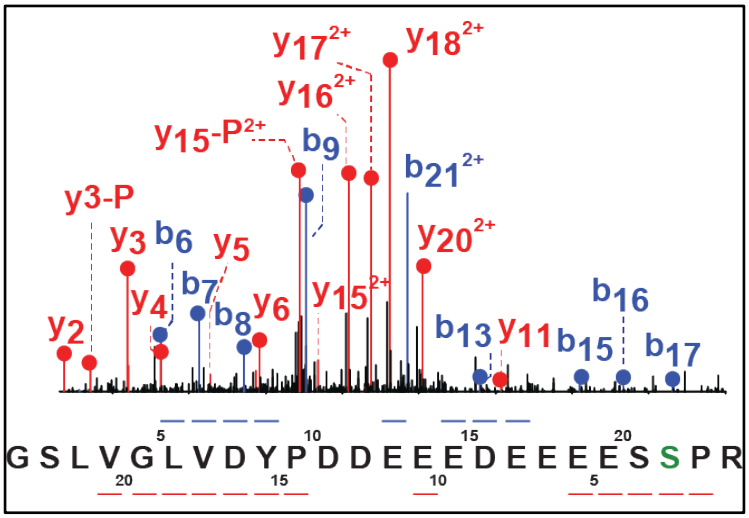

B

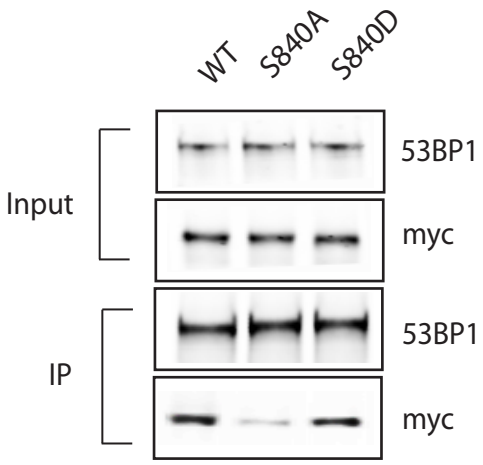

Figure 3.4: MS/MS analysis reveals phosphorylation of R3β S840 in mitosis.
(A) MS/MS spectrum of tryptic peptide from R3β C5 domain. N-terminal and C-terminal fragment ions are marked in blue and red, respectively. Sequence coverage confirms phosphorylation on S840, indicated as the green residue in the amino acid sequence. **(B)** Endogenous 53BP1 pull-down in 293T cells transfected with myc-tagged R3β wildtype (WT), S840A or S840D mutants. Cells were stalled in mitosis by an 8h treatment with nocodazole (100 ng/ml).

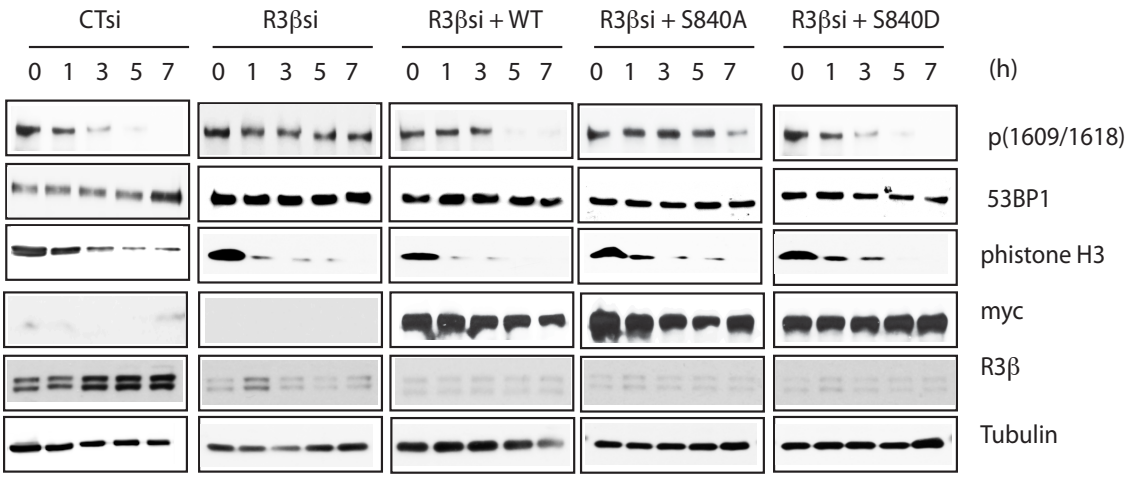

Figure 3.5: 53BP1 dephosphorylation kinetics in cells expressing R3β mutants. HeLa cells were transfected with indicated siRNAs and si-resistant myc-tagged R3β mutants. Cells were arrested in mitosis using 8h treatment with nocodazole and released into G1. Indicated time points were taken to monitor 53BP1 phosphorylation using the p (1609/1618) antibody. The phospho-Histone H3 (phistone H3) antibody was used to monitor release from mitosis to G1. Myc and R3β blots present expression of myc-tagged R3β mutants and R3β siRNA efficiency, respectively.

that while asynchronous cells show minimal 53BP1-R3β interaction, cells released from RO-3306 block display increased association starting at ~0.5h post release. The peak of this interaction occurs at ~1-2h post release after which the interaction is gradually reduced at later time points. The cell cycle status of samples used for 53BP1 pull-down in Fig. 3.6A was also analyzed in parallel using propidium iodide (PI) staining (Fig. 3.6B). This strategy does not allow us to comment on the precise timing of 53BP1-R3β interaction, but broadly, we observe that the interaction is enhanced during late mitosis. This is consistent with the dephosphorylation of 53BP1 occurring during the transition from mitosis to G1.

In order to identify the kinase responsible for phosphorylating R3β S840, we used the MIT Scansite prediction algorithm (Obenauer et al., 2003), that predicts cell signaling interactions based on short sequence motifs. Using this algorithm we predicted two kinases, namely CDK5 and Cdc2 (CDK1), that potentially phosphorylate R3β S840 (Fig. 3.7A). Both proteins belong to the Ser/Thr family of cyclin-dependent kinases and have distinct roles during the cell cycle. At steady state, CDK1 activity is essential for mitotic progression and its activity is also a key target of the G2/M checkpoint response (Li and Zou, 2005; Lukas et al., 2004; Vassilev et al., 2006). CDK1 activity during mitosis leads to the phosphorylation of a number of cellular substrates including those involved in DDR. For example, it was recently shown that RNF8, an E3 ubiquitin ligase necessary for recruitment of 53BP1 to DNA breaks, is phosphorylated by CDK1 during mitosis preventing it from interacting with the upstream DDR factor MDC1(Orthwein et al., 2014). These observations make CDK1 an attractive prediction in our analysis. However, we reasoned that modulating CDK1

activity to investigate its potential role in R3β phosphorylation would be detrimental to cells progressing through mitosis, and therefore decided to first focus on CDK5.

CDK5 is an unusual kinase that has traditionally been studied in the context of neuronal development and proliferation and has been implicated in neuronal responses to oxidative stress and DNA damaging agents (Dhavan and Tsai, 2001; Lee and Kim, 2007; Liebl et al., 2011; Strocchi et al., 2003; Tian et al., 2009). However, so far it has not been studied in DDR in a non-neuronal context. To test whether CDK5 phosphorylates R3β, we performed an *in vitro* kinase assay using purified human CDK5 and His-tagged R3β wild-type or S840A mutant C5 fragment (Fig. 3.7B). We found that incubating the wildtype C5 fragment with recombinant human CDK5 produced a strong autorad signal that was indicative of R3β phosphorylation. This signal was completely lost when wildtype C5 in the reaction was replaced with the S840A mutant (Fig. 3.7B). Ponceau stained R3β and CDK5 were used as loading controls. Based on this result, we reasoned that if CDK5 was indeed phosphorylating R3β at S840, then absence of CDK5 should be phenotypically similar to the S840A mutant (as in Fig. 3.4B). To test this idea, we depleted CDK5 using siRNA, introduced myc-tagged R3β WT or S840A mutant in 293T cells and arrested cells in mitosis using nocodazole. In cells treated with control siRNA, wildtype R3β showed strong interaction with 53BP1 and as expected, expression of the S840A mutant reduced the R3β-53BP1 interaction. However, in cells expressing wildtype R3β that were also depleted of CDK5, we saw a striking decrease in R3β-53BP1 interaction (Fig. 3.7C). This decrease was similar in

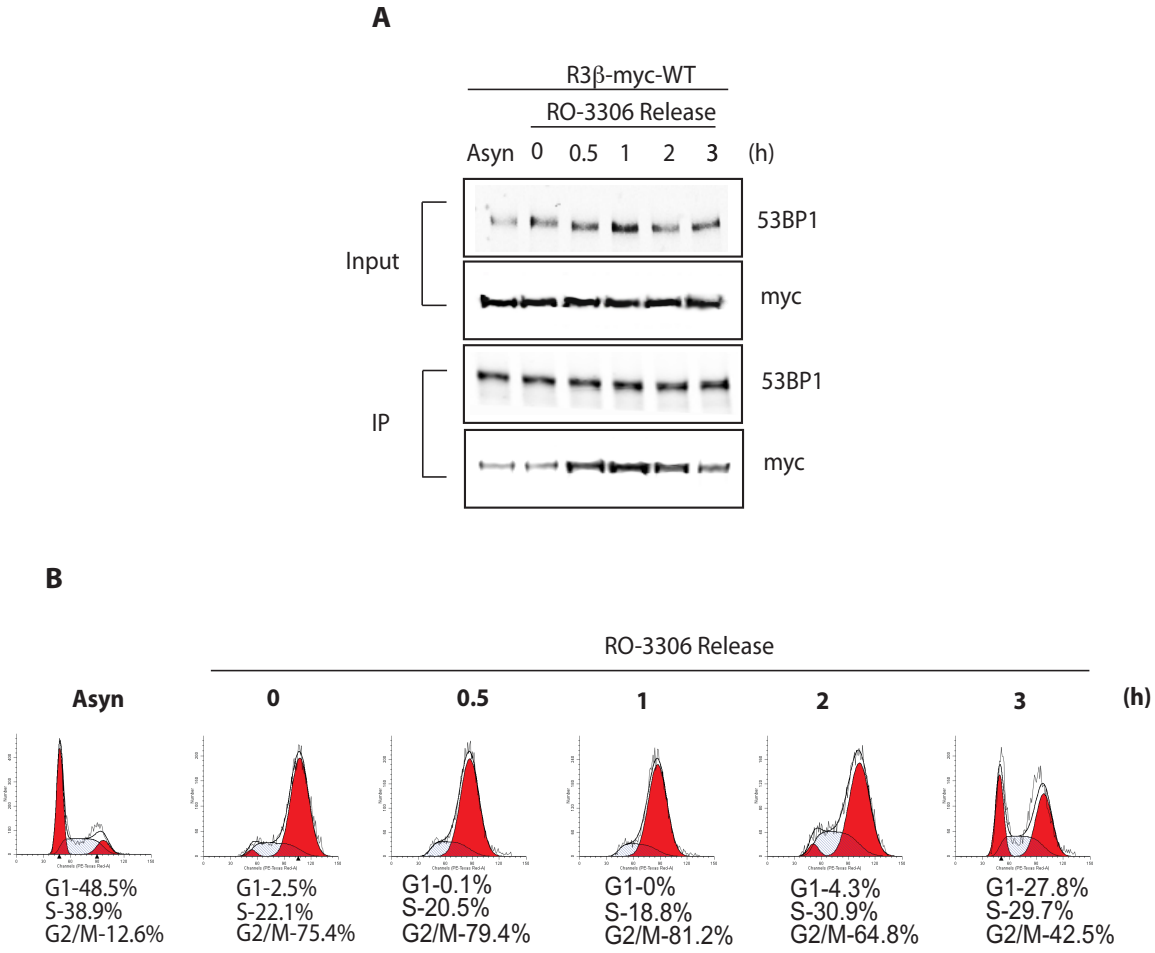

Figure 3.6: Peak of 53BP1-R3β interaction occurs between 1-2 h after release from RO-3306 block.

(**A)** U2OS cells expressing myc-tagged R3β wildtype (WT) were synchronized at the G2/M boundary and released into mitosis. Cells were harvested at different time points and subjected to 53BP1 immunoprecipitation to examine extent of 53BP1-R3β interaction. **(B)** Propidium iodide staining of U2OS cells used in (A). Percent cells in G1/S/G2M phases are denoted below cell cycle profiles for the indicated time points.

A

Proline-dependent serine/threonine kinase group (Pro_ST_kin)				
Cdk5 Kinase			Gene Card CDK5	
Site	Score	Percentile	Sequence	SA
S840	0.2468	0.009 %	EDEEEESSPRKRPRL	4.317
Cdc2 Kinase			Gene Card CDC2	
Site	Score	Percentile	Sequence	SA
S840	0.3410	0.026 %	EDEEEESSPRKRPRL	4.317
Cdk5 Kinase			Gene Card CDK5	
Site	Score	Percentile	Sequence	SA
S155	0.3893	0.164 %	LVTSVLSSPIRREKL	0.721
Cdc2 Kinase			Gene Card CDC2	
Site	Score	Percentile	Sequence	SA
S155	0.4452	0.200 %	LVTSVLSSPIRREKL	0.721

B

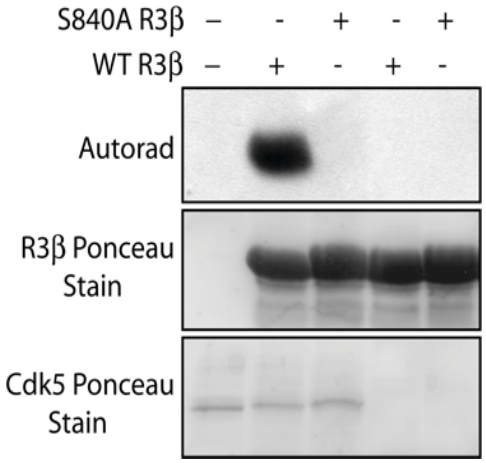

C

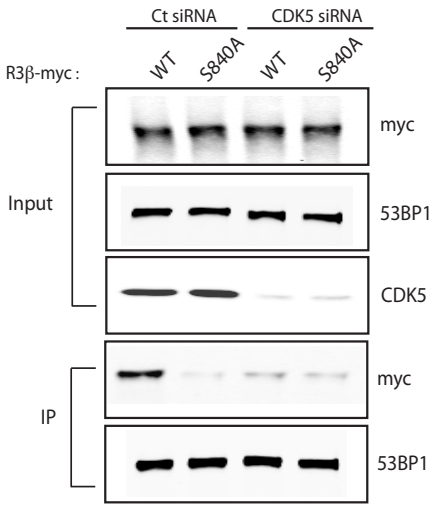

Figure 3.7: CDK5 mediates the interaction of 53BP1 and R3β by phosphorylating R3β S840.

(A) ScanSite prediction algorithm results predicting CDK5 and Cdc2 as two potential R3β S840 phosphorylating kinases. **(B)** In vitro kinase assay involving recombinant human CDK5 and purified wild-type C5 fragment (WT R3β) or S840A C5 mutant (S840A R3β). Ponceau staining was used as a loading control. **(C)** 53BP1 immunoprecipiration in 293T cells transfected with R3β wildtype (WT) or S840A mutant in the presence or absence of CDK5. Cells were treated with nocodazole for mitotic arrest. Input shows efficiency of siRNA-mediated CDK5 depletion.

magnitude to that obtained after expression of the S840A mutant suggesting that CDK5 likely contributes to the phosphorylation of R3β S840 in mitosis.

To study R3β phosphorylation by CDK5 in greater detail, we have generated a phospho-antibody that recognizes R3β phosphorylated at S840. Myc pull-down experiments confirmed that the phospho-antibody is specific to S840 phosphorylation since introducing the S840A mutant significantly lowered the antibody signal (Fig. 3.8)

As reported here, CDK5-mediated R3β S840 phosphorylation is required for R3β-53BP1 interaction and R3β-mediated dephosphorylation of 53BP1 is necessary for its recruitment to DSBs (Lee et al., 2014b). Therefore we asked whether CDK5 impacted 53BP1 recruitment to DSBs in G1 cells. To answer this question, we transiently depleted CDK5 in U2OS cells treated with RO-3306, and released them for 2h before exposure to ionizing radiation (IR, 10 Gy). At 2h after IR, 53BP1 recruitment to DSBs was monitored by immunofluorescence. Indeed, we found that CDK5 knockdown caused a significant reduction in endogenous 53BP1 foci marked by γ–H2AX (Fig. 3.9), suggesting that CDK5 influences the recruitment of 53BP1 to DSBs by regulating the phosphorylation of R3β. Since the reduction in 53BP1 foci number after depleting CDK5 was less severe than that obtained by depleting R3β, it is likely that other non-CDK5 dependent mechanisms may also impinge upon the 53BP1-specific function of R3β.

If CDK5 indeed regulates 53BP1 recruitment to DSBs by phosphorylating R3β S840, then it is conceivable that the phenotype obtained in the absence of CDK5 can be reversed by expression of the R3β phosphomimic mutant. Consistent with this notion, expression of myc-tagged R3β S840D in U2OS cells transiently depleted of

CDK5 restored 53BP1 recruitment to DSBs (Fig. 3.10). In this scenario, expression of both R3β WT and R3β S840A were unable to restore 53BP1 recruitment.

For temporal suppression of CDK5 activity, which is not feasible via siRNA, we used a chemical inhibitor. Currently known inhibitors of CDKs affect multiple kinases, which complicates the functional analysis of a specific CDK. For example, roscovitine-mediated inhibition is specific to CDK1, CDK2, and CDK5 (Bach et al., 2005; Bain et al., 2007; Liebl et al., 2011). To specifically inhibit CDK5 without inhibiting other CDKs, we used a newly synthesized selectiveCDK5 chemical inhibitor 20-223 (Pfizer compound, collaboration with Amar Natarajan's laboratory at the University of Nebraska Medical Center) that was found to be 5.7 times more selective for CDK5 than CDK2 (Fig. 3.11).

We synchronized U2OS cells at the G2/M boundary and released them into mitosis/early G1 for 1.5 hours. At this stage, we inhibited CDK5 by adding inhibitor 20-223 at different concentrations and measured 53BP1 foci formation using immunofluorescence (Fig. 3.12). Cells treated with siRNA against R3β served as a positive control. We found that compound 20-223 had a dose-dependent impact on 53BP1 foci formation with significant inhibition occurring at 2 and 5 μM concentrations.

Although the result with this CDK5 inhibitor is promising it does not allow us to rule out any side-effects on other CDKs. To specifically inhibit CDK5 in cells we will utilize a novel chemical genetics approach, developed by Shokat and colleagues (Bishop et al., 2001; Bishop et al., 2000; Shah, 2005). This chemical genetics based strategy elegantly combines both the temporal control afforded by using small

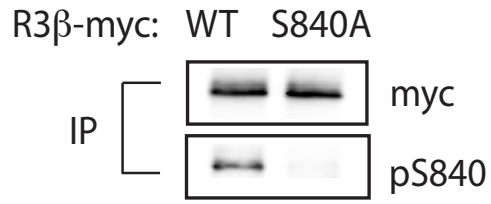

Figure 3.8: R3β S840 specific phospho-antibody detects phosphorylated S840.

Validation of phospho-S840 antibody. U2OS cells were transfected with R3β wildtype (WT) or S840A mutant and immunoprecipitated using anti-myc agarose beads. Phospho-S840 and myc blots are presented.

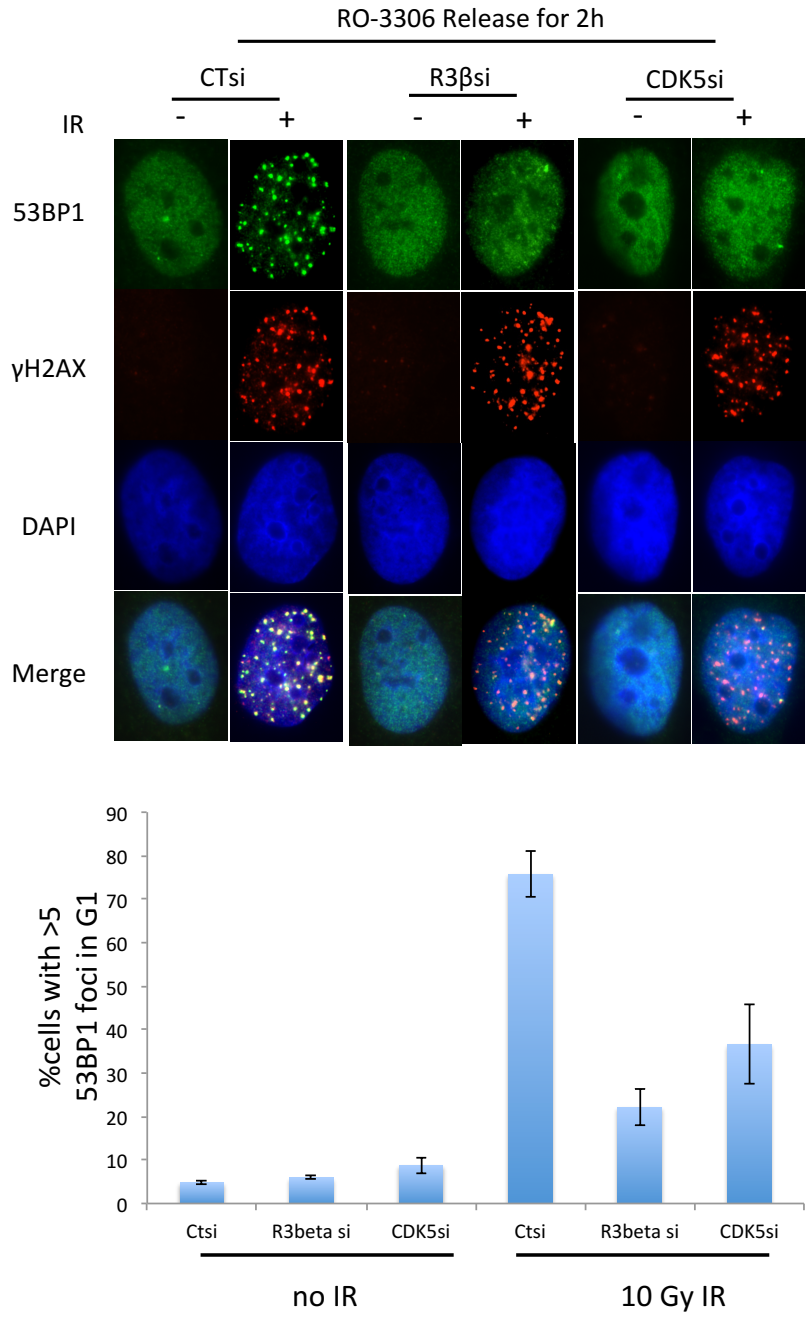

Figure 3.9: Absence of CDK5 reduces 53BP1 accumulation at DSBs.
Upper panel: U2OS cells transfected with Control (CTsi), R3β (R3βsi), or CDK5 siRNA (CDK5si) were released from RO-3306 block for 2h and irradiated at 10 Gy or left unirradiated. Cells were harvested following an additional 2h incubation and 53BP1 IR-induced foci formation was measured by immunofluorescence. γ-H2AX was used to mark DSBs. *Lower panel:* Quantitation shows percentage cells with 53BP1 foci in G1. More than 100 cells were quantified per condition. Error bars represent SEM; n=3 experiments.

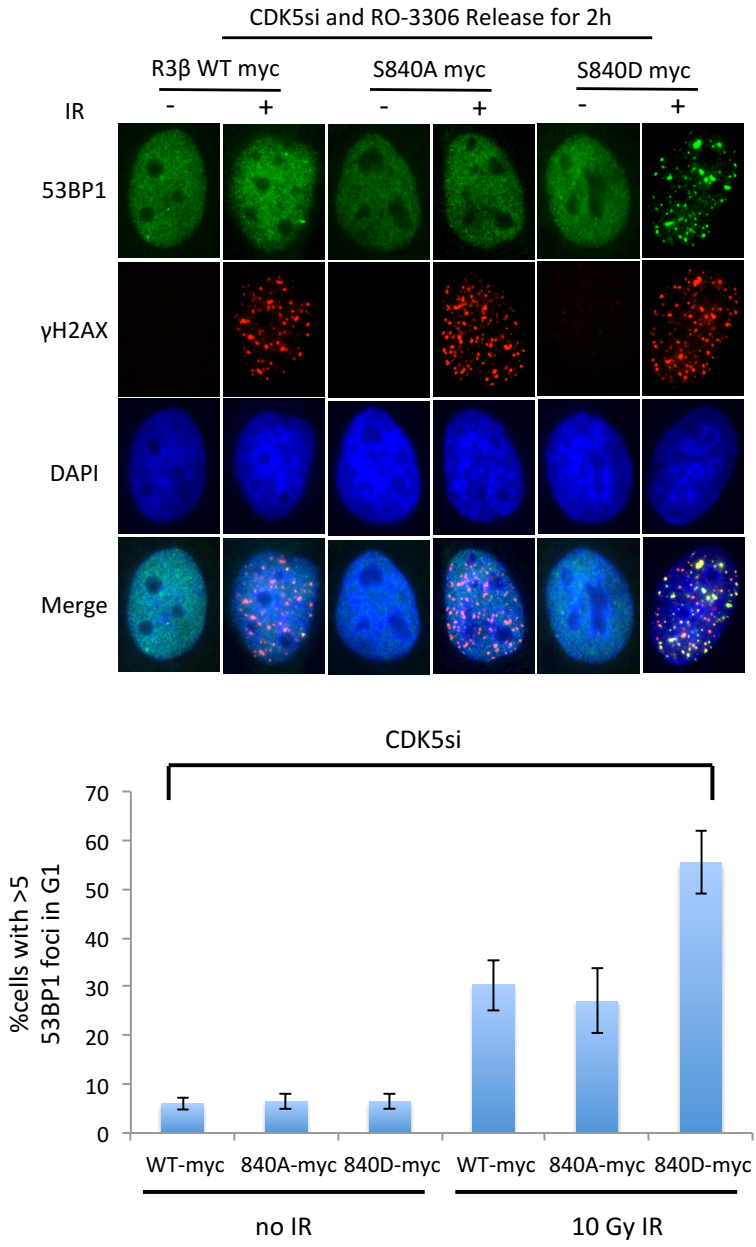

Figure 3.10: Ectopic expression of R3β S840D rescues loss of 53BP1 foci in the absence of CDK5.

Upper panel: U2OS cells transfected with CDK5 siRNA (CDK5si) and myc-tagged R3β wildtype (WT), S840A, or S840D mutant were released from RO-3306 block (9 μM) for 2h and irradiated at 10 Gy. Irradiated and unirradiated cells Figure were harvested following a 2h incubation and 53BP1 IR-induced foci formation was measured by immunofluorescence. γ–H2AX was used to mark DSBs. *Lower panel:* Quantitation shows percentage cells with greater than five 53BP1 foci in G1. More than 100 cells were quantified per condition. Error bars represent SEM; n=3 experiments.

molecule inhibitors with the specificity imparted by gene ablation, and can be used to generate mono-specific inhibitors of any kinase in the genome. The residue chosen for creating the active-site mutation is generally a 'gatekeeper' residue, which typically governs inhibitor selectivity among kinases. The gatekeeper residue is generally mutated to alanine or glycine, which creates a binding pocket for the analog inhibitor. We used this approach to generate an F80G gatekeeper mutation in the active site of CDK5 thereby engineering an analog-sensitive version of CDK5 capable of responding to the 1-NM-PP1 inhibitor (Fig. 3.13) (Collaboration with Kavita Shah's laboratory, Purdue University). Shah and colleagues have utilized this method to identify novel CDK5 substrates in neurons, and importantly demonstrate that the analog sensitive F80G-mutant CDK5 is functionally equivalent to wildtype CDK5.

We are using the CRISPR (clustered regularly interspaced short palindromic repeats)-technology to knockout endogenous CDK5, and replace with F80G-mutant CDK5. A schematic for depletion of CDK5 in U2OS cells using different guide RNAs and the corresponding knockout efficiency in pools of CRISPR cells are shown in Fig. 3.14. Since CDK5 has been implicated in both survival and proliferation of neuronal and cancer cells and mice deficient in CDK5 die perinatally (Liebl et al., 2011), it is plausible that continued loss of CDK5 is likely to be detrimental to cell survival.

Indeed, we observed a loss of cell viability in CRISPR knockout cell lines exhibiting continued depletion of CDK5. Therefore, we are reconstituting our CRISPR cells with F80G-mutant CDK5 that is potentially capable of functioning exactly like its wildtype counterpart while also being amenable to chemical inhibition by 1-NM-PP1. Theoretically, this should allow cells to regain wildtype CDK5 function in the absence

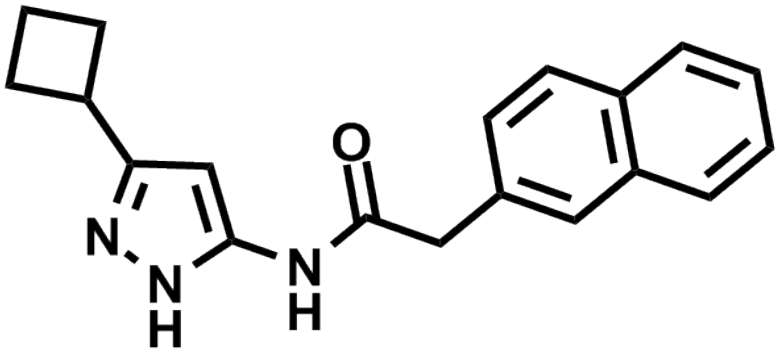

Figure 3.11: Synthesis of aminopyrazole analog 20-223, a selective CDK5 inhibitor.
The aminopyrazole analog (CP-668863 or 20-223) was reported at the Society for Medicines Research Symposium as a selective CKD5 inhibitor (Eli Lilly Research Center, Surrey UK, June 2007). The analog was reported to have a Ki = 2.9 nM versus CDK5 and was 5.7-fold selective versus CDK2. We synthesized 20-223 in four steps from commercially available starting materials with an overall yield of 32%. (Synthesis performed in the laboratory of Amarnath Natarajan, University of Nebraska Medical Center.)

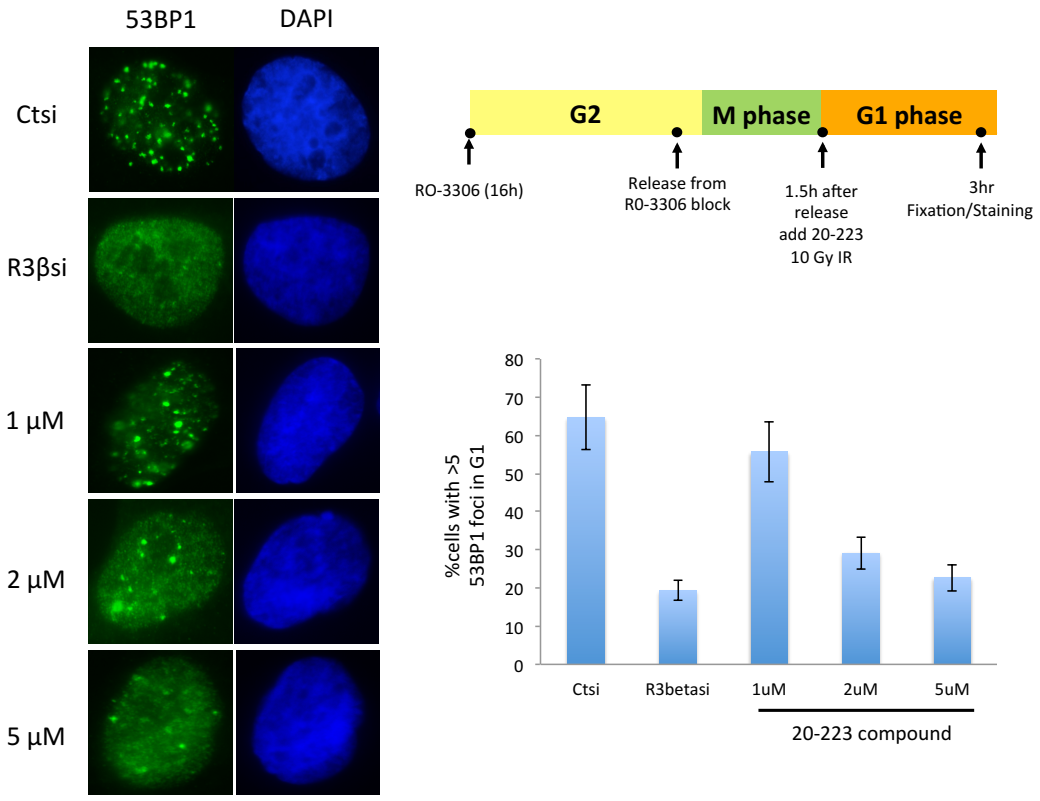

Figure 3.12: Selective inhibition of CDK5 using compound 20-223 reduces 53BP1 accumulation at DNA breaks.
U2OS cells were synchronized at the G2/M boundary with RO-3306 (9 μM) for 16 h followed by release into mitosis for 1.5h. At the end of mitosis, cells were treated with CDK5 inhibitor 20-223 at the indicated concentrations, irradiated (10 Gy) in early G1, and harvested at 3 h following damage for immunofluorescence imaging. Percent 53BP1 foci in G1 were quantified by counting nuclei for each condition (n = 50-100).

of the endogenous protein. Single-cell clones are being scored to assess successful depletion of endogenous CDK5 and detectable expression of the analog-sensitive kinase version. Inhibition of CDK5 F80G in the CRISPR cells using 1-NM-PP1 will allow us to truly delineate the role of CDK5 in mediating 53BP1-R3β interaction.

Finally, to assess the physiological relevance of R3β phosphorylation we mined the cBioPortal Cancer Genomics database (Cerami et al., 2012; Gao et al., 2013) and found a cancer-relevant R3β S840F mutation in melanoma (Hodis et al., 2012). We evaluated the interaction of the R3β S840F mutant with 53BP1 by immunoprecipitation and found that, similar to S840A, the S840F mutant abrogated 53BP1-R3β interaction (Fig. 3.15A). One possibility is that the R3β S840F mutant loses its ability to interact with the phosphatase catalytic subunit PP4C. However, immunoprecipitating myc-tagged versions of S840 mutants including S840A and S840D showed that interaction of R3β with PP4C was not affected (Fig 3.15B). It is therefore conceivable that loss of R3β function can contribute to the deregulation of DNA repair in cancer cells contributing to the cancer pathogenesis.

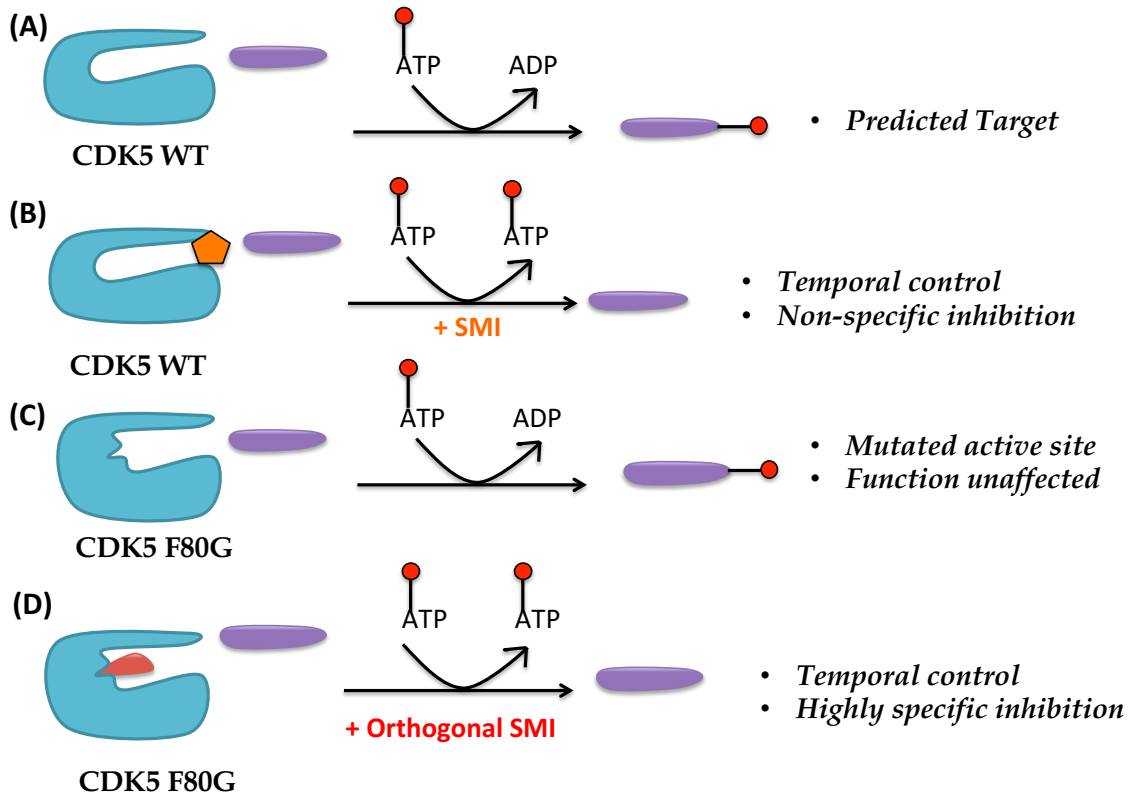

Figure 3.13: Schematic describing strategy for orthogonal inhibition of analog-sensitive CDK5.
(A) Absence of inhibitor allows CDK5 to phosphorylate its targets by utilizing ATP. **(B)** Small molecule inhibitors (such as roscovitine), afford the ability to block kinase activity at a specific time at the cost of specificity. **(C)** Creating a gatekeeper mutation in the active site of CDK5 by mutating the F80 residue to F80G does not affect the normal function of CDK5.**(D)** However, the mutated CDK5 is rendered sensitive to specific inhibition by an orthogonal inhibitor such as 1-NM-PP1 allowing highly specific depletion of CDK5.

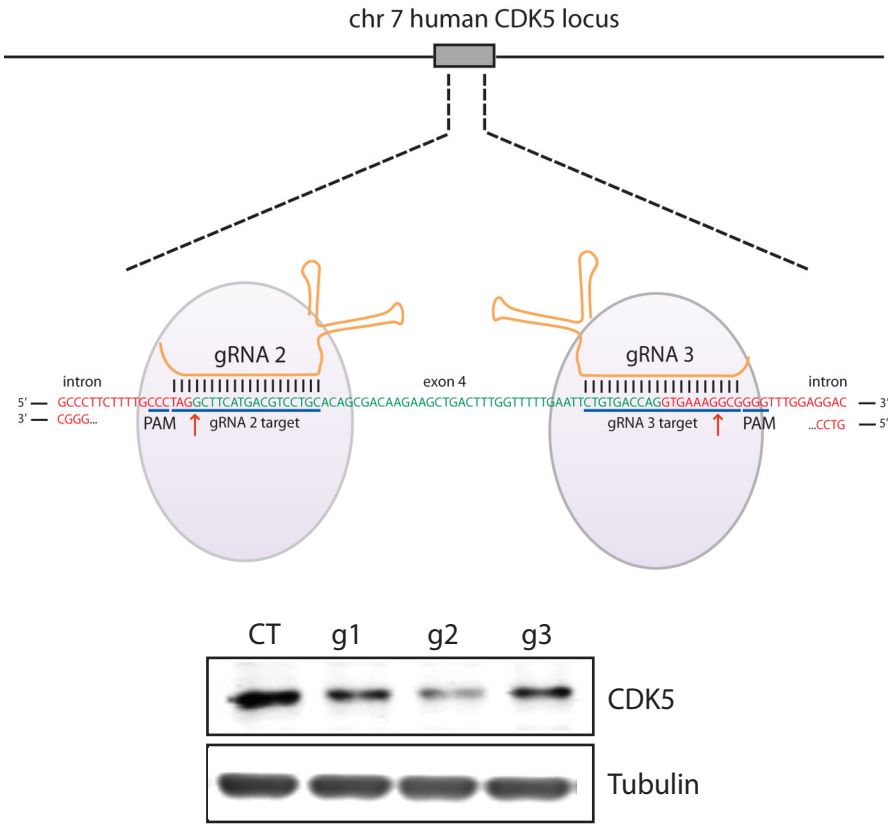

Figure 3.14: CRISPR-mediated knockout of CDK5 in U2OS cells.

(A) Schematic of CRISPR-Cas9 mediated genome editing at the CDK5 locus on chromosome 7. Guide RNA-mediated knockdown of CDK5 can be performed with individual guides or in combination. A strategy to knockdown CDK5 with two guide RNA target sequences and adjoining PAM sequences are shown. Exon 4 (green) and flanking introns (red). Guide RNA 2 and 3 sequences and corresponding PAM sequences (blue underline). Site of Cas9 cleavage (red arrows). **(B)** CDK5 knockdown efficiency in U2OS cells transduced with the indicated guide RNA sequences.

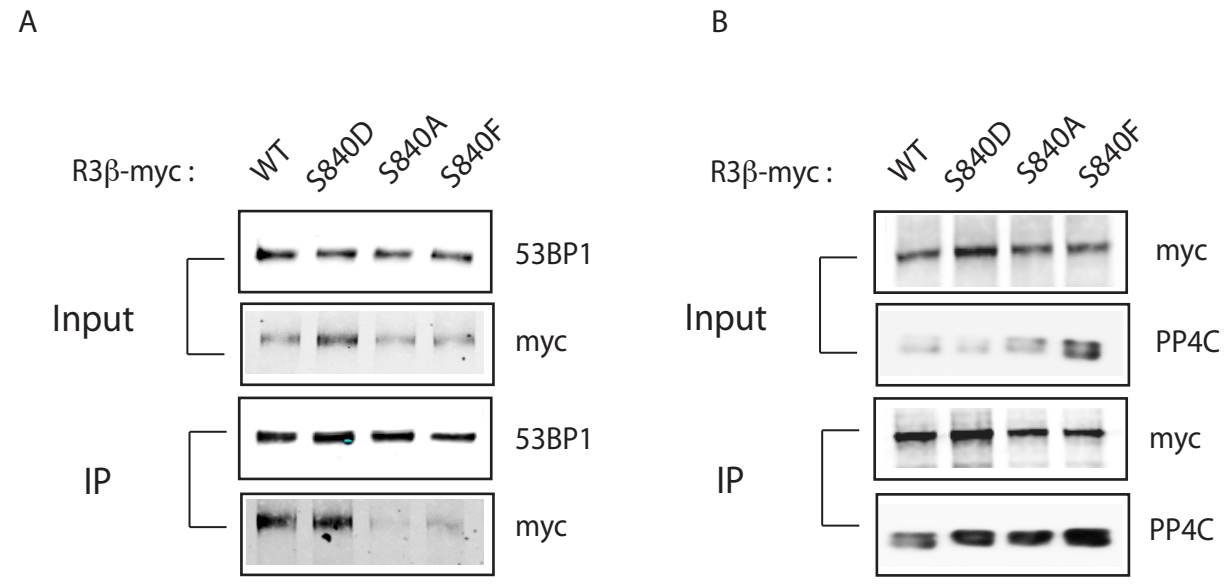

Figure 3.15: Cancer relevant R3β S840F mutation abrogates R3β binding with 53BP1.
(A) 53BP1 immunoprecipitations were performed in U2OS cells expressing the indicated R3β-myc constructs. **(B)** Expression of the same constructs as in (A) in U2OS cells followed by myc immunoprecipitation using anti-myc agarose. Interaction of mutants with PP4C is presented.

DISCUSSION

In this chapter, we investigated the regulation of the PP4 regulatory subunit R3β, which has recently been shown to dephosphorylate the DNA damage mediator protein 53BP1 during the cell cycle. The observation that R3β preferentially interacts with 53BP1 in mitosis and specifically dephosphorylates 53BP1 as cells enter G1, motivated us to study the details of the R3β-53BP1 interaction. We report here that productive interaction of R3β and 53BP1 requires the phosphorylation of S840, a residue at the C-terminal end of R3β. Furthermore, we delineate the timing of this interaction and identify CDK5 as the kinase that phosphorylates R3β at S840.

The effector stages of the DDR response are suppressed during mitosis as mitotic kinases CDK1 and PLK1 phosphorylate targets that inhibit CHK1 and CHK2. Recent work on 53BP1 regulation during mitosis shows that 53BP1 is excluded from DSBs by a combination of post-translational mechanisms. First, the E3 ubiquitin ligases RNF8 and RNF168, whose activity is necessary for 53BP1 recruitment, are restricted from localizing to chromatin until late mitosis (Giunta et al., 2010; Giunta and Jackson, 2011; Heijink et al., 2013). Second, work from our group and others has shown that phosphorylation of the 53BP1 UDR at T1609 and S1618 by mitotic kinases inhibits binding of 53BP1 to ubiquitylated nucleosome core particles (Lee et al., 2014a; Orthwein et al., 2014). Here, we report yet another regulatory mechanism that limits 53BP1 recruitment in mitosis by temporally regulating the phosphorylation of R3β. By allowing R3β S840 phosphorylation only during mid-to-late mitosis, the cell ensures that 53BP1 cannot localize to DSBs until early G1 when activation of effector mechanisms can re-establish DNA damage checkpoints. Indeed, ectopic reactivation

of 53BP1 during mitosis was shown to cause chromosomal abnormalities and telomere fusions in the above studies validating this hypothesis.

We also predicted CDK5 as an essential component of R3β- based regulation of 53BP1. Consistent with the catalytic activity of other CDKs, CDK5 is a proline-directed kinase that phosphorylates residues of the type (S/T)PX(K/H/R) and this consensus sequence can be located in a number of identified CDK5 neuronal substrates (Smith et al., 2001). An examination of the predicted CDK5 site on R3β confirmed that S840 is a prototypical proline-directed site (Fig. 3.2). Indeed, depletion of CDK5 had a negative impact on 53BP1 IR-induced foci similar to depletion of R3β or expression of the phosphonull S840A mutant. By rescuing this phenotype using the phospho-mimetic mutant we were able to show that the effect of CDK5 on 53BP1 was indeed mediated by R3β. Nevertheless, predictions can have a certain level of error and CDKs are known to have redundant functions. We therefore performed *in vitro* experiments with purified human CDK5 and purified R3β C5 fragment (wildtype or S840A) and found that CDK5 effectively phosphorylated S840 in the kinase reaction (collaboration with Kavita Shah's laboratory, Fig. 3.7B).

Future work will focus on developing a clearer understanding of the timing of R3β-53BP1 interaction at a single cell level. While biochemical experiments have helped define the window (1-2h after RO-3306 release) for this interaction, they cannot help us define its precise timing. We therefore intend to focus on studying this interaction at single-cell resolution (collaboration with David Pellman's group). Furthermore, our data regarding CDK5 strongly suggests that it phosphorylates R3β. However we cannot formally rule out the contribution of other mitotic kinases in also

phosphorylating R3β. Notable among these are CDK1 that was also predicted as a phosphorylating kinase. Monitoring 53BP1 foci formation in CDK5-deficient CRISPR cells complemented with analog-responsive CDK5 will answer this question. We also plan to apply this chemical genetics approach to study the contribution of CDK1 in this process.

REFERENCES

Bach, S., Knockaert, M., Reinhardt, J., Lozach, O., Schmitt, S., Baratte, B., Koken, M., Coburn, S.P., Tang, L., Jiang, T.*, et al.* (2005). Roscovitine targets, protein kinases and pyridoxal kinase. J Biol Chem *280*, 31208-31219.

Bain, J., Plater, L., Elliott, M., Shpiro, N., Hastie, C.J., McLauchlan, H., Klevernic, I., Arthur, J.S., Alessi, D.R., and Cohen, P. (2007). The selectivity of protein kinase inhibitors: a further update. The Biochemical journal *408*, 297-315.

Beausoleil, S.A., Villen, J., Gerber, S.A., Rush, J., and Gygi, S.P. (2006). A probability-based approach for high-throughput protein phosphorylation analysis and site localization. Nat Biotechnol *24*, 1285-1292.

Benada, J., Burdova, K., Lidak, T., von Morgen, P., and Macurek, L. (2015). Polo-like kinase 1 inhibits DNA damage response during mitosis. Cell cycle *14*, 219-231.

Bennetzen, M.V., Larsen, D.H., Bunkenborg, J., Bartek, J., Lukas, J., and Andersen, J.S. (2010). Site-specific phosphorylation dynamics of the nuclear proteome during the DNA damage response. Mol Cell Proteomics *9*, 1314-1323.

Bensimon, A., Schmidt, A., Ziv, Y., Elkon, R., Wang, S.Y., Chen, D.J., Aebersold, R., and Shiloh, Y. (2010). ATM-dependent and -independent dynamics of the nuclear phosphoproteome after DNA damage. Sci Signal *3*, rs3.

Bishop, A.C., Buzko, O., and Shokat, K.M. (2001). Magic bullets for protein kinases. Trends in cell biology *11*, 167-172.

Bishop, A.C., Ubersax, J.A., Petsch, D.T., Matheos, D.P., Gray, N.S., Blethrow, J., Shimizu, E., Tsien, J.Z., Schultz, P.G., Rose, M.D.*, et al.* (2000). A chemical switch for inhibitor-sensitive alleles of any protein kinase. Nature *407*, 395-401.

Cerami, E., Gao, J., Dogrusoz, U., Gross, B.E., Sumer, S.O., Aksoy, B.A., Jacobsen, A., Byrne, C.J., Heuer, M.L., Larsson, E.*, et al.* (2012). The cBio cancer genomics portal: an open platform for exploring multidimensional cancer genomics data. Cancer discovery *2*, 401-404.

Chen, G.I., Tisayakorn, S., Jorgensen, C., D'Ambrosio, L.M., Goudreault, M., and Gingras, A.C. (2008). PP4R4/KIAA1622 forms a novel stable cytosolic complex with phosphoprotein phosphatase 4. J Biol Chem *283*, 29273-29284.

Chowdhury, D., Xu, X., Zhong, X., Ahmed, F., Zhong, J., Liao, J., Dykxhoorn, D.M., Weinstock, D.M., Pfeifer, G.P., and Lieberman, J. (2008). A PP4-phosphatase complex dephosphorylates gamma-H2AX generated during DNA replication. Mol Cell *31*, 33-46.

Cohen, P.T., Philp, A., and Vazquez-Martin, C. (2005). Protein phosphatase 4--from obscurity to vital functions. FEBS letters *579*, 3278-3286.

Dhavan, R., and Tsai, L.H. (2001). A decade of CDK5. Nat Rev Mol Cell Biol *2*, 749-759.

Gao, J., Aksoy, B.A., Dogrusoz, U., Dresdner, G., Gross, B., Sumer, S.O., Sun, Y., Jacobsen, A., Sinha, R., Larsson, E.*, et al.* (2013). Integrative analysis of complex cancer genomics and clinical profiles using the cBioPortal. Sci Signal *6*, pl1.

Giunta, S., Belotserkovskaya, R., and Jackson, S.P. (2010). DNA damage signaling in response to double-strand breaks during mitosis. The Journal of cell biology *190*, 197-207.

Giunta, S., and Jackson, S.P. (2011). Give me a break, but not in mitosis: the mitotic DNA damage response marks DNA double-strand breaks with early signaling events. Cell cycle *10*, 1215-1221.

Grosstessner-Hain, K., Hegemann, B., Novatchkova, M., Rameseder, J., Joughin, B.A., Hudecz, O., Roitinger, E., Pichler, P., Kraut, N., Yaffe, M.B.*, et al.* (2011). Quantitative phospho-proteomics to investigate the polo-like kinase 1-dependent phospho-proteome. Mol Cell Proteomics *10*, M111 008540.

Heijink, A.M., Krajewska, M., and van Vugt, M.A. (2013). The DNA damage response during mitosis. Mutation research *750*, 45-55.

Hodis, E., Watson, I.R., Kryukov, G.V., Arold, S.T., Imielinski, M., Theurillat, J.P., Nickerson, E., Auclair, D., Li, L., Place, C.*, et al.* (2012). A landscape of driver mutations in melanoma. Cell *150*, 251-263.

Hornbeck, P.V., Zhang, B., Murray, B., Kornhauser, J.M., Latham, V., and Skrzypek, E. (2015). PhosphoSitePlus, 2014: mutations, PTMs and recalibrations. Nucleic Acids Res *43*, D512-520.

Lee, D.H., Acharya, S.S., Kwon, M., Drane, P., Guan, Y., Adelmant, G., Kalev, P., Shah, J., Pellman, D., Marto, J.A.*, et al.* (2014a). Dephosphorylation Enables the Recruitment of 53BP1 to Double-Strand DNA Breaks. Mol Cell *54*, 512-525.

Lee, D.H., Acharya, S.S., Kwon, M., Drane, P., Guan, Y., Adelmant, G., Kalev, P., Shah, J., Pellman, D., Marto, J.A.*, et al.* (2014b). Dephosphorylation enables the recruitment of 53BP1 to double-strand DNA breaks. Molecular cell *54*, 512-525.

Lee, D.H., and Chowdhury, D. (2011). What goes on must come off: phosphatases gate-crash the DNA damage response. Trends in biochemical sciences *36*, 569-577.

Lee, D.H., Pan, Y., Kanner, S., Sung, P., Borowiec, J.A., and Chowdhury, D. (2010). A PP4 phosphatase complex dephosphorylates RPA2 to facilitate DNA repair via homologous recombination. Nat Struct Mol Biol *17*, 365-372.

Lee, J.H., and Kim, K.T. (2007). Regulation of cyclin-dependent kinase 5 and p53 by ERK1/2 pathway in the DNA damage-induced neuronal death. Journal of cellular physiology *210*, 784-797.

Li, L., and Zou, L. (2005). Sensing, signaling, and responding to DNA damage: organization of the checkpoint pathways in mammalian cells. Journal of cellular biochemistry *94*, 298-306.

Liebl, J., Furst, R., Vollmar, A.M., and Zahler, S. (2011). Twice switched at birth: cell cycle-independent roles of the "neuron-specific" cyclin-dependent kinase 5 (Cdk5) in non-neuronal cells. Cellular signalling *23*, 1698-1707.

Lukas, J., Lukas, C., and Bartek, J. (2004). Mammalian cell cycle checkpoints: signalling pathways and their organization in space and time. DNA repair *3*, 997-1007.

Nakada, S., Chen, G.I., Gingras, A.C., and Durocher, D. (2008). PP4 is a gamma H2AX phosphatase required for recovery from the DNA damage checkpoint. EMBO reports *9*, 1019-1026.

Obenauer, J.C., Cantley, L.C., and Yaffe, M.B. (2003). Scansite 2.0: Proteome-wide prediction of cell signaling interactions using short sequence motifs. Nucleic Acids Res *31*, 3635-3641.

Orthwein, A., Fradet-Turcotte, A., Noordermeer, S.M., Canny, M.D., Brun, C.M., Strecker, J., Escribano-Diaz, C., and Durocher, D. (2014). Mitosis inhibits DNA double-strand break repair to guard against telomere fusions. Science *344*, 189-193.

Shah, K. (2005). Orthogonal chemical genetic approaches for unraveling signaling pathways. IUBMB life *57*, 397-405.

Smith, D.S., Greer, P.L., and Tsai, L.H. (2001). Cdk5 on the brain. Cell growth & differentiation : the molecular biology journal of the American Association for Cancer Research *12*, 277-283.

Strocchi, P., Pession, A., and Dozza, B. (2003). Up-regulation of cDK5/p35 by oxidative stress in human neuroblastoma IMR-32 cells. Journal of cellular biochemistry *88*, 758-765.

Sun, K.H., de Pablo, Y., Vincent, F., Johnson, E.O., Chavers, A.K., and Shah, K. (2008). Novel genetic tools reveal Cdk5's major role in Golgi fragmentation in Alzheimer's disease. Molecular biology of the cell *19*, 3052-3069.

Tarricone, C., Dhavan, R., Peng, J., Areces, L.B., Tsai, L.H., and Musacchio, A. (2001). Structure and regulation of the CDK5-p25(nck5a) complex. Mol Cell *8*, 657-669.

Tian, B., Yang, Q., and Mao, Z. (2009). Phosphorylation of ATM by Cdk5 mediates DNA damage signalling and regulates neuronal death. Nat Cell Biol *11*, 211-218.

Vassilev, L.T., Tovar, C., Chen, S., Knezevic, D., Zhao, X., Sun, H., Heimbrook, D.C., and Chen, L. (2006). Selective small-molecule inhibitor reveals critical mitotic functions of human CDK1. Proc Natl Acad Sci U S A *103*, 10660-10665.

Zheng, X.F., Kalev, P., and Chowdhury, D. (2015). Emerging role of protein phosphatases changes the landscape of phospho-signaling in DNA damage response. DNA repair *32*, 58-65.

Zheng, Y.L., Amin, N.D., Hu, Y.F., Rudrabhatla, P., Shukla, V., Kanungo, J., Kesavapany, S., Grant, P., Albers, W., and Pant, H.C. (2010). A 24-residue peptide (p5), derived from p35, the Cdk5 neuronal activator, specifically inhibits Cdk5-p25 hyperactivity and tau hyperphosphorylation. J Biol Chem *285*, 34202-34212.

CHAPTER 4

Serum microRNAs are early indicators of survival after radiation-induced hematopoietic injury

Sanket S. Acharya, Wojciech Fendler, Jacqueline Watson, Abigail Hamilton, Yunfeng Pan, Emily Gaudiano, Patryk Moskwa, Payel Bhanja, Subhrajit Saha, Chandan Guha, Kalindi Parmar and Dipanjan Chowdhury

ABSTRACT

Accidental radiation exposure is a threat to human health that necessitates effective clinical planning and diagnosis. Minimally invasive biomarkers that can predict long-term radiation injury are urgently needed for optimal management after a radiation accident. We have identified serum microRNA (miRNA) signatures that indicate long-term impact of total body irradiation in mice when measured within 24 hours of exposure. Impact of TBI on the hematopoietic system was assessed to determine a correlation of residual hematopoietic stem cells with increasing doses of radiation. Serum miRNA signatures distinguished untreated mice from animals exposed to radiation and correlated with the impact of radiation on HSCs. Mice exposed to sublethal (6.5 Gy) and lethal (8 Gy) doses of radiation were indistinguishable for 3-4 weeks after exposure. A serum miRNA signature detectable 24 hours after radiation exposure consistently segregated these two cohorts. Furthermore, using either a radio-protective agent prior to, or radiation mitigation after, lethal radiation we determined that the serum miRNA signature correlated with the impact of radiation on animal health rather than the radiation dose. Lastly, using humanized mice that had been engrafted with human CD34+ HSCs, we determined that the serum miRNA signature indicated radiation-induced injury to the human bone marrow cells. Our data suggest that serum miRNAs can serve as functional dosimeters of radiation, representing a potential breakthrough in early assessment of radiation-induced hematopoietic damage and timely use of medical countermeasures to mitigate the long-term impact of radiation.

INTRODUCTION

Exposure to high doses of radiation in the event of industrial accidents, terrorist attacks or use of nuclear weapons in military settings poses a significant threat to human life (Chin, 2007; Coleman et al., 2004; Waselenko et al., 2004). While substantial advancements in characterizing the effects of radiation on different organs and systems have been made, treatment options to exposed individuals are still dependent on a slow manifestation of symptoms (Waselenko et al., 2004). For example, delayed damage to the hematopoietic system at moderately high doses of radiation can take several weeks or months to appear, and existing biodosimetry techniques do not effectively predict the severity of injury sustained. In such situations, medical intervention is complicated by the difficulty in triaging individuals exposed to low, moderate, or high doses of radiation.

The radiation LD_{50} for untreated humans is about 4 Gy (Christensen et al., 2014). Low to moderate radiation exposures in humans lead to progressive development of acute radiation syndrome (ARS) consisting of dose-dependent hematopoietic, gastrointestinal, and cerebrovascular malignancies (Waselenko et al., 2004). The hematopoietic system is the most vulnerable tissue to the damaging effects of radiation (Mauch et al., 1995). Exposure to low or moderate doses of radiation leads to a rapid decrease in blood cell counts, including loss of lymphocytes, neutrophils, thrombocytes, and a severe decrease in hematopoietic progenitors. Radiation injury is also linked to increased risk of cancer and infection. Exposure to high doses of radiation causes severe, non-recoverable

bone marrow damage, resulting in pancytopenia owing to complete loss of hematopoietic stem cell (HSC) populations eventually leading to death. At 2-6 Gy exposure in humans, the hematopoietic component of ARS appears in a few weeks to 2 months. At higher doses of 8-12 Gy, lethal gastro-intestinal (GI) as well as bone marrow toxicity is observed and death is probable in 1-3 weeks (Coleman et al., 2004; Waselenko et al., 2004).

MicroRNAs (miRNAs) have recently emerged as promising biomarkers for different pathological conditions. Deregulation of miRNAs has been implicated in the pathogenesis of various conditions ranging from cancer to autoimmune and cardiovascular disease (Mendell and Olson, 2012). miRNAs are present in body fluids, such as serum and plasma (Cortez et al., 2011; Mendell and Olson, 2012), and several studies have correlated levels of specific serum/plasma miRNA with various pathological conditions, including after exposure to ionizing radiation (Cui et al., 2011; Templin et al., 2011). The inherent stability of serum miRNAs under harsh conditions and reproducible levels in individuals of the same species make miRNAs attractive candidates for use as noninvasive biomarkers (Mitchell et al., 2008).

This study was designed to assess whether changes in serum miRNAs immediately after exposure may accurately predict the long-term impact of radiation-induced hematopoietic injury in murine models. We discovered unique miRNA signatures that effectively distinguished between control, sub-lethal (low dose), sub-lethal (high dose), and lethal total body irradiation (TBI) cohorts within 24 hours after radiation and correlated these signatures with the radiation-

induced loss of HSCs. Importantly, 24 hours after exposure, this serum miRNA signature distinguished fatal versus non-fatal hematopoietic injury. Treatment with a radioprotective agent prior to lethal TBI or radiation mitigation by bone marrow transplant after lethal radiation exposure produced serum miRNA signatures that correlated with the functional impact of radiation. The human relevance of the serum miRNA signature was observed using a humanized mouse model. The serum miRNA signature indicated radiation-induced injury to human bone marrow cells in this model system, suggesting that miRNAs can be used to detect radiation-induced hematopoietic injury in affected human populations within hours of radiation exposure.

MATERIALS AND METHODS

Study design

This study was designed to investigate whether serum miRNAs can predict radiation-induced hematopoietic damage early after radiation exposure. Differential expression of miRNAs in response to radiation was investigated in two model systems, strongly suggesting the applicability of miRNAs as radiation-specific markers of latent hematopoietic injury. Animals were also treated with radioprotective and radiomitigating agents to correlate levels of specific miRNAs with animal survival at 30 days post-irradiation. All animal procedures performed were approved by the Institutional Animal Care and Use Committee (IACUC) at Dana-Farber Cancer Institute (DFCI). Animals were maintained in the animal facility and given *ad libitum* access to food and water. Body condition scores (BCS) as described in (Nunamaker et al., 2013) was used to standardize endpoints. A BCS of 3 was regarded as the endpoint for all irradiated animals irrespective of treatment group, at which point animals were considered moribund and euthanized. Mouse serum samples used for miRNA profiling were randomized before analysis and experiments were generally repeated three times.

Power analysis was performed using the Hierarchical Clustering Explorer 3.5 tool (Seo et al., 2006). The number of samples was estimated to be sufficient to provide statistical power of at least 80% needed to obtain a p value of less than 0.01 for differentially expressed miRNAs with a fold change 0 >1.5 or <0.67 in between group comparisons. The p value threshold was lowered from 0.05 to

account for multi-group post-hoc testing. A sample size of 10 per group was thus calculated to allow us to confirm statistically significant differences for the top 95 differentially expressed miRNAs with the predetermined effect sizes.

Mice and total body irradiation

C57BL/6J male mice (10 week old) were obtained from Jackson Labs (Bar Harbor, Maine) and acclimated in the Animal Research Facility (ARF) at DFCI before irradiation at the age of 12-13 weeks. All procedures performed were approved by IACUC at DFCI. Animals were exposed to TBI in an irradiation pie cage (Braintree Scientific). Irradiation was performed using a ^{137}Cs source at a dose rate of 110 cGy/min using a ^{137}Cs source (Gamma Cell 40 Exactor, Best Theratronics). Instrument calibration was performed according to vendor instructions in accordance with the DFCI Office of Radiation Safety. After irradiation, bone marrow was harvested and cells were counted by flow cytometry.

HuCD34$^+$ NOD *scid* gamma chain deficient (NSG) mice

HuCD34$^+$ "humanized" NSG mice were obtained from Jackson Labs and housed in a BL2/N facility at DFCI. All procedures were approved by IACUC at DFCI. During the generation of these mice at Jackson Labs, 3 week old female NSG mice were irradiated at 1.4 Gy to deplete their bone marrow and injected with CD34$^+$ human HSCs. At 12 weeks after transplant, each mouse was tested by FACS for engraftment of human CD45$^+$ and murine CD45$^+$ cells. Animals were obtained at DFCI approximately 10 weeks after engraftment confirmation at

Jackson Labs. Peripheral blood and bone marrow from animals in the untreated control arm was reconfirmed for the presence of human $CD45^+$ cells at DFCI with anti-human CD45 FITC (clone 2D1 from BD).

Murine miRNA profiling

miRCURY LNA Universal RT miRNA PCR Rodent Panel I&II containing 742 assays was used to profile miRNAs differentially expressed in mouse serum from animals exposed to different doses of radiation (Exiqon). Normalization of data was performed using the global mean of 170 miRNAs most-commonly expressed in all samples. RNA spike-in control (UniSp6) was used to test the efficiency of the cDNA synthesis reaction while DNA spike-in control (UniSp3) tested the efficiency of qPCR amplification. Spike-in controls were used throughout the study for profiling and validation. In order to negate the possibility of hemolysis, ΔCp for miR-451 and miR-23a-3p was computed for each sample as previously reported (Blondal et al., 2013).

Bone marrow harvest and flow cytometry

Bone marrow was harvested as per protocols described in (Parmar et al., 2010). Briefly, animals were dissected to isolate femurs and tibia from mouse hind limb. Extracted bones were flushed with a 23 gauge needle using Hank's Balanced Salt Solution (HBSS, Gibco) supplemented with 2% Fetal Bovine Serum (FBS) and 1% 10 mM HEPES (Gibco) to obtain bone marrow. Cells were then passed through an 18 gauge needle to obtain a single cell suspension. BM-

MNC count was determined by counting cells using 3% Acetic Acid with Methylene Blue Solution (Stem Cell Technologies). For LKS (lineage, cKit, Sca1) staining to visualize HPCs and HSCs, whole bone marrow was stained with biotinylated anti-lineage cocktail (anti-Mac1, Gr-1, CD3e, B220, and Ter119), APC-conjugated anti-cKit (clone 2B8), and PECy7-conjugated anti-Sca1 (clone D7) antibodies. Following primary antibody staining, cells were washed and incubated in PE-conjugated streptavidin secondary antibody to visualize lineage positive cells. All primary and secondary antibodies were obtained from BD Biosciences. Samples were acquired using an LSR Fortessa instrument (BD) and data was analyzed using FlowJo software (TreeStar).

Complete blood counts

Blood collection for CBCs (100 µl) was performed by retro-orbital bleeding after anesthesia in EDTA-coated tubes (BD Biosciences). CBCs were recorded with a Hemavet 950 FS hematology analyzer (Drew Scientific).

Colony assays

To assess colony-forming ability, whole bone marrow isolated after flushing mouse femurs and tibiae were plated in 12-well plates at a density of 20,000 and 100,000 cells/well in mouse or human methylcellulose medium (Stem Cell Technologies). Cells from all samples were plated in triplicates and incubated at 37ºC in 5% CO_2 for 7 days at which time hematopoietic colonies (colony-forming units in culture, CFU-Cs) were scored.

HSC and bone marrow transplantation

Short-term and long-term repopulating ability was assessed by transplantation of either sorted HSCs or unfractionated whole bone marrow from donor mice (C56BL/6J CD45.2 congenic) into lethally irradiated (10 Gy) recipients (B6.SJL-Ptprc^{a} Pep3^{b}/BoyJ CD45.1 congenic) as described in (Parmar et al., 2010). Donor mice were exposed to 2 and 6.5 Gy TBI and allowed to recover for 3 months, at which time animals were sacrificed, bone marrow was isolated by flushing, and HSCs were sorted on a FACSAria (BD Biosciences). For transplants involving sorted HSCs, a total of 2000 LKS+ cells from CD45.2 donor mice were mixed with 250,000 support bone marrow cells (CD45.1^{+}) and injected IV per lethally irradiated CD45.1 recipient. For transplants involving unfractionated bone marrow, a total of 500,000 whole bone marrow cells from CD45.2 donor mice were mixed with 250,000 support bone marrow cells (CD45.1^{+}) and injected IV per lethally irradiated CD45.1 recipient. Peripheral blood samples collected at 1 and 4 months post-transplant were used to assess short-term and long-term repopulation, respectively. Donor-cell chimerism in recipients was assessed by staining peripheral blood with FITC-conjugated anti-CD45.2 (clone 104) and PE-conjugated anti-CD45.1 (clone A20) antibodies. To measure the extent of multi-lineage reconstitution, the percentage of donor-derived B cells, T cells, and myeloid cells was calculated by co-staining with PE-conjugated anti-B220 (clone RA3-6B2), PE-anti-CD3e (clone 145-2C11), and PE- anti-Mac1/anti-Gr1 (clones M1/70 and RB6-8C5), respectively. All antibodies

were obtained from BD Biosciences. Stained samples were acquired on an LSR Fortessa instrument (BD) and analyzed using FlowJo software (TreeStar).

Serum preparation

Peripheral blood was collected by retro-orbital bleeding after anesthesia. Up to 200 µl of blood was collected in DNAse/RNAse- free Eppendorf tubes and incubated at room temperature (RT) for 2 h to allow clotting. Blood samples were then spun in an Eppendorf 5415C centrifuge at 14,000 rpm (15,996 g) for 5 min at RT. The supernatant was collected and re-spun at the above conditions to remove any remaining cellular contamination. The resulting supernatant (serum) was stored in aliquots at -80ºC.

RNA extraction and cDNA synthesis

Total RNA was isolated from serum samples by using the miRCURY RNA Isolation Kit – Biofluids from 50 µl mouse serum as per manufacturer's manual. Total RNA was eluted in 50 µl of RNAse-free H_2O and stored at -80ºC long-term. Because only small RNA can be isolated, RNA concentration measurement by Nanodrop or spectrophotometry is not reliable. Hence, as per manufacturer's recommendations, input volumes for serum RNA were optimized for the cDNA synthesis reaction. cDNA was synthesized in 10-µl reactions using the Universal cDNA Synthesis Kit II and was diluted 50-fold in RNAse/DNAse-free H_2O for use in quantitative PCR. Reagents for RNA extraction and cDNA synthesis obtained from Exiqon.

Quantitative PCR

Diluted cDNA was subjected to quantitative PCR analysis in Pick-N-Mix plates designed in a 96-well format (Exiqon). SYBR Green qPCR Master Mix was mixed 1:1 with diluted cDNA and added to specific wells in pre-designed Pick-N-Mix plates containing dried-down LNA primers specific for selected miRNAs. The Pick-N-Mix plates also contained number of controls including miR-101a and miR-19b (normalization controls), UniSp6 (RNA spike-in control) and UniSp3 (DNA spike-in control). Built-in interplate calibrator (IPC) reactions were used to control for inter-plate variability. Pick-N-Mix qPCR plates were run on an Applied Biosystems 7500 FAST Real-Time PCR System. Data was generally normalized using miR-101a. However, normalization using miR-19b produced similar results. miR-451 and miR-23a were used to assess extent of hemolysis. All reagents used for quantitative PCR were obtained from Exiqon.

Radioprotection with amifostine

Amifostine was given to both C57BL/6J and huCD34^{+} NSG ("humanized") mice intraperitoneally (IP) at 200 mg/kg body weight 1 h prior to TBI.

Bone marrow adherent stromal cell culture and transplantation

All studies were performed under the guidelines and protocols of the Institutional Animal Care and Use Committee (IACUC) of the Albert Einstein College of Medicine. The animal use protocol for this study was reviewed and approved by IACUC at Albert Einstein. Five- to 6-weeks-old male C57BL/6J

(NCI-Fort Dietrich) mice were maintained *ad libitum*. TBI (10.4 Gy) was performed on anesthetized animals (intraperitoneal ketamine and xylazine 7:1 mg/ml for 100 µl/mouse) using a Shephard ^{137}Cs irradiator at a dose rate of 236 cGy/min following biosafety guidelines of the Albert Einstein College of Medicine. Donor bone marrow cells were harvested using sterile techniques from the long bones of C57BL/6J mice and cultured in mesenchymal stem cell (MSC) basal medium (Cambrex-Lonza) supplemented with 10% heat-inactivated FBS, 1% glutamine, and 1% Penicillin/Streptomycin for 4 days. This was followed by collection of adherent bone marrow stromal cells (BMSCs). BMSCs (2×10^6 cells/mouse) were injected intravenously via tail vein into C57BL/6J recipients at 24 and 72 hours after irradiation.

Statistical analysis

MicroRNA Profiling: Normalization of miRNA serum levels was performed using 170 commonly expressed miRNA. Analysis of variance (ANOVA) was used to determine which miRNAs differed significantly between groups. To adjust for multiple comparisons testing the Benjamini-Hochberg correction was applied. A threshold of $p<0.05$ in ANOVA was selected as the level of statistical significance. Tukey's test was used to determine between-group significance in post-hoc comparisons. MiRNAs with p values <0.05 in ANOVA were used in hierarchical-clustering analysis to visualize expression patterns. Differentially expressed miRNAs were tested in pairwise comparisons with a Benjamini-Hochberg adjusted Student's t-test to determine between-group differences.

Validation with real-time qPCR: One-way ANOVA was used to confirm global significance. Dunnett's post-hoc testing procedure was used to compare miRNA levels in the 8.5 Gy + Saline group against the other three experimental groups. Univariate comparisons were performed using the student's t-test or the student's t-test for paired samples. Pearson's correlation coefficient was used for correlation testing. Survival analysis was performed using the log-rank (Mantel-Cox) test.

RESULTS

Characterization of hematopoietic injury in mice following exposure to different doses of TBI

To test our hypothesis that serum miRNAs may be used to predict long-term impact of radiation-induced damage to the hematopoietic system we systematically assessed radiation induced hematopoietic injury by exposing C57BL/6J mice to different doses of radiation. Consistent with previous reports (Cui et al., 2011; Wang et al., 2006), at 2 and 6.5 Gy TBI doses, all animals survived, and the 8 Gy dose was lethal for majority (65%) of mice (Fig. 4.1). Therefore, 2 and 6.5 Gy were chosen as the sub-lethal low and sub-lethal high doses, respectively, and 8 Gy was considered the lethal dose for subsequent experiments.

Complete blood count (CBC) of irradiated animals displayed a reduction in white blood cells (WBCs) when compared with un-irradiated controls at days 1, 7, and 15 following TBI. By day 30, the 2 and 6.5 Gy cohorts showed a near complete recovery in their WBC levels whereas the 8 Gy animals did not survive (Fig. 4.2A) Hemoglobin levels plummeted in the 6.5 and 8 Gy animals until day 15; however, by day 30, these levels returned to normal in the 6.5 Gy cohort (Fig. 4.2B). Platelet levels followed a similar trend reaching a nadir at day 7 for 6.5 Gy and day 15 for 8 Gy animals. By day 30, platelet levels in the 6.5 Gy cohort improved and were comparable to the 2 Gy cohort (Fig. 4.2C). Animals exposed to 8 Gy succumbed to bone marrow failure by day 30, but there was complete

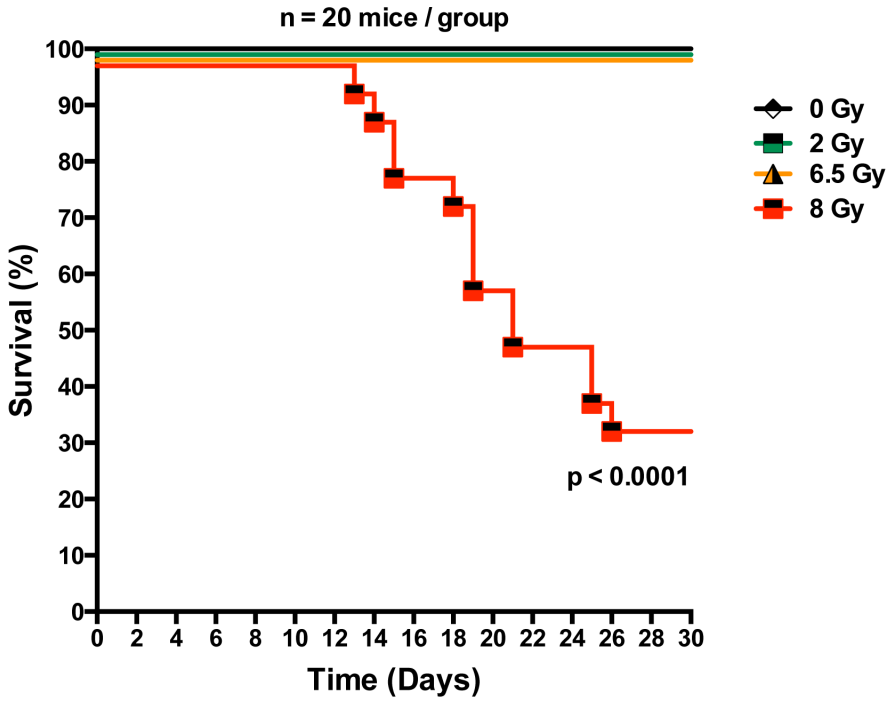

Figure 4.1: Survival curve after exposure to different doses of radiation. Establishment of sublethal and lethal dose in C57BL/6J mice. Kaplan-Meier survival curves of C57BL/6J male mice exposed to 0 (control), 2, 6.5, or 8 Gy TBI (*n* = 20/group). P-value determined by log-rank (Mantel-Cox) test.

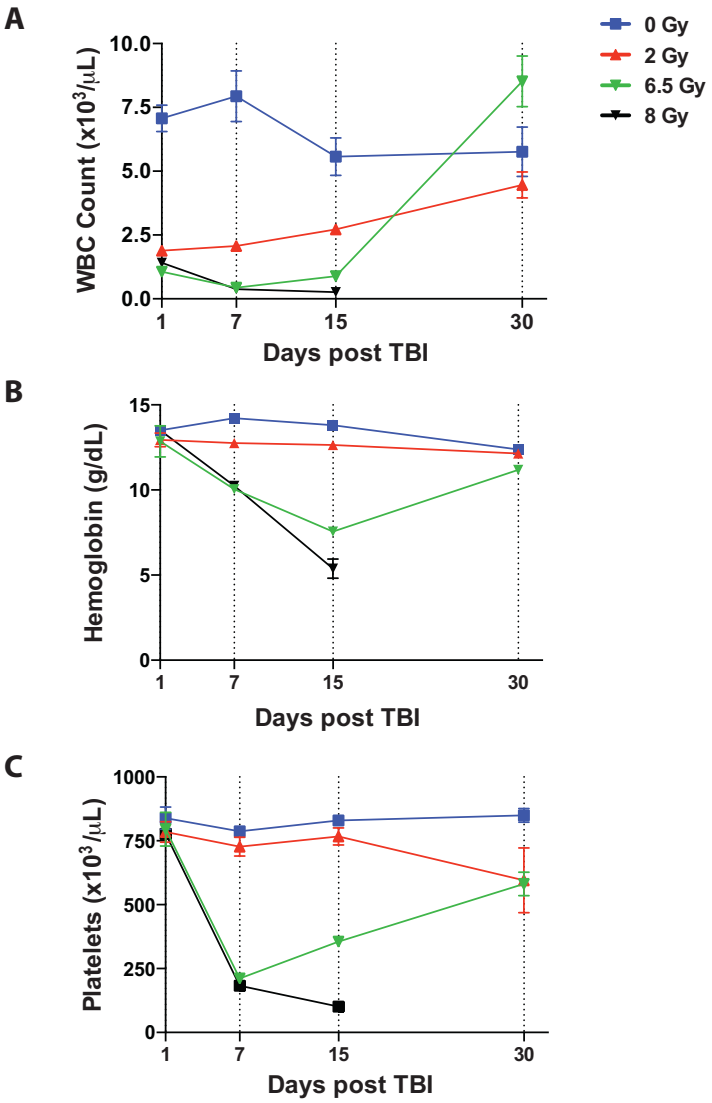

Figure 4.2: Analysis of peripheral blood CBC parameters following TBI-induced hematopoietic damage.
Total WBC count (**A**), hemoglobin (**B**), and platelets (**C**) at 24 h (day 1), 7, 15, and 30 days are shown for mice irradiated with the indicated doses. Data are averages ± SEM (*n* = 5 mice per group). The same mice were used for bone marrow analysis in Fig. 4.3; one-way ANOVA followed by Dunnett's test.

recovery in CBC levels in animals exposed to lower doses of irradiation (Fig. 4.2).

Decrease in bone-marrow cellularity is an important measure of hematopoietic injury. Therefore, we examined kinetics of bone marrow mononuclear cell (BM-MNC) depletion after exposure to different doses of TBI (2-8 Gy). We observed a dose-dependent reduction in the cellularity at 24 h post radiation (Fig. 4.3B). By days 7 and 15, we observed complete recovery of BM-MNCs in the hind limbs of mice exposed to 2 Gy, whereas for mice exposed to 6.5 and 8 Gy, the BM-MNC count remained very low. Mice exposed to 6.5 Gy showed significant recovery of BM-MNCs by 1 month, and complete recovery by 3 months compared to the 15 day time point ($P < 0.01$, paired t-test) (Fig. 4.3B). Following a similar pattern of injury and recovery, by day 15 hematopoietic progenitor function post-TBI had significantly decreased for all doses, and the 6.5 and 8 Gy cohorts were indistinguishable from each other with very low colony-forming unit-in culture (CFU-C) counts (Fig. 4.3C). At subsequent time-points, bone marrow from both 2 and 6.5 Gy groups displayed improved progenitor function, but mice in the 8 Gy group failed to recover.

To further evaluate the bone marrow hematopoietic progenitor population in control and irradiated animals we quantified the LKS^{-} ($lineage^{-}/c\text{-}kit^{+}/Sca\text{-}1^{-}$) population, which is enriched in hematopoietic progenitor cells (HPCs), and the LKS^{+} ($lineage^{-}/c\text{-}kit^{+}/Sca\text{-}1^{+}$) population, which is enriched in HSCs. Severe reduction in the HPC content was observed at 24 hours after TBI in all irradiated animals (Fig. 4.4A). The kinetics of recovery for the HPC population (LKS^{-} cells)

in the weeks and months after TBI were consistent with hematopoietic function (Fig. 4.3B and C). Importantly, the numbers of HPCs in the 6.5 and 8 Gy cohorts remained comparably low and indistinguishable from each other at day 15 after TBI.

Collectively, our data reveal that dose-dependent hematopoietic injury occurs after TBI, but animals exposed to sub-lethal high (6.5 Gy) and lethal (8 Gy) TBI doses remain largely indistinguishable up to 15 days post TBI. Animals exposed to sub-lethal high doses do show substantial recovery, unlike their 8 Gy counterparts.

Residual HSCs in sub-lethally irradiated mice retain the capacity to repopulate the bone marrow

Sub-lethal doses of TBI can cause permanent damage to the stem cell compartment leading to stem cell senescence and decrease in the engraftment potential of HSCs (Shao et al., 2014; Wang et al., 2006). Our hematopoietic analysis in Fig. 4.3 and Fig. 4.4A suggested that TBI at sub-lethal doses caused a severe reduction but not complete depletion of HPCs in the 2 and 6.5 Gy irradiated animals. We observed a similar trend in the HSC population (LKS^+ cells) with striking ablation until 7 days in all TBI cohorts, and detectable recovery at the 15 day time point in the 2 Gy irradiated animals (Fig. 4.4B). By comparison, HSC content in 6.5 and 8 Gy irradiated animals 15 days post-TBI was significantly lower.

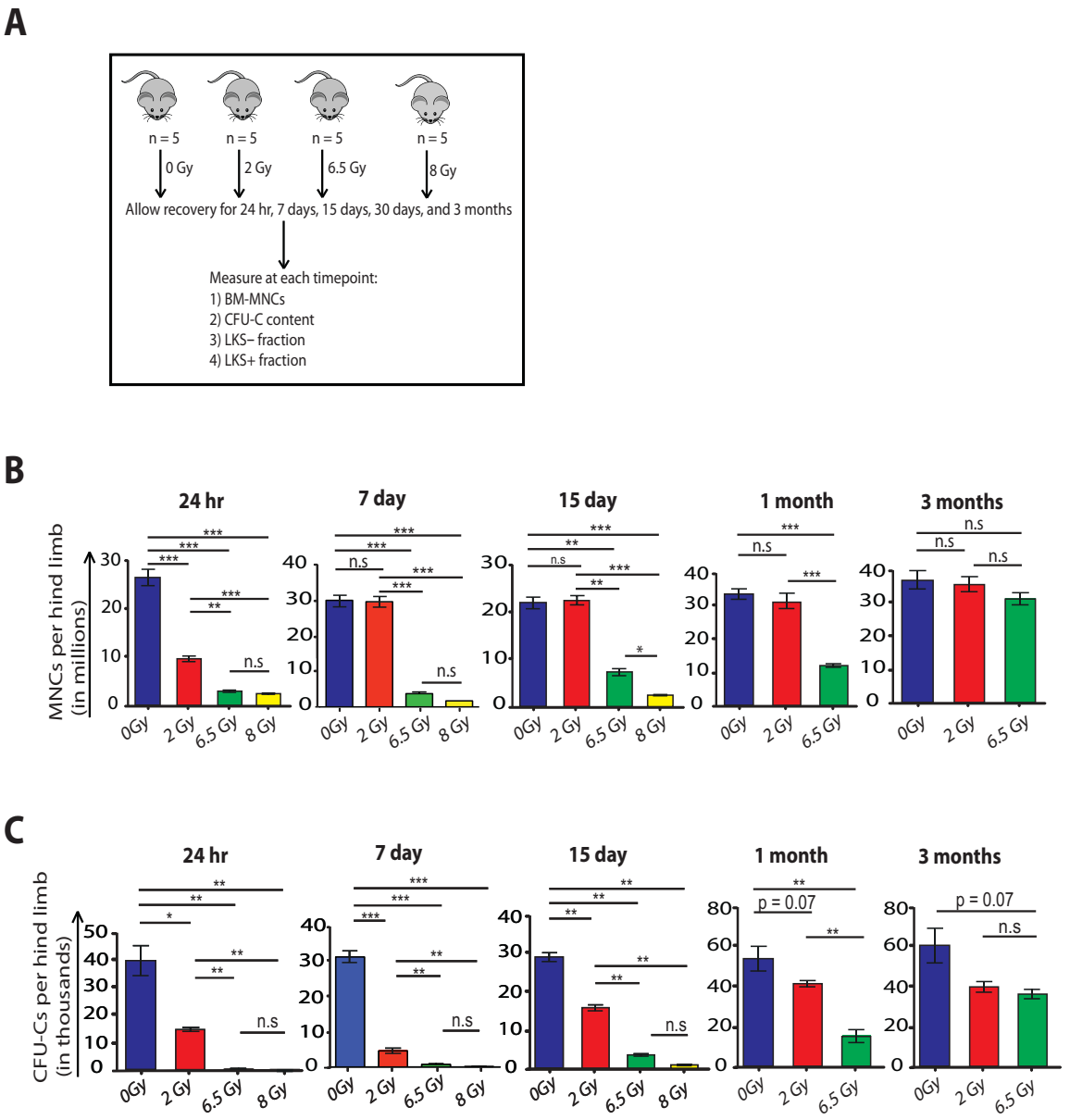

Figure 4.3: Analysis of BM-MNCs and CFU-C content in mice exposed to TBI.

(A-C) C57BL/6J mice were exposed to TBI at the indicated doses and allowed to recover for up to 3 months (A). At each time point, animals were sacrificed and bone marrow was analyzed for number of BM-MNCs (B) and CFU-C content (C). Frequency of LKS^- HPCs (E) per hind limb. Data are means ± SEM (*n* = 5/group; two independent experiments). **P*< 0.05; ***P* < 0.01; ****P* < 0.001; *****P* < 0.0001; n.s., not significant; one-way ANOVA followed by Tukey's test.

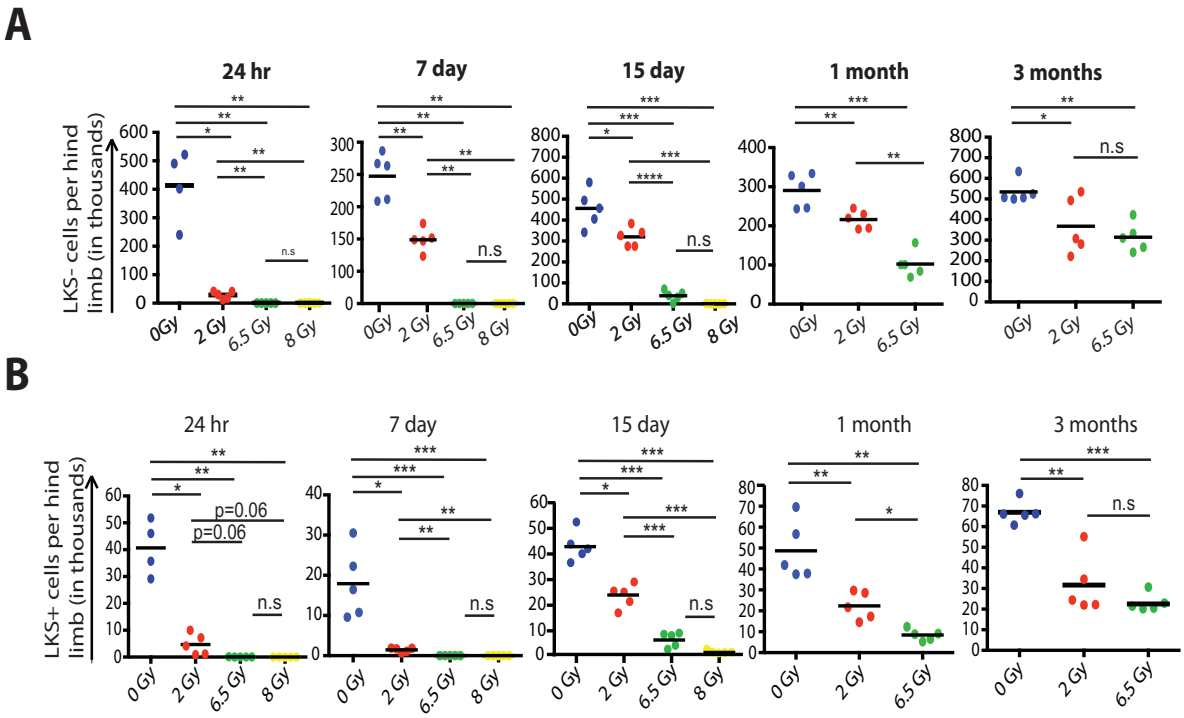

Figure 4.4: **Analysis of LKS- and LKS+ cells in mice exposed to TBI.**
(A-B) C57BL/6J mice were exposed to TBI as in Fig. 4.3A and allowed to recover for up to 3 months. At each time point, animals were sacrificed and bone marrow was analyzed for frequency of LKS^- HPCs (A) per hind limb and total number of HSCs (LKS^+ cells) (B) per hind limb post-TBI as measured by FACS. Data are individual animals and horizontal bars are means. Data are individual animals and horizontal bars are means. *P< 0.05; **P < 0.01; ***P < 0.001; ****P < 0.0001; n.s., not significant; one-way ANOVA followed by Tukey's test.

To confirm that the recovered residual HSCs from 2 and 6.5 Gy animals were indeed functional in their ability to repopulate the hematopoietic system, we performed HSC transplantation experiments and measured engraftment by peripheral blood chimerism at 1 and 4 months post-transplant (Fig. 4.5A). Bone marrow HSCs from TBI-treated mice were taken at 3 months post-irradiation and transplanted in unirradiated animals. Representative FACS profiles of control, 2 Gy, and 6.5 Gy donor bone marrow at 3 months after irradiation are presented in Fig. 4.5B. Sorted cells were gated on the LKS^{+} population. Donor cell engraftment (total leukocytes) at 1 and 4 months post-transplant showed an approximate 4- and 15-fold decrease in irradiated recipients transplanted with sorted HSCs from 2 and 6.5 Gy irradiated animals, respectively, compared to control (Fig. 4.5C). When multi-lineage reconstitution of T cells, B cells, and myeloid cells was investigated, a similar defect in peripheral blood chimerism was observed (Fig. 4.6 and 4.7). Competitive repopulation assays performed with unfractionated whole bone marrow showed similar defects in the chimerism of total leukocytes (Fig. 4.5C) and lineage-restricted cells in peripheral blood (Fig. 4.8). These data suggest that, although most of the HSCs in sub-lethally irradiated animals are severely impaired in their repopulating potential, rare functional HSCs do exist and maintain the hematopoietic system.

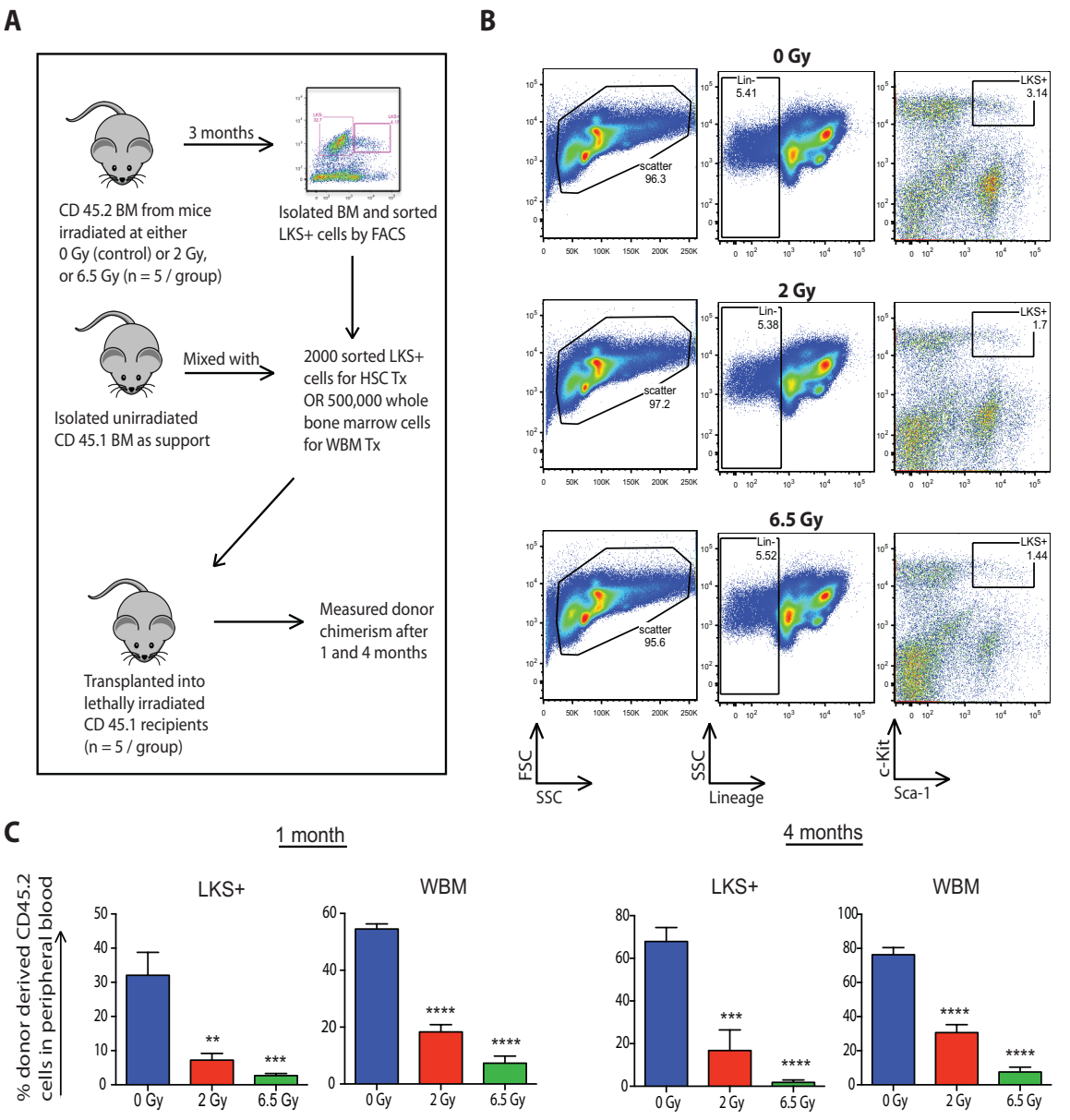

Figure 4.5: Stem cell transplantation from irradiated mice reveals a defect in short-term and long-term repopulating ability.
(A) Schematic to describe transplantation (Tx) of HSCs or unfractionated whole bone marrow (WBM) into lethally irradiated recipients. BM, bone marrow. **(B)** Representative FACS profiles of stained bone marrow from control and irradiated donor mice used to sort HSCs for transplant. Individual profiles show total scatter, Lineage- (lin-) and LKS$^+$ gates. **(C)** Donor cell engraftment in peripheral blood of recipients transplanted with either HSCs or WBM. Total leukocyte engraftment at 1 and 4 months post-transplant is shown. Data are means ± SEM (n = 5/group for HSC, n = 4/group for WBM). *P< 0.05; **P < 0.01; ***P < 0.001; ****P < 0.0001; n.s., not significant; compared to control (0 Gy) mice; one-way ANOVA followed by Tukey's test.

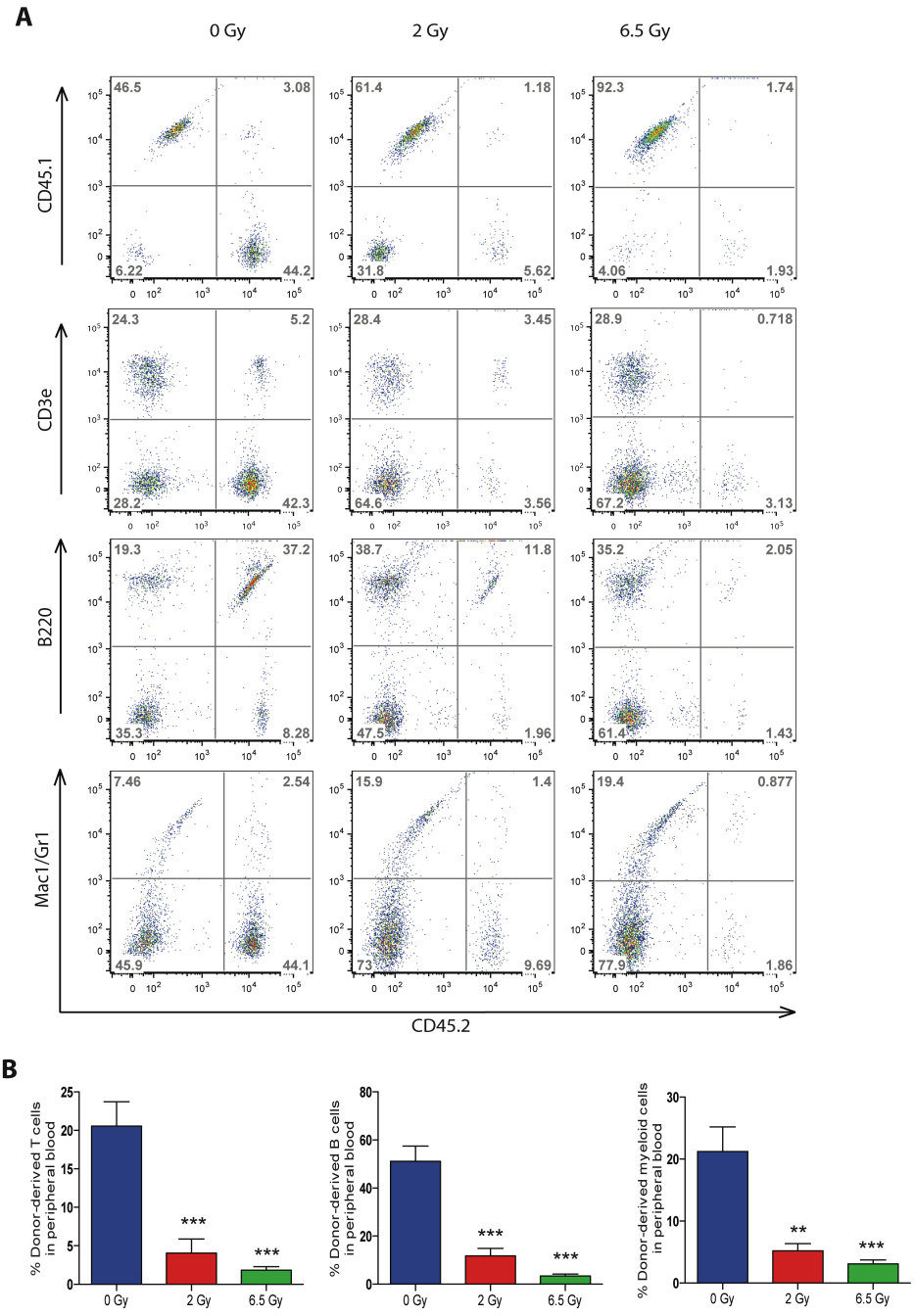

Figure 4.6: Repopulation analysis at 1 month after HSC transplant.
Per the experimental protocol in Fig. 4.5A, donor mice were left unirradiated (control, 0 Gy) or exposed to TBI doses of 2 or 6.5 Gy and allowed to recover for 3 months followed by HSC sorting and transplantation into recipient animals. (**A**) Representative FACS plots of donor-cell chimerism measured at 1 month post-transplant. Peripheral blood from recipient animals was harvested and stained for CD45.1 (recipient marker), CD45.2 (donor marker), CD3e (T cells), B220 (B cells), and Mac1/Gr1 (myeloid cells). (**B**) Multi-lineage reconstitution in recipients

Figure 4.6 (Continued):
transplanted with HSCs (percent donor-derived T, B, and myeloid cells at 1 month post-transplant). Total leukocyte chimerism at 1 month is shown in Fig. 4.5C. Data are means ± SEM (*n* = 5 mice per recipient group); ***P* < 0.01, ****P* < 0.001 compared to control 0 Gy; one-way ANOVA followed by Tukey's test.

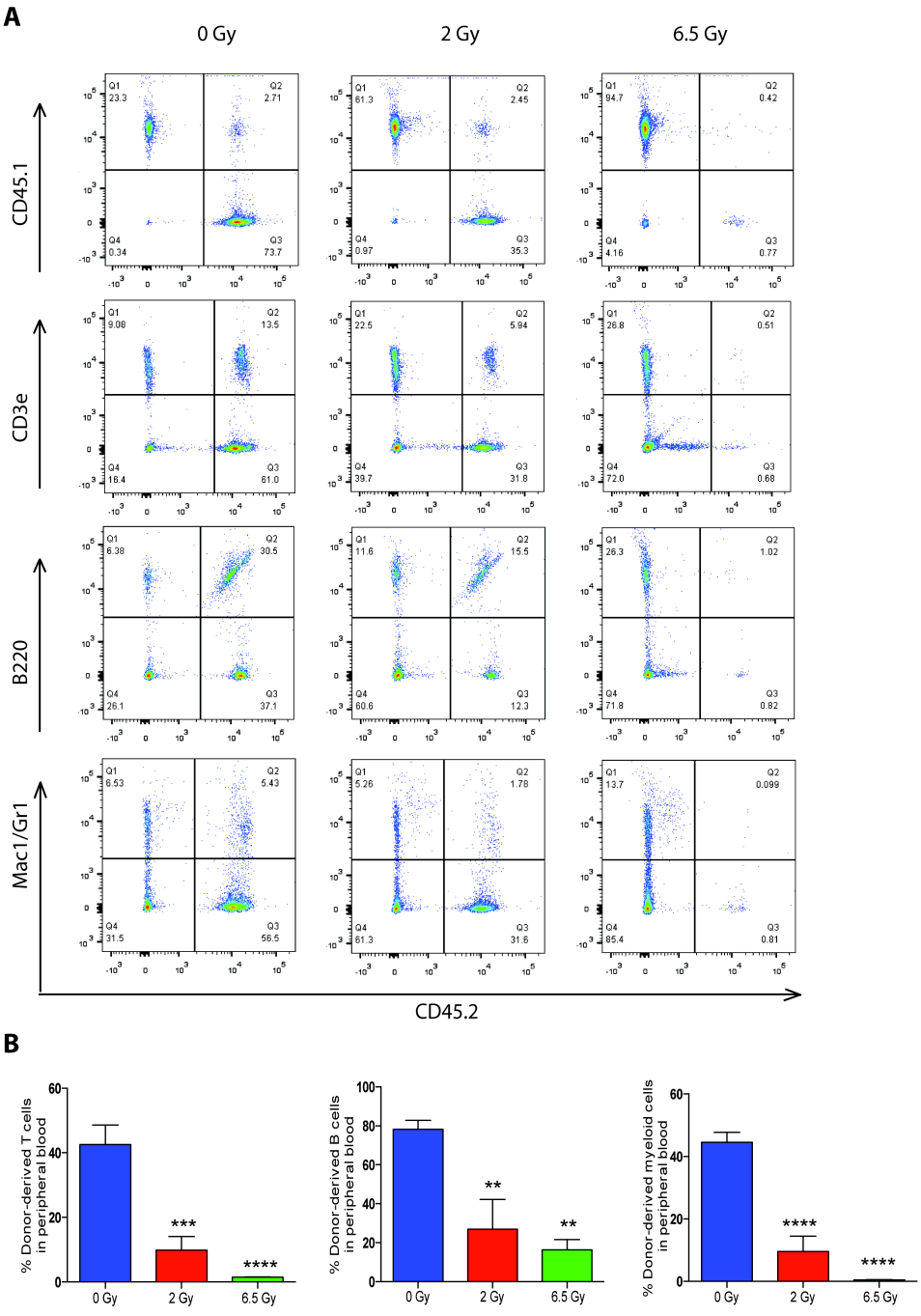

Figure 4.7: Repopulation analysis at 4 months after HSC transplant.
Following repopulation analysis at 1 month reported in Fig. 4.6, animals were reanalyzed at 4 months post- transplant. (**A**) Representative FACS plots of donor-cell chimerism in peripheral blood measured at 4 months post-transplant. (**B**) Multilineage reconstitution in recipients transplanted with HSCs. Percent donor-derived T, B, and myeloid cells at 4 months are shown. Total leukocyte

Figure 4.7 (Continued):
chimerism at 4 months is shown in Fig 2D. Data in (B) are means ± SEM (*n* = 5 mice per recipient group); ***P* < 0.01, ****P* < 0.001, *****P* < 0.0001 compared with control (0 Gy); one-way ANOVA followed by Tukey's test.

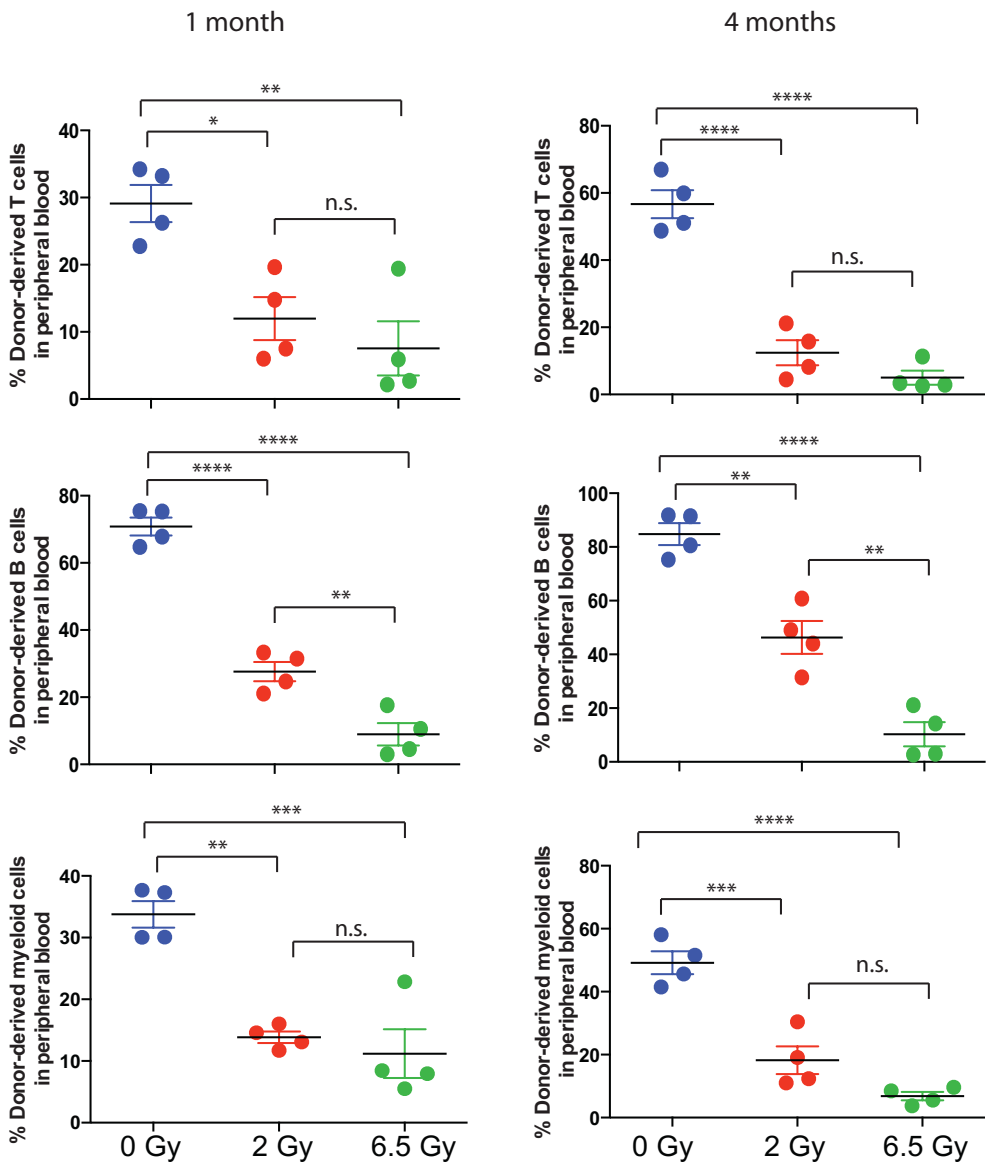

Figure 4.8: Repopulation analysis following unfractionated whole bone marrow transplant.

The transplant protocol followed outline in Fig. 4.5A. A total of 500,000 CD45.2 whole bone marrow cells and 250,000 CD45.1 support cells were injected in lethally irradiated CD45.1 recipients. Peripheral blood from recipient animals was harvested and stained for CD45.1 (recipient), CD45.2 (donor), CD3e (T cells), B220 (B cells), and Mac1/Gr1 (myeloid cells). Multi-lineage (T, B, and myeloid cell) reconstitution at 1 and 4 months post-transplant is presented, with results of total leukocyte chimerism at 1 and 4 months in Fig. 2D. Data are individual animals with horizontal and vertical bars representing means ± SEM (n = 4 animals per recipient group); *P < 0.05; **P < 0.01; ***P < 0.001; ****P < 0.0001; n.s., not significant; one-way ANOVA followed by Tukey's test.

Serum miRNA profiling and identification of radiation dose–specific miRNA signatures

To test whether changes in serum miRNA levels after TBI correlate with hematopoietic injury and predict long-term damage, we profiled serum miRNAs in mice exposed to 0 (control), 2, 6.5, or 8 Gy TBI 24 hours after radiation (*n* = 10 animals per group). The number of miRNAs detected per sample (count) and the average amplification threshold (Cp) value for miRNAs were evaluated and reproducibility confirmed (Fig. 4.9A and B). Red blood cell contamination was ruled out by calculating ΔCp of miR-451 (expressed in red blood cells) and miR-23a-3p (relatively stable in serum) (Blondal et al., 2013) (Fig. 4.9C).

Out of 170 miRNAs detected in each sample, 68 were found to be significantly altered by radiation (Table 4.1) and were considered dose-responsive (Fig. 4.11). A heatmap representing the top 8 of the 68 miRNAs that effectively separated irradiated from non-irradiated samples is shown in Fig. 4.10. These miRNAs—namely 150-5p, 142-5p, 142-3p, 136-5p, 33-5p, 320-3p, 30c-5p, and 126-3p—were the top significant hits in ANOVA analysis consisting of all irradiated samples (Table 4.1).

We investigated whether serum miRNA expression can distinguish the 0 versus 2 Gy cohorts 24 hours after exposure, and whether these miRNAs correlated with BM-MNC or HPC/HSC counts at the 7 day time point. Based on our profiling, five serum miRNAs were effective in segregating the two groups 24 hours after radiation exposure (Fig. 4.12A). MiR-130a-3p showed an increase,

Table 4.1: Fold changes of 68 statistically significant miRNAs at different doses of TBI with respect to controls. The table ranks miRNAs based on the Benjamini-Hochberg corrected *P*-value. Of the 224 miRNAs analyzed for differential expression, 68 had $P < 0.05$, and are presented here.

miRNA	Rank	Benjamini-Hochberg corrected p-value	Fold change (versus 0 Gy)		
			2Gy	6.5Gy	8Gy
mmu-miR-142-5p	1	6.14552E-10	0.744	0.550	0.468
mmu-miR-150-5p	2	6.41729E-10	0.335	0.360	0.347
mmu-miR-320-3p	3	6.83112E-06	0.962	1.188	1.321
mmu-miR-136-5p	4	8.17096E-06	1.038	0.465	0.412
mmu-miR-33-5p	5	4.8463E-05	1.006	0.548	0.412
mmu-miR-142-3p	6	4.8463E-05	0.910	0.579	0.513
mmu-miR-30c-5p	7	0.000365	1.041	1.124	1.375
mmu-miR-126-3p	8	0.000365	0.961	1.524	1.398
mmu-miR-706	9	0.000466	0.399	0.356	0.634
mmu-miR-375-3p	10	0.000466	1.234	2.136	2.284
mmu-miR-29a-5p	11	0.000466	0.888	0.965	0.709
mmu-miR-193a-3p	12	0.000530	1.168	0.649	0.436
mmu-miR-99b-5p	13	0.000530	0.996	1.344	1.513
mmu-miR-30a-3p	14	0.001069	0.990	1.062	1.586
mmu-miR-194-5p	15	0.001069	0.812	0.610	0.446
mmu-miR-151-3p	16	0.001069	1.130	1.467	1.309
mmu-let-7d-3p	17	0.001069	0.971	1.221	1.202
mmu-miR-486-5p	18	0.001407	1.188	1.463	2.066
mmu-miR-423-5p	19	0.001407	1.049	1.296	1.434
mmu-miR-30b-5p	20	0.002091	1.039	1.119	1.227
mmu-miR-191-5p	21	0.002343	1.139	1.432	1.633
mmu-miR-497-5p	22	0.003355	0.937	0.749	0.620
mmu-miR-32-5p	23	0.003528	1.080	0.628	0.605
mmu-miR-214-5p	24	0.003992	0.725	0.703	0.472
mmu-miR-326-3p	25	0.005364	1.239	0.851	0.796
mmu-miR-1195	26	0.005478	0.968	1.091	1.829
mmu-miR-122-5p	27	0.005478	0.933	0.348	0.149
mmu-miR-1839-3p	28	0.006650	1.317	1.534	2.031
mmu-miR-500-3p	29	0.007062	0.985	0.799	0.577
mmu-miR-30e-3p	30	0.008429	0.996	1.118	1.448
mmu-miR-191-5p	31	0.008476	1.111	1.337	1.549
mmu-miR-322-3p	32	0.008829	0.848	1.319	1.179
mmu-miR-709	33	0.012398	1.171	1.284	2.016
mmu-miR-486-3p	34	0.012398	1.156	1.263	2.007
mmu-miR-133a-3p	35	0.013008	0.858	1.809	2.389
mmu-miR-676-3p	36	0.013063	1.025	1.200	1.261
mmu-miR-744-5p	37	0.013451	1.119	1.206	1.301
mmu-miR-27a-3p	38	0.013751	0.897	0.908	0.702
mmu-miR-29a-3p	39	0.014569	0.931	0.847	0.760
mmu-miR-1839-5p	40	0.014569	1.087	1.277	1.317
mmu-miR-30a-5p	41	0.014569	1.055	1.182	1.346
mmu-miR-199b-5p	42	0.016705	0.864	0.514	0.633
mmu-miR-125a-5p	43	0.022629	0.959	1.092	1.262
mmu-miR-133b-3p	44	0.024815	0.872	1.659	2.116

Table 4.1 (Continued):					
mmu-miR-24-3p	45	0.024815	0.980	1.184	1.119
mmu-miR-21a-5p	46	0.024815	1.115	0.831	0.790
mmu-miR-503-5p	47	0.024815	1.171	0.806	0.784
mmu-miR-328-3p	48	0.024815	1.133	1.308	1.338
mmu-let-7g-5p	49	0.024815	1.099	1.139	1.417
mmu-miR-362-3p	50	0.024815	0.888	0.804	0.663
mmu-miR-199a-5p	51	0.025155	0.904	0.602	0.631
mmu-miR-342-3p	52	0.027478	0.740	1.132	1.058
mmu-miR-34b-3p	53	0.028987	0.726	1.610	1.543
mmu-miR-15a-3p	54	0.028987	1.117	0.720	0.588
mmu-miR-139-5p	55	0.033183	0.892	1.180	1.070
mmu-miR-17-3p	56	0.033183	1.205	0.631	0.880
mmu-miR-130a-3p	57	0.033183	1.230	0.993	0.943
mmu-miR-149-5p	58	0.033183	0.911	1.294	1.527
mmu-miR-29b-3p	59	0.033183	1.023	0.816	0.739
mmu-miR-1a-3p	60	0.035135	0.709	1.330	2.129
mmu-miR-23b-3p	61	0.036567	0.966	1.179	1.113
mmu-miR-215-5p	62	0.036567	0.745	0.696	0.475
mmu-miR-204-5p	63	0.040650	0.856	1.631	1.808
mmu-miR-187-3p	64	0.041980	0.940	0.938	0.563
mmu-miR-200b-5p	65	0.041980	1.187	1.538	1.668
mmu-miR-25-3p	66	0.041980	1.093	1.171	1.537
mmu-miR-338-3p	67	0.046951	1.095	0.857	0.812
mmu-miR-196b-5p	68	0.049110	1.316	1.065	0.734

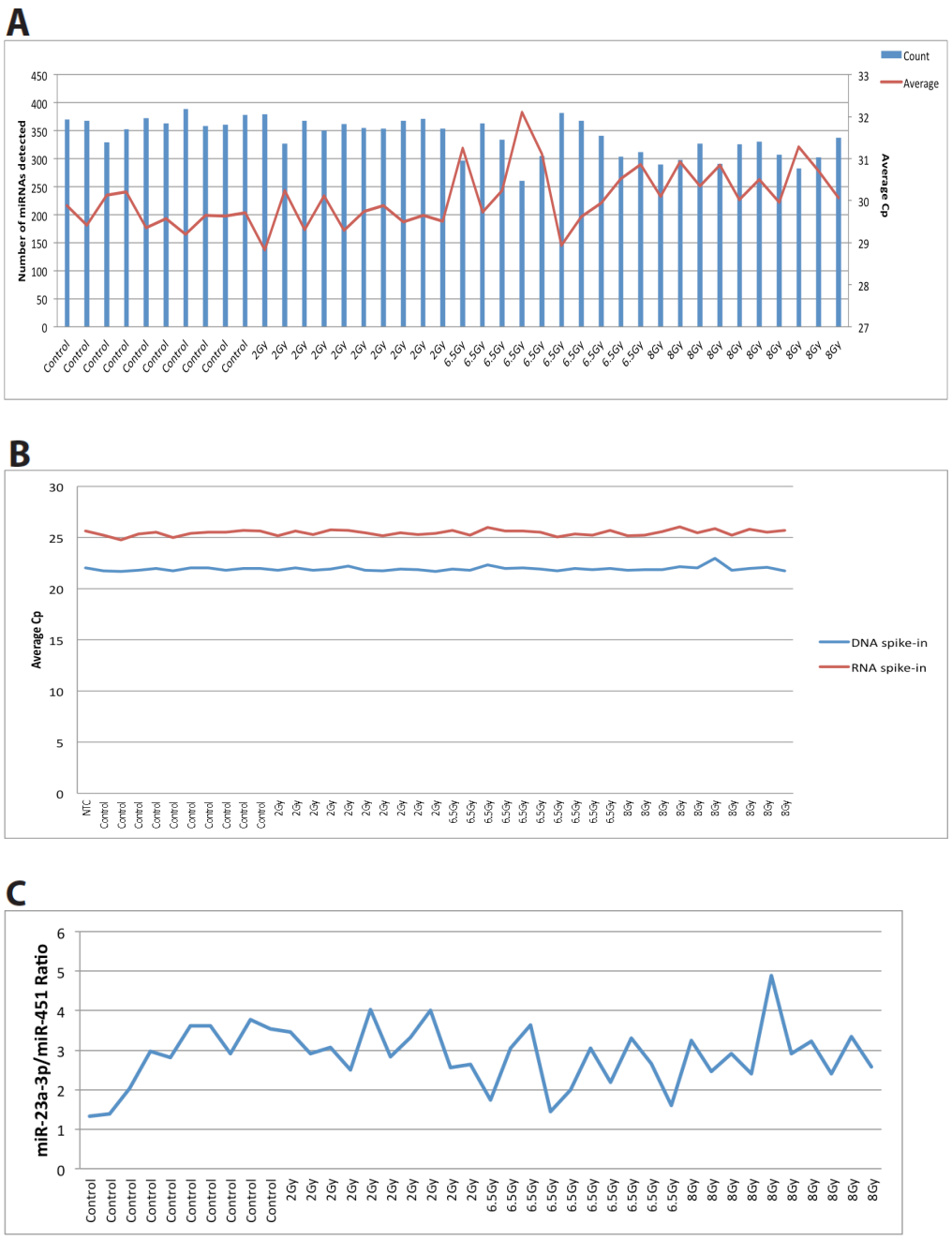

Figure 4.9: Serum miRNA profiling.
C57BL/6J mice were exposed to 0, 2, 6.5, or 8 Gy TBI (*n* = 10 animals per group). Serum collected from these animals 24 h after TBI was subjected to miRNA profiling. (**A**) Number of miRNAs detected per sample (count) and the average amplification threshold (Cp) value for miRNAs in each sample. (**B**) Built-in RNA (UniSp6) and DNA (UniSp3) spike-in controls used to test technical performance of samples. (**C**) Hemolysis controls to test for red blood cell contamination of serum miRNAs. ΔCp values consisting of miR-451 (expressed in red blood cells) and miR-23a-3p (relatively stable in serum) was used to

Figure 4.9 (Continued):
estimate likelihood of hemolysis (see Materials and Methods). Data in (A to C) represent each of the samples used in the original profiling experiment.

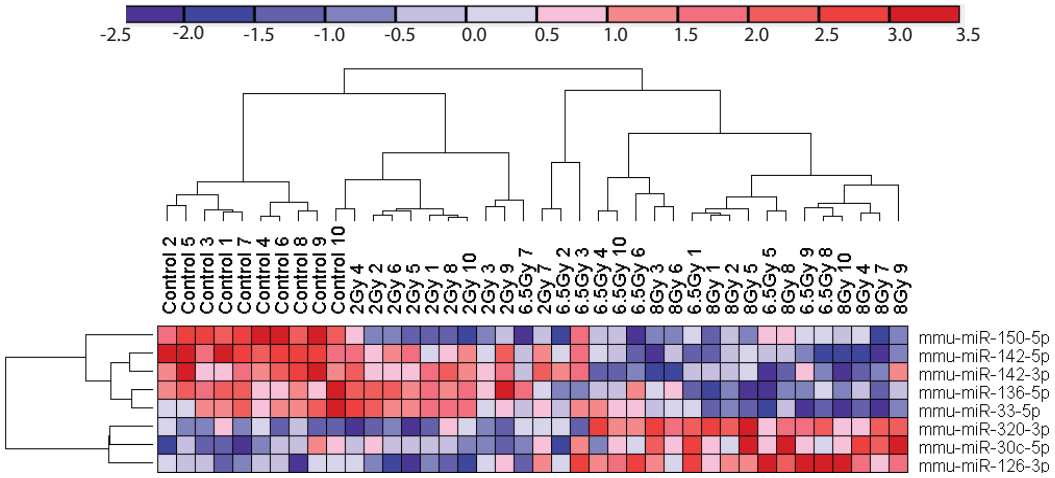

Figure 4.10: miRNAs significantly altered in all irradiated samples.
Heat map shows expression changes in levels of eight miRNAs significantly altered in all irradiated samples (2, 6.5, and 8 Gy) with respect to un-irradiated controls (0 Gy). Hierarchical clustering was performed to depict relationship between samples.

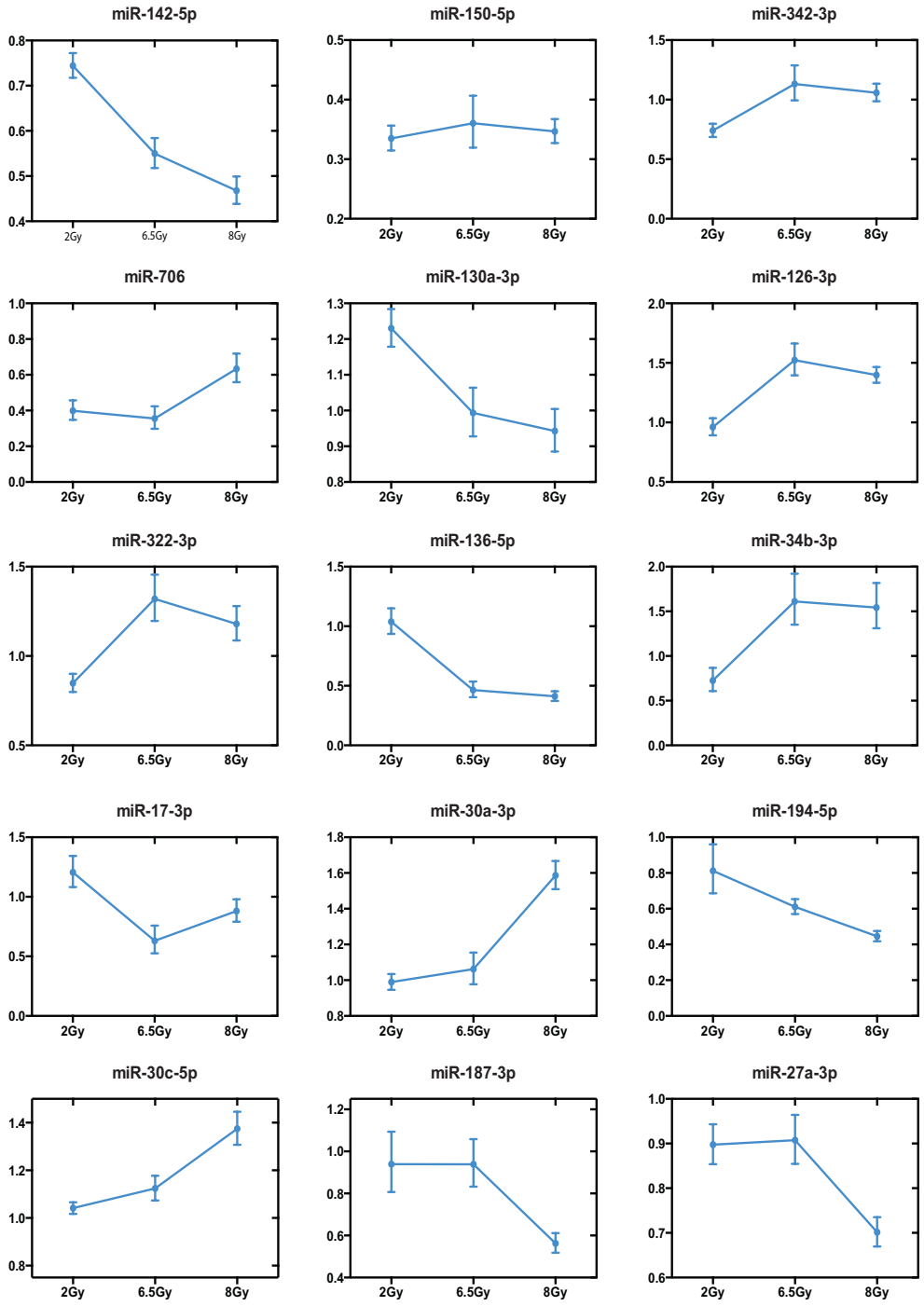

Figure 4.11: Radiation dose–dependence of select miRNAs.
Average fold change for each miRNA identified in one of the three signatures is presented at the three radiation doses (2, 6.5, and 8 Gy). Profiling data were reanalyzed to determine dose-dependence by calculating fold change with respect to the same miRNA level in control unirradiated samples. Data are averages ± SEM (*n* = 10 animals per group).

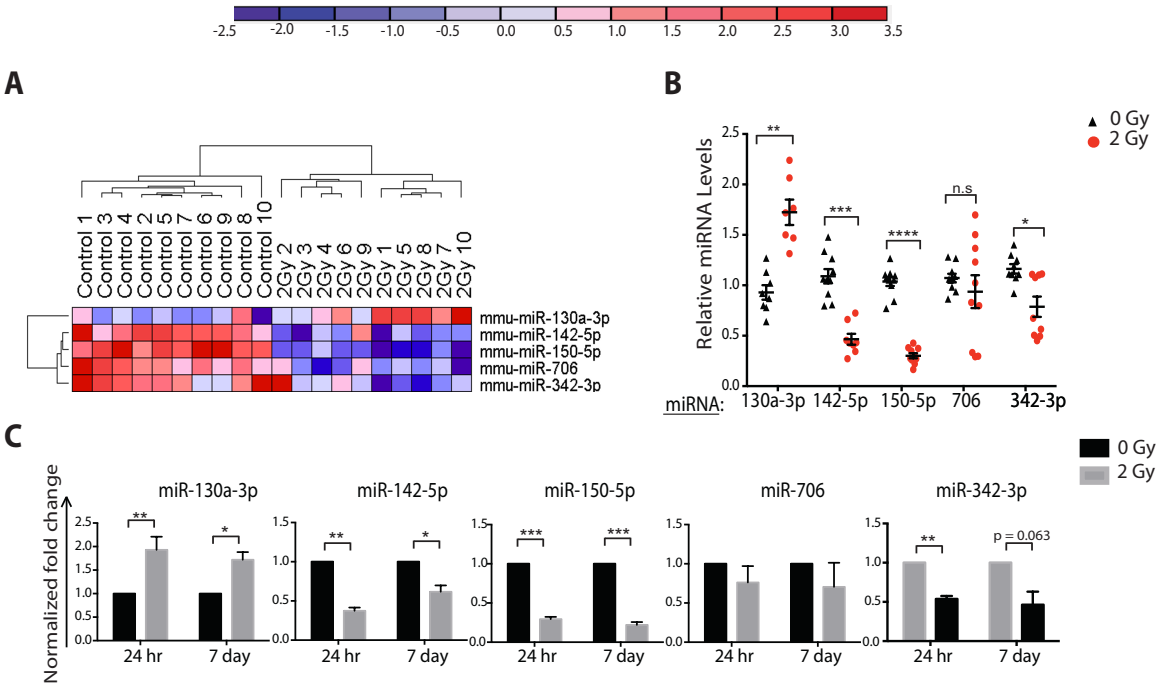

Figure 4.12: Serum miRNA profiling and identification of radiation dose–specific 0 vs 2 Gy miRNA signature.
C57BL/6J mice were exposed to 0, 2, 6.5, or 8 Gy TBI (*n* = 10/group). Serum collected from these animals 24 h after TBI was subjected to miRNA profiling. Three signatures – 0 vs 2 Gy, 2 vs 6.5 Gy, and 6.5 vs 8 Gy - consisting of the most highly altered 5 miRNAs in each comparison were generated. The 0 vs. 2 Gy signature is presented here. **(A)** Control (0 Gy) versus 2 Gy miRNA signature with hierarchical clustering depicting relationship between individual samples. **(B)** Validation of the 0 vs 2 Gy signature in (A) with an independent set of animals. **(C)** miRNA fold changes in 2 Gy irradiated animals compared to 0 Gy controls at 24 h and 7 days post-TBI. Data in (B and C) are normalized to miR-101a or miR-19b. Data in (B) are individual animals with means ± SEM (*n* = 6-10/group, two independent experiments). Data in (C) are means ± SEM (*n* = 4-5/group). **P* < 0.05; ***P* < 0.01; ****P* < 0.001; *****P* < 0.0001; n.s., not significant; paired t test.

whereas miR-150-5p, miR-142-5p, miR-706, and miR-342-3p showed significant decreases. We validated this signature using an independent set of animals that were left untreated or exposed to a TBI dose of 2 Gy and observed that all but one miRNA (miR-706) distinguished control and 2 Gy irradiated samples after 24 hours (Fig. 4.12B). The serum miRNA pattern continued to distinguish the 0 versus 2 Gy cohorts at the 7 day post-radiation time point (Fig. 4.12C), and was consistent with the diminished numbers of HSCs and HPCs in the 2 Gy cohort compared with unirradiated controls (Fig. 4.4A and B). It is noteworthy that, unlike the serum miRNA signature, BM-MNC counts 1 week after radiation exposure did not differentiate the unirradiated versus 2 Gy cohorts (Fig. 4.3B).

Next, we asked whether serum miRNAs can be used to distinguish between low and high sub-lethal doses of radiation. Such a miRNA signature may be useful in distinguishing individuals that incurred mild radiation-related toxicity at low sub-lethal doses and more severe (often non-recoverable) bone marrow damage at high sub-lethal doses (Greenberger and Epperly, 2009; Mauch et al., 1988). To address this question, we revisited our profiling data to identify miRNAs differentially expressed in the sera of mice exposed to 2 and 6.5 Gy TBI. Five miRNAs—miR-136-5p, miR-17-3p, miR-126-3p, miR-322-3p, and miR-34b-3p—showed the highest differential expression (Fig. 4.13A). We independently confirmed that miR-34b-3p, miR-126-3p, and miR-17-3p effectively distinguished between low and high sub-lethal TBI doses at 24 h (Fig. 4.13B). Interestingly, these three miRNAs continued to separate the two sub-lethal groups at day 7 (Fig. 4.13C).

Serum miRNA signature distinguishes animals exposed to sub-lethal and lethal dose

Similar to the 0 versus 2 Gy scenarios, analysis of hematopoietic damage alone was unable to differentiate between animals exposed to high sub-lethal (6.5 Gy) and lethal (8 Gy) dose of TBI until 15 days following radiation (Figs. 4.3 and 4.4). Although a relatively small difference (1.5 Gy), this increase in radiation dose is lethal. We therefore mined our profiling data in search of a set of serum miRNAs that were significantly different between 6.5 and 8 Gy treatment groups at 24 hours post-radiation. The five differentially expressed miRNAs are in Fig. 4.14A; two were higher at 8 Gy (miRs 30a-3p and 30c-5p) and three were lower at 8 Gy (187-3p, 194-5p, and 27a-3p). In a separate cohort of animals, four of the five miRNAs remained significant (Fig. 4.14B). Interestingly, none of the miRNAs that distinguished 0 from 2 Gy, 2 from 6.5 Gy, or 6.5 from 8 Gy overlapped. The focus of our study was to identify distinct sets of miRNAs with the highest differences between certain TBI comparisons, so our signatures represent the most highly altered miRNAs. However, there may be other miRNAs that continue to change with increasing doses (Table 4.1).

We further characterized the sub-lethal versus lethal serum miRNA signature to ask whether the miRNAs differentially expressed between the two groups continued to show differences at later time points. Sera were collected from mice at 24 hours, 3 days, and 7 days after TBI doses of 6.5 and 8 Gy. Only miR-30a-3p and miR-30c-5p continued to differentiate 6.5 versus 8 Gy at days 3 and 7 post-TBI (Fig. 4.14C), suggesting that these miRNAs may allow

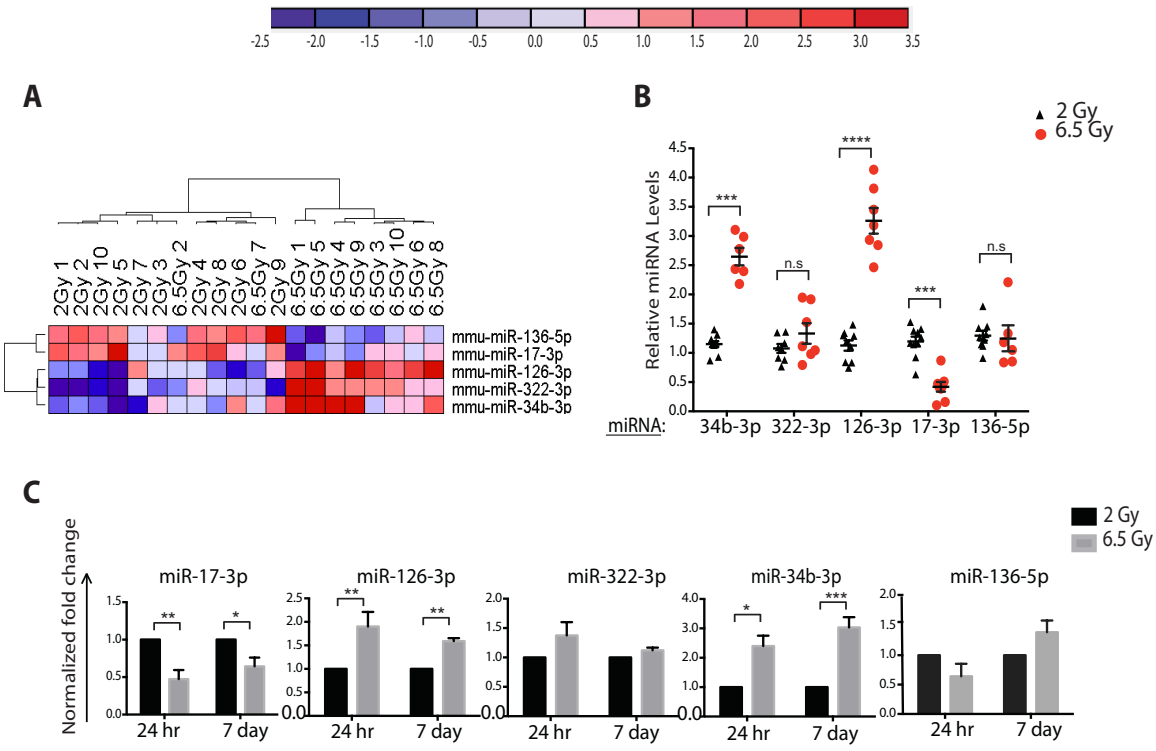

Figure 4.13: Serum miRNA profiling and identification of radiation dose–specific 2 vs 6.5 Gy miRNA signature.
Signature was generated as described in Fig. 4.12. **(A)** Signature for 2 versus 6.5 Gy with hierarchical clustering depicting relationship between individual samples. **(B)** Validation of the 2 vs 6.5 Gy signature in (D) with an independent set of animals. **(C)** miRNA fold changes in 6.5 Gy irradiated animals compared to 2 Gy at 24 h and 7 days post-TBI. Data in (B and C) are normalized to miR-101a or miR-19b. Data in (B) are individual animals with means ± SEM (*n* = 6-10/group, two independent experiments). Data in (C) are means ± SEM (*n* = 4-5/group). **P* < 0.05; ***P* < 0.01; ****P* < 0.001; *****P* < 0.0001; n.s., not significant; paired t test.

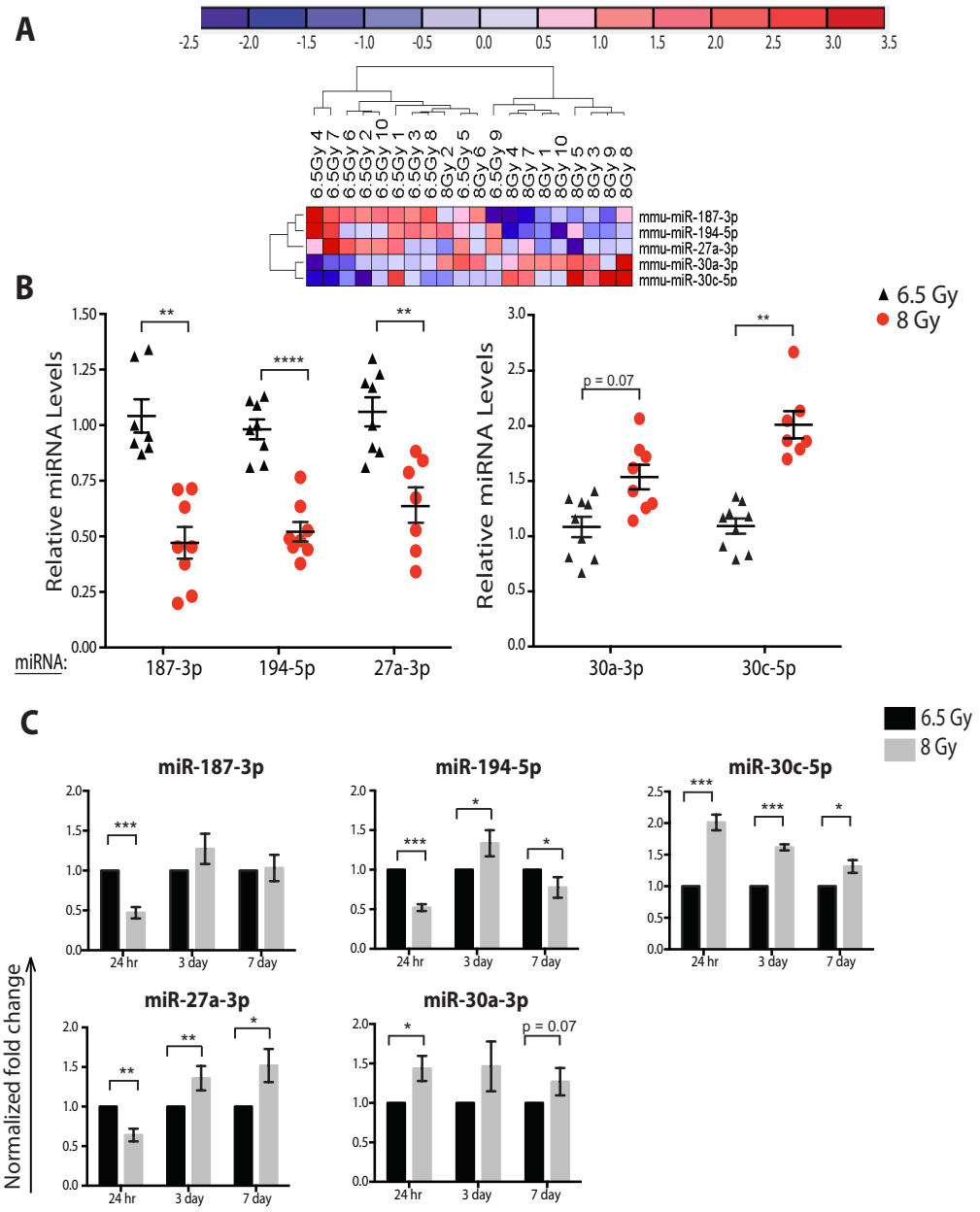

Figure 4.14: The 6.5 vs 8 Gy miRNA signature can differentiate between sub-lethal and lethal radiation exposure.
Signature was generated as described in Fig. 4.12 **(A)** The 6.5 versus 8 Gy miRNA signature presented with hierarchical clustering showing relationship between individual samples. **(B)** Validation of the 6.5 versus 8 Gy signature in (A) with an independent set of animals. Data are individual animals with means normalized to miR-101a ± SEM (*n* = 7-9/group, two independent experiments). **(C)** miRNA fold changes in 8 Gy irradiated animals compared to 6.5 Gy at 24 h, 3 days, and 7 days post-TBI. Data in (C) are means normalized to miR-101a ± SEM (*n* = 4-5/group). *$P < 0.05$; **$P < 0.01$; ***$P < 0.001$; ****$P < 0.0001$; n.s., not significant; paired t test.

differentiation of sub-lethal versus lethally irradiated samples up to 7 days after initial exposure.

Serum miRNAs distinguishing sub-lethal and lethal radiation, not only radiation dose, correlates with survival and radioprotection

Next, we determined whether the sub-lethal versus lethal serum miRNA signature correlated only with the radiation dose, or if it was also linked to overall survival. To address this question, we used a radioprotective agent amifostine, which is known to extend survival in mice and in humans by decreasing radiation-related cytotoxicity (Andreassen et al., 2003; Hosseinimehr, 2007). We hypothesized that if serum miRNAs are indeed linked to the impact of radiation on health, then serum miRNA levels in animals treated with amifostine prior to lethal TBI should correlate with the protective effect of this drug.

Cohorts of mice were treated with saline or amifostine prior to 8.5 Gy TBI and sera were collected 24 hours following exposure (Fig. 4.15A). All mice exposed to lethal radiation and injected with saline died around day 16, whereas 100% of animals treated with amifostine survived (Fig. 4.15B). All miRNAs in the sublethal versus lethal signature from Fig. 4.14A were significantly altered when comparing differences between groups (Table 4.2) and when comparing saline-treated versus amifostine-treated irradiated animals (Table 4.3). The serum miRNA signature only changed in response to amifostine treatment after lethal radiation (not after control 0 Gy) (Fig. 4.16A). Remarkably, the serum miRNA levels correlated with the radio-protective function of amifostine; that is, the

amifostine-treated lethal radiation cohort resembled the control sub-lethal radiation cohorts (Fig. 4.16A). This result strongly suggests that a serum miRNA signature distinguishing sub-lethal versus lethal radiation correlates with impact of radiation rather than dose.

To further substantiate this point we correlated relative miRNA expression for animals irradiated with 8.5 Gy in the radioprotection study (amifostine) with relative expression ratios of 8 and 6.5 Gy TBI cohorts in the original profiling study (Figs. 4.14A and 4.15A). We hypothesized that, if the serum miRNA signature distinguishing sub-lethal versus lethal radiation correlates with viability rather than radiation dose, the changes in these miRNAs in the radioprotection experiment will statistically correlate with the changes in the 8- and 6.5 Gy TBI cohorts. That is, the amifostine-treated lethal radiation cohort will truly represent the sub-lethally radiated 6.5 Gy cohort. Consistent with our hypothesis, we uncovered a significant correlation ($r= 0.97$; $p = 0.0067$, Pearson's correlation) (Fig. 4.16B), suggesting that the five miRNAs (187-3p, 194-5p, 27a-3p, 30a-3p, and 30c-5p) may serve as markers of radiation-induced loss of viability in mice.

We next asked whether this miRNA signature also corresponds to the protective effects of radio-mitigating agents introduced post-radiation. Transplantation of bone marrow stromal cells (BMSCs) after lethal radiation exposure promotes recovery of bone marrow cellularity, HPCs, and HSCs in mice (Chute et al., 2007). We therefore transplanted lethally irradiated (10.4 Gy) C57Bl/6J mice with two doses of BMSCs after radiation and monitored survival for 30 days (Fig. 4.17A). All animals in the TBI group succumbed to lethal

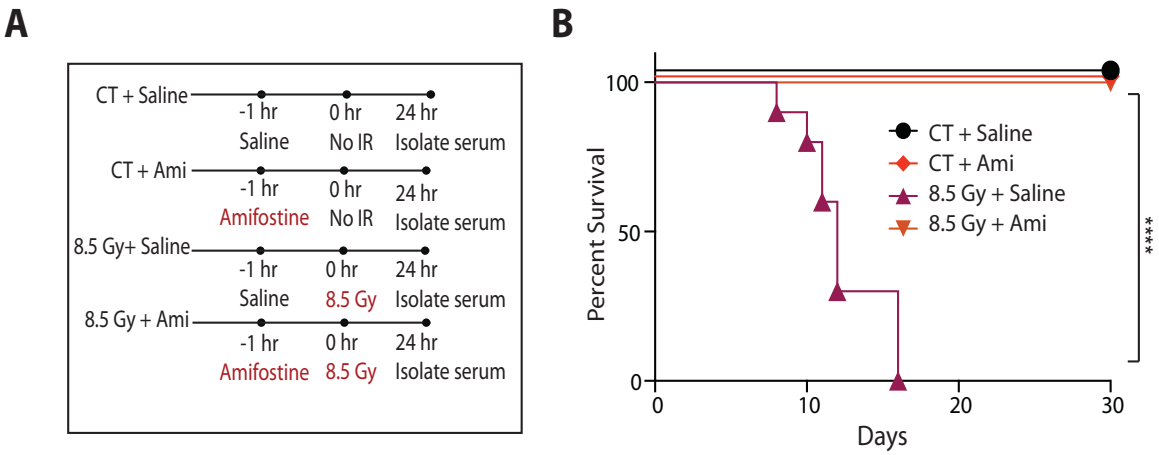

Figure 4.15: Radioprotective agent amifostine protects C57BL/6J mice from lethal TBI.

(A) Schematic of experiment with C57BL/6J mice given amifostine or saline 1 h before 0 or 8.5 Gy TBI (*n* = 10/ group). Serum was isolated for miRNA profiling 24 h later. **(B)** Kaplan-Meier survival curves of mice. P-value determined by log-rank (Mantel-Cox) test.

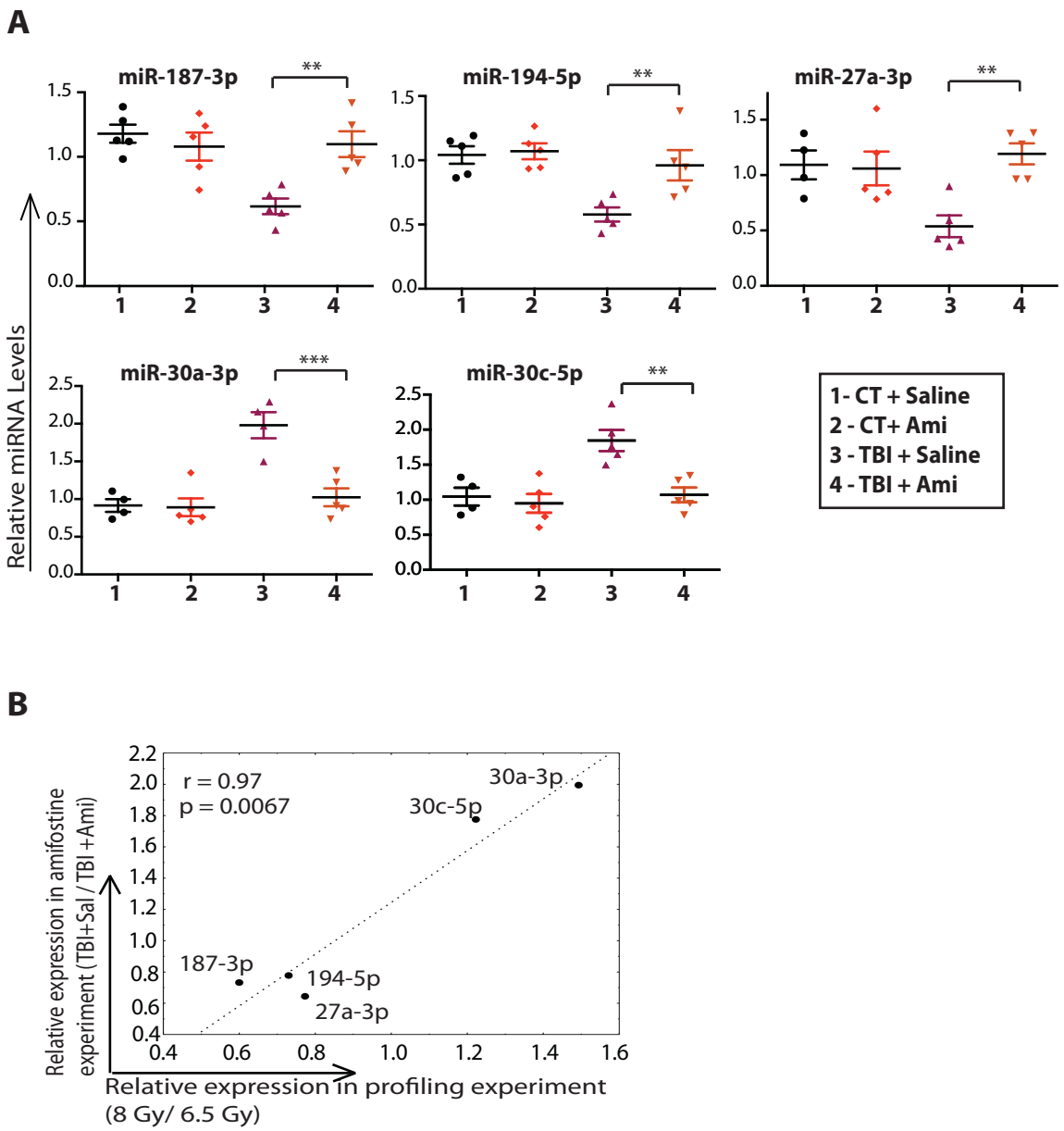

Figure 4.16: The sublethal versus lethal miRNA signature predicts impact of radioprotective agents.

Experiment was performed as per the protocol in Fig 4. 15A. **(A)** Relative levels of indicated miRNAs in the sera of mice. Data are individual animals with means normalized to miR-101a ± SEM (*n* = 5/group; two independent experiments). **(B)** Correlation of relative expression ratios of miRNAs in the 6.5 versus 8 Gy signature from two separate experiments: those described in 4.15A and in Fig. 4.14A (r = 0.97; *P* = 0.0067, Pearson's correlation). ***P*< 0.01; ****P*< 0.001; *****P*< 0.0001; n.s., not significant; one-way ANOVA followed by Dunnett's test.

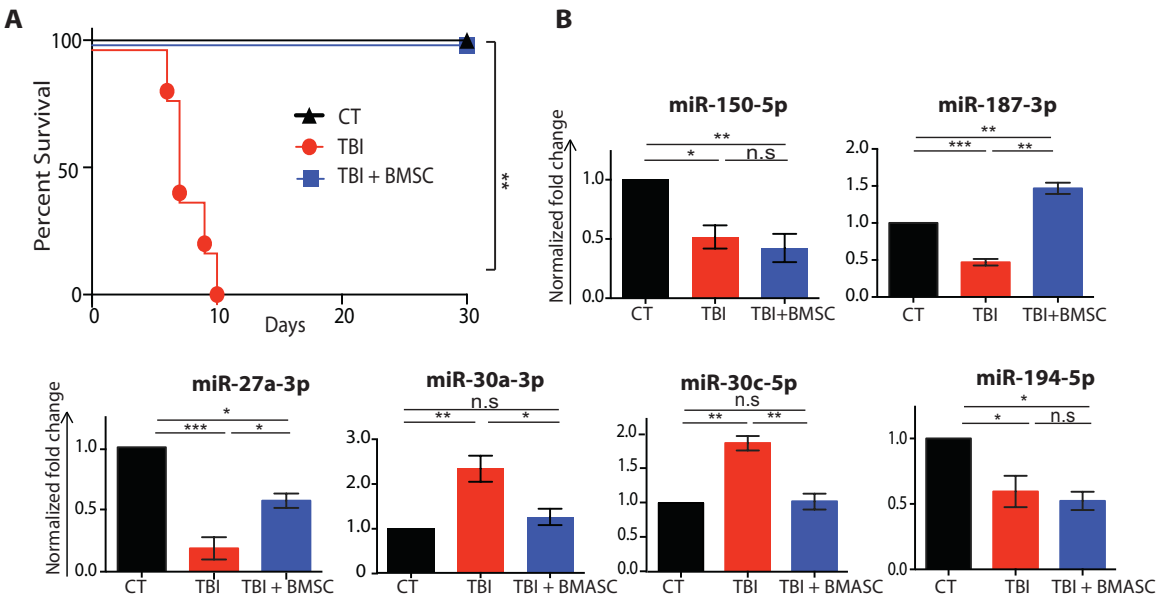

Figure 4.17: **The sublethal versus lethal miRNA signature predicts impact of radiomitigating agents.**
(A) Survival curve of C57BL/6J mice exposed to 10.4 Gy TBI followed by transplantation of BMSCs (*n* = 5/group). P-value determined by log-rank (Mantel-Cox) test. **(B)** Fold change of indicated miRNAs from sera of animals in (A) at day 5- post TBI. Data are means normalized to miR-101a ± SEM. **P*< 0.05; ***P*< 0.01; ****P*< 0.001; n.s., not significant; one-way ANOVA followed by Dunnett's test.

Table 4.2: Significantly altered miRNAs between 6.5 and 8 Gy irradiation and pre-treatment with amifostine. Per the protocol in Fig. 5A, mice were treated with amifostine 1 h prior to 8.5 Gy TBI dose to study whether miRNAs in the 6.5 versus 8 Gy signature were predictors of animal viability (*n* = 10 per group). Differences in expression values of indicated miRNAs in the four treatment groups (CT + Saline, CT + Ami, 8.5 Gy + Saline, 8.5 Gy + Ami) were compared by one-way ANOVA.

miRNA	***P***
miR-187-3p	0.0013
miR-194-5p	0.0016
miR-27a-3p	0.0063
miR-30a-3p	<0.0001
miR-30c-5p	0.0006

Table 4.3: MiRNAs in the 6.5 versus 8 Gy signature as indicators of survival after TBI. Mice were treated per protocol in Fig. 5A (*n* = 10 per group). *P* values for comparison of specific miRNA expression changes between the 8.5 Gy + Saline group and the other three experimental groups (CT + saline, CT + amifostine, 8.5 Gy + Ami) are presented. One-way ANOVA followed by Dunnett's test.

miRNA	CT + Saline	CT + Ami	TBI + Ami
miR-187-3p	0.0009	0.0046	0.0034
miR-194-5p	0.0022	0.0013	0.0097
miR-27a-3p	0.0182	0.0183	0.0038
miR-30a-3p	0.0002	<0.0001	0.0003
miR-30c-5p	0.0023	0.0005	0.0018

radiation by day 10, but 100% of animals transplanted with BMSCs survived, exhibiting the protective effect of BMSC transplantation.

Furthermore, four out of five miRNAs in the sublethal versus lethal signature (not miR-194-5p) indicated radio-mitigation by BMSCs at day 5 post exposure (Fig. 4.17B). Decrease in miR-150-5p has emerged as a consistent marker of radiation exposure in mice (Cui et al., 2011; Jacob et al., 2013) including our 0 versus 2 Gy miRNA signature (Fig. 4.12A). However, as anticipated from our data, miR-150-5p did not differ between TBI and TBI with BMSC treatment.

Validation of the serum miRNA signature in humanized mice

To test the relevance and potential applicability in humans, we validated miRNA levels in a second, "humanized" model system. We used NOD *scid* gamma (NSG) mice engrafted with human $CD34^+$ HSCs. NSG mice support robust long-term engraftment of human HSCs and their multilineage differentiation (Pearson et al., 2008). Initial engraftment percentages of human $CD45^+$ cells in peripheral blood of mice are in Table 4.4. CD45 staining of bone marrow and peripheral blood in animals approximately 12 weeks after initial assessment of engraftment showed similar or higher percentages of human cells (Fig. 4.18A).

Four to 4.5 Gy of TBI causes 100% mortality in NSG mice (Shultz et al., 2005). Therefore, we exposed huCD34+ NSG mice to a lethal dose of 4.5 Gy TBI, and considering the reconstitution of the hematopoietic compartment with

human cells, we focused on bone marrow injury, peripheral blood counts, and the potential for marrow recovery by amifostine. Exposure to lethal radiation showed near complete depletion of BM-MNCs in the saline-treated TBI cohort, whereas prior treatment with amifostine showed rescue of bone marrow cellularity, and moderate recovery of human $CD45^+$ cells and bone marrow CFU-Cs cultured in human medium (Fig. 4.18B-D). Peripheral blood counts of moribund animals indicated a significant decrease in all blood cell parameters except WBCs, as well as a substantial improvement in hemoglobin, RBC levels, and hematocrit levels was observed in the amifostine-treated group (Table 4.5). These data suggest that $huCD34^+$ NSG mice are sensitive to the effects of radiation and that amifostine treatment led to protection of the human cells.

The sequences of the miRNAs in the sublethal-versus-lethal signature in mice are identical to those of humans (Fig. 4.20)(Kiezun et al., 2012). To assess whether the effect of lethal radiation with amifostine treatment is reflected in the levels of miRNAs in the sublethal-versus-lethal signature, we isolated serum from these humanized animals 24 hr after radiation and measured miRNA levels (Fig. 4.19). Consistent with previous results in C57Bl/6J mice, miR-150-5p and four out of five miRNAs in the in the 6.5 vs. 8 Gy signature (miR-27a-3p, miR-187-3p, miR-30a-3p, and miR-30c-5p) were altered in response to radiation in $huCD34^+$ NSG mice. Furthermore, amifostine pretreatment rescued levels of three of the miRNAs (miR-187-3p, miR-27a-3p, and miR-30a-3p). Together these results suggest that serum miRNA signatures may be conserved between mice and

humans, and thus have the potential to serve as indicators of radiation injury in humans.

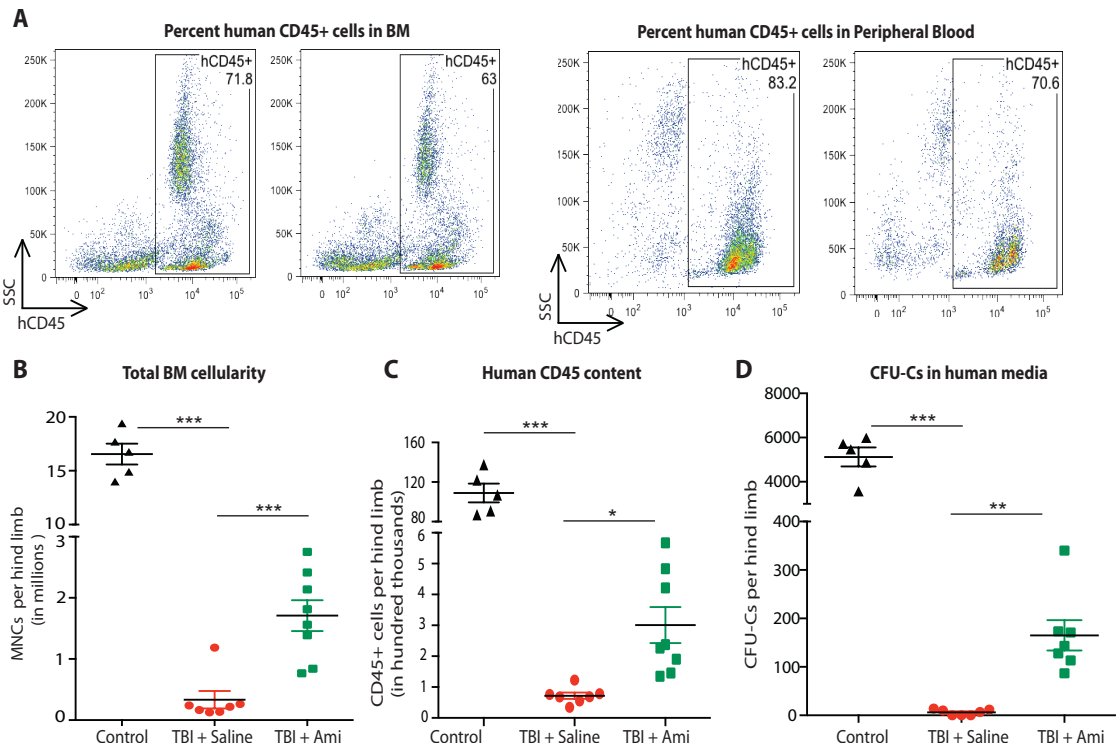

Figure 4.18: Sublethal versus lethal miRNA signature correlates with the protective effect of amifostine in NSG mice engrafted with human CD34$^+$ HSCs.

(A) Representative (*n* = 5) FACS plots showing percent engraftment of human CD45$^+$ cells in the bone marrow and peripheral blood of NSG mice transplanted with human CD34$^+$ HSCs. **(B** to **D)** Humanized NSG mice were pretreated with amifostine or saline and exposed to 4.5 Gy TBI. Control animals received no pretreatment and 0 Gy irradiation. Moribund animals were analyzed for total bone marrow cellularity (B), number of human CD45$^+$ cells per hind limb (C), and CFU-Cs measured at 7 days after plating in human methylcellulose media (D). Data are individual animals with means ± SEM (*n* = 5-8/group); paired t-test (B, C, and D).

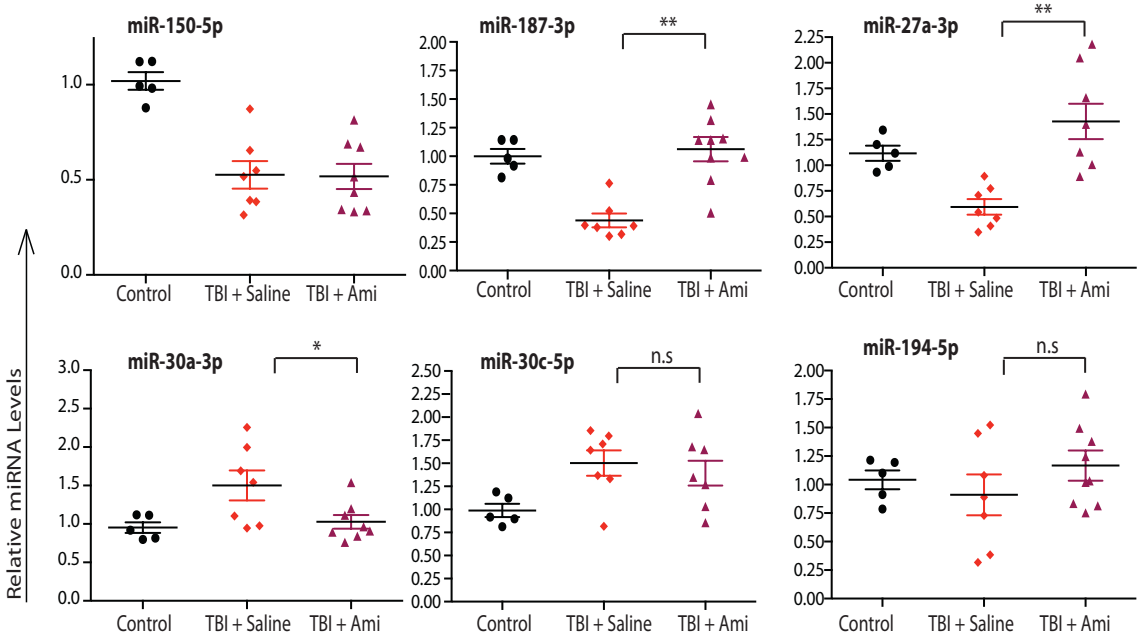

Figure 4.19: Sublethal versus lethal miRNA signature correlates with the protective effect of amifostine in NSG mice engrafted with human CD34^{+} HSCs.

Relative miRNA levels in the sera of humanized mice at 24 hr after exposure to TBI. Data are individual animals with means normalized to miR-101a ± SEM. *P < 0.05; **P < 0.01; ***P < 0.001; n.s., not significant, one-way ANOVA followed by Dunnett's test (E).

Fig. 4.20: Identical mature miRNA sequences in human and mouse.
Genomic sequences of miRNAs in the 6.5 versus 8 Gy signatures were aligned using microRNAviewer. Mature sequences are highlighted in blue. Asterisks (*) indicate base conservation.
<http://people.csail.mit.edu/akiezun/microRNAviewer/index.html>

Table 4.4: Percent human CD45$^+$ cell engraftment in individual huCD34$^+$ NSG (humanized) mice. Vendor provided engraftment percentages analyzed at 12 weeks after transplantation. Animals were grouped into three groups, namely Control untreated (*n* = 5), TBI + Saline (*n* = 7), and TBI + Amifostine (*n* = 8). Human CD45$^+$ cell engraftment was reconfirmed at the end of the experiment in control untreated animals.

Mouse	hCD45+ engraftment in mouse peripheral blood (%)	Treatment
1	75.2	TBI + Saline
2	49.8	TBI + Saline
3	52.1	TBI + Saline
4	60.2	TBI + Saline
5	50.9	TBI + Saline
6	65	TBI + Saline
7	55.8	TBI + Saline
8	58.2	TBI + Amifostine
9	52.5	TBI + Amifostine
10	62.1	TBI + Amifostine
11	74.3	TBI + Amifostine
12	67.5	TBI + Amifostine
13	52.1	TBI + Amifostine
14	49.6	TBI + Amifostine
15	61.4	TBI + Amifostine
16	51.8	Control
17	50.8	Control
18	55.9	Control
19	58.8	Control
20	65.8	Control

Table 4.5: Peripheral blood complete blood count in individual huCD34^{+} NSG (humanized) mice. Peripheral blood was harvested from moribund TBI-treated animals or unirradiated controls. Average and SEM of CBC parameters are calculated per group.

Group	Mouse #	CBC				
		WBC (x 10^3/µl)	RBC (x 10^6/µl)	Hb (g/dl)	HCT (%)	PLT (x 10^3/µl)
TBI + Saline	2	1.20	0.24	1.90	1.60	20
	5	1.30	0.19	2.80	1.20	4
	7	0.56	1.64	2.80	3.00	88
	Avg	1.02	0.69	2.50	1.93	37.33
	SEM	0.23	0.48	0.30	0.55	25.75
TBI + Amifostine	8	1.28	2.55	4.80	17.00	213
	9	1.19	1.65	3.20	11.00	44
	13	1.20	2.92	4.80	4.80	56
	Avg	1.22	2.37	4.27	10.93	104.33
	SEM	0.03	0.38	0.53	3.52	54.44
Control	16	1.20	4.75	11.00	38.50	345
	17	1.32	5.35	10.50	39.60	609
	18	2.16	5.66	12.40	42.20	686
	19	1.77	5.89	11.60	45.30	645
	20	1.44	5.41	10.70	40.60	577
	Avg	1.58	5.41	11.24	41.24	572.40
	SEM	0.17	0.19	0.34	1.18	59.69

Table 4.6: Target sequences of individual miRNAs. MiRNAs in the three signatures reported in Fig. 3 and their target sequences detected using Pick-N-Mix plates are shown. Sequences for miR-101a and miR-19b, identified as stable miRNAs in the sera of C57BL/6J mice and used for normalization of miRNA validation and expression data, are also listed. UniSp6 and UniSp3 sequences are proprietary (Exiqon).

	miRNA	Target sequence
Control miRNA	mmu-miR-101a-3p	UACAGUACUGUGAUAACUGAA
Control miRNA	mmu-miR-19b-3p	UGUGCAAAUCCAUGCAAAACUGA
RNA spike-in	UniSp6	Exiqon Proprietary Sequence
DNA spike-in	UniSp3	Exiqon Proprietary Sequence
0 Gy v. 2 Gy signature	mmu-miR-130a-3p	CAGUGCAAUGUUAAAAGGGCAU
	mmu-miR-142-5p	CAUAAAGUAGAAAGCACUACU
	mmu-miR-150-5p	UCUCCCAACCCUUGUACCAGUG
	mmu-miR-706	AGAGAAACCCUGUCUCAAAAAA
	mmu-miR-342-3p	UCUCACACAGAAAUCGCACCCGU
2Gy v. 6.5 Gy signature	mmu-miR-34b-3p	AAUCACUAACUCCACUGCCAUC
	mmu-miR-322-3p	AAACAUGAAGCGCUGCAACAC
	mmu-miR-126-3p	UCGUACCGUGAGUAAUAAUGCG
	mmu-miR-17-3p	ACUGCAGUGAGGGCACUUGUAG
	mmu-miR-136-5p	ACUCCAUUUGUUUUGAUGAUGG
6.5 Gy v. 8 Gy signature	mmu-miR-187-3p	UCGUGUCUUGUGUUGCAGCCGG
	mmu-miR-194-5p	UGUAACAGCAACUCCAUGUGGA
	mmu-miR-27a-3p	UUCACAGUGGCUAAGUUCCGC
	mmu-miR-29a-3p	UAGCACCAUCUGAAAUCGGUUA
	mmu-miR-30a-3p	CUUUCAGUCGGAUGUUUGCAGC
	mmu-miR-30c-5p	UGUAAACAUCCUACACUCUCAGC

DISCUSSION

Current use of diagnostic screening to estimate dose of accidental radiation exposure is mainly based on three factors: time to onset of radiation sickness, kinetics of lymphocyte depletion, and analysis of chromosomal abnormalities (Dainiak et al., 2003; Waselenko et al., 2004). These techniques are time-consuming and are often not quantitative enough to draw definite conclusions. Serum miRNAs fall under the emerging “omic” biodosimetry assays and represent a simple technology that may effectively determine whether an individual was exposed to radiation (if so, whether the dose was sublethal or lethal), and predict long-term survival of exposed individuals. With current progress in miniaturization of quantitative PCR, a miRNA-based assay has the potential to become a point-of-care technology that can be performed outside the lab. It can allow longer lag time post-exposure before the first sample can be taken compared to lymphocyte depletion kinetics and DNA damage assay using γ–H2AX and provide results within the 12-24 hrs following exposure.

Here, we successfully profiled and identified novel serum miRNAs that were differentially expressed in response to TBI and correlated well with injury at sub-lethal and lethal doses. Recent studies (Cui et al., 2011; Jacob et al., 2013; Templin et al., 2011) have identified circulating (serum/plasma) miRNAs that are altered in response to TBI, and there is partial overlap with some of the candidate miRNAs (miR-126-3p, miR-150, miR-342-3p, miR-151-3p, miR-139-3p and miR-142) that emerged from our analysis. A possible cause for the differences is the miRNA expression profiling platform. Recently a study (Mestdagh et al., 2014)

systematically compared 12 different miRNA expression platforms. Specifically for serum miRNAs there was a 12-fold difference between the highest and lowest number of detected miRNA when identical samples were profiled by different platforms. According to this report, the LNA-based platform from Exiqon—which we use in our study—had the highest specificity.

A key issue we addressed in this study is the correlation of serum miRNAs with the impact of radiation, specifically with hematopoietic injury and animal viability. Working with a narrow dose range, we identified serum miRNAs that distinguish between sub-lethal (6.5 Gy) and lethal (8 Gy) exposure. This is of paramount importance because during a radiologic emergency, doses sustained will almost never be in specific increments and distinction between lethal and sub-lethal doses is the key challenge. Moreover this miRNA signature also predicted the impact of radiation on animal survival following pre-treatment with the radio-protective agent, amifostine or mitigation using BMSC. Interestingly, most of the serum miRNAs (miR-187-3p, miR-27a-3p, miR-30a-3p, and miR-30c-5p) that correlated with amifostine radioprotection also predicted survival of animals transplanted with BMSCs. Finally, our experiments with huCD34+ NSG humanized mice suggest that the miRNAs identified in the C57BL/6J mouse model may also be relevant in humans. Together, these findings highlight the utility of miRNAs in predicting the functional impact of both radio-protective and radio-mitigating agents and broadly suggest a potential application of serum miRNAs in prognosticating the impact of radiation. Future studies, however, will

be needed in human samples to validate these miRNAs or discover new signatures that differentiate lethal from sublethal radiation effects.

Broadly our results provide the first evidence that serum miRNAs may effectively predict the impact of radiation on long-term viability of animals. Our work represents an advance in early assessment of radiation damage, which can help alleviate hematopoietic symptoms, facilitate timely intervention after exposure, and improve overall survival of exposed individuals.

REFERENCES

Andreassen, C.N., Grau, C., and Lindegaard, J.C. (2003). Chemical radioprotection: a critical review of amifostine as a cytoprotector in radiotherapy. Semin Radiat Oncol *13*, 62-72.

Blondal, T., Jensby Nielsen, S., Baker, A., Andreasen, D., Mouritzen, P., Wrang Teilum, M., and Dahlsveen, I.K. (2013). Assessing sample and miRNA profile quality in serum and plasma or other biofluids. Methods *59*, S1-6.

Chin, F.K. (2007). Scenario of a dirty bomb in an urban environment and acute management of radiation poisoning and injuries. Singapore Med J *48*, 950-957.

Christensen, D.M., Iddins, C.J., Parrillo, S.J., Glassman, E.S., and Goans, R.E. (2014). Management of ionizing radiation injuries and illnesses, part 4: acute radiation syndrome. The Journal of the American Osteopathic Association *114*, 702-711.

Chute, J.P., Muramoto, G.G., Salter, A.B., Meadows, S.K., Rickman, D.W., Chen, B., Himburg, H.A., and Chao, N.J. (2007). Transplantation of vascular endothelial cells mediates the hematopoietic recovery and survival of lethally irradiated mice. Blood *109*, 2365-2372.

Coleman, C.N., Stone, H.B., Moulder, J.E., and Pellmar, T.C. (2004). Medicine. Modulation of radiation injury. Science *304*, 693-694.

Cortez, M.A., Bueso-Ramos, C., Ferdin, J., Lopez-Berestein, G., Sood, A.K., and Calin, G.A. (2011). MicroRNAs in body fluids--the mix of hormones and biomarkers. Nat Rev Clin Oncol *8*, 467-477.

Cui, W., Ma, J., Wang, Y., and Biswal, S. (2011). Plasma miRNA as biomarkers for assessment of total-body radiation exposure dosimetry. PLoS One *6*, e22988.

Dainiak, N., Waselenko, J.K., Armitage, J.O., MacVittie, T.J., and Farese, A.M. (2003). The hematologist and radiation casualties. Hematology / the Education Program of the American Society of Hematology. American Society of Hematology. Education Program, 473-496.

Greenberger, J.S., and Epperly, M. (2009). Bone marrow-derived stem cells and radiation response. Semin Radiat Oncol *19*, 133-139.

Hosseinimehr, S.J. (2007). Trends in the development of radioprotective agents. Drug Discov Today *12*, 794-805.

Jacob, N.K., Cooley, J.V., Yee, T.N., Jacob, J., Alder, H., Wickramasinghe, P., Maclean, K.H., and Chakravarti, A. (2013). Identification of sensitive serum microRNA biomarkers for radiation biodosimetry. PLoS One *8*, e57603.

Kiezun, A., Artzi, S., Modai, S., Volk, N., Isakov, O., and Shomron, N. (2012). miRviewer: a multispecies microRNA homologous viewer. BMC research notes *5*, 92.

Mauch, P., Constine, L., Greenberger, J., Knospe, W., Sullivan, J., Liesveld, J.L., and Deeg, H.J. (1995). Hematopoietic stem cell compartment: acute and late effects of radiation therapy and chemotherapy. Int J Radiat Oncol Biol Phys *31*, 1319-1339.

Mauch, P., Rosenblatt, M., and Hellman, S. (1988). Permanent loss in stem cell self renewal capacity following stress to the marrow. Blood *72*, 1193-1196.

Mendell, J.T., and Olson, E.N. (2012). MicroRNAs in stress signaling and human disease. Cell *148*, 1172-1187.

Mestdagh, P., Hartmann, N., Baeriswyl, L., Andreasen, D., Bernard, N., Chen, C., Cheo, D., D'Andrade, P., DeMayo, M., Dennis, L.*, et al.* (2014). Evaluation of quantitative miRNA expression platforms in the microRNA quality control (miRQC) study. Nature methods *11*, 809-815.

Mitchell, P.S., Parkin, R.K., Kroh, E.M., Fritz, B.R., Wyman, S.K., Pogosova-Agadjanyan, E.L., Peterson, A., Noteboom, J., O'Briant, K.C., Allen, A.*, et al.* (2008). Circulating microRNAs as stable blood-based markers for cancer detection. Proc Natl Acad Sci U S A *105*, 10513-10518.

Nunamaker, E.A., Artwohl, J.E., Anderson, R.J., and Fortman, J.D. (2013). Endpoint refinement for total body irradiation of C57BL/6 mice. Comparative medicine *63*, 22-28.

Parmar, K., Kim, J., Sykes, S.M., Shimamura, A., Stuckert, P., Zhu, K., Hamilton, A., Deloach, M.K., Kutok, J.L., Akashi, K.*, et al.* (2010). Hematopoietic stem cell defects in mice with deficiency of Fancd2 or Usp1. Stem Cells *28*, 1186-1195.

Pearson, T., Greiner, D.L., and Shultz, L.D. (2008). Creation of "humanized" mice to study human immunity. Current protocols in immunology / edited by John E. Coligan ... [et al.] *Chapter 15*, Unit 15 21.

Seo, J., Gordish-Dressman, H., and Hoffman, E.P. (2006). An interactive power analysis tool for microarray hypothesis testing and generation. Bioinformatics *22*, 808-814.

Shao, L., Feng, W., Li, H., Gardner, D., Luo, Y., Wang, Y., Liu, L., Meng, A., Sharpless, N.E., and Zhou, D. (2014). Total body irradiation causes long-term mouse BM injury via induction of HSC premature senescence in an Ink4a- and Arf-independent manner. Blood *123*, 3105-3115.

Shultz, L.D., Lyons, B.L., Burzenski, L.M., Gott, B., Chen, X., Chaleff, S., Kotb, M., Gillies, S.D., King, M., Mangada, J.*, et al.* (2005). Human lymphoid and

myeloid cell development in NOD/LtSz-scid IL2R gamma null mice engrafted with mobilized human hemopoietic stem cells. Journal of immunology *174*, 6477-6489.

Templin, T., Amundson, S.A., Brenner, D.J., and Smilenov, L.B. (2011). Whole mouse blood microRNA as biomarkers for exposure to gamma-rays and (56)Fe ion. Int J Radiat Biol *87*, 653-662.

Wang, Y., Schulte, B.A., LaRue, A.C., Ogawa, M., and Zhou, D. (2006). Total body irradiation selectively induces murine hematopoietic stem cell senescence. Blood *107*, 358-366.

Waselenko, J.K., MacVittie, T.J., Blakely, W.F., Pesik, N., Wiley, A.L., Dickerson, W.E., Tsu, H., Confer, D.L., Coleman, C.N., Seed, T.*, et al.* (2004). Medical management of the acute radiation syndrome: recommendations of the Strategic National Stockpile Radiation Working Group. Ann Intern Med *140*, 1037-1051.

CHAPTER 5

Discussion

Paradigm of DNA Damage Induced Phospho-Signaling and an Emerging Role for Phosphatases in DDR

In this dissertation we provide new evidence for the involvement of the PP4 serine/threonine phosphatase in regulating the early steps of DDR. We also present this regulation in the context of the cell cycle. The traditional paradigm for DNA damage induced phospho-signaling states that sensors of DNA damage activate specific kinases. Targets of these kinases (which are mediators and effectors of DDR) are then activated and it is the combination of mediators and effectors that produce different effector responses (Petrini, 2007)(Fig. 5.1). An excellent example of this paradigm is 53BP1, which acts as a DDR mediator. ATM phosphorylation and distinct chromatin modifications allow 53BP1 to localize to DSBs following DNA damage. After chromatinization 53BP1 acts as a platform for localization of other key DDR factors. Recent literature has identified specific effectors of 53BP1, namely RIF1 and PTIP that interact with 53BP1 by distinct phospho-protein interactions leading to distinct effector responses (Callen et al., 2013; Chapman et al., 2013; Di Virgilio et al., 2013; Escribano-Diaz et al., 2013; Zimmermann et al., 2013).

Our laboratory has asked the broad question of whether phosphatases, which reverse the action of kinases, have any role in this process. The traditional view has been that phosphatases dissociate the mediator-effector complexes formed and restore cells to a pre-DNA damage state. Several examples of this important function of phosphatases exist (Chowdhury et al., 2008; Lee et al., 2010; Nakada et al., 2008). However, recent evidence from our lab suggests that

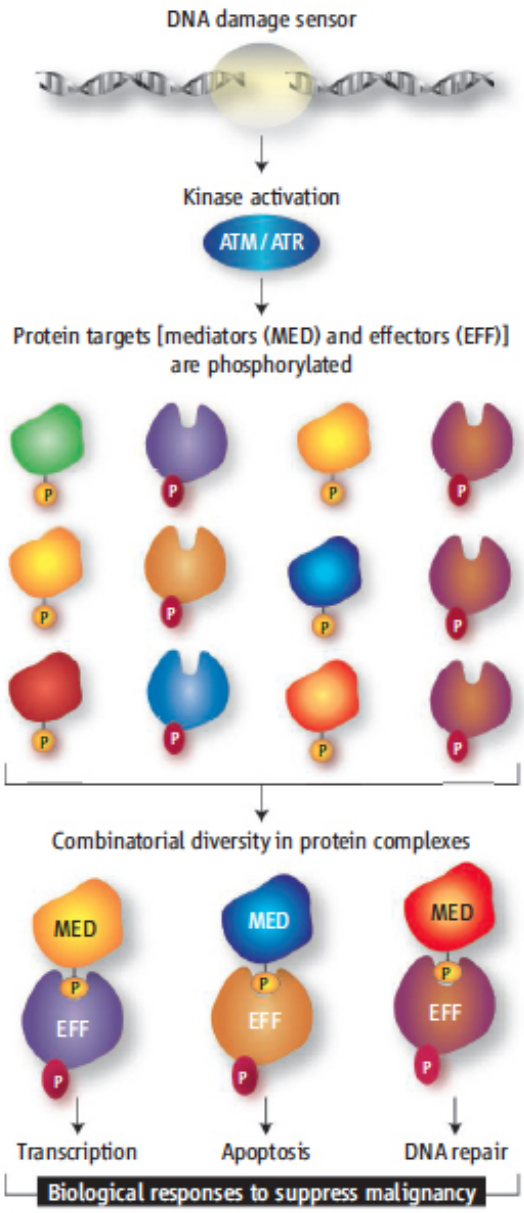

Figure 5.1: Paradigm of DNA Damage Induced Phospho-Signaling (Petrini, 2007).

in addition to resetting DNA damage, phosphatases play a crucial role during the activation of DDR. In this dissertation, we present an example of one such regulation mediated by the PP4/R3□ phosphatase complex. We report that 53BP1 is hyperphosphorylated in mitosis at two key residues (T1609 and S1618) located in the conserved UDR motif and this correlates with its exclusion from DNA breaks. As the cells exit mitosis and enter G1, efficient recruitment of 53BP1 to DSBs requires dephosphorylation of the UDR residues, a process dependent on the activity of the PP4/R3□ complex (Figs. 5.2 and 5.3A). This example brings to light a potential role for PP4 and other DDR phosphatases in regulating DDR activation.

Cell Cycle Regulation of Other DDR Proteins by Phosphatases

When examining the cell-cycle regulation of DDR proteins, multiple parallels can be drawn with the example of 53BP1 and common themes begin to emerge. Like 53BP1, XRCC4 is another NHEJ factor that acts as a recruitment platform linking the essential steps of processing and ligation of broken DNA ends (Koch et al., 2004; Lieber, 2010; Weterings and Chen, 2008). XRCC4 activity is also suppressed during mitosis and correlates with its mitosis specific phosphorylation of Ser326 by CDK1/PLK1 (Fig. 5.3B) (Terasawa et al., 2014). Activating XRCC4 in mitosis leads to increased occurrence of anaphase bridges, which can be suppressed by inhibition of NHEJ. Thus, phosphorylation of XRCC4 prevents its recruitment to DNA breaks in mitosis thereby avoiding the formation

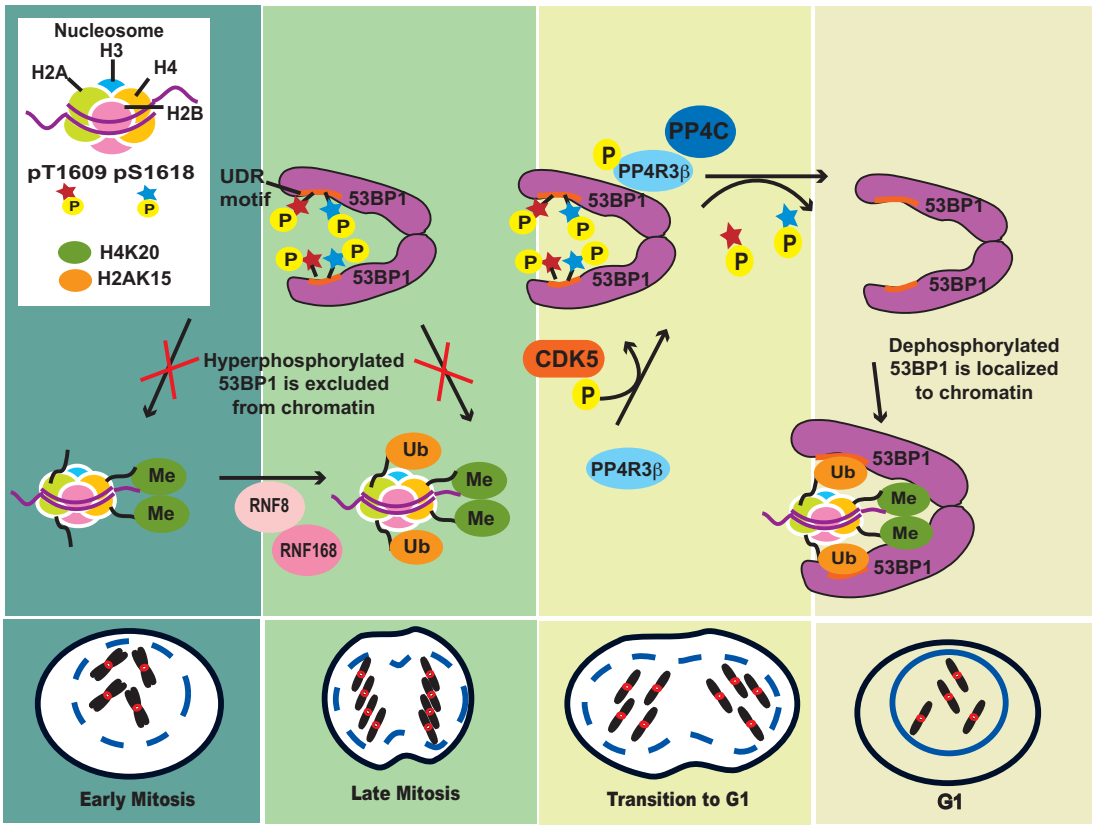

Figure 5.2: Model for regulation of 53BP1 by PP4/R3□.
53BP1 is hyperphosphorylated in mitosis to disable its recruitment to DSBs. A PP4/R3□ complex dephosphorylates 53BP1 at T1609 and S1618 during the transition from mitosis to G1. The interaction of 53BP1-R3□ is regulated by CDK5-mediated phosphorylation of R3□ S840. The action of CDK5 enables temporal control of the R3□-53BP1 interaction allowing 53BP1 to relocalize at DSBs in G1 (Lee et al., 2014 and this dissertation).

of mitotic defects. This mode of regulation is very similar to what we observed for 53BP1 and therefore it is tempting to speculate that a phosphatase complex dephosphorylates XRCC4 at Ser326 at the end of mitosis re-allowing it to participate in NHEJ in G1.

Yet another interesting example of phosphatase-based activation of function is that of YEN1 (Yen1 Holiday junction resolvase), which belongs to the XPG family of nucleases. YEN1 forms a complex with the MUS81-MMS4 junction-specific endonucleases that promote formation of crossover products by cleaving HR intermediates (Blanco et al., 2010; Ho et al., 2010; Tay and Wu, 2010). Since non-crossover products are favored over crossover products in mitotic cells to prevent loss of heterozygosity (LOH) (Ira et al., 2003), it is essential to exclude YEN1 from participating in the resolution of HR intermediates during mitosis. Indeed, CDKs target YEN1 starting as early as S phase, thereby sequestering its nuclear localization and inhibiting its participation in HR until the anaphase stage (Kosugi et al., 2009; Loog and Morgan, 2005; Ubersax et al., 2003). Interestingly, the phosphatase CDC14 was shown to be responsible for countering this phosphorylation to allow nuclear relocalization of YEN1 thereby restimulating its activity (Fig. 5.3C) (Blanco et al., 2014). The above discussed examples of 53BP1, XRCC4, and YEN1 suggest that phosphatases ‘prime’ the activity of DDR factors in a cell-cycle dependent manner by countering the phosphorylation of mitotic kinases.

Cell-cycle Regulation of 53BP1 and PP4 In S/G2

53BP1 has been extensively studied during the cell cycle. In the G1 phase, when NHEJ is more common, 53BP1 exerts its pro-NHEJ effects by suppressing end-resection and inhibiting BRCA1 accumulation at DSBs via RIF1 (Callen et al., 2013; Chapman et al., 2013; Di Virgilio et al., 2013; Escribano-Diaz et al., 2013; Zimmermann et al., 2013). As cells enter S/G2, the action of BRCA1 specifically excludes 53BP1 from DSBs, thereby promoting end resection, which is a key bottleneck for DSB repair by HR (Chapman et al., 2012; Feng Lin, 2015). The Chapman study used super-resolution microscopy to show that 53BP1 is capable of accumulating at DNA repair foci in G1, S, and G2 phases. However, in S and G2 it is removed from core S phase foci in a BRCA1-dependent fashion. Furthermore, it was recently shown that BRCA1 excludes 53BP1 and RIF1 from DSBs via its interaction with CTIP (Escribano-Diaz et al., 2013; Feng et al., 2013).

Consistent with this notion of restricting 53BP1 from localizing to DSBs in S and G2, we have observed an increase in phosphorylation of 53BP1 T1609 and S1618 using the p (1609/1618) antibody as cells enter S and G2 phases (Fig. 5.4). It is tempting to speculate that the same kinases that phosphorylate these residues in mitosis may be responsible for phosphorylating them in late S and G2 phases. It is also conceivable that a separate pool of 53BP1 is phosphorylated in S/G2 and suppressed from DSB localization. While our observations are preliminary, they indicate that phosphorylation-based regulation of 53BP1 may not be restricted only to mitosis but is likely to occur throughout the cell cycle. Indeed, a recent study reported mitosis-specific phosphorylations occurring at the

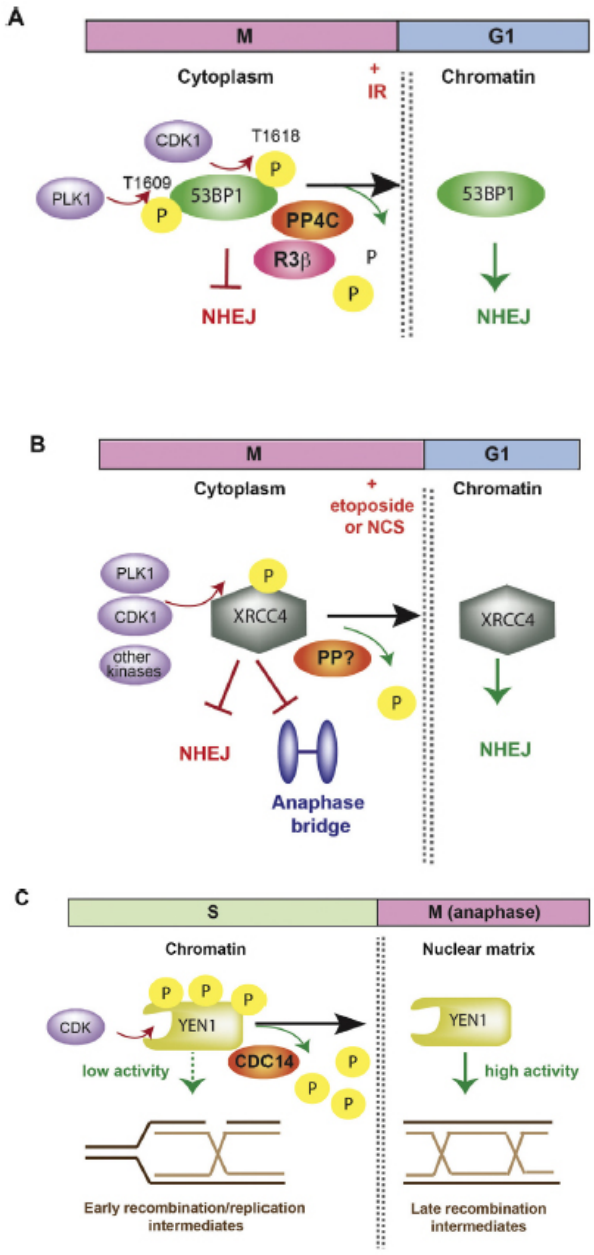

Figure 5.3: Regulation of DDR factors by dephosphorylation during the cell cycle. A model for regulation of 53BP1 **(A)** and XRCC4 **(B)** by dephosphorylation during mitosis/G1. **(C)** YEN1 regulation by dephosphorylation during S phase and mitosis (Zheng et al., 2015).

Noc release: 0 6 8 10 12 14 16 (h)

%G1	1.82	70.0	63.72	44.13	33.78	18.73	7.86
%S	3.42	17.28	22.35	43.34	63.94	60.7	51.16
%G2/M	94.7	12.41	13.93	12.53	2.27	20.56	40.98

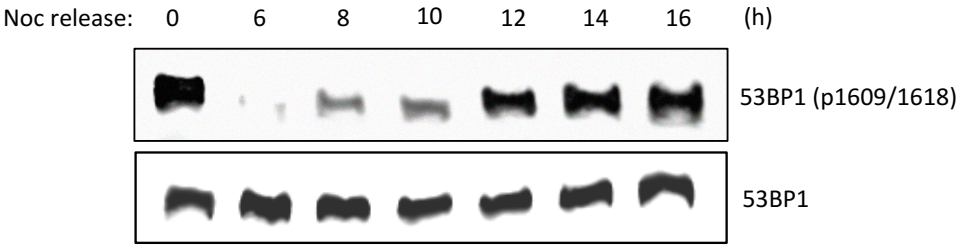

Figure 5.4: Phosphorylation of T1609/S1618 increases as cells enter S/G2. *Upper panel:* Percent HeLa cells in indicated cell cycle phases at each time point after release from nocodazole (Noc) treatment. *Lower panel:* Assessment of 53BP1 phosphorylation using the p (1609/1618) antibody. Total 53BP1 is shown as a loading control.

completion of S phase. Specifically, the study reported that PLK1 is active ~5 hours before mitotic entry (Akopyan et al., 2014). Furthermore, in one of the studies mentioned earlier, Escribano-Diaz and colleagues showed that the ability of BRCA1-CTIP to inhibit RIF1 foci formation in S/G2 is dependent on CTIP S327 and S487 phosphorylation. Both these sites are phosphorylated by CDKs suggesting that CDKs are active in S phase (Escribano-Diaz et al., 2013).

It will be interesting to see whether concurrent phosphorylation of 53BP1 during S/G2 by mitotic kinases regulates 53BP1 exclusion from DSB foci as a parallel regulatory mechanism. Experiments involving ectopic expression of 53BP1-AA mutant (T1609A/S1618A) in Fucci cells can address this question. On the other hand, it will also be interesting to see if ectopic expression of 53BP1-ED mutant (T1609E/S1618D) allows BRCA1 to accumulate at DSBs in G1. We intend to answer these questions in the near future.

Similar to 53BP1, we also plan to study whether PP4 is regulated during S/G2 phases. According to our preliminary observations cited above, after PP4-mediated dephosphorylation of 53BP1 in G1, T1609 and S1618 appear to be re-phosphorylated in preparation for the next phase of mitosis. In this scenario, it is conceivable that PP4C/ R3β is somehow inhibited from accessing 53BP1 and this may occur through a few possible mechanisms. First, the localization of PP4 may be regulated by multiple post-translational modifications sequestering it from the nucleus during S/G2. While an interesting idea, this does not seem likely since the role of PP4 in dephosphorylating nuclear proteins, H2AX and RPA2 during S phase has been established (Chowdhury et al., 2008; Lee et al., 2010; Nakada et

al., 2008). Second, the association of the R3β regulatory subunit responsible for substrate specificity with the catalytic PP4C subunit may be prevented. Thus, even though R3β can interact with 53BP1, it cannot dephosphorylate in the absence of PP4C. Third, interaction of either 53BP1 or PP4 with an unknown factor may impede 53BP1/PP4 interaction. Future studies will focus on testing these hypotheses by identifying novel substrates and/or interacting partners of PP4. Recent advances in phosphoproteomic technologies offer increasingly unbiased approaches to identifying phosphatase substrates and specific phosphorylation sites (Zhou et al., 2010). Use of such approaches will develop a better understanding of phosphatase-based regulation of DDR.

We also report here a novel role for CDK5, which by phosphorylating R3□ at S840 in mitosis regulates the timing of 53BP1-R3□ interaction. In our experiments, siRNA-mediated depletion of CDK5 and also its inhibition by a new small molecule inhibitor reduced the localization of 53BP1 to DSBs. We therefore propose a model wherein CDK5-mediated phosphorylation of R3□ in mitosis ultimately regulates 53BP1 localization in G1 (Fig. 5.2). Interestingly, in neuronal cells, CDK5 plays a role in DDR by directly phosphorylating ATM at Ser794 thereby activating ATM and its downstream targets (Tian et al., 2009). However, the study we present here is one of the first reports implicating CDK5 in the regulation of a DDR factor in cancer cells. Future experiments focusing on the regulation of CDK5 during the cell cycle and the identification of regulatory feed-forward loops similar to CDK5-R3□-53BP1 involving other DDR factors will allow us to better understand the role of CDK5 during the repair of DSBs.

Biomarkers Indicating the Extent of Hematopoieitic Injury

A part of this dissertation also focused on the impact of DNA damage at the organismal level. Radiation-induced DNA damage caused by industrial accidents, terrorist attacks, or the use of nuclear weapons in military settings can have a substantial negative impact on human life and limited options exist for both the diagnosis and treatment of exposed individuals (Waselenko et al., 2004). In this study, we correlated radiation-induced DNA damage in animal models to the presence of specific miRNAs in the serum with the goal of identifying miRNA signatures that can effectively predict the severity of injury sustained before the appearance of symptoms. Our findings, recently published (Acharya et al., 2015), identify three different miRNA signatures that can effectively predict extent of radiation-induced hematopoietic damage and correlate with the impact of radiation on animal survival.

Existing technologies used to assess the extent of radiation have notable limitations. For example, one of the hallmarks of the lymphocyte depletion kinetics assay is the fact that it can be performed outside the laboratory, but a drawback is that several measurements are needed to get a dose estimate (Goans et al., 1997; Parker and Parker, 2007). The ideal time frame for DNA damage assays using □-H2AX is 0.5 to 2 hours post-exposure (Andrievski and Wilkins, 2009; Riecke et al., 2010; Sullivan et al., 2013), which may not be enough time for individuals to report to a medical countermeasures facility. The dicentrics chromosome assay is very specific to radiation and is considered the “gold standard” for determining the dose, but it has a long processing time, tedious

scoring methods, and relatively narrow range for dose determination (Pinto et al., 2010; Sullivan et al., 2013). Thus, there is a critical need to develop radiation-specific indicators that are capable of predicting latent damage to various organs and systems immediately after radiation exposure.

Although the miRNAs identified here can forecast the extent of hematopoietic injury and predict for survival immediately after exposure, it is possible that radiation victims may not report to a medical countermeasures facility in the first 24 hours. In such a scenario, biomarkers that persist longer will need to be identified. Profiling of serum miRNAs at later time points, such as 5 or 7 days, will allow detection of more persistent miRNAs that continue to follow a specific trend after radiation. As a proof of principle, miR-30a-3p and miR-30c-5p in our sub-lethal versus lethal signature continued to display an increase until day 7. Future studies should focus on defining the cell of origin of specific serum miRNAs and investigate their physiological relevance. This will help determine whether serum miRNAs are passive bystanders secreted in the wake of radiation injury or act as potential alarm signals communicating a state of distress to different parts of the body (Cortez et al., 2011; Mendell and Olson, 2012). Indeed, several groups have reported identification of circulating miRNAs found in exosomes (Valadi et al., 2007), apoptotic bodies (Zernecke et al., 2009), high-density lipoprotein (Vickers et al., 2011) and RNA-binding proteins (Arroyo et al., 2011) as a form of cell-to-cell communication (Cui et al., 2011; Kosaka et al., 2013) providing a rationale for future experimentation. Validation of serum

miRNAs identified here in non-human primates and patient samples will allow the application of these signatures in humans.

REFERENCES

Acharya, S.S., Fendler, W., Watson, J., Hamilton, A., Pan, Y., Gaudiano, E., Moskwa, P., Bhanja, P., Saha, S., Guha, C.*, et al.* (2015). Serum microRNAs are early indicators of survival after radiation-induced hematopoietic injury. Science translational medicine *7*, 287ra269.

Akopyan, K., Silva Cascales, H., Hukasova, E., Saurin, A.T., Mullers, E., Jaiswal, H., Hollman, D.A., Kops, G.J., Medema, R.H., and Lindqvist, A. (2014). Assessing kinetics from fixed cells reveals activation of the mitotic entry network at the S/G2 transition. Mol Cell *53*, 843-853.

Andrievski, A., and Wilkins, R.C. (2009). The response of gamma-H2AX in human lymphocytes and lymphocytes subsets measured in whole blood cultures. Int J Radiat Biol *85*, 369-376.

Arroyo, J.D., Chevillet, J.R., Kroh, E.M., Ruf, I.K., Pritchard, C.C., Gibson, D.F., Mitchell, P.S., Bennett, C.F., Pogosova-Agadjanyan, E.L., Stirewalt, D.L.*, et al.* (2011). Argonaute2 complexes carry a population of circulating microRNAs independent of vesicles in human plasma. Proc Natl Acad Sci U S A *108*, 5003-5008.

Blanco, M.G., Matos, J., Rass, U., Ip, S.C., and West, S.C. (2010). Functional overlap between the structure-specific nucleases Yen1 and Mus81-Mms4 for DNA-damage repair in S. cerevisiae. DNA repair *9*, 394-402.

Blanco, M.G., Matos, J., and West, S.C. (2014). Dual control of Yen1 nuclease activity and cellular localization by Cdk and Cdc14 prevents genome instability. Mol Cell *54*, 94-106.

Callen, E., Di Virgilio, M., Kruhlak, M.J., Nieto-Soler, M., Wong, N., Chen, H.T., Faryabi, R.B., Polato, F., Santos, M., Starnes, L.M.*, et al.* (2013). 53BP1 mediates productive and mutagenic DNA repair through distinct phosphoprotein interactions. Cell *153*, 1266-1280.

Chapman, J.R., Barral, P., Vannier, J.B., Borel, V., Steger, M., Tomas-Loba, A., Sartori, A.A., Adams, I.R., Batista, F.D., and Boulton, S.J. (2013). RIF1 is essential for 53BP1-dependent nonhomologous end joining and suppression of DNA double-strand break resection. Mol Cell *49*, 858-871.

Chapman, J.R., Sossick, A.J., Boulton, S.J., and Jackson, S.P. (2012). BRCA1-associated exclusion of 53BP1 from DNA damage sites underlies temporal control of DNA repair. Journal of cell science *125*, 3529-3534.

Chowdhury, D., Xu, X., Zhong, X., Ahmed, F., Zhong, J., Liao, J., Dykxhoorn, D.M., Weinstock, D.M., Pfeifer, G.P., and Lieberman, J. (2008). A PP4-phosphatase complex dephosphorylates gamma-H2AX generated during DNA replication. Mol Cell *31*, 33-46.

Cortez, M.A., Bueso-Ramos, C., Ferdin, J., Lopez-Berestein, G., Sood, A.K., and Calin, G.A. (2011). MicroRNAs in body fluids--the mix of hormones and biomarkers. Nat Rev Clin Oncol *8*, 467-477.

Cui, W., Ma, J., Wang, Y., and Biswal, S. (2011). Plasma miRNA as biomarkers for assessment of total-body radiation exposure dosimetry. PLoS One *6*, e22988.

Di Virgilio, M., Callen, E., Yamane, A., Zhang, W., Jankovic, M., Gitlin, A.D., Feldhahn, N., Resch, W., Oliveira, T.Y., Chait, B.T.*, et al.* (2013). Rif1 prevents resection of DNA breaks and promotes immunoglobulin class switching. Science *339*, 711-715.

Escribano-Diaz, C., Orthwein, A., Fradet-Turcotte, A., Xing, M., Young, J.T., Tkac, J., Cook, M.A., Rosebrock, A.P., Munro, M., Canny, M.D.*, et al.* (2013). A cell cycle-dependent regulatory circuit composed of 53BP1-RIF1 and BRCA1-CtIP controls DNA repair pathway choice. Mol Cell *49*, 872-883.

Feng, L., Fong, K.W., Wang, J., Wang, W., and Chen, J. (2013). RIF1 counteracts BRCA1-mediated end resection during DNA repair. J Biol Chem *288*, 11135-11143.

Feng Lin, L.N., Li Yujing, Wang Jiadong, Gao Min, Wang Wenqi, Chen Junjie (2015). Cell cycle-dependent inhibition of 53BP1 signaling by BRCA1. Cell Discovery *1*, 15019; doi:15010.11038/celldisc.12015.15019.

Goans, R.E., Holloway, E.C., Berger, M.E., and Ricks, R.C. (1997). Early dose assessment following severe radiation accidents. Health physics *72*, 513-518.

Ho, C.K., Mazon, G., Lam, A.F., and Symington, L.S. (2010). Mus81 and Yen1 promote reciprocal exchange during mitotic recombination to maintain genome integrity in budding yeast. Mol Cell *40*, 988-1000.

Ira, G., Malkova, A., Liberi, G., Foiani, M., and Haber, J.E. (2003). Srs2 and Sgs1-Top3 suppress crossovers during double-strand break repair in yeast. Cell *115*, 401-411.

Koch, C.A., Agyei, R., Galicia, S., Metalnikov, P., O'Donnell, P., Starostine, A., Weinfeld, M., and Durocher, D. (2004). Xrcc4 physically links DNA end processing by polynucleotide kinase to DNA ligation by DNA ligase IV. The EMBO journal *23*, 3874-3885.

Kosaka, N., Yoshioka, Y., Hagiwara, K., Tominaga, N., Katsuda, T., and Ochiya, T. (2013). Trash or Treasure: extracellular microRNAs and cell-to-cell communication. Front Genet *4*, 173.

Kosugi, S., Hasebe, M., Tomita, M., and Yanagawa, H. (2009). Systematic identification of cell cycle-dependent yeast nucleocytoplasmic shuttling proteins by prediction of composite motifs. Proc Natl Acad Sci U S A *106*, 10171-10176.

Lee, D.H., Acharya, S.S., Kwon, M., Drane, P., Guan, Y., Adelmant, G., Kalev, P., Shah, J., Pellman, D., Marto, J.A.*, et al.* (2014). Dephosphorylation enables the recruitment of 53BP1 to double-strand DNA breaks. Mol Cell *54*, 512-525.

Lee, D.H., Pan, Y., Kanner, S., Sung, P., Borowiec, J.A., and Chowdhury, D. (2010). A PP4 phosphatase complex dephosphorylates RPA2 to facilitate DNA repair via homologous recombination. Nat Struct Mol Biol *17*, 365-372.

Lieber, M.R. (2010). The mechanism of double-strand DNA break repair by the nonhomologous DNA end-joining pathway. Annu Rev Biochem *79*, 181-211.

Loog, M., and Morgan, D.O. (2005). Cyclin specificity in the phosphorylation of cyclin-dependent kinase substrates. Nature *434*, 104-108.

Mendell, J.T., and Olson, E.N. (2012). MicroRNAs in stress signaling and human disease. Cell *148*, 1172-1187.

Nakada, S., Chen, G.I., Gingras, A.C., and Durocher, D. (2008). PP4 is a gamma H2AX phosphatase required for recovery from the DNA damage checkpoint. EMBO reports *9*, 1019-1026.

Parker, D.D., and Parker, J.C. (2007). Estimating radiation dose from time to emesis and lymphocyte depletion. Health physics *93*, 701-704.

Petrini, J.H. (2007). Cell signaling. A touching response to damage. Science *316*, 1138-1139.

Pinto, M.M., Santos, N.F., and Amaral, A. (2010). Current status of biodosimetry based on standard cytogenetic methods. Radiation and environmental biophysics *49*, 567-581.

Riecke, A., Ruf, C.G., and Meineke, V. (2010). Assessment of radiation damage-the need for a multiparametric and integrative approach with the help of both clinical and biological dosimetry. Health physics *98*, 160-167.

Sullivan, J.M., Prasanna, P.G., Grace, M.B., Wathen, L.K., Wallace, R.L., Koerner, J.F., and Coleman, C.N. (2013). Assessment of biodosimetry methods for a mass-casualty radiological incident: medical response and management considerations. Health physics *105*, 540-554.

Tay, Y.D., and Wu, L. (2010). Overlapping roles for Yen1 and Mus81 in cellular Holliday junction processing. J Biol Chem *285*, 11427-11432.

Terasawa, M., Shinohara, A., and Shinohara, M. (2014). Canonical non-homologous end joining in mitosis induces genome instability and is suppressed by M-phase-specific phosphorylation of XRCC4. PLoS genetics *10*, e1004563.

Tian, B., Yang, Q., and Mao, Z. (2009). Phosphorylation of ATM by Cdk5 mediates DNA damage signalling and regulates neuronal death. Nat Cell Biol *11*, 211-218.

Ubersax, J.A., Woodbury, E.L., Quang, P.N., Paraz, M., Blethrow, J.D., Shah, K., Shokat, K.M., and Morgan, D.O. (2003). Targets of the cyclin-dependent kinase Cdk1. Nature *425*, 859-864.

Valadi, H., Ekstrom, K., Bossios, A., Sjostrand, M., Lee, J.J., and Lotvall, J.O. (2007). Exosome-mediated transfer of mRNAs and microRNAs is a novel mechanism of genetic exchange between cells. Nat Cell Biol *9*, 654-659.

Vickers, K.C., Palmisano, B.T., Shoucri, B.M., Shamburek, R.D., and Remaley, A.T. (2011). MicroRNAs are transported in plasma and delivered to recipient cells by high-density lipoproteins. Nat Cell Biol *13*, 423-433.

Waselenko, J.K., MacVittie, T.J., Blakely, W.F., Pesik, N., Wiley, A.L., Dickerson, W.E., Tsu, H., Confer, D.L., Coleman, C.N., Seed, T*., et al.* (2004). Medical management of the acute radiation syndrome: recommendations of the Strategic National Stockpile Radiation Working Group. Ann Intern Med *140*, 1037-1051.

Weterings, E., and Chen, D.J. (2008). The endless tale of non-homologous end-joining. Cell Res *18*, 114-124.

Zernecke, A., Bidzhekov, K., Noels, H., Shagdarsuren, E., Gan, L., Denecke, B., Hristov, M., Koppel, T., Jahantigh, M.N., Lutgens, E*., et al.* (2009). Delivery of microRNA-126 by apoptotic bodies induces CXCL12-dependent vascular protection. Sci Signal *2*, ra81.

Zheng, X.F., Kalev, P., and Chowdhury, D. (2015). Emerging role of protein phosphatases changes the landscape of phospho-signaling in DNA damage response. DNA repair *32*, 58-65.

Zhou, H., Albuquerque, C.P., Liang, J., Suhandynata, R.T., and Weng, S. (2010). Quantitative phosphoproteomics: New technologies and applications in the DNA damage response. Cell cycle *9*, 3479-3484.

Zimmermann, M., Lottersberger, F., Buonomo, S.B., Sfeir, A., and de Lange, T. (2013). 53BP1 regulates DSB repair using Rif1 to control 5' end resection. Science *339*, 700-704.